Tensor networks, quantum spin chains, and quantum field theory

by

Yijian Zou

A thesis
presented to the University of Waterloo
in fulfillment of the
thesis requirement for the degree of
Doctor of Philosophy
in
Physics

Waterloo, Ontario, Canada, 2020

Examining Committee Membership

The following served on the Examining Committee for this thesis. The decision of the Examining Committee is by majority vote.

External Examiner:	German Sierra Professor, Instituto de Fisica Teorica
Supervisor(s):	Guifre Vidal Adjunct Faculty, Dept. of Physics, University of Waterloo, Senior Faculty, Perimeter Institute for Theoretical Physics Yin-Chen He Adjunct Faculty, Dept. of Physics, University of Waterloo, Junior Faculty, Perimeter Institute for Theoretical Physics
Internal Member:	Roger Melko Professor, Dept. of Physics, University of Waterloo
Internal-External Member:	Eduardo Martin-Martinez Assistant Professor, Dept. of Applied Mathematics, University of Waterloo
Other Member(s):	Chong Wang Adjunct Faculty, Dept. of Physics, University of Waterloo, Junior Faculty, Perimeter Institute for Theoretical Physics

Author's Declaration

I hereby declare that I am the sole author of this thesis. This is a true copy of the thesis, including any required final revisions, as accepted by my examiners.

I understand that my thesis may be made electronically available to the public.

Statement of Contributions

Yijian Zou was the sole author for Chapters 1, 2 and 7 which were written under the supervision of Prof. Guifre Vidal and were not written for publication. Prof. Guifre Vidal was a senior faculty of Perimeter Institute. Research at Perimeter Institute is supported by the Government of Canada through the Department of Innovation, Science and Economic Development Canada and by the Province of Ontario through the Ministry of Research, Innovation and Science. Guifre Vidal received support from Simons Foundation (Many Electron Collaboration) and Compute Canada in the period of working on this thesis.

This thesis consists in part of three manuscripts written for publication, as follows.

Research presented in Chapters 3 and 4:

Dr. Ashley Milsted was a postdoc at Perimeter Institute. This research was conducted by Yijian Zou under the supervision of Guifre Vidal and Ashley Milsted. Yijian Zou contributed to theoretical derivations, part of code writing, part of numerical simulations. Ashley Milsted contributed to part of code writing and part of numerical simulations.

Yijian Zou, Ashley Milsted, and Guifre Vidal. Conformal data and renormalization group flow in critical quantum spin chains using periodic uniform matrix product states. Phys. Rev. Lett., 121:230402, Dec 2018. DOI:10.1103/PhysRevLett.121.230402

Research presented in Chapter 5:

Dr. Ashley Milsted was a postdoc at Perimeter Institute. This research was conducted by Yijian Zou under the supervision of Guifre Vidal and Ashley Milsted. Yijian Zou contributed to theoretical derivations, all code writing and part of numerical simulations. Ashley Milsted contributed to part of numerical simulations.

Yijian Zou, Ashley Milsted, and Guifre Vidal. Conformal fields and operator product expansion in critical quantum spin chains. Phys. Rev. Lett., 124:040604, Jan 2020. DOI:10.1103/PhysRevLett.124.040604

Research presented in Chapter 6:

This research was conducted solely by Yijian Zou under the supervision of Guifre Vidal.

Yijian Zou and Guifre Vidal. Emergence of conformal symmetry in quantum spin chains: Antiperiodic boundary conditions and supersymmetry. Phys. Rev. B, 101:045132, Jan 2020. DOI:10.1103/PhysRevB.101.045132

Abstract

Understanding the universality class of continuous phase transition is of central importance in condensed matter physics. In one spatial dimension, the universal properties are encoded in the conformal field theory (CFT), which is in turn specified by the conformal data. In this thesis, we propose a systematic method to extract complete and accurate conformal data from the critical quantum spin chain based on the operator-state correspondence, thus completing the project initiated by Cardy and others in the 80's.

Our method is based on the low-energy eigenstates of the critical quantum spin chain with periodic boundary conditions. First, scaling dimensions and conformal spins are extracted by the energies and momenta. Second, the primary states and conformal towers are identified by using the Koo-Saleur lattice Virasoro generators. Third, we propose a systematic way of identifying lattice operators with CFT operators, which enables us to compute operator product expansion coefficients from the low-energy eigenstates. Finally, the whole approach is generalized to critical quantum spin chains with antiperiodic boundary condition. In order to reduce finite-size corrections, we put forward the periodic uniform matrix product state (puMPS) algorithm which enables us to compute low-energy eigenstates of a critical quantum spin chain up to several hundreds of spins. Our method also enables us to study nonperturbatively the renormalization group flow between two CFTs as well as explore the emergence of extended symmetries beyond conformal symmetry.

We test our method with the Ising model and its generalization due to O'Brien and Fendley. The latter model is featured by a tricritical point described by the tricritical Ising CFT and a line of critical points interpolating between the Ising CFT and the tricritical Ising CFT. We extract complete conformal data from the two models and find excellent agreement with analytical results. Furthermore, we study the spectral renormalization group flow between the two CFTs nonperturbatively. At the tricritical point, the underlying CFT has an extended symmetry, the superconformal symmetry. We propose lattice operators that correspond to supervirasoro generators and verify their action on low-energy eigenstates. In this way we study the emergence of superconformal symmetry in critical quantum spin chains.

Acknowledgements

First and foremost, I would like to thank Prof. Guifre Vidal, without whom this thesis would be never possible. I have been greatly intrigued and affected by his sharp intuition and deep understanding of physics. I would also like to thank Dr. Ashley Milsted and Ruoshui Wang for nice collaboration and fruitful discussion that is indispensible for the research that we have done.

In addition, I would like to thank Martin Ganahl, Qi Hu, Adrian Franco Rubio, Stefan Kuhn, Markus Hauru, Jacob Bridgeman for the Tensor Network Therapy weekly meeting where we made research a pleasure. I am grateful to Yin-Chen He, Chong Wang and Roger Melko who took their time to join my committee.

I would like to also thank my colleagues Jingxiang Wu, Shanming Ruan, Weicheng Ye, Yan-yan Li and Zi-wen Liu for help in daily life and emotional support. Finally, I would like to thank my parents who support me throughout my past life.

Table of Contents

List of Figures xiii

List of Tables xviii

1 Introduction 1

2 Conformal field theory 4

2.1 Universality in continuous phase transitions 4

2.1.1 Phase transitions 4

2.1.2 Quantum field theory 5

2.1.3 Renormalization group 6

2.2 Conformal field theory on the plane 7

2.2.1 Conformal symmetry 7

2.2.2 Virasoro algebra 8

2.2.3 Scaling dimension and conformal spin 8

2.2.4 Primary operator 8

2.2.5 Conformal tower 9

2.2.6 Operator-state correspondence 10

2.2.7 Operator product expansion 11

2.2.8 Conformal data 12

2.3 Conformal field theory on the cylinder 13

2.3.1 Mapping from the plane to the cylinder . . . 13
2.3.2 Virasoro generators . . . 14
2.3.3 OPE coefficients . . . 15
2.4 Examples of conformal field theory . . . 15
2.4.1 Ising CFT . . . 16
2.4.2 TCI CFT . . . 17

3 Periodic uniform matrix product states 18
3.1 Quantum spin chains . . . 18
3.1.1 Hilbert space . . . 18
3.1.2 Entanglement . . . 20
3.2 Matrix product states . . . 21
3.2.1 Notation . . . 21
3.2.2 Uniform infinite matrix product states . . . 21
3.2.3 Canonical forms . . . 23
3.2.4 Gradient descent optimiztion . . . 24
3.3 Periodic uniform matrix product states . . . 27
3.3.1 Gradient descent algorithm . . . 27
3.3.2 Preconditioning . . . 30
3.4 Excited states . . . 30
3.4.1 puMPS Bloch states . . . 32
3.4.2 The generalized eigenvalue problem . . . 33
3.4.3 Fidelity for the Ising model . . . 35
3.4.4 Validlity for generic critical quantum spin chains . . . 36

4 Conformal data and renormalization group flow in critical quantum spin chains 39
4.1 Extraction of conformal data from a critical quantum spin chain . . . 39

4.1.1 Scaling dimensions and conformal spins . . . 39
4.1.2 Koo-Saleur lattice Virasoro generators . . . 40
4.1.3 Finite-size corrections . . . 41
4.2 Numerical results . . . 42
4.2.1 Conformal towers . . . 42
4.2.2 Conformal data . . . 44
4.2.3 Comparison with other methods . . . 46
4.3 Spectral renormalization group flow . . . 46
4.3.1 Setup in quantum field theory . . . 46
4.3.2 Spectral RG flow in the OF model . . . 48
4.3.3 Comparsion with integrable field theory . . . 49
4.3.4 Spectral RG flow in the ANNNI model . . . 50
4.4 Conclusion . . . 51

5 Conformal fields and operator product expansion 58
5.1 Exciting the CFT vacuum with local operators . . . 59
5.1.1 Primary operators . . . 60
5.1.2 Derivative descendants . . . 62
5.1.3 General descendants . . . 63
5.2 Lattice operators as CFT scaling operators . . . 63
5.2.1 Constraining lattice operators without OPE coefficients . . . 63
5.2.2 Algorithm . . . 65
5.3 Example: critical Ising model . . . 66
5.3.1 Lattice operators as CFT operators . . . 66
5.3.2 CFT operators as lattice operators . . . 69
5.3.3 Exact solution . . . 70
5.4 Source of error . . . 78
5.4.1 General lattice models . . . 79
5.4.2 Example of critical Ising model . . . 82
5.5 Conclusion . . . 88

6 Anti-periodic boundary conditions and supersymmetry **91**
6.1 Anti-periodic boundary conditions (APBC) . . . 92
6.1.1 APBC for spin chains . . . 92
6.1.2 APBC for CFT . . . 94
6.2 Extraction of conformal data from spin chains with APBC . . . 95
6.2.1 The Hilbert space . . . 95
6.2.2 Scaling dimensions and conformal spins . . . 95
6.2.3 Virasoro generators . . . 96
6.2.4 Local operators and OPE coefficients . . . 97
6.2.5 String operators and OPE coefficients . . . 98
6.3 puMPS techniques for APBC . . . 100
6.3.1 Symmetric tensors . . . 101
6.3.2 puMPS for eigenstates in APBC . . . 102
6.4 Ising model with APBC . . . 104
6.4.1 Ising CFT . . . 104
6.4.2 Scaling dimensions, conformal spins and central charge from the Ising model . . . 105
6.4.3 OPE coefficients from the Ising model . . . 107
6.5 The O'Brien-Fendley model with APBC . . . 110
6.5.1 TCI CFT . . . 111
6.5.2 Scaling dimensions, conformal spins and central charge from the TCI model . . . 113
6.5.3 OPE coefficients from the TCI model . . . 115
6.6 Emergence of superconformal symmetry . . . 118
6.6.1 $\mathcal{N} = 1$ supersymmetry and the OF model . . . 118
6.6.2 The superconformal algebra . . . 119
6.6.3 Supervirasoro primary states in the TCI CFT . . . 121
6.6.4 Lattice supervirasoro generators . . . 123
6.7 Conclusion . . . 127

7 Conclusion and Future directions **129**

References **131**

APPENDICES **143**

A Matrix product operators **144**

A.1 Hamiltonian and H_n operator 144

A.2 Fourier mode of simple local operators 146

B Fourier modes of multi-site operators **148**

C Details of the puMPS algorithm for APBC **151**

C.1 Computing low-energy eigenstates 151

C.2 Computing matrix elements of local operators 153

C.3 Computing matrix elements of string operators 154

List of Figures

3.1 Basic examples of tensor networks. (a) A bipartite state $|\psi\rangle_{AB}$. (b) The reduced density matrix of A of the state. (c) The square of the norm of the state $\langle\psi|\psi\rangle$. (d) The expectation value of O on subsystem A, $\langle\psi|O_A|\psi\rangle$ (e) The Schmidt decomposition, Eq. (3.15). (f) An uniform infinite MPS, Eq. (3.19). (g) A puMPS, Eq. (3.34). (h) The square of the norm of the puMPS, $\langle\Psi(\bar{A})|\Psi(A)\rangle$. 22

3.2 Tensor networks used in the gradient descent algorithm for uniform infinite MPS. Top: the square of the norm of locally deformed MPS with central tensor A_C. It equals the vector norm of the tensor A_C, Eq. (3.26). Bottom: derivative of the auxiliary energy function $E_{A_L}(A_C)$ with respect to the central tensor A_C in Eq. (3.29), where red tensors form a matrix product operator representation of the shifted Hamiltonian $\tilde{H}$. 26

3.3 Top: the tensor network for the local effective norm matrix (3.37) for the deformed puMPS in the left canonical gauge. Bottom: the tensor network for the derivative of the auxiliary energy function with respect to the puMPS tensor A_C in (3.29), assuming that the puMPS is normalized. The red tensors form a matrix product operator representation of the shifted Hamiltonian $\tilde{H}$. 29

3.4 Convergence of the puMPS gradient descent algorithm with preconditioning for the critical Ising model with $N = 128$. The dashed lines are the convergence of the gradient norm η, and the solid lines represent the energy difference of puMPS from the exact ground state energy at each step of energy minimization. (a) Bond dimension $D = 18$, initial state chosen with the pre-optimized puMPS tensor for $N = 64, D = 18$ (red), and random initial state (blue). (b) Bond dimension $D = 30$, initial state chosen by enlarging the optimized puMPS tensor from $D = 18, N = 128$ (red), and random initial state (blue). Iterations are stopped when $\eta < 10^{-6}$. 31

3.5 Top: the tensor network for the effective norm matrix $N_{\mu\nu,C}(p)$ for puMPS tangent states parametrized with A_L and $B_C = B\lambda$. Bottom: the tensor network for the effective Hamiltonian $H_{\mu\nu,C}(p)$ when $p_\alpha = p_\beta = p$, or for the effective H_n matrices $H_{n,\mu\nu,C}(p_\alpha, p_\beta)$, where the red tensors in the middle form a matrix product operator representation of the Hamiltonian or its Fourier modes, respectively. 34

3.6 Nonzero eigenvalues of the effective norm matrix in momentum zero sector of the Ising model with $N = 64, D = 24$, sorted in descending order. Green: $N_{\mu\nu}(p = 0)$ in (3.45) where the puMPS tensor A is fixed as the left canonical tensor A_L. Red: $N_{\mu\nu,C}(p = 0)$ in (3.49). The blue vertical line is at $\mu = (d-1)D^2 + 1$, the number of nonzero eigenvalues resulting from the gauge freedom of puMPS tangent state in momentum zero sector. 35

3.7 Fidelity of the first 41 exactly diagonalized eigenstates of the Ising model ($N = 20$) with their variational, puMPS Bloch-state counterparts. Top: fidelity of all 41 states for fixed bond dimension $D = 12$. Primary states are labeled with diamonds and descendant states are labeled with dots. Different colors label states in different conformal towers. Bottom: fidelity of four selected states for bond dimensions $6 \leq D \leq 16$. All ground states are converged to $\eta < 10^{-6}$. 37

4.1 (a) Exact Ising CFT scaling operator spectrum, with diamonds marking primary operators. (b) Ising model spectrum, colored according to numerical conformal-tower identification, for $N = 64$ sites using Bloch states on top of a puMPS variational ground state with $D = 24$, converged to $\eta < 10^{-6}$ (error on ground-state energy density $\approx 10^{-11}$). The numerically-assigned conformal towers are consistent with the CFT result up to level 7, where some states are misidentified. **Note:** We displace data points slightly along the x-axis to show degeneracies. 43

4.2 (Top) Low-energy spectrum of the TCI model with PBC at $N = 56$, diagonalized using puMPS with bond dimension $D = 36$. Different colors indicate different conformal towers, with diamonds labeling the primary states. (Bottom) The spectrum of the TCI CFT up to $\Delta^{CFT} \leq 3.2$ for PBC. 45

4.3 Extrapolation of scaling dimensions for primary states and central charge for the Ising CFT with finite size simulations of the Ising model. Data points include $N = 64, 96, 128, 160, 192, 228$ with bond dimension $D = 28, 34, 38, 42, 45, 49$ respectively. The $T\bar{T}$ state suffers from significant finite D effects for large systems with moderate bond dimensions. 52

4.4 Extrapolation of scaling dimensions for primary states and central charge for the Tri-Critical Ising CFT, with finite size simulations of the OF model near the TCI point. Data points include $N = 36, 40, 56, 64, 128$ with bond dimensions $D = 28, 32, 32, 32, 44$ respectively, except for $\Delta_{\epsilon''}$, which uses $N = 20, 24, 28, 32, 40$ with $D = 24, 28, 28, 32, 32$. We chose system sizes to avoid severe corrections due to finite bond-dimension effects, which have a stronger effect on higher-energy excitations, and in order to remain in a regime where the scaling is apparently dominated by an irrelevant operator with $\Delta = 4$. 53

4.5 **Top:** Scaling operator spectra of (a) the Ising and (b) the TCI CFTs (with a selection of operators labeled). **Bottom:** Approximate scaling dimensions and conformal-tower identification for the OF model at $\lambda = 0.4$ with (c) $N = 256, D = 52$ and (d) $N = 32, D = 32$, corresponding to points of Fig. 4.6. We label a selection of states according to a numerical identification of the corresponding CFT operators [80]. **Note:** We displace data points slightly along the x-axis to show degeneracies. 54

4.6 Spectral RG flow (crosses) of the first 5 energy levels (as apparent scaling dimensions Δ) at momentum zero, excluding $\Delta = 0$, extracted from the OF model with $\lambda = 0.4$, using puMPS with $D \leq 52$. For comparison, we also plot the exact scaling dimensions of the Ising and TCI CFTs (dots, diamonds). The crossover between the two highest levels plotted, which we confirm by tracking conformal tower membership using H_n matrix elements, is consistent with these states belonging to different Kramers-Wannier self-duality sectors. 55

4.7 Connection of the spectral RG flow of Fig. 4.6 (left) to the "flow" of OF model energy levels as a function of λ at fixed system size $N = 32$, computed using puMPS with $D = 28$. Note how the apparent scaling dimensions agree with the TCI CFT values at the TCI point $\lambda_{TCI} \approx 0.428$. 56

4.8 Flow of the first spectral gap from Fig. 4.6 compared with the integrable field theory result of [67], conjectured to describe the equivalent flow in the continuum. 56

4.9 Spectral RG flow of the first 5 approximate scaling dimensions (crosses), excluding $\Delta = 0$, extracted from the ANNNI model at momentum zero, for $\gamma = 10$, using $D \leq 46$. For comparison, we also plot the exact scaling dimensions of the Ising and TCI CFTs. Note the crossover between the two largest scaling dimensions plotted, which we confirm by also tracking the ϵ-tower membership using H_n matrix elements. 57

4.10 The first 5 approximate scaling dimensions (crosses), excluding $\Delta = 0$, as function of γ, extracted from the ANNNI model at momentum zero, for $N = 80, D = 38$. We also plot exact CFT scaling dimensions. Furthermore, we show to the left how the "flow" with γ links up at $\gamma = 10$ with the spectral RG flow of Fig. 4.9. We confirm the crossover between the two highest-Δ curves by tracking fidelities of excited states at different γ. . . . 57

5.1 Extrapolation of the coefficients of Eq. (5.39) for the lattice operator $\mathcal{O} = XZ + ZX$. The extrapolated values are $a_\sigma = 0.803121$, $a_{\partial_\tau \sigma} = 0.0000$, $a_{\partial_\tau^2 \sigma} = 0.820$, $a_{\partial_x^2 \sigma} = -0.736$. See Table 5.4. 67

5.2 Error in the OPE coefficient $C_{\sigma\sigma\epsilon}$ as a function of system size for the two lattice realizations (5.54) and (5.55) of σ^{CFT}. Lines correspond to N^{-2} (red) and N^{-4} (blue) scaling. 70

5.3 Convergence of the coefficients with Eq. (5.128) for $\mathcal{O} = ZZ$. Coefficients are obtained by minimizing the cost function for systems sizes $18 \leq N \leq 48$. 84

5.4 Convergence of the coefficients with Eq. (5.123) for $\mathcal{O} = X$. Coefficients are obtained by minimizing the cost function for systems sizes $18 \leq N \leq 48$. . 85

5.5 Convergence of the coefficients with Eq. (5.123) for $\mathcal{O} = -i(YZ + ZY)$. Coefficients are obtained by minimizing the cost function for systems sizes $36 \leq N \leq 96$. 85

5.6 Convergence of the OPE coefficients $C_{\sigma\sigma\epsilon}$ with $\sigma^{CFT} \sim \mathcal{O}_{\sigma 1}, \mathcal{O}_{\sigma 2}$. Sizes $18 \leq N \leq 48$ are used. Linear extrapolation with $1/N^2$ is used. The intercept the the extrapolation are approximately 0.5000003 and 0.49994 respectively. The slope are approximately -0.315 and -15.34 respectively. 87

5.7 Convergence of the OPE coefficient $C_{\sigma\epsilon\sigma}$ with $\sigma^{CFT} \sim \mathcal{O}_{\epsilon 1}, \mathcal{O}_{\epsilon 2}, \mathcal{O}_{\epsilon 3}$. Sizes $18 \leq N \leq 48$ are used. Linear extrapolation with $1/N^4$ is used. The intercept of the extrapolations are approximately 0.4999999, 0.4999999 and 0.4999997 respectively. Only $\mathcal{O}_{\epsilon 3}$ has significant finite-size error in this OPE coefficient, with a slope approximately 0.61 in the extrapolation. 89

6.1 (Top two) Low-energy spectrum of the Ising model with the PBC and the APBC at $N = 64$, diagonalized using puMPS with bond dimension $D = 28$. Different colors indicate different conformal towers, with diamonds labeling the primary states. We have only shown the states with conformal spins $|s| \leq 3$. (Bottom two) The spectrum of the Ising CFT up to $\Delta^{CFT} \leq 6 + 1/8$ and $-3 \leq s^{CFT} \leq 3$. 106

6.2 Extrapolation of the scaling dimensions Δ_μ (left) and Δ_ψ (right) for the Ising model with $32 \leq N \leq 160$. 107

6.3 Extrapolation of the real (top) and imaginary (bottom) part of the OPE coefficient $C_{\psi\mu\sigma}$. 110

6.4 (Top two) Low-energy spectrum of the TCI model with PBC and APBC at $N = 56$, diagonalized using puMPS with bond dimension $D = 36$. Different colors indicate different conformal towers, with diamonds labeling the primary states. The exceptions are that the $\sigma(\sigma')$ and $\mu(\mu')$ towers are plotted with the same color. (Bottom two) The spectrum of the TCI CFT up to $\Delta^{CFT} \leq 3.2$ for PBC and $\Delta^{CFT} \leq 2.7$ for APBC. 114

6.5 Spectrum of the TCI CFT in the NS sector. Primary states are labelled as diamonds. Arrows indicate that the primary states are related by the supervirasoro generators G_m^{CFT}. 123

6.6 The central charge from Eqs. (4.8),(6.118). 125

6.7 Matrix elements of G_n in the NS sector of the TCI model. The dashed lines represent the corresponding CFT matrix element Eqs. (6.116),(6.117),(6.119). The CFT matrix elements Eqs. (6.116),(6.117) have the same modulus, so we only show one of them in the figure. 126

6.8 Matrix elements of G_n in the R sector of the TCI model. The dashed lines represent the corresponding CFT matrix elements in Eqs. (6.113),(6.114). 126

C.1 (Top) The tensor network for $N_{\mu\nu}^{APBC}(p)$ in Eq. (C.6). The green tensor $U_B \equiv U_B(\mathcal{Z})$ in Eq. (6.55). (Bottom) The tensor network for $H_{\mu\nu}^{APBC}(p)$ in Eq. (C.7) if the red tensors form a matrix product operator (MPO) for the Hamiltonian H and $p_\alpha = p_\beta = p$. It also represents $O_{\mu\nu}(p_\alpha, p_\beta)$ in Eq. (C.9) if the red tensors form a MPO for $\tilde{O}^s$. 152

List of Tables

2.1 Primary operators of the Ising CFT. 16

2.2 Virasoro primary operators of the TCI CFT. 17

4.1 Central charge and selected scaling dimensions from lattice Virasoro matrix elements [80] and energy gaps derived from puMPS Bloch states. For the Ising model, we used system sizes $N \leq 228$ and bond dimensions $24 \leq D \leq 49$. For the OF model near its Tri-Critical Ising (TCI) point, we used $N \leq 128$ and $28 \leq D \leq 44$ (requiring more computational time than used for the Ising model). Note the good agreement in the latter case, despite being slightly off-critical. 44

4.2 Central charge and selected scaling dimensions extracted from the critical Ising model, comparing the puMPS techniques we employ to finite entanglement scaling (FES) with infinite matrix product states [116], the tensor renormalization group (TRG) [73], and tensor network renormalization (TNR) [36]. Note that, for FES, the scaling dimensions ≈ 1.125 correspond to the *spatial*-derivative operators $\partial_x\sigma$ and $\partial_x\epsilon$ (denoted $d\sigma$ and $d\varepsilon$ in [116]), which are mixtures of $\partial\sigma$, $\overline{\partial}\sigma$ and $\partial\varepsilon$, $\overline{\partial}\varepsilon$, respectively. To indicate this, we have placed these values *between* rows. Also, values marked with $*$ were not assigned to particular CFT operators in [36] so we have simply listed them in ascending order. Finally, in the puMPS data, the values for Δ_T and $\Delta_{\bar{T}}$ (marked with $**$) are exact because these scaling dimensions were used to fix the overall normalization. The bond dimensions used were $28 \leq D \leq 49$ for puMPS, $32 \leq D \leq 64$ for FES, 64 for TRG, and 24 for TNR. 47

5.1 Expansion (5.39) for simple lattice operators in the Ising model. Two-spin operators $A(j)B(j+1)$ are organized into terms that are even or odd terms under exchange $j \leftrightarrow j+1$, e.g. $XY \pm YX$. The set $\mathcal{A}$ of CFT operators is given in Eqs. (5.51)-(5.53). Coefficients smaller than 5×10^{-3} are not shown. The number of significant digits is determined case by case by requiring that a particular digit does not change under extrapolation with different sets of system sizes up to $N = 96$. Note that we omit the superscript $_{CFT}$ on the CFT scaling operators. 68

5.2 Lattice operators with even Z_2 symmetry and their representation using Majorana fermion operators 71

5.3 Correspondence between lattice operators and CFT operators for the Ising model. The truncated set of CFT operators contains $\mathbf{1}, T, \bar{T}, \epsilon, \partial_\tau\epsilon, \partial_\tau^2\epsilon$. Coefficients are obtained analytically in the top table. The bottom table is the same as the top table except that coefficients are shown their approximate values to 5 digits to compare with numerical results. The subscript "CFT" is omitted in the column of CFT operators. 79

5.4 Correspondence of lattice objects and CFT objects. The "$\approx$" means equal up to finite-size corrections. 90

6.1 Correspondence of lattice objects and CFT objects for spin chains with APBC 100

6.2 Primary fields of the Ising CFT. 104

6.3 Scaling dimensions from the Ising model with $32 \le N \le 160$. 108

6.4 Correspondence between lattice operators and CFT operators for the Ising model. (Top) Lattice operators expressed as a linear combination of a truncated set of CFT operators. (Bottom) CFT primary operators expressed as a linear combination of lattice operators by inverting the top table. 109

6.5 OPE coefficients computed from the Ising model with $20 \le N \le 96$. Numerical data are kept up to 6 digits. 111

6.6 Virasoro primary fields of the TCI CFT. 112

6.7 Scaling dimensions from the TCI model. All numerical values are extrapolated using $40 \le N \le 80$, except $\Delta_{\epsilon''}$ where we use $20 \le N \le 56$. All numerical values are kept to 4 significant digits. 115

6.8 Correspondence between lattice operators and CFT operators for the O'Brien-Fendley model. (Top) Correspondence between some lattice operators and a linear combination of CFT primary operators. We have neglected the contribution from the ϵ''^{CFT} operator because it has a larger scaling dimension and contributes to higher order in $1/N$ in all matrix elements. (Bottom) Lattice operators that correspond to CFT primary operators (except ϵ''^{CFT}), obtained by inverting the top table. 116

6.9 OPE coefficients of the TCI CFT computed from the TCI model. The organization of the table follows the exact results listed before. All numerical results are kept to the last significant digits, and the exact results are shown with the same number of significant digit. All OPE coefficients involving ϵ'' are extrapolated with data from $20 \leq N \leq 56$, while those not involving ϵ'' are extrapolated with data from $32 \leq N \leq 72$. 117

6.10 OPE coefficients of the TCI CFT computed from the TCI model (continued). 117

B.1 Position assignment x_j of local operators $\mathcal{O}_j$ and string operators $\mathcal{S}_{\mathcal{O},j}$. . . 150

Chapter 1

Introduction

In a long time of the history, people believed that the whole universe could be constructed if we know all fundamental laws of nature. This belief has led to tremendous progress in modern physics, including Newtonian mechanics and Maxwell's electromagnetic theory. However, this constructionism perspective has been challenged in the past century by the flourishing of condensed matter physics. It was discovered that a wide range of natural phenomena, such as phase transitions and superconductivity, cannot be easily explained using the underlying fundamental laws, i.e., quantum mechanics of few particles. The reason is that many macroscopic properties of matter only emerge when there are a macroscopic number of, or even infinite number of, particles. The theory of many-body physics uses terminologies that are absent in few-body physics, such as phases and symmetry breaking. It was argued by Anderson in the famous paper *More is different* [6] that different conceptual frameworks have to be used for physics at different scales, and that many-body physics is as fundamental as the physics of elementary particles.

This thesis focuses a particular phenomenon of many-body physics, namely continuous phase transitions. In the 80s, people have realized that long-distance physics of most continuous phase transitions can be described by a conformal field theory (CFT) [9, 46], a quantum field theory with conformal symmetry. (Interestingly, CFT is also a building block of string theory that describes the most fundamental constituents of nature so far.) The CFT encodes all universal information of the continuous phase transition. A CFT involves degrees of freedom (conformal fields) that are very different from the microscopic degrees of freedom (typically spins on a lattice), and has much richer symmetries than the microscopic system. Despite the conceptual differences between microscopic models and CFT, this thesis is aimed to connect the two languages. Given a microscopic model at its critical point, some of the questions that this thesis is trying to answer are

- How can we obtain all the information (conformal data) of the underlying CFT?
- How do the microscopic degrees of freedom correspond to the degrees of freedom in the CFT?
- How do symmetries of the CFT manifest themselves in the microscopic model?

Some of these questions have been partially addressed in the literature. Much of the past results rely on special properties of the microscopic model, such as symmetry, duality and integrability. In this thesis we will systematically answer these questions for generic critical quantum spin chains. We will exploit two classical results, (i) As pointed out by Cardy and others [19, 10, 20, 22, 3], the low-energy eigenstates of a critical quantum spin chain with periodic boundary conditions (PBC) is in one to one correspondence with CFT scaling operators. The energies and momenta of the eigenstates correspond to scaling dimensions and conformal spins of the CFT scaling operators. (ii) As first exploited by Koo and Saleur [68, 102, 33, 119, 49, 50, 13] in integrable systems, Fourier modes of the Hamiltonian density of the spin chain corresponds to Virasoro generators that implement infinitesimal conformal transformations. We can then identify the primary operators and conformal towers in the low-energy eigenstates of the critical quantum spin chain, as well as extract scaling dimensions and conformal spins of primary operators.

Another ingradient of conformal data is the operator product expansion (OPE) coefficients. In order to extract OPE coefficients from the lattice model, we first propose a systematic way to identify lattice operators with CFT operators. All OPE coefficients are then extracted by computing the corresponding matrix elements of lattice operators in the low-energy eigenstates. This completes the extraction of conformal data from the critical quantum spin chains. The whole approach only needs the critical lattice Hamiltonian as its input.

We then generalize the approach above to critical quantum spin chains with anti-periodic boundary conditions (APBC). We first generalize the Koo-Saleur lattice Virasoro generators to APBC and use it to the identify primary operators. We then generalize the identification of lattice operators and CFT operators to APBC. We find that string operators on the lattice correspond to CFT operators in the APBC sector, and that the OPE coefficients of involving those CFT operators can be obtained by matrix elements of string operators in low-energy eigenstates.

There are finite-size errors in the conformal data extracted from a finite spin chain. In order to obtain the low-energy eigenstates, we may use exact diagonalization (ED), but it has exponentially growing numerical cost in the total number of spins due to exponential

growth of the dimension of Hilbert space. This severely limits the sizes that ED can reach and results in large finite-size errors in the conformal data. During the past two decades, tensor network techniques [129, 39, 125, 28, 117, 132, 38, 116, 36, 109] have proven extremely useful to solve the low-energy eigenstates of quantum spin chains with a large number of spins. The underlying reason is that tensor networks select the subspace of the total Hilbert space relevant to the low-energy eigenstates of quantum spin chains. In this thesis, we focus on one type of tensor network, the matrix product states (MPS). Specifically, we will develop the periodic uniform matrix product state (puMPS) techniques that are suited for critical quantum spin chains on a circle. Making use of the puMPS techniques, we obtain low-energy eigenstates for critical quantum spins chains with up to several hundreds of spins. This enables us to extract accurate and precise information of the emergent CFT.

In this thesis, we illustrate our approach with two models, the Ising model and the O'Brien-Fendley (OF). The Ising model is exactly solvable and its underlying CFT is well known. It is used as a benchmark of our approach. The O'Brien-Fendley model [83] has a critical phase described by the Ising CFT and a tricritical point described by the tricritical Ising (TCI) CFT. It interpolates between the Ising CFT and the TCI CFT and displays a spectral renormalization group (RG) flow between the two CFTs. We will extract the information of the two CFTs from the OF model and study the spectral RG flow between them using puMPS techniques. At the tricritical point, the OBF model has an emergent superconformal symmetry beyond usual conformal symmetry in a CFT. We will study how the superconformal symmetry is manifest in the OF model with PBC and APBC.

This thesis is organized as follows. In Chapter 2 we will review the basic concept of continuous phase transitions and the aspects of conformal field theory related to our work. In Chapter 3 we describe the puMPS techniques for critical quantum spin chains. In Chapter 4 we describe how to extract central charge and scaling dimensions of CFT based on low-energy eigenstates of critical quantum spin chains with PBC. We will study the Ising and the OF models and simulate the spectral RG flow in the OF model. In Chapter 5 we explain how to relate lattice operators to CFT operators and extract OPE coefficients. We will examine in detail how it works for the Ising model. In Chapter 6 we generalize the approach to critical quantum spin chains with APBC. We then apply it to the Ising model and the OF model at the tricritical point. In the latter case, we will explain how the emergent superconformal symmetry manifests itself in the OF model. In Chapter 7 we study the emergence of Kac-Moody symmetry in the XXZ model using techniques developed in Chapters 4 and 5. We will conclude in Chapter 8 with remarks on future directions.

Chapter 2

Conformal field theory

In this chapter we review the basic concept of continuous phase transitions and conformal field theory. We first review universality in continuous phase transitions and the underlying physical argument, the renormalization group (RG). This leads to the central topic of the thesis, conformal field theory (CFT). A CFT is a fixed point of the RG flow and encodes all universal information of the continuous phase transition. We then review conformal data which completely characterizes the CFT. We will study how conformal data determined various properties of the CFT on the plane and on the cylinder. Finally we will give examples of CFTs relevant to the rest of the thesis.

2.1 Universality in continuous phase transitions

2.1.1 Phase transitions

In classical thermodynamics, a *phase transition* [21] is characterized by nonanalyticity of the free energy. A classical phase transition is a *continuous phase transition* if first-order derivatives of the free energy is continuous. Remarkably, microscopically very different systems can exhibit universal long-distance behavior near continuous phase transitions. (e.g., they may share the same critical exponents.) Therefore, continuous phase transitions are classified by their *universality classes* that encode their universal long-distance properties.

In quantum systems, a *quantum phase transition* [106] can happen due to quantum fluctuations. Consider a quantum Hamiltoian $H(g)$ that depends on one parameter g, and its ground state energy $E_0(g)$ as a function of g, a quantum phase transition happens at

$g = g_c$ if $E_0(g)$ is not analytic at $g = g_c$. Let $E_1(g)$ be the energy of the first excited state, a quantum phase transition is continuous if the spectral gap

$$\Delta = E_1(g) - E_0(g) \tag{2.1}$$

goes to zero as g goes to g_c. In a continuous quantum phase transition, g_c is called a *critical point*, and the system is *gapless*. Like classical phase transitions, continuous quantum phase transitions also exhibit universality. Given a quantum phase transition in d spatial dimensions, there is often a corresponding classical phase transition in $d+1$ dimensions in the same universality class, where the extra dimension in the classical system corresponds to imaginary time in the quantum system. From now on, we focus on quantum phase transitions in $d = 1$ spatial dimension, and we refer to the quantum system as $1+1$ dimensional.

It is worth noting that phase transitions only happen at infinite volume, since in finite-size systems nonanalyticity can never occur. However, as we will see, critical systems at finite-sizes also show universal behaviors, and we will exploit them to extract universal information of the phase transition in the following chapters.

2.1.2 Quantum field theory

Given a microscopic Hamiltonian $H(g)$ with a microscopic length scale (typically a lattice spacing a), we tune the coupling $g \to g_c$, such that the energy gap Δ closes. The correlation length $\xi \sim \Delta^{-1} \to \infty$. In dimensionless parameters, $\xi/a \to \infty$ as we tune $g \to g_c$. Alternatively, we can view the tuning as $a \to 0$ with ξ fixed. This implies that long-distance properties of $H(g)$ near g_c can be described by a quantum theory of continuous degrees of freedom, i.e., a quantum field theory (QFT) [88, 115, 128].

Let us consider a QFT in 1+1 dimensional Euclidean spacetime, where x denotes the spatial coordinate and τ denotes the imaginary time coordinate. A QFT has a number of fields $\psi_\alpha(z, \bar{z})$, where $z = \tau + ix$ and $\bar{z} = \tau - ix$. The theory is equipped with a Lagrangian density $\mathcal{L}[\psi_\alpha](z, \bar{z})$ and an action

$$S[\psi] = \int dz d\bar{z}\, \mathcal{L}[\psi_\alpha](z, \bar{z}). \tag{2.2}$$

A *symmetry* in a QFT is a transformation $\psi_\alpha(z, \bar{z}) \to \psi'_\alpha(z', \bar{z}')$ such that the action is invariant,

$$S[\psi] = S[\psi']. \tag{2.3}$$

We will be interested in QFTs with scale invariance and rotational invariance, for reasons that are evident shortly. In such a QFT, we have a set of *scaling operators* $\psi_\alpha(z, \bar{z})$ that are covariant under rotation and scale transformations,

$$z' = \lambda z, \;\; \psi'_\alpha(z', \bar{z}') = \lambda^{-\Delta_\alpha} \psi_\alpha(z, \bar{z}), \tag{2.4}$$

where $\lambda > 0$, and Δ_α is the *scaling dimension* of the scaling operator ψ_α, and

$$z' = e^{i\theta} z, \;\; \psi'_\alpha(z', \bar{z}') = e^{-i\theta s_\alpha} \psi_\alpha(z, \bar{z}), \tag{2.5}$$

where $0 \leq \theta < 2\pi$ and s_α is the *conformal spin* of ψ_α.

2.1.3 Renormalization group

A physical explanation for universality is based on *renormalization group* (RG) [131, 130]. RG implements a scale transformation of a QFT such that short-distance degrees of freedom are discarded and long-distance properties are kept unchanged. By doing RG on a system, we are probing the system with larger length scales and lower energy scales.

Coupling constants in the Lagrangian flow under RG. *Irrelevant* coupling constants die off, and *relevant* coupling constants grow. Given a QFT in the ultraviolet (UV), it often flows in the infared (IR) to fixed points, a scale invariant QFT. Continuous phase transitions are described by such RG fixed points, which will encode all universal information of the phase transition. A RG fixed point is characterized by all relevant couplings, which typically depend only on symmetries and dimensionality of the system. The fact that RG fixed points do not depend on microscopic details explains universality of continuous phase transitions.

At a RG fixed point in 1+1 dimensions, an operator $\psi_\alpha(z, \bar{z})$ is relevant if

$$\Delta_\alpha < 2 \tag{2.6}$$

and irrelevant if

$$\Delta_\alpha > 2. \tag{2.7}$$

This means that if we perturb a fixed-point theory with an irrelevant operator ψ_α with $\Delta_\alpha > 2$, at long distances the theory will be described by the same fixed point, because irrelevant couplings die off under RG flow. On the other hand, if we perturb a RG fixed point with a relevant operator with $\Delta_\alpha < 2$, then in the IR the theory will flow to another RG fixed point, which can describe another universality class of phase transitions. We will see such an example in Chapter 4.

2.2 Conformal field theory on the plane

In this section we review basic ingredients of *conformal field theory* (CFT). CFTs are RG fixed points with conformal symmetry, and describe a large class of continuous phase transitions. We will reach the concept of conformal data, a set of data that completely characterizes the CFT.

2.2.1 Conformal symmetry

Conformal transformations in 1+1 dimensional are holomorphic maps,

$$z' = w(z) \tag{2.8}$$

An infinitesimal conformal transformation $z' = z + \epsilon(z)$ can be parameterized using a Laurent expansion,

$$\epsilon(z) = \sum_{n=-\infty}^{\infty} \epsilon_n z^{n+1}. \tag{2.9}$$

Let l_n be the vector fields associated with the infinitesimal transformations,

$$l_n = -z^{n+1}\partial_z, \tag{2.10}$$

then it can be verified that

$$[l_n, l_m] = (n-m)l_{n+m}. \tag{2.11}$$

We can regard z and $\bar{z}$ as independent variables, then there are similar vector fields $\bar{l}_n$ that generate conformal transformations of $\bar{z}$. They satisfy the same commutation relation as l_n,

$$[\bar{l}_n, \bar{l}_m] = (n-m)\bar{l}_{n+m} \tag{2.12}$$

and

$$[l_n, \bar{l}_m] = 0. \tag{2.13}$$

Eqs. (2.11)(2.12)(2.13) define the *Witt algebra* of the generators of the conformal group. Note that $l_0 + \bar{l}_0$ and $l_0 - \bar{l}_0$ generate dilations (scale transformations) and rotations, respectively.

2.2.2 Virasoro algebra

It is well known that generators of a symmetry are represented as operators in a QFT. In a CFT, the generators of conformal symmetry are denoted as L_n and $\bar{L}_m$. They form the *Virasoro algebra*, a central extension of the Witt algebra,

$$[L_n^{CFT}, L_m^{CFT}] = (n-m)L_{n+m}^{CFT} + \frac{c^{CFT}}{12} n(n^2-1)\delta_{n+m,0} \tag{2.14}$$

$$[\bar{L}_n^{CFT}, \bar{L}_m^{CFT}] = (n-m)\bar{L}_{n+m}^{CFT} + \frac{c^{CFT}}{12} n(n^2-1)\delta_{n+m,0} \tag{2.15}$$

$$[L_n^{CFT}, \bar{L}_m^{CFT}] = 0, \tag{2.16}$$

where c^{CFT} is called the *central charge* of the CFT. The central extension appears because in a quantum theory a symmetry can be represented projectively [128].

2.2.3 Scaling dimension and conformal spin

In a CFT, $D^{CFT} = L_0^{CFT} + \bar{L}_0^{CFT}$ and $R^{CFT} = L_0^{CFT} - \bar{L}_0^{CFT}$ generate dilations and rotations. Scaling operators $\psi_\alpha^{CFT}(0,0)$ are eigenvectors of D^{CFT} and R^{CFT}, with eigenvalues Δ_α^{CFT} and s_α^{CFT},

$$[D^{CFT}, \psi_\alpha^{CFT}(0,0)] = \Delta_\alpha^{CFT}\psi_\alpha^{CFT}(0,0) \tag{2.17}$$

$$[R^{CFT}, \psi_\alpha^{CFT}(0,0)] = s_\alpha^{CFT}\psi_\alpha^{CFT}(0,0). \tag{2.18}$$

The above commutation comes from infinitesimal dilations and rotations in Eqs. (2.4)(2.5). It will be convenient to define holomorphic (anti-holomorphic) conformal dimensions $h_\alpha^{CFT} \equiv (\Delta_\alpha^{CFT} + s_\alpha^{CFT})/2$ and $\bar{h}_\alpha^{CFT} \equiv (\Delta_\alpha^{CFT} - s_\alpha^{CFT})/2$, which are eigenvalues of L_0^{CFT} and $\bar{L}_0^{CFT}$.

Scale invariance and rotational invariance imply that two point correlation functions are of the form

$$\langle \psi_\alpha^{CFT}(z,\bar{z})\psi_\beta^{CFT}(0,0)\rangle = \frac{d_{\alpha\beta}}{z^{h_\alpha^{CFT}+h_\beta^{CFT}}\bar{z}^{\bar{h}_\alpha^{CFT}+\bar{h}_\beta^{CFT}}}. \tag{2.19}$$

2.2.4 Primary operator

Virasoro generators L_n^{CFT} and $\bar{L}_n^{CFT}$ with $n < 0$ are raising operators with respect to dilation D^{CFT} – they raise the scaling dimension by $|n|$, while those with $n > 0$ lower the scaling

dimension by n,

$$[D^{CFT}, [L_n^{CFT}, \psi_\alpha^{CFT}(0,0)]] = (\Delta_\alpha^{CFT} - n)[L_n^{CFT}, \psi_\alpha^{CFT}(0,0)] \tag{2.20}$$
$$[D^{CFT}, [\bar{L}_n^{CFT}, \psi_\alpha^{CFT}(0,0)]] = (\Delta_\alpha^{CFT} - n)[\bar{L}_n^{CFT}, \psi_\alpha^{CFT}(0,0)]. \tag{2.21}$$

Likewise, it can be shown that L_{-n}^{CFT} and $\bar{L}_n^{CFT}$ raise the conformal spin by n. *Primary operators* are scaling operators whose scaling dimensions cannot be lowered,

$$[L_n^{CFT}, \phi_\alpha^{CFT}(0,0)] = 0, [\bar{L}_n^{CFT}, \phi_\alpha^{CFT}(0,0)] = 0 \quad (n > 0). \tag{2.22}$$

Under a conformal transformation Eq. (2.8), a primary operator transforms as

$$\phi_\alpha^{CFT'}(z', \bar{z}') = \left(\frac{dw}{dz}\right)^{-h_\alpha^{CFT}} \left(\frac{d\bar{w}}{d\bar{z}}\right)^{-\bar{h}_\alpha^{CFT}} \phi_\alpha^{CFT}(z, \bar{z}). \tag{2.23}$$

Two-point correlation function of primary operators are further restricted,

$$\langle \phi_\alpha^{CFT}(z, \bar{z}) \phi_\beta^{CFT}(0,0) \rangle = \frac{\delta_{\alpha\beta}}{z^{2h_\alpha^{CFT}} \bar{z}^{2\bar{h}_\alpha^{CFT}}}. \tag{2.24}$$

One may check that Eq. (2.24) is the only form that is invariant under dilations, rotations, and $w = 1/z$.

2.2.5 Conformal tower

Each primary operator expands a *conformal tower*, composed of the primary operator and its *descendant operators*. Descendant operators are obtained by applying raising operators $L_n^{CFT}, \bar{L}_n^{CFT}$ $(n < 0)$ to the primary operator, e.g. $L_{-1}^{CFT}\phi_\alpha^{CFT}$, $L_{-2}^{CFT}\bar{L}_{-1}^{CFT}\phi_\alpha^{CFT}$ etc. A general descendant

$$L_{-k_1}^{CFT} L_{-k_2}^{CFT} \cdots L_{-k_n}^{CFT} \bar{L}_{-\bar{k}_1}^{CFT} \bar{L}_{-\bar{k}_2}^{CFT} \cdots \bar{L}_{-\bar{k}_m}^{CFT} \phi_\alpha^{CFT} \tag{2.25}$$

has scaling dimension $\Delta_\alpha^{CFT} + l$, where

$$l = \sum_{i=1}^{n} k_i + \sum_{\bar{i}=1}^{m} \bar{k}_{\bar{i}} \tag{2.26}$$

is the *level* of the descendant.

A special type of descendant operators is

$$\phi_{\alpha,(k,\bar{k})}^{CFT} \equiv (L_{-1}^{CFT})^k (\bar{L}_{-1}^{CFT})^{\bar{k}} \phi_\alpha^{CFT}. \tag{2.27}$$

They are called derivative descendants because

$$\phi^{CFT}_{\alpha,(k,\bar{k})} = \partial^k \bar{\partial}^{\bar{k}} \phi^{CFT}_{\alpha}, \tag{2.28}$$

where $\partial \equiv \partial_z = (\partial_\tau + i\partial_x)/2$ and $\bar{\partial} \equiv \partial_{\bar{z}} = (\partial_\tau - i\partial_x)/2$.

There is a unique primary operator, the identity operator $\mathbf{1}^{CFT}$ that does not have any derivative descendants. The identity operator has $\Delta^{CFT}_{\mathbf{1}} = s^{CFT}_{\mathbf{1}} = 0$. However, it has other descendants, the most important example being the holomorphic *stress tensor*,

$$T^{CFT} = L^{CFT}_{-2}\mathbf{1}^{CFT} \tag{2.29}$$

with $\Delta^{CFT}_{T} = s^{CFT}_{T} = 2$ and similarly the anti-holomorphic stress tensor

$$\bar{T}^{CFT} = \bar{L}^{CFT}_{-2}\mathbf{1}^{CFT} \tag{2.30}$$

with $\Delta^{CFT}_{\bar{T}} = -s^{CFT}_{\bar{T}} = 2$. Virasoro generators can be expressed by the stress tensors as

$$L^{CFT}_n = \frac{1}{2\pi i}\oint dz\, z^{n+1} T^{CFT}(z) \tag{2.31}$$

$$\bar{L}^{CFT}_n = \frac{1}{2\pi i}\oint d\bar{z}\, \bar{z}^{n+1} \bar{T}^{CFT}(\bar{z}), \tag{2.32}$$

where the integration contour can be chosen as the $|z| = 1$ circle.

Descendant operators transform in a non-trivial way under conformal transformations, but the rules are completely determined by the conformal dimensions of the primary operator and the central charge. For example, the stress tensor transforms under Eq. (2.8) as

$$T^{CFT'}(z') = \left(\frac{dw}{dz}\right)^{-2}\left(T^{CFT}(z) - \frac{c^{CFT}}{12}\{w,z\}\right), \tag{2.33}$$

where

$$\{w,z\} = \frac{d^3w/dz^3}{dw/dz} - \frac{3}{2}\left(\frac{d^2w/dz^2}{dw/dz}\right)^2 \tag{2.34}$$

is the *Schwarzian derivative*.

2.2.6 Operator-state correspondence

A scaling operator creates a state in a CFT,

$$|\psi^{CFT}_{\alpha}\rangle = \psi^{CFT}_{\alpha}(0,0)|0^{CFT}\rangle, \tag{2.35}$$

where $|0^{CFT}\rangle$ is the vacuum state. Reversely, any state in a CFT can be created by acting with a local operator at the origin. This is known as *operator-state correspondence*. Note that operator-state correspondence is a special property of a CFT and is not generally true in QFTs. Each state $|\psi_\alpha^{CFT}\rangle$ is a simultaneous eigenvector of D^{CFT} and R^{CFT},

$$D^{CFT}|\psi_\alpha^{CFT}\rangle = \Delta_\alpha^{CFT}|\psi_\alpha^{CFT}\rangle, \tag{2.36}$$
$$R^{CFT}|\psi_\alpha^{CFT}\rangle = s_\alpha^{CFT}|\psi_\alpha^{CFT}\rangle. \tag{2.37}$$

A state $|\phi_\alpha^{CFT}\rangle$ is a *primary state* if the corresponding operator is a primary operator. Analogous to Eq. (2.22), a state $|\phi_\alpha^{CFT}\rangle$ is a primary state if and only if

$$L_n^{CFT}|\phi_\alpha^{CFT}\rangle = 0,\ \bar{L}_n^{CFT}|\phi_\alpha^{CFT}\rangle = 0\ (\forall n > 0). \tag{2.38}$$

Note that the Virasoro algebra Eq. (2.14) implies that the above equalities hold for all $n > 0$ if they hold for $n = 1, 2$, since other generators can be obtained by commutators of those with $n = 1, 2$. Acting with raising operators $L_{-n}, \bar{L}_{-n}$ on the primary state gives all *descendant states* that correspond to descendant operators. The vacuum state $|0^{CFT}\rangle$, corresponding to the $\mathbf{1}^{CFT}$ operator, is a primary state. It is also annihilated by $L_{-1}^{CFT}, \bar{L}_{-1}^{CFT}$ because it does not have derivative descendants, then

$$L_n^{CFT}|0^{CFT}\rangle = 0,\ \bar{L}_n^{CFT}|0^{CFT}\rangle = 0\ (\forall n \geq -1). \tag{2.39}$$

The descendants of identity with lowest scaling dimensions are the stress tensor states,

$$\sqrt{\frac{c^{CFT}}{2}}|T^{CFT}\rangle = L_{-2}^{CFT}|0^{CFT}\rangle,\ \sqrt{\frac{c^{CFT}}{2}}|\bar{T}^{CFT}\rangle = \bar{L}_{-2}^{CFT}|0^{CFT}\rangle, \tag{2.40}$$

where $\sqrt{c^{CFT}/2}$ is a normalization constant.

2.2.7 Operator product expansion

The scaling operators form an associative algebra, the *operator product expansion* (OPE), which relates the product of two scaling operators to a linear superposition of scaling operators. Let us consider the product of two primary operators,

$$\phi_\alpha^{CFT}(z,\bar{z})\phi_\beta^{CFT}(0,0) = \sum_\gamma C_{\alpha\beta\gamma}(z,\bar{z})\phi_\gamma^{CFT}(0,0) + \text{descendants}, \tag{2.41}$$

where

$$C_{\alpha\beta\gamma}(z,\bar{z}) = \frac{C_{\alpha\beta\gamma}^{CFT}}{z^{h_\alpha^{CFT}+h_\beta^{CFT}-h_\gamma^{CFT}}\bar{z}^{\bar{h}_\alpha^{CFT}+\bar{h}_\beta^{CFT}-\bar{h}_\gamma^{CFT}}} \tag{2.42}$$

is fixed by conformal symmetry, up to constants $C^{CFT}_{\alpha\beta\gamma}$. $C^{CFT}_{\alpha\beta\gamma}$ is known as the *OPE coefficients*. It can be shown that the rest of Eq. (2.41) is completely determined by $C^{CFT}_{\alpha\beta\gamma}$ and c^{CFT}. The OPE coefficients are invariant under cyclic permutations of indices, and are complex conjugated under odd permutations. OPE involving the identity operator is trivial, $C^{CFT}_{\alpha\beta\mathbf{1}} = \delta_{\alpha\beta}$.

In Eq. (2.41) let $z = \bar{z} = 1$ and using Eq. (2.24) we obtain

$$C^{CFT}_{\alpha\beta\gamma} = \langle \phi^{CFT}_\gamma(\infty)\phi^{CFT}_\alpha(1,1)\phi^{CFT}_\beta(0,0)\rangle, \tag{2.43}$$

where

$$\phi^{CFT}_\gamma(\infty) \equiv \lim_{z,\bar{z}\to\infty} z^{2h^{CFT}_\gamma}\bar{z}^{2\bar{h}^{CFT}_\gamma}\phi^{CFT}_\gamma(z,\bar{z}). \tag{2.44}$$

Eq. (2.43) can be alternatively expressed as

$$C^{CFT}_{\alpha\beta\gamma} = \langle \phi^{CFT}_\gamma|\phi^{CFT}_\alpha(1,1)|\phi^{CFT}_\beta\rangle, \tag{2.45}$$

where we have used the definition of the ket state Eq. (2.35) and the definition of the bra state

$$\langle\phi^{CFT}_\gamma| \equiv \langle 0^{CFT}|\phi^{CFT}_\gamma(\infty). \tag{2.46}$$

This definition is such that the bra states and ket states form an orthonormal basis.

2.2.8 Conformal data

Finally we come to the *conformal data* that completely characterizes the CFT. The conformal data is composed of $(\Delta^{CFT}_\alpha, s^{CFT}_\alpha)$ of primary operators, OPE coefficients $C^{CFT}_{\alpha\beta\gamma}$ of primary operators, and the central charge c^{CFT}.

Let us reiterate how conformal data determines all correlation functions of the CFT. The scaling dimensions and conformal spins determine all two-point correlation functions of primary operators by Eq. (2.24). Correlation functions of descendant operators are then determined by conformal symmetry. The OPE reduces higher-point correlation functions to two-point correlation functions, such as Eq. (2.43). OPE involving descendant fields is determined by $C^{CFT}_{\alpha\beta\gamma}$ and c^{CFT}. As a result, all correlation functions are determined by the conformal data.

2.3 Conformal field theory on the cylinder

In this section we review how conformal data manifests themselves for a CFT on the cylinder. As we will see, our method of extracting conformal data from a critical quantum spin chain comes directly from CFT results in this section.

2.3.1 Mapping from the plane to the cylinder

A conformal transformation

$$w = \frac{L}{2\pi} \log z \tag{2.47}$$

maps the complex plane to a cylinder (Fig. 1). Let $w = \tau + ix$, then $x \in [0, L)$ is the angular coordinate of the cylinder and $\tau \in (-\infty, \infty)$ labels the axial coordinate. Physically τ is the imaginary time and x is the compactified spatial coordinate. We will assign each equal τ circle a Hilbert space $\mathcal{H}_\tau$. States on different time slice are related by a Hamiltonian evolution. It can be seen that translations in τ and x on the cylinder are mapped to dilations and rotations on the complex plane. In particular, the $\tau = 0$ circle corresponds to the $|z| = 1$ circle on the complex plane.

The Hamiltonian and momentum are the integrals of the Hamiltonian and momentum density $h^{CFT}(x)$ and $p^{CFT}(x)$ on the time slice $\tau = 0$,

$$H^{CFT} = \int_0^L dx\, h^{CFT}(x) \tag{2.48}$$

$$P^{CFT} = \int_0^L dx\, p^{CFT}(x), \tag{2.49}$$

where we have omitted the τ coordinate in the fields for simplicity. The Hamiltonian and momentum densities are related to the stress tensors by

$$h^{CFT}(x) = \frac{1}{2\pi} \left(T^{CFT}(x) + \bar{T}^{CFT}(x) \right) \tag{2.50}$$

$$p^{CFT}(x) = \frac{1}{2\pi} \left(T^{CFT}(x) - \bar{T}^{CFT}(x) \right), \tag{2.51}$$

where $T^{CFT}(x), \bar{T}^{CFT}(x)$ on the cylinder is determined by Eqs (2.33),(2.47). Combined with Eqs. (2.31)(2.32)(2.48)(2.49)(2.50)(2.51), we can derive the Hamiltonian and momentum

on the cylinder

$$H^{CFT} = \frac{2\pi}{L}\left(L_0^{CFT} + \bar{L}_0^{CFT} - \frac{c}{12}\right) \tag{2.52}$$

$$P^{CFT} = \frac{2\pi}{L}\left(L_0^{CFT} - \bar{L}_0^{CFT}\right). \tag{2.53}$$

Note that the integrals of Eqs. (2.48)(2.49) are mapped to the contour integrals of Eqs. (2.31)(2.32) in the conformal mapping Eq. (2.47).

The operator-state correspondence [9, 46, 19, 10] implies that all simultaneous eigenstates $|\psi_\alpha^{CFT}\rangle$ of H^{CFT} and P^{CFT} are in one to one correspondence with scaling operators ψ_α^{CFT}. The energy and momentum are thus related to scaling dimensions and conformal spins by

$$E_\alpha^{CFT} = \frac{2\pi}{L}\left(\Delta_\alpha^{CFT} - \frac{c}{12}\right) \tag{2.54}$$

$$P_\alpha^{CFT} = \frac{2\pi}{L} s_\alpha^{CFT}. \tag{2.55}$$

Eqs. (2.54)(2.55) will be useful to extract scaling dimensions and conformal spins.

2.3.2 Virasoro generators

It can be further shown [68, 80] that Fourier modes of $h(x)$ and $p(x)$ are linear combinations of Virasoro generators. In particular, the Fourier modes of $h^{CFT}(x)$,

$$H_n^{CFT} \equiv \frac{L}{2\pi}\int_0^L dx\, h^{CFT}(x) e^{inx2\pi/L} \tag{2.56}$$

equal

$$H_n^{CFT} = L_n^{CFT} + \bar{L}_{-n}^{CFT} - \frac{c^{CFT}}{12}\delta_{n,0}. \tag{2.57}$$

The special case $n = 0$ is equivalent to Eq. (2.52).

The two Virasoro generators L_{-n}^{CFT} and $\bar{L}_n^{CFT}$ in H_n^{CFT}, Eq. (2.57), raise scaling dimensions and lower scaling dimensions respectively for $n \neq 0$. The definition of a primary state Eq. (2.38) is equivalent to

$$P_{\phi_\alpha}^{CFT} H_n^{CFT} |\phi_\alpha^{CFT}\rangle = 0 \quad (n = \pm 1, \pm 2), \tag{2.58}$$

where $P^{CFT}_{\phi_\alpha}$ is a projector onto the subspace spanned by states whose energy is lower than that of ϕ^{CFT}_α.

The central charge is related to the matrix element of H^{CFT}_n with $n = -2$,

$$c^{CFT} = 2|\langle T^{CFT}|H^{CFT}_{-2}|0^{CFT}\rangle|^2, \tag{2.59}$$

which follows from Eq. (2.39) and Eq. (2.40). Eqs. (2.57)(2.58)(2.59) will be useful to identify conformal towers and compute the central charge.

2.3.3 OPE coefficients

OPE coefficients of primary fields are related to matrix elements of primary operators,

$$\langle \phi^{CFT}_\alpha|\phi^{CFT}_\beta(x=0)|\phi^{CFT}_\gamma\rangle = \left(\frac{2\pi}{L}\right)^{\Delta^{CFT}_\beta} C^{CFT}_{\alpha\beta\gamma}, \tag{2.60}$$

which follows from Eq. (2.23) and Eq. (2.45). Translation invariance of the eigenstates allow us to express the OPE coefficients in terms of the Fourier mode of the CFT operator,

$$\langle \phi^{CFT}_\alpha|\phi^{CFT,s_\alpha - s_\gamma}_\beta|\phi^{CFT}_\gamma\rangle = \left(\frac{2\pi}{L}\right)^{\Delta^{CFT}_\beta} C^{CFT}_{\alpha\beta\gamma}, \tag{2.61}$$

where the Fourier mode of any CFT operator is defined as

$$\mathcal{O}^{CFT,s} \equiv \frac{1}{L}\int_0^L dx\, \mathcal{O}^{CFT}(x) e^{-isx2\pi/L}. \tag{2.62}$$

Eq. (2.61) will be useful to compute OPE coefficients.

2.4 Examples of conformal field theory

In the section we review conformal data of the Ising CFT, the tricritical Ising (TCI) CFT and the free compactified boson CFT. We will only consider the primary operators relevant to periodic boundary conditions of the quantum spin chains in Chapters 4 and 5. There are other primary operators relevant to anti-periodic boundary conditions of the spin chains. And we will not consider them until Chapter 6.

2.4.1 Ising CFT

The Ising CFT belongs to unitary minimal models [9, 46, 22] that can be solved exactly. Minimal models have a finite number of primary operators, resulting in a finite set of conformal data.

Conformal data

The central charge is $c^{CFT} = 1/2$ and there are three primary fields, namely the identity operator $\mathbf{1}$ (present in any CFT), the spin operator σ and the energy density operator ϵ. They all have conformal spin $s_{\mathbf{1}}^{CFT} = s_{\sigma}^{CFT} = s_{\epsilon}^{CFT} = 0$ and their scaling dimensions are $\Delta_{\mathbf{1}}^{CFT} = 0$, $\Delta_{\sigma}^{CFT} = 1/8$, and $\Delta_{\epsilon}^{CFT} = 1$, respectively. They are summarized in Table 2.1.

ϕ_α^{CFT}	Δ_α^{CFT}	s_α^{CFT}
$\mathbf{1}$ (identity)	0	0
ϵ (spin)	1	0
σ (energy)	1/8	0

Table 2.1: Primary operators of the Ising CFT.

The only nonzero OPE coefficients (up to permutations of the indices) are $C_{\alpha\beta\mathbf{1}}^{CFT} = \delta_{\alpha\beta}$ and $C_{\sigma\sigma\epsilon}^{CFT} = 1/2$. It can be seen that the OPE coefficients are invariant under a $\mathbb{Z}_2$ symmetry, $\mathbf{1} \to \mathbf{1}, \sigma \to -\sigma, \epsilon \to \epsilon$. Therefore σ is odd under the $\mathbb{Z}_2$ symmetry and the other two primary operators are even.

conformal towers

Scaling operators of the Ising CFT with $\Delta^{CFT} \leq 6 + 1/8$ is plotted in Fig. 2.

A generic property of minimal models is that each primary operator has descendants that annihilate the vacuum. Such a descendant is called a null field. In the Ising CFT we have null fields at level 2.

$$\chi_\sigma \equiv \left(L_{-2}^{CFT} - \frac{4}{3}(L_{-1}^{CFT})^2\right)\sigma \tag{2.63}$$

$$\chi_\epsilon \equiv \left(L_{-2}^{CFT} - \frac{3}{4}(L_{-1}^{CFT})^2\right)\epsilon. \tag{2.64}$$

Null fields do not correspond to any state. As a result, all descendants of σ and ε at level 2 are derivative descendants. The lowest descendant that is not a derivative descendant is $L_{-3}^{CFT}\sigma$ in the σ tower and $L_{-4}^{CFT}\epsilon$ in the ϵ tower (and those with $\bar{L}_{-n}^{CFT}$). This fact will be important in Chapter 5 where we analyze the correspondence between lattice operators and CFT operators.

2.4.2 TCI CFT

TCI CFT also belongs to unitary minimal models. The central charge is $c^{CFT} = 0.7$. It has 6 primary operators, listed in Table 2.2.

ϕ_α^{CFT}	Δ_α^{CFT}	s_α^{CFT}
$\mathbf{1}$ (identity)	0	0
ϵ (energy)	1/5	0
ϵ' (vacancy)	6/5	0
ϵ'' (irrelevant)	3	0
σ (spin)	3/40	0
σ' (subleading spin)	7/8	0

Table 2.2: Virasoro primary operators of the TCI CFT.

The scaling operators with $\Delta^{CFT} \leq 3.2$ are plotted in Fig. 3.

Nonzero OPE coefficients that do not involve the identity operator are [81]

$$C_{\epsilon\epsilon\epsilon'}^{CFT} = c_1, \quad C_{\epsilon'\epsilon'\epsilon'}^{CFT} = c_1, \quad C_{\epsilon\epsilon'\epsilon''}^{CFT} = 3/7 \tag{2.65}$$

$$C_{\sigma\sigma\epsilon}^{CFT} = 3c_1/2, \quad C_{\sigma\sigma\epsilon'}^{CFT} = c_1/4, \quad C_{\sigma\sigma\epsilon''}^{CFT} = 1/56 \tag{2.66}$$

$$C_{\sigma\sigma'\epsilon}^{CFT} = 1/2, \quad C_{\sigma\sigma'\epsilon'}^{CFT} = 3/4, \quad C_{\sigma'\sigma'\epsilon''}^{CFT} = 7/8, \tag{2.67}$$

where

$$c_1 = \frac{2}{3}\sqrt{\frac{\Gamma(4/5)\Gamma^3(2/5)}{\Gamma(1/5)\Gamma^3(3/5)}} \approx 0.61030. \tag{2.68}$$

We note that the OPE coefficient $C_{\sigma'\sigma'\epsilon''}^{CFT}$ was written (wrongly) in [70] as $7c_1/8$, instead of 7/8 in Eq. (6.76). The TCI CFT also has a $\mathbb{Z}_2$ symmetry where σ and σ' are odd.

The TCI CFT has a celebrated superconformal symmetry that relates different primary operators. We will come back to it in Chapter 6.

Chapter 3

Periodic uniform matrix product states

In this chapter, we describe in detail the periodic uniform matrix product state (puMPS) techniques that are used to diagonalize low-energy eigenstates of a critical quantum spin chain with periodic boundary conditions (PBC). Compared with the exponential growth of numerical cost for ED, the puMPS method scales polynomially with the system size. This chapter is relevant to readers interested in the details of the algorithm. Readers solely interested in the extraction of conformal data may read section 3.1 and skip to the next chapter.

We will first review entanglement properties in quantum spin chains. Then we introduce tensor network methods, and in particular the uniform infinite MPS. Next we consider gradient optimization of puMPS for the ground state. Finally we use puMPS tangent states to compute low-energy excitations. We will illustrate the technique with the critical Ising model.

3.1 Quantum spin chains

3.1.1 Hilbert space

A quantum spin chain is composed of spin S degrees of freedom on a lattice. The Hilbert space is $\mathcal{H} = \mathcal{H}_S^{\otimes N}$, where N is the total number of spins and $\mathcal{H}_S$ is the Hilbert space for

a single spin, with dimension $\dim(\mathcal{H}_S) = d = 2S + 1$. The total dimension of the Hilbert space is

$$\dim(\mathcal{H}) = d^N. \tag{3.1}$$

We will be interested in $S = 1/2$ spin chains, the local dimension being $d = 2$, and the Pauli matrices are

$$X = \begin{bmatrix} 0 & 1 \\ 1 & 0 \end{bmatrix}, Y = \begin{bmatrix} 0 & -i \\ i & 0 \end{bmatrix}, Z = \begin{bmatrix} 1 & 0 \\ 0 & -1 \end{bmatrix}. \tag{3.2}$$

The Hamiltonian is a sum of local terms,

$$H = \sum_{j=1}^{N} h_j, \tag{3.3}$$

where h_j is supported near site j. We will consider translation invariant Hamiltonian with PBC. The action of the translation operator $\mathcal{T}$ is,

$$\mathcal{T} h_j \mathcal{T}^\dagger = h_{j+1}, \tag{3.4}$$

where the site $j = N + 1$ is identified with site $j = 1$. The Hamiltonian with PBC is then

$$H = \sum_{j=1}^{N} \mathcal{T}^{j-1} h_1 \mathcal{T}^{\dagger j-1}. \tag{3.5}$$

In all cases that we will consider, the spin chain has a global $\mathbb{Z}_2$ spin flip symmetry. The representation of the $\mathbb{Z}_2$ generator is

$$\mathcal{Z} = \prod_{j=1}^{N} \mathcal{Z}_j, \tag{3.6}$$

where

$$\mathcal{Z}_j = \mathcal{Z}_j^\dagger = \mathcal{Z}_j^{-1}. \tag{3.7}$$

The Hamiltonian density is invariant under the $\mathbb{Z}_2$ transformations,

$$h_j = \mathcal{Z} h_j \mathcal{Z}^\dagger. \tag{3.8}$$

For convenience, we will write the Hamiltonian in a basis such that $\mathcal{Z}_j = Z_j$.

Energy eigenstates can be labelled by eigenvalues of $H^{PBC}, \mathcal{T}, \mathcal{Z}$ in the PBC,

$$H|\psi_\alpha\rangle = E_\alpha|\psi_\alpha\rangle \tag{3.9}$$
$$\mathcal{T}|\psi_\alpha\rangle = e^{iP_\alpha}|\psi_\alpha\rangle \tag{3.10}$$
$$\mathcal{Z}|\psi_\alpha\rangle = \mathcal{Z}_\alpha|\psi_\alpha\rangle, \tag{3.11}$$

where $\mathcal{Z}_\alpha = \pm 1$ and

$$P_\alpha = \frac{2\pi}{N} s_\alpha, \tag{3.12}$$

with $s_\alpha \in \mathbb{Z}$.

The simplest example of critical quantum spin chain that we will use is the critical *Ising model*, where

$$h_j = -X_j X_{j+1} - Z_j. \tag{3.13}$$

At long distance the model is described by the Ising CFT. We will also consider its generalization, the *O'Brien-Fendley (OBF) model*,

$$h_j = -X_j X_{j+1} - Z_j + \lambda(X_j X_{j+1} Z_{j+2} + Z_j X_{j+1} X_{j+2}). \tag{3.14}$$

In the range of $0 \leq \lambda < \lambda^*$, the model is described by the Ising CFT. At $\lambda = \lambda^* \approx 0.428$, the model is described by the TCI CFT. λ^* is known as the *tricritical point*.

3.1.2 Entanglement

Given a state $|\psi\rangle \in \mathcal{H}$ and a bipartition of the spin chain into A and B, there is a *Schmidt decomposition*

$$|\psi\rangle = \sum_i \lambda_i |\phi_i\rangle_A |\phi_i\rangle_B, \tag{3.15}$$

where $|\psi_i\rangle_{A/B}$ are orthonormal states in $\mathcal{H}_{A/B}$. λ_i is the Schmidt coefficient, and encodes the entanglement between A and B. The entanglement entropy is

$$S_A = -\sum_i \lambda_i^2 \log \lambda_i^2. \tag{3.16}$$

Let A be contagious l spins where $1 \ll l \ll N$, and $|\psi\rangle$ be the ground state of a critical quantum spin chain, then it can be shown [17] that

$$S_A = \frac{c^{CFT}}{3} \log l + S_0, \tag{3.17}$$

where c^{CFT} is the central charge of the CFT. Eq. (3.17) is an example of universal behavior at long distances. In a gapped quantum spin chain, there is no logarithmic growth of entanglement entropy. Instead, we have the *area law* [34],

$$S_A \leq S_{\max}, \tag{3.18}$$

where $S_{\max}$ is a non-universal number independent of l and N.

3.2 Matrix product states

Given the exponential growth of the dimension of the Hilbert space Eq. (3.1), it becomes exponentially costly to solve the eigenstates by exact diagonalization (ED). However, the ground state of a local Hamiltonian has a special structure of entanglement, e.g., the entropy satisfies Eq. (3.18) for a gapped Hamiltonian or Eq. (3.17) for a gapless (critical) Hamiltonian. Tensor network states [129, 39, 125, 28, 117, 132, 38, 116, 36, 109] ultilize these properties and dramatically decrease the numerical cost to $O(\text{Poly}(N))$ or even independent of N. In this section we will review a special type of tensor network, namely the uniform infinite matrix product state (MPS) that is suited for gapped spin chains on an infinite line. The puMPS algorithm will be analogous to the gradient descent optimization of the uniform infinite MPS.

3.2.1 Notation

A tensor $A_{i_1 i_2 \cdots i_n}$ with rank n is represented by a circle (or box) with n legs. Each leg corresponds to an index, and has the same dimension as this index. Contraction of two tensors is represented by connecting contracted legs, called bonds, whose dimensions are *bond dimensions*. After contraction, the tensor network may have external legs that are not contracted, whose dimensions are called *physical dimensions*. External legs of a tensor network state correspond to the Hilbert space in which it lives. A tensor network with no external legs represents a scalar. Some basic examples are shown in Figure 3.1.

3.2.2 Uniform infinite matrix product states

A uniform infinite MPS is defined as

$$|\Psi(A)\rangle = \sum_{\vec{s}} v_L^\dagger (\cdots A^{s_{-1}} A^{s_0} A^{s_1} \cdots) v_R |\vec{s}\rangle, \tag{3.19}$$

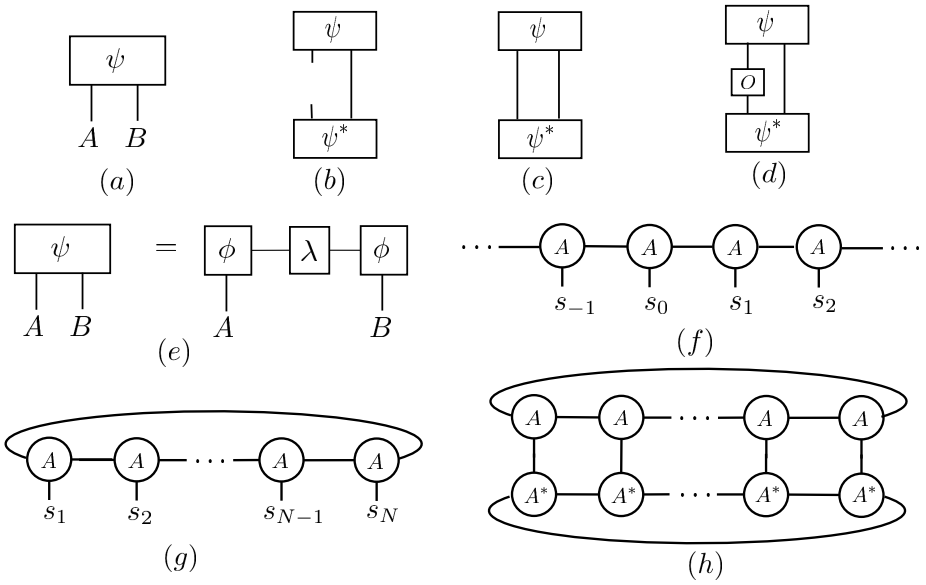

Figure 3.1: Basic examples of tensor networks. (a) A bipartite state $|\psi\rangle_{AB}$. (b) The reduced density matrix of A of the state. (c) The square of the norm of the state $\langle\psi|\psi\rangle$. (d) The expectation value of O on subsystem A, $\langle\psi|O_A|\psi\rangle$ (e) The Schmidt decomposition, Eq. (3.15). (f) An uniform infinite MPS, Eq. (3.19). (g) A puMPS, Eq. (3.34). (h) The square of the norm of the puMPS, $\langle\Psi(\bar{A})|\Psi(A)\rangle$.

where $s_i = 1, 2, \cdots d$ labels a basis of the local Hilbert space on the site with position i, $\vec{s} = \cdots s_{-1} s_0 s_1 \cdots$, and A^{s_i} is a set of d matrices with size $D \times D$ that specifies the infinite MPS. D is the *bond dimension* of the MPS.

It can be shown that the maximal entanglement entropy between the left and the right of the MPS is

$$S \leq \log D, \tag{3.20}$$

since there are at most D nonvanishing Schmidt coefficients. Therefore, the MPS can only faithfully represent the ground state of a gapped Hamiltonian. There are both analytical and extensive numerical evidence that the ground state of any gapped Hamiltonian can be represented as a MPS (either uniform or non-uniform) [126, 122, 121, 56, 58, 109, 137]. In additional to a numerical tool, MPS has also been used to classify of topological phases in 1D [25, 26].

Given a Hamiltonian H, we can minimize the energy function

$$E(A, \bar{A}) = \frac{\langle \Psi(\bar{A}) | H | \Psi(A) \rangle}{\langle \Psi(\bar{A}) | \Psi(A) \rangle} \tag{3.21}$$

with respect to the tensor A to get an approximation to the ground state. One may then compute correlation functions from $|\Psi(A)\rangle$.

It is well known that when applying infinite MPS to a critical system the finite bond dimension D introduces an artificial finite correlation length $\xi(D)$ which grows with D. Despite the fact that long distance physics beyond the correlation length is not captured, algebraically decaying correlation functions at shorter distances can be faithfully reproduced, and conformal data such as scaling dimensions and the central charge can be extracted. In order to obtain higher accuracy, one may minimize the energy with a series of increasing D and extrapolate to the $D \to \infty$ limit. Such a way is known as *finite entanglement scaling* (FES) [117, 116]. We will compare FES with our method based on puMPS in Chapter 4.

3.2.3 Canonical forms

The variational ansatz Eq. (3.19) has a gauge freedom. Two sets of matrices A^s and A'^s describe the same state, i.e. $|\Psi(A)\rangle = |\Psi(A')\rangle$ if they are related by a gauge transformation, $A'^s = g^{-1} A^s g$, where g is a $D \times D$ invertible matrix. We can enforce certain conditions for the tensor A for any uniform infinite MPS by exploiting this gauge freedom. One convenient condition is the *left canonical gauge*, where we fix $A = A_L$ that satisfies

$$\sum_s A_L^{\dagger s} A_L^s = \mathbf{1} \tag{3.22}$$

and

$$\sum_s A_L^s \lambda^2 A_L^{\dagger s} = \lambda^2, \tag{3.23}$$

where λ is a $D \times D$ diagonal matrix consisting of descending positive numbers λ_i as its diagonal elements. The λ_i's are the Schmidt coefficients of the bipartition of the infinite chain into left and right semi-infinite chains. Given the original tensor A of the MPS, the left canonical tensor A_L can be obtained with a standard procedure [109]. We will use the left canonical gauge in the following. Then the optimization of Eq. (3.21) is equivalent to optimizing

$$E(A_L, \bar{A}_L) = \frac{\langle \Psi(\bar{A}_L)|H|\Psi(A_L)\rangle}{\langle \Psi(\bar{A}_L)|\Psi(A_L)\rangle} \tag{3.24}$$

over all possible left canonical tensor A_L.

3.2.4 Gradient descent optimiztion

The gradient optimization was originally proposed in [51] as an energy minimization algorithm for continuous matrix product states. Here we will adapt it to the case of uniform infinite MPS. First, let us review how gradient descent works in general numerical analysis [2]. Given a smooth functon $f : M \to R$ where M is a Kahler manifold with local coordinates $z^\mu, \bar{z}^\mu$, we want to find the minimum of f. Starting with an initial guess $(z, \bar{z})$, The gradient descent optimization consists of two iterative steps,

1. Compute the gradient $\partial f/\partial \bar{z}^\nu$.
2. Change the coordinate $z^\mu \to z^\mu - \alpha g^{\mu\nu}\partial f/\partial \bar{z}^\nu$ where $g^{\mu\nu}$ is the metric tensor and α is a step size obtained by a line search.

Consider a local deformation of the MPS that changes the tensor only on the site 1 into another tensor. The deformed state

$$|\Psi_{A_L}(A_C)\rangle = \sum_{\vec{s}} v_L^\dagger (\cdots A_L^{s_0}(A_C^{s_1}\lambda^{-1})A_L^{s_2}\cdots)v_R|\vec{s}\rangle \tag{3.25}$$

depends on a $d \times D \times D$ tensor A_C, which is referred to as the *central tensor*. The choice of A_C to parametrize the local deformation is justified by (3.26) below. If $A_C = A_L\lambda$, the state $|\Psi_{A_L}(A_C)\rangle$ comes back to the original state $|\Psi(A_L)\rangle$.

It can be shown that the expectation value of any one site operator O on site 1 for the deformed state is $\langle O_1\rangle = \mathrm{Tr}(O_{ss'}A_C^s A_C^{s'\dagger})$, where repeated upper and lower indices are

implicitly summed. In particular, the square of the norm of the deformed MPS equals the vector norm of tensor A_C,

$$\langle \Psi_{\bar{A}_L}(\bar{A}_C)|\Psi_{A_L}(A_C)\rangle = \delta_{\mu\nu}\bar{A}_C^{\mu}A_C^{\nu}, \tag{3.26}$$

where we use $\mu = (s, a, b)$ to denote the combination of the physical index s and matrix indices (a, b), that is $A^{\mu} \equiv A^s_{ab}$. The fact that the metric tensor in Eq. (3.26) is $\delta_{\mu\nu}$ leads to a crucial simplification of the gradient optimization of MPS. We will see in the next section that the norm of a locally deformed puMPS is related to the central tensor A_C not by an identity matrix, but a general positive definite matrix, which results in additional complexity in the gradient algorithm for puMPS.

Now we explain how gradient optimization works. We will not work with the highly nonlinear cost function Eq. (3.24) directly. Instead, we will work with an auxiliary energy function

$$E_{A_L}(A_C, \bar{A}_C) = \frac{\langle \Psi_{\bar{A}_L}(\bar{A}_C)|H|\Psi_{A_L}(A_C)\rangle}{\langle \Psi_{\bar{A}_L}(\bar{A}_C)|\Psi_{A_L}(A_C)\rangle} \tag{3.27}$$

which only depends on the central tensor A_C on site 1. The auxiliary energy function satisfies the following properties: (i) $E_{A_L}(A_C, \bar{A}_C) = E(A_L, \bar{A}_L)$ if $A_C = A_L\lambda$. (ii) Under an infinitesimal change of tensor $A'_L = A_L + \delta A_L$, the change in the original energy function $\delta E(A_L, \bar{A}_L) \equiv E(A'_L, \bar{A}'_L) - E(A_L, \bar{A}_L)$ is related to the change in the auxiliary energy function $\delta E_{A_L}(A_C, \bar{A}_C) \equiv E_{A_L}(A'_C, \bar{A}'_C) - E_{A_L}(A_C, \bar{A}_C)$ by

$$\delta E(A_L, \bar{A}_L) = N\delta E_{A_L}(A_C, \bar{A}_C) + O((\delta A_L)^2), \tag{3.28}$$

where $A_C = A_L\lambda$ and $A'_C = A'_L\lambda$, and N is the size of the system. Thus, if an infinitesimal change δA_C away from $A_C = A_L\lambda$ decreases the auxiliary energy function, (3.27), the corresponding change $\delta A_L = \delta A_C\lambda^{-1}$ also decreases the original energy function, (3.24). We expect that this is still true for a finite but small change. Therefore, to minimize the energy function Eq. (3.24) iteratively, we first identify the direction of change ΔA_C in A_C that decreases (3.27), and then change A_L according to $\delta A_L = \delta A_C\lambda^{-1}$.

To be more concrete, given an initial MPS, we compute its left canonical tensor A_L and the diagonal matrix λ. Next, taking the derivative of $E_{A_L}(A_C, \bar{A}_C)$ with respect to the central tensor $\bar{A}_C$ on site 1, we obtain the local gradient

$$\frac{\partial E_{A_L}(A_C, \bar{A}_C)}{\partial \bar{A}_C^{\nu}} = \langle (\partial/\partial \bar{A}_C^{\nu})\Psi_{\bar{A}_L}(\bar{A}_C)|\tilde{H}|\Psi_{A_L}(A_C)\rangle \tag{3.29}$$

where $\tilde{H} = H - \langle \Psi(\bar{A}_L)|H|\Psi(A_L)\rangle$ is the shifted Hamiltonian, and we have assumed the normalization

$$\langle \Psi_{\bar{A}_L}(\bar{A}_C)|\Psi_{A_L}(A_C)\rangle = 1. \tag{3.30}$$

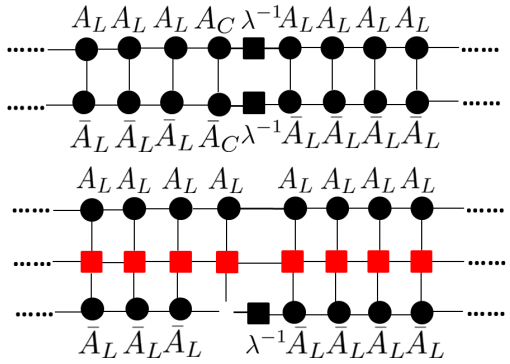

Figure 3.2: Tensor networks used in the gradient descent algorithm for uniform infinite MPS. Top: the square of the norm of locally deformed MPS with central tensor A_C. It equals the vector norm of the tensor A_C, Eq. (3.26). Bottom: derivative of the auxiliary energy function $E_{A_L}(A_C)$ with respect to the central tensor A_C in Eq. (3.29), where red tensors form a matrix product operator representation of the shifted Hamiltonian $\tilde{H}$.

Contracting the tensor network representing Eq. (3.29) gives us the local gradient, see Fig. 3.2, where we have used the matrix product operator (MPO) representation of the Hamiltonian. More details about the MPO are discussed in Appendix A. The direction of ΔA_C is then chosen as opposite to the direction of the local gradient,

$$\Delta A^{\mu}_{C} = -\delta^{\mu\nu}\frac{\partial E_{A_L}(A_C,\bar{A}_C)}{\partial \bar{A}^{\nu}_{C}}. \tag{3.31}$$

The appearance of $\delta^{\mu\nu}$ is related to the fact that the vector space of A_C inherits a flat metric from the norm of the locally deformed MPS, as already noted in (3.26). Next, we change A_L in the direction of $\Delta A_C\lambda^{-1}$,

$$A'_L = A_L + \alpha(\Delta A_C\lambda^{-1}) \tag{3.32}$$

where $\alpha > 0$ is a step size obtained by either a line search or empirical observations to optimally minimize the energy function. Finally, we replace the tensor A of the MPS with A'_L, and use the standard procedure [109] to put it back to the left canonical form. Note that A'_L does not fulfill the left canonical condition (3.22)(3.23) in general. In the next iteration we first need to compute the left canonical tensor A_L from of the updated MPS $|\Psi(A'_L)\rangle$.

We iterate the steps above until the *norm of the gradient*

$$\eta = \sqrt{\delta^{\mu\nu}\frac{\partial E_{A_L}(A_C,\bar{A}_C)}{\partial A^{\mu}_{C}}\frac{\partial E_{A_L}(A_C,\bar{A}_C)}{\partial \bar{A}^{\nu}_{C}}} \tag{3.33}$$

is sufficiently small. Notice that η would vanish if we had reached the minimum of the energy function. In practice, we observe that the error in ground state energy is on the order of η^2, thus we may stop when η equals the square root of the expected precision in energy.

The most costly part of the algorithm is the computation of the local gradient (3.29) at $\mathcal{O}(D^3)$ per iteration, comparable to the cost of the infinite density matrix renormalization group (iDMRG) [77, 109], while we have the additional advantage of keeping explicit translation invariance. Other optimization schemes, such as the infinite time evolution block decimation (iTEBD) [124] and the time dependent variational principle (TDVP) [56, 92], though keep translation invariance explicitly, converge slower than the gradient optimization because they follow an imaginary time evolution trajectory.

3.3 Periodic uniform matrix product states

A puMPS on a finite circle is a finite size analog of the translation invariant MPS on an infinite line. A puMPS on N sites is defined as

$$|\Psi(A)\rangle = \sum_{\vec{s}=1}^{d} \mathrm{Tr}(A^{s_1} A^{s_2} \cdots A^{s_N}) |\vec{s}\rangle, \tag{3.34}$$

where $\vec{s} = s_1 \dots s_N$ and d is the dimension of the Hilbert space for a single site. It can represent the ground state of critical spin chains with high fidelity provided that the bond dimension D grows polynomially with the system size N [123, 121]. This can be seen by the fact that the maximal entanglement entropy of a contagious region in a puMPS is

$$S \leq 2 \log D, \tag{3.35}$$

and that the entanglement entropy in the ground state of a critical spin chain scales logarithmically with N.

3.3.1 Gradient descent algorithm

The optimization of a periodic MPS, which typically costs $\mathcal{O}(ND^5)$ or higher, is numerically more costly than open boundary MPS [123, 89] which costs $\mathcal{O}(ND^3)$. In a gapped system, one may reduce the cost of optimizing a puMPS to $\mathcal{O}(ND^3)$ by truncating singular values of the transfer matrix [92]. However, in a critical system, the truncation will introduce

larger errors. Therefore, here we will not follow such a strategy. Instead, we propose a local gradient descent method that resembles the gradient optimization for open boundary MPS introduced in the previous section, but with cost $\mathcal{O}(ND^5)$. It also shares some features with the TDVP method although we do not follow an imaginary time evolution trajectory.

The energy minimization goes as follows. First, we treat the tensor A as if it belonged to an infinite MPS and compute A_L and λ that satisfy the left canonical condition (3.22)(3.23). Then we define the locally deformed puMPS as

$$|\Psi_{A_L}(A_C)\rangle = \sum_{\vec{s}=1}^{d} \mathrm{Tr}[(A_C^{s_1}\lambda^{-1})A_L^{s_2}\cdots A_L^{s_{N-1}}]|\vec{s}\rangle. \tag{3.36}$$

Here, as in (3.25) for the infinite MPS case, the dependence on A_C is only on site 1.

We can relate the square of the norm of the deformed puMPS to the central tensor A_C with a bilinear form,

$$\langle\Psi_{\bar{A}_L}(\bar{A}_C)|\Psi_{A_L}(A_C)\rangle = \bar{A}_C^{\mu} g_{\mu\nu} A_C^{\nu}. \tag{3.37}$$

We call the positive definite matrix $g_{\mu\nu}$ the *local effective norm matrix* for the central tensor. For an infinite MPS, we can read off $g_{\mu\nu} = \delta_{\mu\nu}$ from (3.26). However, $g_{\mu\nu}$ is nontrivial in the case of puMPS as a result of periodic boundary conditions, as represented in Fig. 3.3. Then, as we did for infinite MPS, we can define the auxiliary energy function as (3.27) with the state substituted by the deformed puMPS. The computation of the local gradient $\partial E_{A_L}(A_C, \bar{A}_C)/\partial \bar{A}_C^{\nu}$ is also simplified by using the shifted Hamiltonian, which leads to the same expression for the local gradient as (3.29) but the state substituted by the deformed puMPS. It is represented as a tensor network in Fig. 3.3. These tensor networks can be contracted with time cost $\mathcal{O}(ND^5)$.

Next, we compute the direction of change ΔA_C in the central tensor A_C with gradient descent. The optimal direction ΔA_C that decreases the auxiliary energy function now becomes

$$\Delta A_C^{\mu} = -g^{\mu\nu}\frac{\partial E_{A_L}(A_C, \bar{A}_C)}{\partial \bar{A}_C^{\nu}}, \tag{3.38}$$

where $g^{\mu\nu}$ is the inverse of the nontrivial metric $g_{\mu\nu}$ as given by the local effective norm matrix in (3.37), satisfying $g^{\mu\nu}g_{\nu\rho} = \delta^{\mu}_{\rho}$. This results from the fact that the space of A_C now inherits the nontrivial metric $g_{\mu\nu}$ from the norm of the locally deformed puMPS, compared to (3.31). The inverse metric, however, does not need to be computed densely, since all we need is to compute (3.38), where the left hand side can be solved for iteratively. The use of the left canonical form, though it does not eliminate the need for inverting the metric,

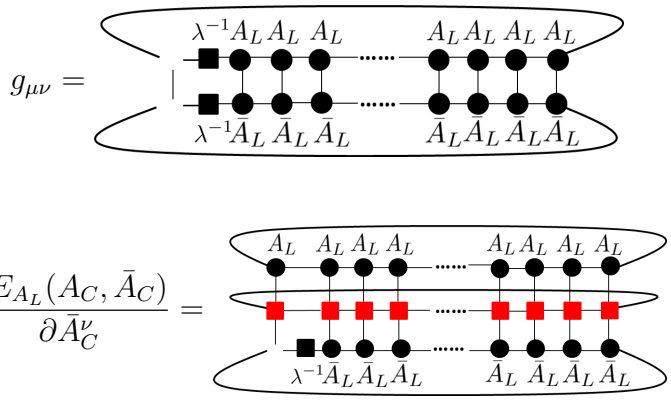

Figure 3.3: Top: the tensor network for the local effective norm matrix (3.37) for the deformed puMPS in the left canonical gauge. Bottom: the tensor network for the derivative of the auxiliary energy function with respect to the puMPS tensor A_C in (3.29), assuming that the puMPS is normalized. The red tensors form a matrix product operator representation of the shifted Hamiltonian $\tilde{H}$.

is advantageous in practice, since it generally leads to a better conditioned local metric favored by iterative linear equation solvers.

Finally, we transform the change of A_C into the change of puMPS tensor A_L by $\Delta A_L = \Delta A_C \lambda^{-1}$, then update the tensor according to

$$A_L' = A_L + \alpha \Delta A_L, \tag{3.39}$$

where $\alpha > 0$ is the step size obtained by either line search or empirical observations. A_L' is then used as the new puMPS tensor (for all sites), resulting in an updated puMPS. The iteration then restarts from computing the left canonical tensor of the updated puMPS.

Convergence is also monitored using the norm of the local gradient with a modified definition

$$\eta = \sqrt{g^{\mu\nu} \frac{\partial E_{A_L}(A_C,\bar{A}_C)}{\partial A_C^\mu} \frac{\partial E_{A_L}(A_C,\bar{A}_C)}{\partial \bar{A}_C^\nu}}. \tag{3.40}$$

We also observe that the error in ground state energy is roughly η^2 for the puMPS gradient descent algorithm. Thus we stop at $\eta < 10^{-6}$ in all the simulations, resulting in a 10^{-12} error in the ground state energy which is negligible compared to other sources of errors in conformal data, such as the non-universal subleading finite size corrections.

The above method shares with TDVP the computation of an effective norm matrix and its inverse matrix. The main difference is that while in TDVP we compute the full

effective norm matrix to follow the trajectory of an imaginary time evolution, which costs $\mathcal{O}(ND^6)$ per iteration for puMPS, in the local gradient descent method above we compute the local effective norm matrix where the dependence of A_C is only kept explicit on one site. In order to find the ground state, it is not necessary to follow the trajectory of an imaginary time evolution. Instead, in many cases [51, 137] including our case, a simpler local gradient method makes energy minimization faster.

3.3.2 Preconditioning

Optimization using gradient descent usually suffers from local minima. *Preconditioning* is a procedure to find an initial state that approximates the global minimum, with which gradient descent converges faster. In the context of puMPS optimization, we observe that starting with a random state only works well for small bond dimension in small systems. For puMPS with larger bond dimension in larger systems, the energy landscape of the variational manifold becomes more complicated, and the algorithm is more likely to get stuck in a local minimum. Here, we use several simple ways of preconditioning.

First, we can directly use the optimized puMPS tensor for system size N_0 as the tensor A for the initial state for slightly larger system sizes $N_1 > N_0$ with the same bond dimension.

Second, for the same system size, as an initial puMPS state with bond dimension D_1, we can use the optimized puMPS tensor with smaller bond dimension D_0, enlarging it to $d \times D_1 \times D_1$ and filling the vacancies with small random numbers.

We compare the convergence of the local gradient descent algorithm in these two cases, with preconditioning or starting with random state, in Fig. 3.4. The results show that preconditioning significantly accelerates convergence and helps produce accurate ground state approximations within a smaller number of iterations.

3.4 Excited states

After iteratively optimizing the ground state puMPS $|\Psi(A)\rangle$ of bond dimension D with respect to a critical Hamiltonian with size N , we can solve low-energy excited states with time cost $O(ND^6)$ using the puMPS *Bloch state* ansatz. We find that puMPS Bloch states can accurately reproduce *all* low-energy eigenstates of *critical* quantum spin chains (that is, up to some appropriate maximum energy). This is remarkable, since the puMPS

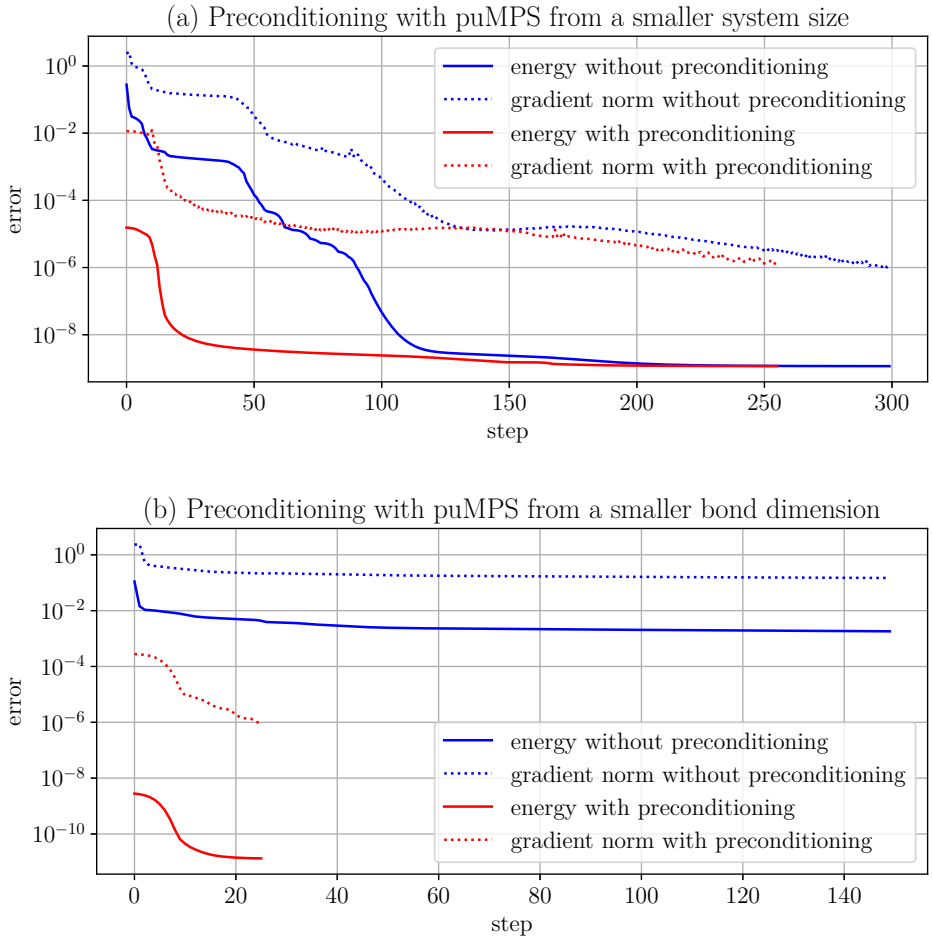

Figure 3.4: Convergence of the puMPS gradient descent algorithm with preconditioning for the critical Ising model with $N = 128$. The dashed lines are the convergence of the gradient norm η, and the solid lines represent the energy difference of puMPS from the exact ground state energy at each step of energy minimization. (a) Bond dimension $D = 18$, initial state chosen with the pre-optimized puMPS tensor for $N = 64, D = 18$ (red), and random initial state (blue). (b) Bond dimension $D = 30$, initial state chosen by enlarging the optimized puMPS tensor from $D = 18, N = 128$ (red), and random initial state (blue). Iterations are stopped when $\eta < 10^{-6}$.

Bloch state is originally designed to capture only *some* (namely single-quasiparticle) low-energy excitations in *gapped* systems [104], where multi-quasiparticle excitations require an alternative, significantly more sophisticated ansatz [118].

3.4.1 puMPS Bloch states

A Bloch state of the optimized puMPS with momentum p is determined by anthoer $d \times D \times D$ tensor B^s_{ab},

$$|\Phi_p(B;A)\rangle = \sum_{n=1}^{N} e^{-ipn}\mathcal{T}^n \sum_{\vec{s}=1}^{d} \mathrm{Tr}\left(B^{s_1}A^{s_2}\dots A^{s_N}\right)|\vec{s}\rangle, \tag{3.41}$$

where $\mathcal{T}$ is the translation operator by one site. The Bloch state is an eigenstate of the translation operator $\mathcal{T}$,

$$\mathcal{T}|\Phi_p(B;A)\rangle = e^{ip}|\Phi_p(B;A)\rangle, \tag{3.42}$$

because

$$\begin{aligned}
& \mathcal{T}|\Phi_p(B;A)\rangle \\
= & \sum_{j=1}^{N} e^{-ipj}\mathcal{T}^{j+1} \sum_{\vec{s}=1}^{d} \mathrm{Tr}(B^{s_1}A^{s_2}\cdots A^{s_N})|\vec{s}\rangle \\
= & \sum_{j=2}^{N+1} e^{-ip(j-1)}\mathcal{T}^{j} \sum_{\vec{s}=1}^{d} \mathrm{Tr}(B^{s_1}A^{s_2}\cdots A^{s_N})|\vec{s}\rangle \\
= & e^{ip}\sum_{j=2}^{N+1} e^{-ipj}\mathcal{T}^{j} \sum_{\vec{s}=1}^{d} \mathrm{Tr}(B^{s_1}A^{s_2}\cdots A^{s_N})|\vec{s}\rangle \\
= & e^{ip}\sum_{j=1}^{N} e^{-ipj}\mathcal{T}^{j} \sum_{\vec{s}=1}^{d} \mathrm{Tr}(B^{s_1}A^{s_2}\cdots A^{s_N})|\vec{s}\rangle \\
= & e^{ip}|\Phi_p(B;A)\rangle,
\end{aligned}$$

where the fourth equality makes use of the fact that $e^{-ip(N+1)}\mathcal{T}^{N+1} = e^{-ip}\mathcal{T}$, as a result of $e^{-ipN} = 1$ and $\mathcal{T}^N = \mathbf{1}$. Following the terminology in [56], we also refer to $|\Phi_p(B;A)\rangle$ as a puMPS *tangent state*, and B the tangent tensor.

The tangent tensor B can be determined by solving a generalized eigenvalue problem, which is detailed below.

3.4.2 The generalized eigenvalue problem

An eigenstate of a Hamiltonian is a saddle point of the expectation value of energy in the Hilbert space. Analogously, we require that

$$\frac{\delta}{\delta \bar{B}^{\mu}} \frac{\langle \Phi_p(\bar{B};\bar{A})|H|\Phi_p(B;A)\rangle}{\langle \Phi_p(\bar{B};\bar{A})|\Phi_p(B;A)\rangle} = 0 \tag{3.43}$$

It can be simplified to a generalized eigenvalue equation [90],

$$H_{\mu\nu}(p)B^{\nu} = EN_{\mu\nu}(p)B^{\nu}, \tag{3.44}$$

where $N_{\mu\nu}(p)$, $H_{\mu\nu}(p)$ are the effective norm matrix and the effective Hamiltonian in each momentum sector,

$$N_{\mu\nu}(p) = \left\langle \frac{\partial}{\partial \bar{B}^{\mu}}\Phi_p(\bar{B},\bar{A}) \middle| \frac{\partial}{\partial B^{\nu}}\Phi_p(B,A) \right\rangle \tag{3.45}$$

$$H_{\mu\nu}(p) = \left\langle \frac{\partial}{\partial \bar{B}^{\mu}}\Phi_p(\bar{B},\bar{A}) \middle| H \middle| \frac{\partial}{\partial B^{\nu}}\Phi_p(B,A) \right\rangle, \tag{3.46}$$

where the derivative is taken with respect to the tensor on *all* sites in contrast with the local effective norm matrix $g_{\mu\nu}$ in the previous section (see Eq. (3.37)).

We have to be a bit cautious when solving the generalized eigenvalue equation Eq. (3.44) by multiplying the inverse of $N_{\mu\nu}(p)$ on both sides. This is because (i) the full effective norm matrix $N_{\mu\nu}(p)$ is only semi-positive definite due to gauge freedom of MPS tangent vectors [92, 58], and (ii) it is not well conditioned, even if we project out its null space, as many positive eigenvalues may be close to zero, see Fig. 3.6 for an example. The first problem is settled if we use the pseudoinverse of the effective norm matrix instead of the ordinary inverse. In order to solve the second problem, we can again make use of the left canonical form of the puMPS. We parametrize the puMPS with the left canonical tensor A_L, and the tangent tensor B is parametrized with B_C by $B = B_C\lambda^{-1}$,

$$|\Phi_p(B_C,A_L)\rangle = \sum_{n=1}^{N} e^{-ipn}\mathcal{T}^n \sum_{\vec{s}=1}^{d} \mathrm{Tr}((B_C^{s_1}\lambda^{-1})A_L^{s_2}\cdots A_L^{s_N})|\vec{s}\rangle. \tag{3.47}$$

Then (3.44) can be rewritten in terms of B_C,

$$H_{\mu\nu,C}(p)B_C^{\nu} = EN_{\mu\nu,C}(p)B_C^{\nu}, \tag{3.48}$$

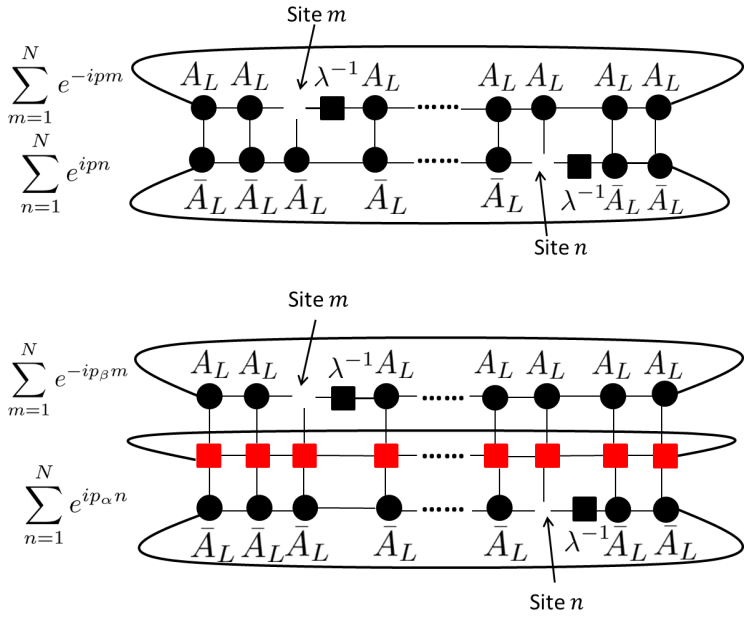

Figure 3.5: Top: the tensor network for the effective norm matrix $N_{\mu\nu,C}(p)$ for puMPS tangent states parametrized with A_L and $B_C = B\lambda$. Bottom: the tensor network for the effective Hamiltonian $H_{\mu\nu,C}(p)$ when $p_\alpha = p_\beta = p$, or for the effective H_n matrices $H_{n,\mu\nu,C}(p_\alpha, p_\beta)$, where the red tensors in the middle form a matrix product operator representation of the Hamiltonian or its Fourier modes, respectively.

where $N_{\mu\nu,C}(p)$ and $H_{\mu\nu,C}(p)$ are obtained by substituting the derivatives in (3.45), (3.46) by derivatives with respect to B_C and $\bar{B}_C$ and setting $A = A_L$,

$$N_{\mu\nu,C}(p) = \left\langle \frac{\partial}{\partial \bar{B}_C^\mu}\Phi_p(\bar{B}_C, \bar{A}_L) \middle| \frac{\partial}{\partial B_C^\nu}\Phi_p(B_C, A_L) \right\rangle \tag{3.49}$$

$$H_{\mu\nu,C}(p) = \left\langle \frac{\partial}{\partial \bar{B}_C^\mu}\Phi_p(\bar{B}_C, \bar{A}_L) \middle| H \middle| \frac{\partial}{\partial B_C^\nu}\Phi_p(B_C, A_L) \right\rangle. \tag{3.50}$$

They are depicted as tensor networks in Fig. 3.5. Contraction of each tensor network costs $O(ND^6)$.

The effective norm matrix $N_{\mu\nu,C}(p)$ with respect with B_C is much better conditioned than the original effective norm matrix $N_{\mu\nu}(p)$ with respect to B in a random gauge. As an example, we fix $A = A_L$ and plot the eigenvalues of $N_{\mu\nu,C}(p = 0)$ and $N_{\mu\nu}(p = 0)$ for the Ising model with $N = 64$ and puMPS bond dimension $D = 24$ to show this explicitly in Fig. 3.6.

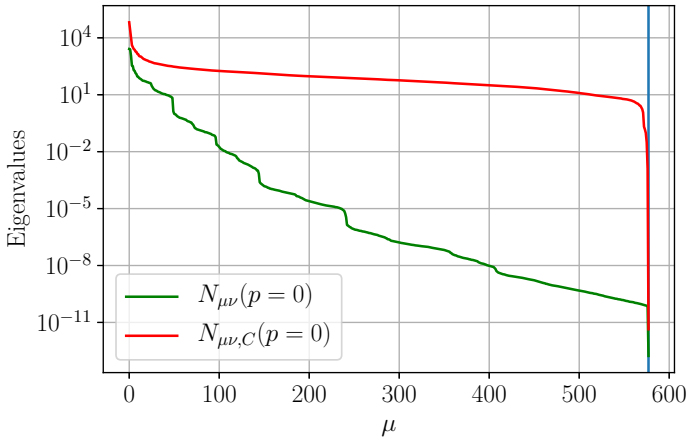

Figure 3.6: Nonzero eigenvalues of the effective norm matrix in momentum zero sector of the Ising model with $N = 64, D = 24$, sorted in descending order. Green: $N_{\mu\nu}(p = 0)$ in (3.45) where the puMPS tensor A is fixed as the left canonical tensor A_L. Red: $N_{\mu\nu,C}(p = 0)$ in (3.49). The blue vertical line is at $\mu = (d-1)D^2+1$, the number of nonzero eigenvalues resulting from the gauge freedom of puMPS tangent state in momentum zero sector.

We then multiply by the *pseudoinverse* $\tilde{N}_C^{\rho\mu}(p)$ of the effective norm matrix on both sides of (3.48) to obtain the ordinary eigenvalue equation,

$$\tilde{N}_C^{\rho\mu}(p)H_{\mu\nu,C}(p)B_C^{\nu} = EB_C^{\rho}. \tag{3.51}$$

Finally we compute a set of low-energy eigenvectors in each momentum sector with (3.51) using the Lanczos algorithm, and multiply B_C by λ^{-1} to get back to B.

The computation of $N_{\mu\nu,C}(p)$ and $H_{\mu\nu,C}(p)$ is the most costly part in the algorihm, which costs $\mathcal{O}(ND^6)$. However, since we only need to construct the matrices once for each momentum sector, the actual time cost is usually less than ground state optimization.

3.4.3 Fidelity for the Ising model

In order to check how well the excited states are captured by the above puMPS Bloch state ansatz, we explicitly compute the fidelity of puMPS tangent vectors obtained above with eigenstates obtained by exact diagonaliztion for the Ising model Eq. (3.13) with $N = 20$. The fidelity is defined as

$$f_\alpha = \langle \phi_\alpha | \phi_\alpha^{\text{exact}} \rangle, \tag{3.52}$$

where $|\phi_\alpha^{\text{exact}}\rangle$ is the αth eigenstate from exactly diagonalizing the full Hamiltonian, and $|\phi_\alpha\rangle = |\Phi_{p_\alpha}(B_\alpha, A)\rangle$ is the corresponding eigenstate represented approximately as a puMPS tangent vector. We compute the first 41 eigenstates, each eigenstate corresponding to a scaling operator with $\Delta \leq 4 + 1/8$ (to be explained in section 4.1). The result is shown in Fig. 3.7.

We can see that although the fidelity decreases as energy increases for a fixed bond dimension, fidelity increases uniformly for each state as the bond dimension increases, regardless of energy and conformal tower of the state. Thus we conclude that the puMPS Bloch state ansatz, Eq. (3.41), can capture all eigenstates in the low-energy subspace with sufficiently small errors, given large enough bond dimension.

3.4.4 Validlity for generic critical quantum spin chains

We have checked that the puMPS Bloch state can represent all low-energy excited states of the critical Ising model ($N = 20$) with high fidelity. Two natural questions arise, the first being how the puMPS Bloch state works for other models and the second being how large sizes can be reached.

In order to answer the first question, we will apply puMPS Bloch states to different models, in particular the non-integrable O'Brien-Fendley (OF) model and the ANNNI model in Chapter 4. We have also checked the validity for 3-state and 4-state Potts model, and the XXZ model in Chapter 7. Combining the puMPS techniques with the method of extracting conformal data from low-energy eigenstates, we find the results in excellent agreement with analytical results. This highly suggests that the puMPS Bloch state is a generic method that works for all low-energy eigenstates of a generic critical quantum spin chain. We also note that in Ref.[] the puMPS Block states are shown to reproduce accurate energies in the Ising model and XXZ model where the theory is integrable.

In order to answer the second question, we note that the bond dimension D needs to grow polynomially with the system size N for a critical quantum spin chain. This can be seen by comparing the entanglement entropy, Eq. (3.17) with Eq. (3.35). It can be also seen that D grows at worst exponentially on the central charge c^{CFT}. Given that the numerical cost grows as $O(ND^5)$ for the ground state energy optimization, the maximal size that we can reach is smaller for models with larger central charge. In practice, we have reached $N \leq 228$ and $D \leq 49$ for the Ising model ($c^{CFT} = 0.5$), which takes several days to run. For the OF model at the TCI point ($c^{CFT} = 0.7$), we reached $N \leq 128$ and $D \leq 44$. For the 4-state Potts model ($c^{CFT} = 1$), we can reach roughly 50 spins within several days of runtime.

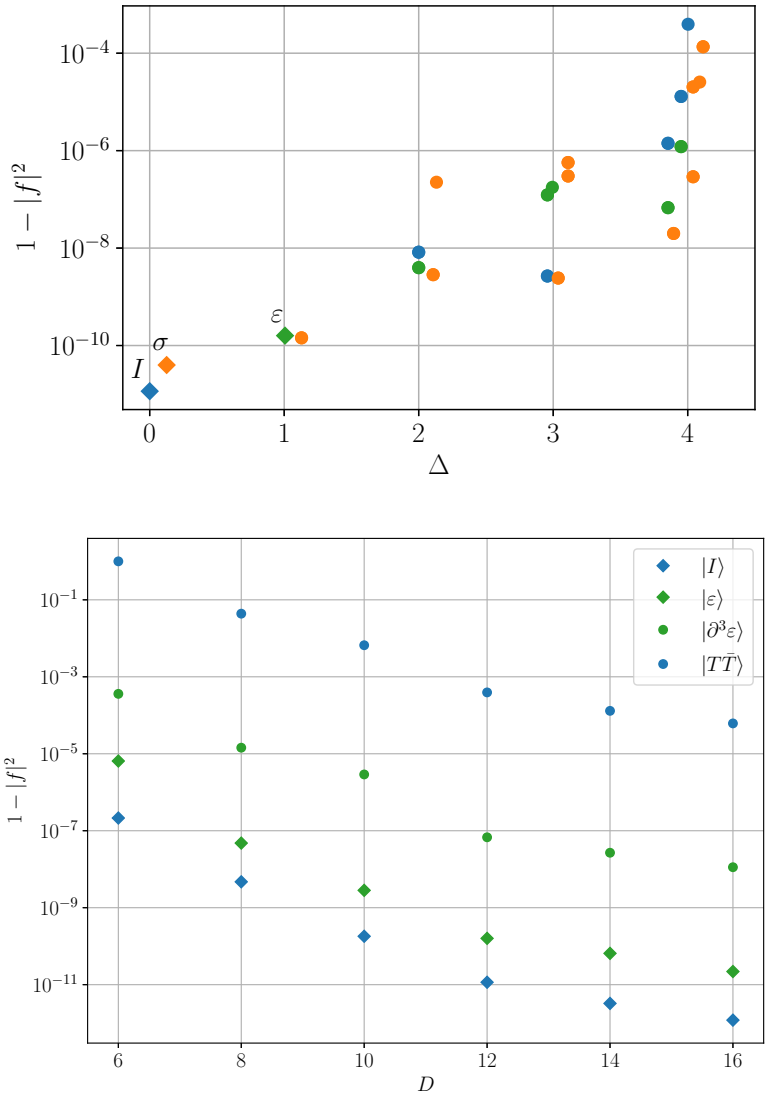

Figure 3.7: Fidelity of the first 41 exactly diagonalized eigenstates of the Ising model ($N = 20$) with their variational, puMPS Bloch-state counterparts. Top: fidelity of all 41 states for fixed bond dimension $D = 12$. Primary states are labeled with diamonds and descendant states are labeled with dots. Different colors label states in different conformal towers. Bottom: fidelity of four selected states for bond dimensions $6 \leq D \leq 16$. All ground states are converged to $\eta < 10^{-6}$.

We remark that it is *a priori* far from obvious that puMPS Bloch states should be an appropriate ansatz for all low-energy excited states. After all, in a noncritical spin chain only single-particle excitations are well captured by this type of ansatz [57], and a different ansatz [118] is needed to capture multiparticle excitations. However, in a critical system (for sufficiently large bond dimension [91]) correlations in the puMPS are long range so that the tensor B of Eq. (3.41) is capable of modifying the ground state wavefunction *more globally* than in the gapped case, making the ansatz more expressive. Note that the ansatz can easily be further improved by considering B tensors that encompass two or more lattice sites, instead of one [58].

Chapter 4

Conformal data and renormalization group flow in critical quantum spin chains

In this chapter we extract conformal data from critical quantum spin chains based on the low-energy eigenstates. We will first introduce two classic results, Cardy's relation of the spectrum of energies and momenta, and Koo-Saleur lattice Virasoro generators. Combined with the puMPS techniques which allow us to obtain accurate approximations to low-energy eigenstates with sufficiently large system sizes, we are able to reproduce (i) highly accurate scaling dimensions, conformal spins, and the central charge and (ii) precise identification of conformal tower. We will apply our method to the Ising model and the OF model, In the latter case, we also nonperturbatively compute the RG flow of the low-energy spectrum between the TCI CFT and the Ising CFT.

4.1 Extraction of conformal data from a critical quantum spin chain

4.1.1 Scaling dimensions and conformal spins

Given a critical quantum spin chain Hamiltonian H with PBC, it is expected that each low-energy eigenstate $|\psi_\alpha\rangle$ of H is in one-to-one correspondence with an eigenstate $|\psi_\alpha^{CFT}\rangle$ of H^{CFT} on the cylinder, and the spectrum of energies and momenta in the low energies

resembles that of a CFT, Eqs. (2.54)(2.55). This is first pointed out by Cardy and coauthors in the 80's. The momenta are quantized, Eq. (3.12), therefore they cannot have any finite-size correction, then

$$P_\alpha = \frac{2\pi}{N} s_\alpha^{CFT}. \tag{4.1}$$

The energies, on the other hand, have finite-size corrections

$$E_\alpha = A + B\frac{2\pi}{N}(\Delta_\alpha^{CFT} - \frac{c^{CFT}}{12}) + O(N^{-x}), \tag{4.2}$$

where A, B and $x > 1$ are non-universal (depending on details of the lattice model). At sufficiently large sizes, the subleading correction $O(N^{-x})$ is negligible. The constants A and B can be numerically estimated by using the fact that scaling dimensions of the ground state and the stress tensor state are always $\Delta_I^{CFT} = 0$, $\Delta_T^{CFT} = 2$ in a unitary CFT. A is the ground state energy density in the thermodynamic limit and

$$B \approx \frac{N}{2}(E_T - E_0). \tag{4.3}$$

We can then extract the scaling dimensions and conformal spins as

$$\Delta_\alpha = 2\frac{E_\alpha - E_0}{E_T - E_0} \tag{4.4}$$

$$s_\alpha = \frac{N}{2\pi} P_\alpha. \tag{4.5}$$

Notice that Δ_α and Δ_α^{CFT} differ by finite-size corrections, but $s_\alpha = s_\alpha^{CFT}$ (up to periodicity N) is exact. To obtain a more accurate approximation to Δ_α^{CFT}, we can compute Δ_α as a function of N at finite sizes and extrapolate to $N \to \infty$ (the thermodynamic limit).

4.1.2 Koo-Saleur lattice Virasoro generators

Eq. (4.4)(4.5) give a spectrum of scaling dimensions and conformal spins of scaling operators. In order to obtain conformal data, we still need to identify the primary operators. We can make use of the *Koo-Saleur lattice Virasoro generators*.

$$H_n \equiv \frac{N}{B}\sum_{j=1}^{N} h_j e^{inj2\pi/N} \sim H_n^{CFT}, \tag{4.6}$$

where $\sim$ means "acting on the low-energy eigenstates as", and H_n^{CFT} is a linear superposition of Virasoro generators, Eq. (2.57). We note that there is an ambiguity in defining

the Fourier mode for multi-site operators. Different choice results in different finite-size corrections in the matrix elements of H_n. This issue is treated carefully in Appendix B.

Denote P_{ϕ_α} the projector onto the subspace spanned by eigenstates whose energies are lower than that of $|\phi_\alpha\rangle$. Then, analogous to Eq. (2.58), primary states can be identified by the condition [80, 140] that

$$P_{\phi_\alpha} H_n |\phi_\alpha\rangle = 0 \quad (n = \pm 1, \pm 2) \tag{4.7}$$

in the thermodynamic limit. Other eigenstates can be approximately obtained by acting with H_n ($n \neq 0$) on the primary states, proceeding in analogy with the CFT. An estimate c of the central charge c^{CFT} is obtained from

$$c = 2|\langle T|H_{-2}|0\rangle|^2, \tag{4.8}$$

analogous to Eq. (2.59). Again, a suitable extrapolation to the thermodynamic limit will be used.

4.1.3 Finite-size corrections

In practice, finite-size corrections are always present. Physical quantities in critical systems usually exhibit power law finite-size scaling. In general, we can relate the finite-size conformal data $\Delta_\alpha(N), c(N)$ to their thermodynamic values Δ_α, c by

$$\Delta_\alpha(N) = \Delta_\alpha + \frac{b_\alpha}{N^{x_\alpha}} + o(N^{-x_\alpha}) \tag{4.9}$$

$$c(N) = c + \frac{b_c}{N^{x_c}} + o(N^{-x_c}), \tag{4.10}$$

where $x_\alpha, x_c, b_\alpha, b_c$ are non-universal numbers to be fitted.

In order to identify conformal towers in the presence of finite-size corrections, we can set an empirical small tolerance ϵ_p that decreases with N such that $|\phi_\alpha\rangle$ is identified as a primary state if

$$\sum_{n=-2}^{2} \sum_{E_\beta < E_\alpha} |\langle \psi_\beta | H_n | \phi_\alpha \rangle|^2 < \epsilon_p. \tag{4.11}$$

Denote the number of primary states as n_p. In order to identify conformal towers in the presence of finite-size corrections, we can proceed as the following. First, we create a matrix $C_{\alpha l}$, where α labels eigenstates and $l = 1, 2 \cdots n_p$ labels the conformal tower. The

matrix is initialized to have all zero entries. Then, set $C_{\alpha(l)l} = 1, \forall l$, where $\alpha(l)$ is the label of the lth primary state. This assigns each primary state to its own conformal tower. Then, for each non-primary state labelled by α, in order of ascending energy, we update

$$C_{\alpha l} \leftarrow \sum_{n=-2}^{+2} \sum_{E_\beta < E_\alpha} |\langle \psi_\alpha | H_n | \psi_\beta \rangle|^2 C_{\beta l}, \tag{4.12}$$

normalizing the vector $C_{\alpha l}$ after each update,

$$C_{\alpha l} \leftarrow C_{\alpha l} \Big/ \sqrt{\sum_{l=1}^{n_p} C_{\alpha l}^2}\,. \tag{4.13}$$

Finally, for each state labelled by α we determine which conformal tower it belongs to according to which component in $C_{\alpha l}$ is the largest.

In the ideal case where the system size is taken to infinity, $C_{\alpha l}$ can only pick up contributions from states within the same conformal tower with scaling dimension 1 or 2 less than that of the state $|\psi_\alpha\rangle$. Then $C_{\alpha l}$ would only have one nonzero entry normalized to 1 for each α, according to which conformal tower it belongs to. In practice, due to finite size effects, $C_{\alpha l}$ has $n_p - 1$ possibly nonzero entries which go to zero with increasing system size N, so that only one entry remains $O(1)$ for sufficiently large system size N.

4.2 Numerical results

4.2.1 Conformal towers

We first apply the puMPS techniques to the Ising model with $N = 64$ and bond dimension $D = 24$. We then identify primary operators and conformal towers as in the previous section. The whole procedure takes roughly 10 minutes on a laptop. The result is shown in Fig. (4.1). The numerically-assigned conformal towers are consistent with the CFT result up to level 7, where some states are misidentified.

Typically, eigenstates of higher energy suffer from stronger finite-size effects. For the Ising model, we find that the finite-size effects cause few problems in conformal tower identification for the low-lying spectrum, as long as the bond dimension of MPS is large enough to represent eigenstates accurately. We present exemplary results in Fig. 4.1. This

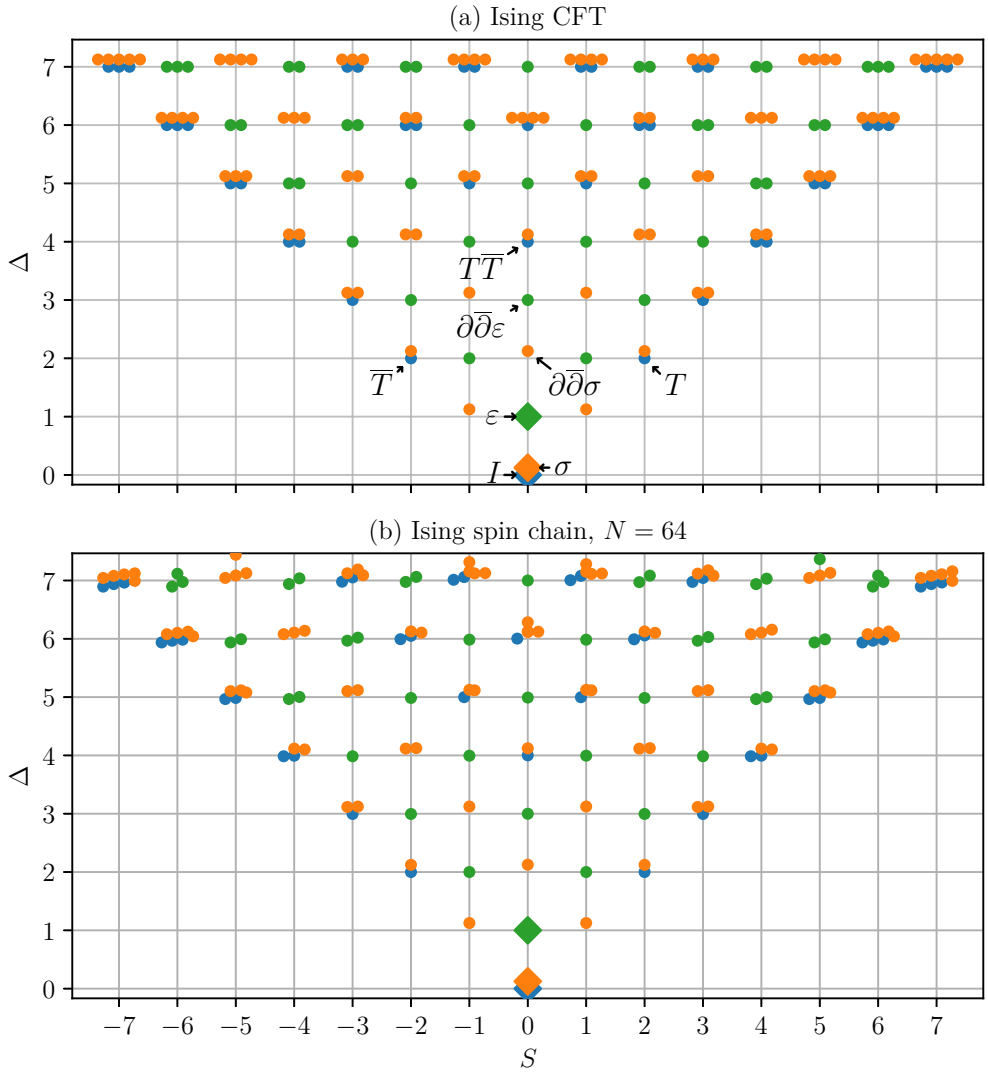

Figure 4.1: (a) Exact Ising CFT scaling operator spectrum, with diamonds marking primary operators. (b) Ising model spectrum, colored according to numerical conformal-tower identification, for $N = 64$ sites using Bloch states on top of a puMPS variational ground state with $D = 24$, converged to $\eta < 10^{-6}$ (error on ground-state energy density $\approx 10^{-11}$). The numerically-assigned conformal towers are consistent with the CFT result up to level 7, where some states are misidentified. **Note:** We displace data points slightly along the x-axis to show degeneracies.

is in accordance with [80], and results from the fact that finite-size perturbation for the Ising model comes from operators in the identity tower.

A similar result for the OF model at the TCI point is plotted in Fig. 4.2. We also see that all eigenstates corresponding to the CFT scaling operators in this range are captured by the puMPS ansatz, and that the identification of the conformal towers are correct up to $\Delta^{CFT} \leq 3.2$. Note that the critical point is only approximate for the OF model. This demonstrates that our approach is stable against slight relevant perturbations.

4.2.2 Conformal data

Following the procedure in the previous section, we first compute $\Delta_\alpha(N), c(N)$ for a series of sizes N and extrapolate to the thermodynamic limit. The extrapolation is shown in Fig. 4.3 for the Ising model and Fig. 4.4 for the OF model. The result is shown in Table 4.1.

Critical Ising model				OF model, TCI point			
	exact	puMPS	error		exact	puMPS	error
c	0.5	0.4999997	10^{-7}	c	0.7	0.6991	10^{-4}
Δ_σ	0.125	0.1249995	10^{-7}	Δ_σ	0.075	0.07492	10^{-5}
Δ_ε	1	0.9999994	10^{-7}	Δ_ε	0.2	0.2001	10^{-4}
$\Delta_{\partial\bar{\partial}\sigma}$	2.125	2.12501	10^{-5}	$\Delta_{\sigma'}$	0.875	0.8747	10^{-4}
$\Delta_{\partial\bar{\partial}\varepsilon}$	3	3.00002	10^{-5}	$\Delta_{\varepsilon'}$	1.2	1.203	10^{-3}
$\Delta_{T\bar{T}}$	4	4.007	10^{-3}	$\Delta_{\varepsilon''}$	3.0	3.002	10^{-3}

Table 4.1: Central charge and selected scaling dimensions from lattice Virasoro matrix elements [80] and energy gaps derived from puMPS Bloch states. For the Ising model, we used system sizes $N \leq 228$ and bond dimensions $24 \leq D \leq 49$. For the OF model near its Tri-Critical Ising (TCI) point, we used $N \leq 128$ and $28 \leq D \leq 44$ (requiring more computational time than used for the Ising model). Note the good agreement in the latter case, despite being slightly off-critical.

We see excellence agreement with the exact results in both cases. The extrapolation produces higher accuracy if finite bond dimension error introduced by puMPS is negligible compared to finite-size corrections. Thus, we have to go to a sufficiently large bond dimension D to lower the finite bond dimension errors. On the other hand, finite D effects become stronger for higher excited states. Thus there is always an eigenstate for which finite D errors become more significant than finite size effect. For example, in Fig. 4.3,

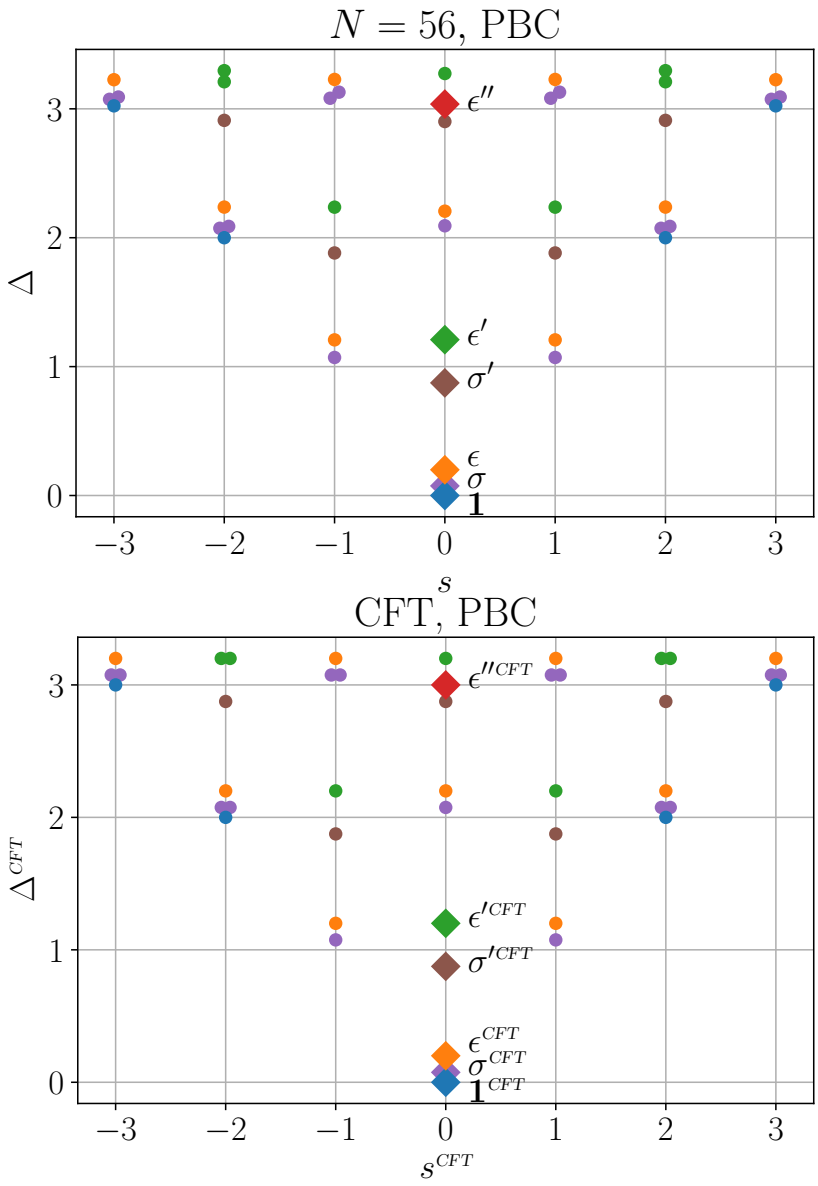

Figure 4.2: (Top) Low-energy spectrum of the TCI model with PBC at $N = 56$, diagonalized using puMPS with bond dimension $D = 36$. Different colors indicate different conformal towers, with diamonds labeling the primary states. (Bottom) The spectrum of the TCI CFT up to $\Delta^{CFT} \leq 3.2$ for PBC.

with the chosen bond dimensions for different system sizes, finite D affects the $T\bar{T}$ state far more seriously than other lower-energy states.

4.2.3 Comparison with other methods

Here we present a comparison of the conformal data extracted from the critical Ising model using puMPS, with similar data (from the literature) computed using other tensor-network methods. We compare our results with finite entanglement scaling (FES) based on infinite matrix product states [116], the tensor renormalization group (TRG) [73], and tensor network renormalization (TNR) [36]. These methods derive conformal data from different quantities: In [116], scaling dimensions are computed from the decay exponents of two-point correlation functions of scaling operators on the lattice and the central charge is extracted from the scaling of the entanglement entropy with the bond dimension. In [36], which presents data for TRG as well as TNR, the central charge and scaling dimensions are extracted from eigenvalues of a coarse-grained transfer matrix.

Examining the results, shown in Table 4.2, we find that the accuracy of conformal data extracted from puMPS is consistently better than for the other methods. We also remark that, in the case of puMPS, a *complete* set of scaling dimensions (and conformal spins) can, in principle, be extracted systematically, together with the *identity* of the scaling operator corresponding to each scaling dimension. This is not the case in [116], where extracting scaling dimensions requires knowledge of lattice versions of each scaling operator of interest, or in TRG/TNR, where the scaling operator corresponding to the computed scaling dimensions was not identified.

4.3 Spectral renormalization group flow

4.3.1 Setup in quantum field theory

Consider a perturbation of the TCI CFT by the ϵ' operator,

$$H^{QFT} = H^{TCI} + \tilde{\delta} \int_0^L dx \epsilon'^{CFT}(x), \tag{4.14}$$

where $\tilde{\delta}$ is the *bare coupling constant* at a UV cutoff scale $\Lambda = 1$. The ϵ' operator has $\Delta_{\epsilon'}^{CFT} = 1.2 < 2$ and it is therefore a relevant operator. Each term in Eq. (4.14) is normalized

	exact	puMPS	FES	TRG	TNR
c	0.5	0.4999997	0.496	0.49982	0.50001
Δ_σ	0.125	0.1249995	0.1246	0.12498	0.1250004
Δ_ε	1	0.9999994	0.998	1.00055	1.00009
$\Delta_{\partial\sigma}$	1.125	1.1249994	1.12485	1.12615*	1.12492*
$\Delta_{\overline{\partial}\sigma}$	1.125	1.1249994		1.12635*	1.12510*
$\Delta_{\partial\varepsilon}$	2	1.9999998	1.9985	2.00243*	1.99922*
$\Delta_{\overline{\partial}\varepsilon}$	2	1.9999998		2.00579*	1.99986*
Δ_T	2	2**	———	2.00750*	2.00006*
$\Delta_{\overline{T}}$	2	2**	———	2.01061*	2.00168*

Table 4.2: Central charge and selected scaling dimensions extracted from the critical Ising model, comparing the puMPS techniques we employ to finite entanglement scaling (FES) with infinite matrix product states [116], the tensor renormalization group (TRG) [73], and tensor network renormalization (TNR) [36]. Note that, for FES, the scaling dimensions ≈ 1.125 correspond to the *spatial*-derivative operators $\partial_x\sigma$ and $\partial_x\epsilon$ (denoted $d\sigma$ and $d\varepsilon$ in [116]), which are mixtures of $\partial\sigma$, $\overline{\partial}\sigma$ and $\partial\varepsilon$, $\overline{\partial}\varepsilon$, respectively. To indicate this, we have placed these values *between* rows. Also, values marked with $*$ were not assigned to particular CFT operators in [36] so we have simply listed them in ascending order. Finally, in the puMPS data, the values for Δ_T and $\Delta_{\bar{T}}$ (marked with $**$) are exact because these scaling dimensions were used to fix the overall normalization. The bond dimensions used were $28 \leq D \leq 49$ for puMPS, $32 \leq D \leq 64$ for FES, 64 for TRG, and 24 for TNR.

according to the following: H^{TCI} is normalized such that the speed of light is 1 and $\epsilon'(x)$ is normalized such that

$$\langle \epsilon'^{CFT} | \epsilon'^{CFT}(x) | 0 \rangle = \left(\frac{2\pi}{L} \right)^{\Delta^{CFT}_{\epsilon'}} . \tag{4.15}$$

Since the perturbation is relevant, H^{QFT} is described by the TCI CFT at short distances. At long distances, the theory becomes strongly coupled, and it turns out that H^{QFT} is described by the Ising CFT. Therefore, the energy spectrum of H^{QFT} goes to that of the TCI CFT for small L and that of the Ising CFT for large L. The flow of the low-energy spectrum with L is referred to as a *spectral RG flow*.

The authors of [67] express the first energy gap of H^{QFT} as

$$E^{QFT}_\sigma - E^{QFT}_0 = \frac{2\pi}{L} e(r), \tag{4.16}$$

where

$$r = L\left(\frac{\tilde{\delta}}{\kappa}\right)^{5/4}. \tag{4.17}$$

The dimensionless quantity $e(r)$ is determined by solving a set of equations, proposed in [67] based on integrable field theory. The constant $\kappa \approx 0.148696$ is needed to match the predictions with those of conformal perturbation theory. The RG flow from TCI CFT to Ising CFT suggests, for example, that $e(0^+) = \Delta_\sigma^{TCI} = 3/40$ and $e(+\infty) = \Delta_\sigma^{Ising} = 1/8$.

The interpolating flow between the TCI and the Ising CFTs has been studied in integrable field theory [66, 134, 67] and in integrable lattice models [43, 87, 42], as well as using the truncated CFT Hilbert space approach [70, 53]. In particular, in ref.[67] the authors conjecture a solution to $e(r)$. Here, we study the spectral RG flow nonperturbatively in the OF model with the puMPS method.

4.3.2 Spectral RG flow in the OF model

Consider the OF model with $\lambda = \lambda^* - \delta$ in the OF model,

$$H = \sum_j (-X_j X_{j+1} - Z_j + (\lambda^* - \delta)(X_j X_{j+1} Z_{j+2} + Z_j X_{j+1} X_{j+2})). \tag{4.18}$$

Comparing Eq. (4.18) with Eq. (4.14) we can identify that δ in the lattice model corresponds to $\tilde{\delta}$ in the QFT Hamiltonian. The spectral RG flow is studied by the low-energy spectrum of H at different system sizes N.

Similar to the QFT, at small N the low-energy spectrum will be determined by the nearby TCI point, while increasing N will eventually reveal the Ising CFT. We observe this flow at e.g. $\lambda = 0.4$, where in Fig. 4.5 we see that the low-energy excitations spectrum at $N = 32$ exhibits some striking similarities to the TCI CFT spectrum, while at $N = 256$ it looks like the Ising CFT spectrum. Also in Fig. 4.5, we show conformal tower membership computed using the Koo-Saleur lattice Virasoro generator, Eq. (4.6). At $N = 32$, despite strong corrections due to the relevant ϵ' perturbation and further irrelevant perturbations, we nevertheless reproduce the low-lying tower-membership results of the TCI. At large N, the state identifications match the Ising CFT.

In Fig. 4.6 we further plot the spectral RG flow at $\lambda = 0.4$ for a selection of states, including some that would correspond to primary operators in the TCI CFT. We find we can easily determine which Ising CFT operators the TCI CFT primaries are mapped to:

TCI operator	I	σ	ϵ	σ'	ϵ'
Ising operator	I	σ	ϵ	$\partial\overline{\partial}\sigma$	$T\overline{T}$

These results match those found in other studies of different microscopic realizations of the same CFTs, e.g. [87], and conform with expectations from symmetry considerations. The identity of ε' in the TCI CFT with $T\overline{T}$ in the Ising CFT matches their both being associated with the λ term in H.

We can better confirm the TCI operator identities of the low-energy states at $\lambda = 0.4$ by tracking them as a function of $\lambda \to \lambda_{TCI}$. This we do in Fig. 4.7 for fixed $N = 32$. We find a very similar pattern to Fig. 4.6, which we would expect if the RG flow of Hamiltonian couplings sends λ to zero for any starting $\lambda < \lambda_{TCI}$. Using both plots we can connect the low-energy eigenstates at $\lambda = 0.4, N = 256$, which we identified with Ising CFT operators, with corresponding eigenstates at $\lambda_{TCI}, N = 32$, where they clearly match up with TCI CFT operators.

4.3.3 Comparsion with integrable field theory

we have to be careful when we compare the spectral RG flow on the lattice with that in the QFT quantitatively. First, we identify L in Eq. (4.14) with the system size N in Eq. (4.18). This means that the lattice spacing is chosen to be $\Lambda^{-1} = 1$. Second, at the TCI point $\delta = 0$, the lattice Hamiltonian H corresponds to H^{TCI}/η^* where the normalization is such that the speed of light is the same. Specifically, η^* is such that in the thermodynamic limit

$$\eta^* \times (E_T^*(N) - E_0^*(N)) = \frac{2\pi}{N} \times 2, \tag{4.19}$$

where E_0^* and E_T^* are the energies of the ground state and the stress-tensor state and $*$ indicates the TCI point. Third, the operator appearing in the δ term is related to the CFT operator ϵ'^{CFT} as

$$X_j X_{j+1} Z_{j+2} + Z_j X_{j+1} X_{j+2} \sim C_{\varepsilon'} \epsilon'^{CFT}(x) + \cdots, \tag{4.20}$$

where $\cdots$ represents irrelevant operators. The precise meaning of the above correspondence is made clear in Chapter 5. The coefficient $C_{\epsilon'}$ can then be estimated using

$$|\langle \varepsilon'^* | X_j X_{j+1} Z_{j+2} + Z_j X_{j+1} X_{j+2} | 0^* \rangle| = C_{\varepsilon'} \left(\frac{2\pi}{N}\right)^{\Delta_{\epsilon'}^{CFT}}, \tag{4.21}$$

where the states are eigenstates of H at the TCI point with sufficiently large N. We can then relate the lattice and QFT parameters as

$$\tilde{\delta} = C_{\varepsilon'} \eta^* \delta. \tag{4.22}$$

Using this identification, we can also relate the flow parameters N and r as

$$N = r \left(\frac{\tilde{\delta}}{\kappa} \right)^{-5/4} . \tag{4.23}$$

Carrying out this procedure, we approximately extract $C_{\varepsilon'} \approx 0.8235$ and $\eta^* \approx 0.6147$ with the numerical data at $N = 128$ and $D = 44$ at the approximate TCI point $\lambda^* \approx 0.428$. In the previous subsection, we study the spectral flow of H at $\lambda = 0.4$, i.e., $\delta \approx 0.028$, which corresponds to $\tilde{\delta} \approx 0.0142$.

Finally, since H corresponds to the Ising CFT in the IR, we rescale H such that the speed of light is 1 as $N \to \infty$, using a normalization constant η given by

$$\eta = \lim_{N\to\infty} \frac{2\pi}{N} \frac{2}{E_T(N) - E_0(N)}, \tag{4.24}$$

where the limit is taken numerically by a linear extrapolation with $1/N \to 0$. Note that the correct normalization constant η of the perturbed Hamiltonian is not exactly the same as η^*, since δ is not infinitesimal. We then compute the scaled gap

$$e(N) = \frac{N}{2\pi}(E_\sigma(N) - E_0(N))\eta, \tag{4.25}$$

which can be compared to the QFT result $e(r)$ via Eq. (4.23).

The comparison is shown in in Fig. 4.8. We find increasingly good agreement for larger system sizes $N \to \infty$, consistent with vanishing finite-size corrections due to lattice effects. We note that our methods should allow us to study nonperturbatively the RG flow of a large number of additional energy levels in *generic* spin chain systems.

4.3.4 Spectral RG flow in the ANNNI model

There are other models that interpolate between the Ising CFT and the TCI CFT. One example is Anisotropic Next-Nearest-Neighbor Ising (ANNNI) model

$$H = -\sum_{j=1}^{N} \left[X_j X_{j+1} + Z_j + \gamma \left(X_j X_{j+2} + Z_j Z_{j+1} \right) \right], \tag{4.26}$$

which includes the critical Ising model at $\gamma = 0$ and a TCI point at $\gamma^* \approx 247$ [98, 79, 99].

Note that the scale of the γ term in (4.26) at γ^* is two orders of magnitude larger than that of the remaining Hamiltonian. Compared to the OF model, this makes the ANNNI model more difficult to study numerically, as the resulting linear algebra problems involved in using puMPS techniques are relatively ill-conditioned. Nevertheless, we were able to extract a spectral RG flow (Fig. 4.9) for the ANNNI model that interpolates between the two CFTs. The gaps are also plotted as a function of γ in Fig. 4.10. Due to very slow convergence of the puMPS ground state, we had difficulty reaching the TCI point with the chosen system size and bond dimension.

4.4 Conclusion

We have demonstrated the use of puMPS and puMPS Bloch states for extraction of conformal data from critical spin chains. The ability to compute accurate variational low-energy eigenstates at large system sizes (far beyond the reach of ED) using these techniques enabled us to extract highly accurate conformal data and identify conformal towers precisely. We have tested our method in the Ising model and the OF model. In the latter case, the availability of a large range of sizes enable us to study a spectral RG flow and identify low-energy eigenstates with CFT operators in both the Ising and TCI CFTs.

Finally we comment on the advantage of extracting conformal data based on operator-state correspondence. Perhaps most importantly, the momentum directly delivers the conformal spin via Eq. (4.5), which is therefore known exactly. Furthermore, distinguishing between degenerate energy eigenstates via momentum makes it easier to isolate states corresponding to particular CFT operators. This will be crucial in Chpater 5 in which we variationally determine lattice operators corresponding to CFT primary field operators, allowing us to compute OPE coefficients for primary fields, thus completing the extraction of conformal data from a generic critical quantum spin chain Hamiltonian.

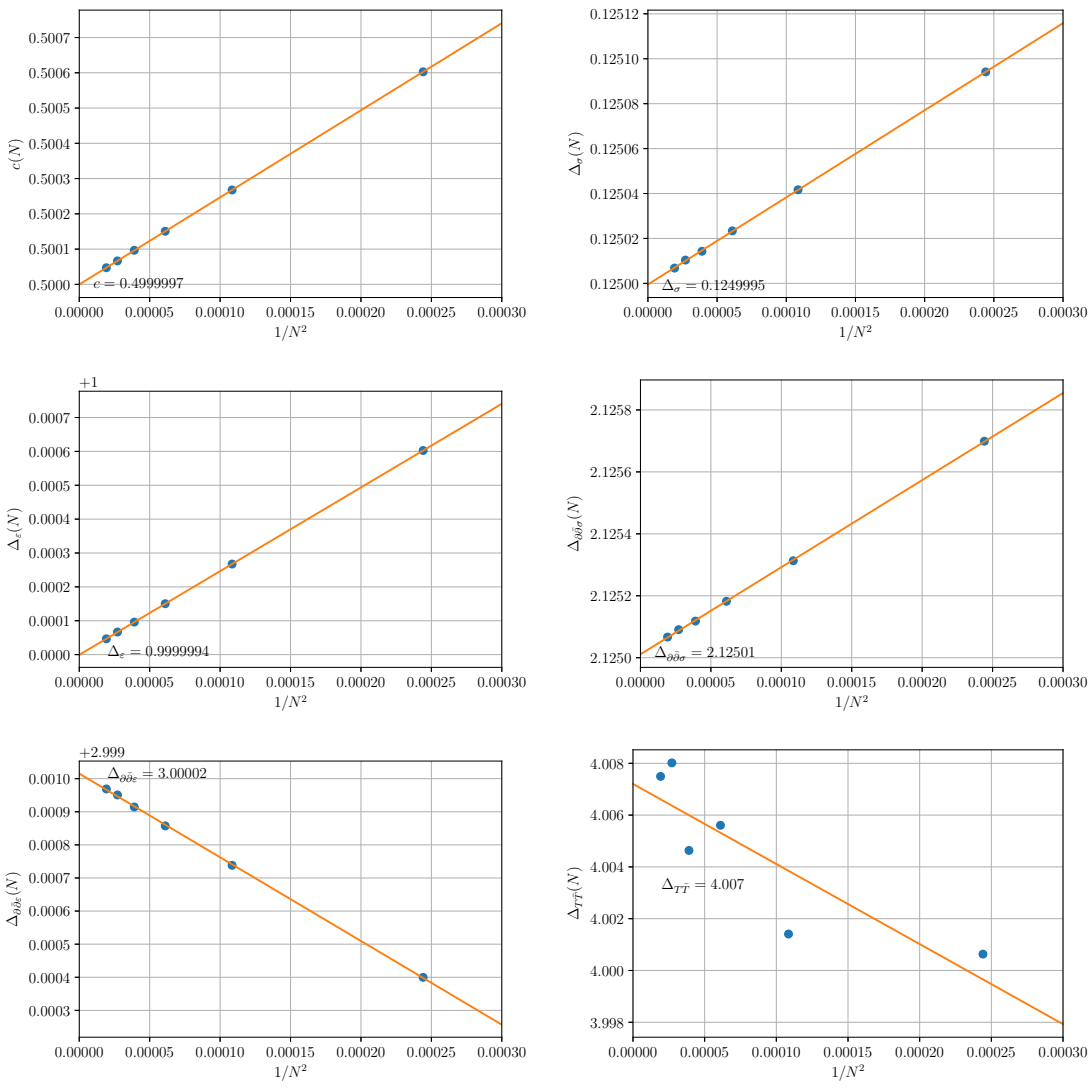

Figure 4.3: Extrapolation of scaling dimensions for primary states and central charge for the Ising CFT with finite size simulations of the Ising model. Data points include $N = 64, 96, 128, 160, 192, 228$ with bond dimension $D = 28, 34, 38, 42, 45, 49$ respectively. The $T\bar{T}$ state suffers from significant finite D effects for large systems with moderate bond dimensions.

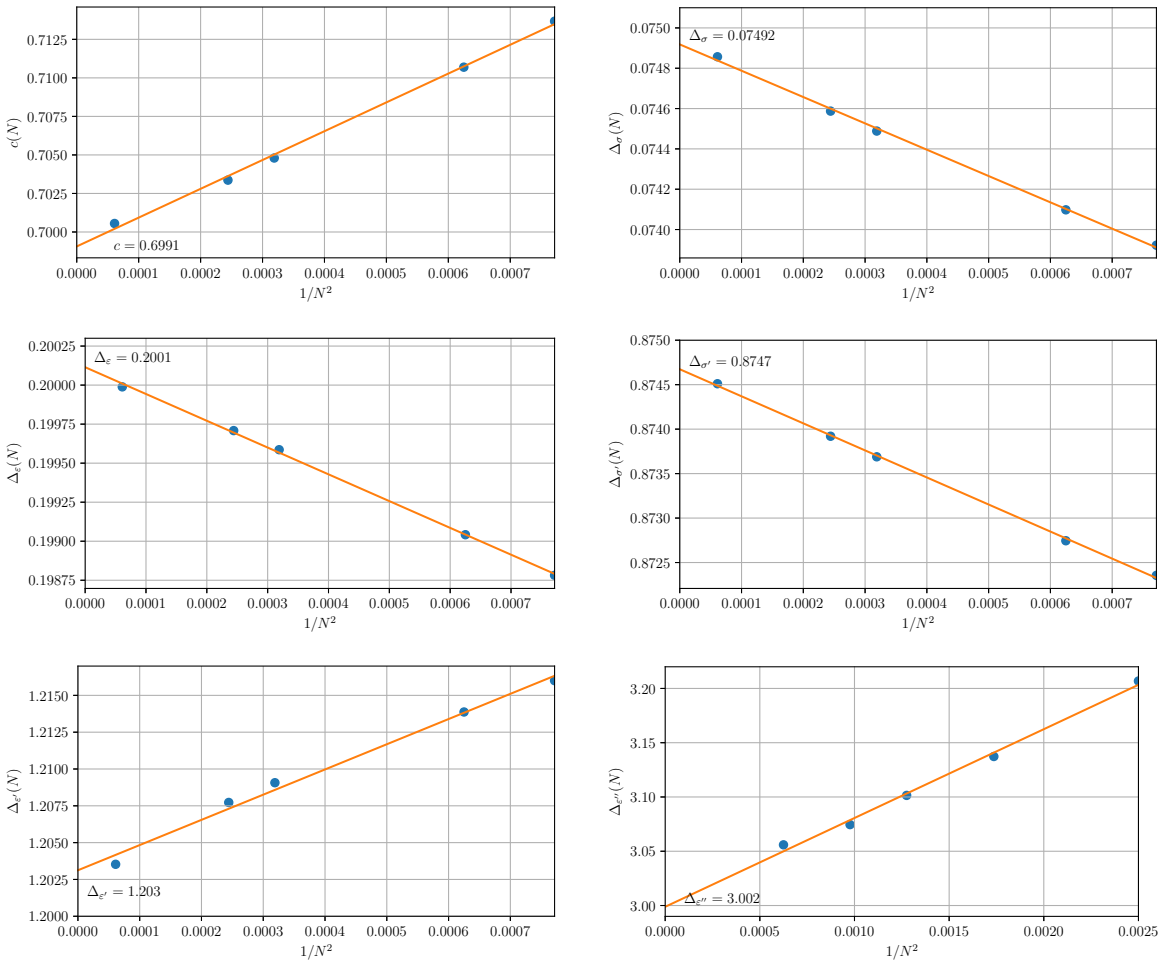

Figure 4.4: Extrapolation of scaling dimensions for primary states and central charge for the Tri-Critical Ising CFT, with finite size simulations of the OF model near the TCI point. Data points include $N = 36, 40, 56, 64, 128$ with bond dimensions $D = 28, 32, 32, 32, 44$ respectively, except for $\Delta_{\epsilon''}$, which uses $N = 20, 24, 28, 32, 40$ with $D = 24, 28, 28, 32, 32$. We chose system sizes to avoid severe corrections due to finite bond-dimension effects, which have a stronger effect on higher-energy excitations, and in order to remain in a regime where the scaling is apparently dominated by an irrelevant operator with $\Delta = 4$.

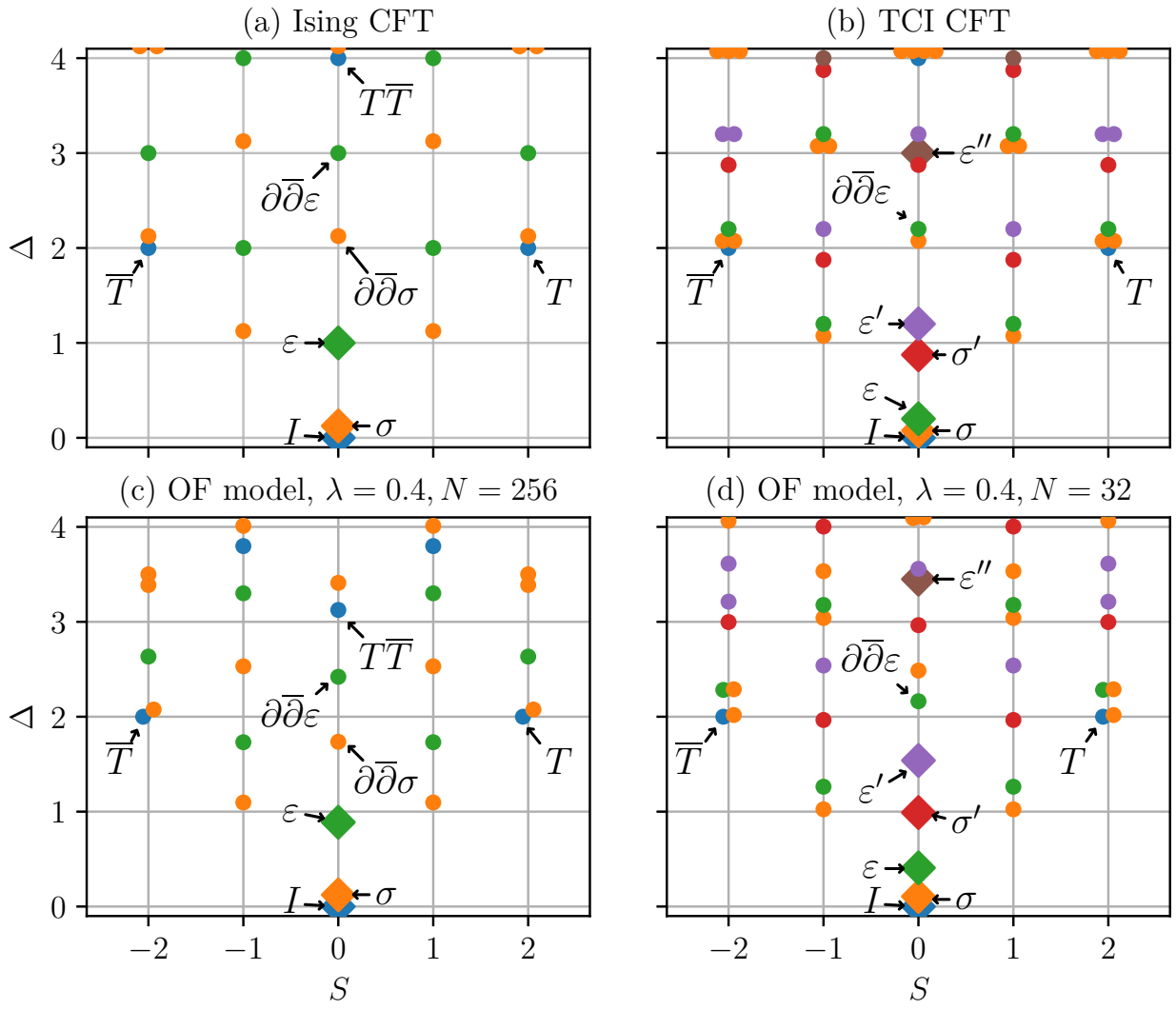

Figure 4.5: **Top:** Scaling operator spectra of (a) the Ising and (b) the TCI CFTs (with a selection of operators labeled). **Bottom:** Approximate scaling dimensions and conformal-tower identification for the OF model at $\lambda = 0.4$ with (c) $N = 256, D = 52$ and (d) $N = 32, D = 32$, corresponding to points of Fig. 4.6. We label a selection of states according to a numerical identification of the corresponding CFT operators [80]. **Note:** We displace data points slightly along the x-axis to show degeneracies.

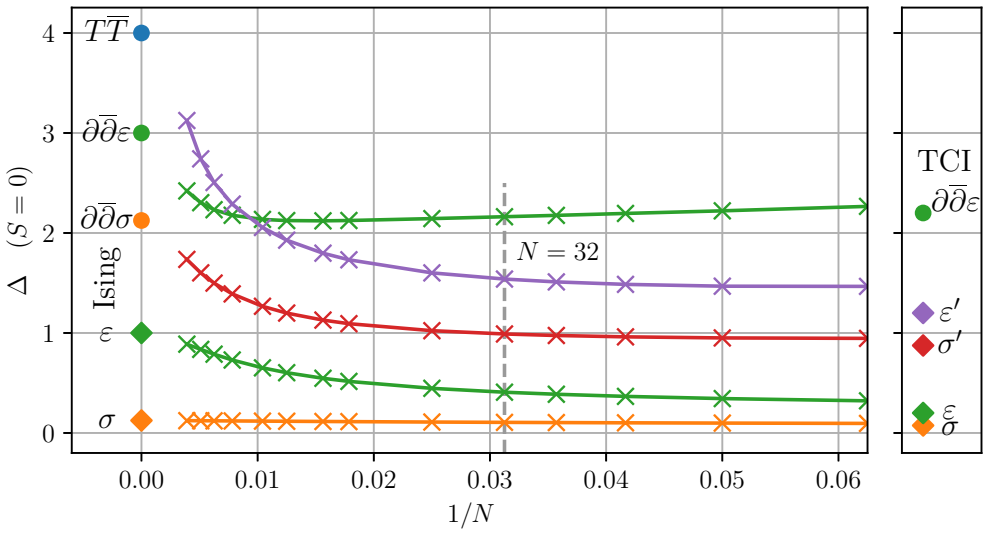

Figure 4.6: Spectral RG flow (crosses) of the first 5 energy levels (as apparent scaling dimensions Δ) at momentum zero, excluding $\Delta = 0$, extracted from the OF model with $\lambda = 0.4$, using puMPS with $D \leq 52$. For comparison, we also plot the exact scaling dimensions of the Ising and TCI CFTs (dots, diamonds). The crossover between the two highest levels plotted, which we confirm by tracking conformal tower membership using H_n matrix elements, is consistent with these states belonging to different Kramers-Wannier self-duality sectors.

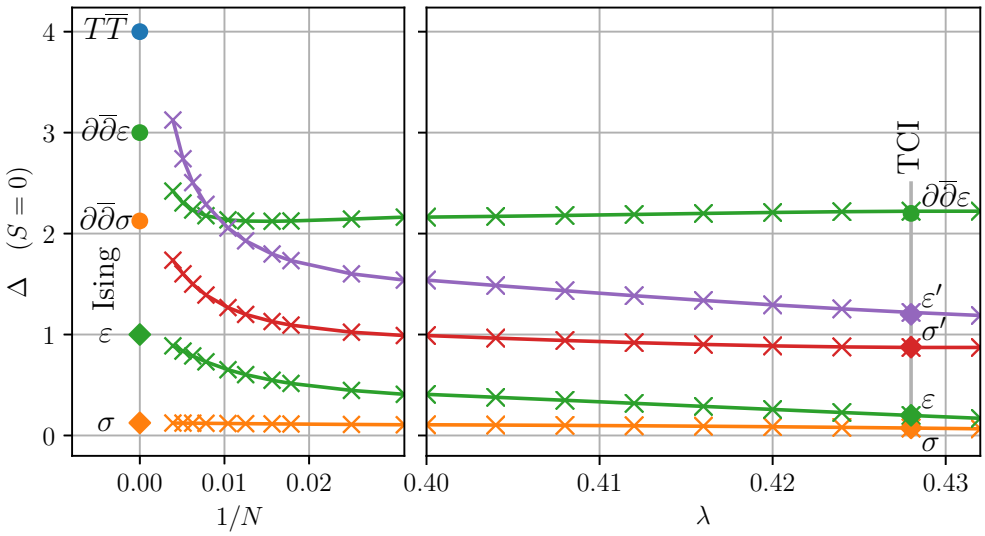

Figure 4.7: Connection of the spectral RG flow of Fig. 4.6 (left) to the "flow" of OF model energy levels as a function of λ at fixed system size $N = 32$, computed using puMPS with $D = 28$. Note how the apparent scaling dimensions agree with the TCI CFT values at the TCI point $\lambda_{TCI} \approx 0.428$.

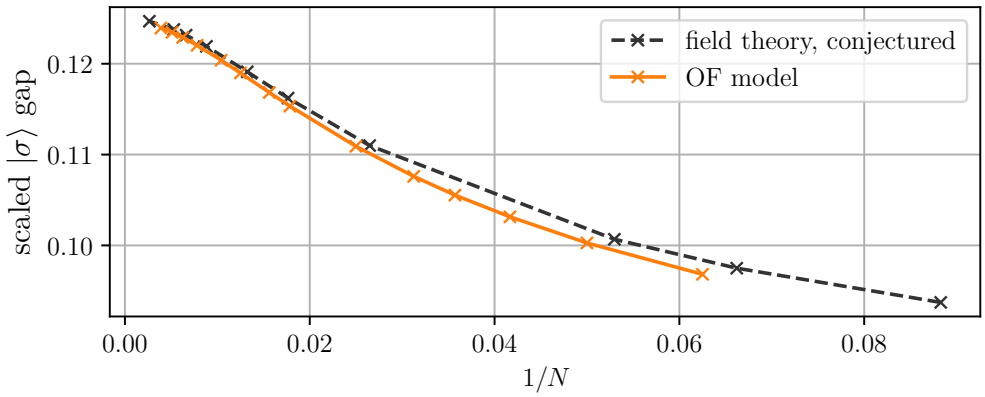

Figure 4.8: Flow of the first spectral gap from Fig. 4.6 compared with the integrable field theory result of [67], conjectured to describe the equivalent flow in the continuum.

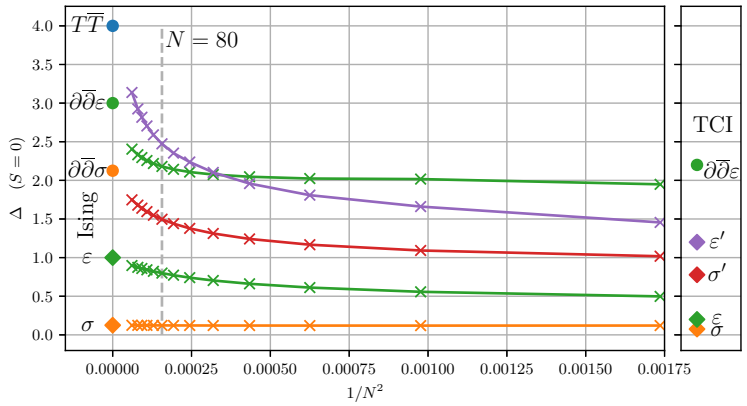

Figure 4.9: Spectral RG flow of the first 5 approximate scaling dimensions (crosses), excluding $\Delta = 0$, extracted from the ANNNI model at momentum zero, for $\gamma = 10$, using $D \leq 46$. For comparison, we also plot the exact scaling dimensions of the Ising and TCI CFTs. Note the crossover between the two largest scaling dimensions plotted, which we confirm by also tracking the ϵ-tower membership using H_n matrix elements.

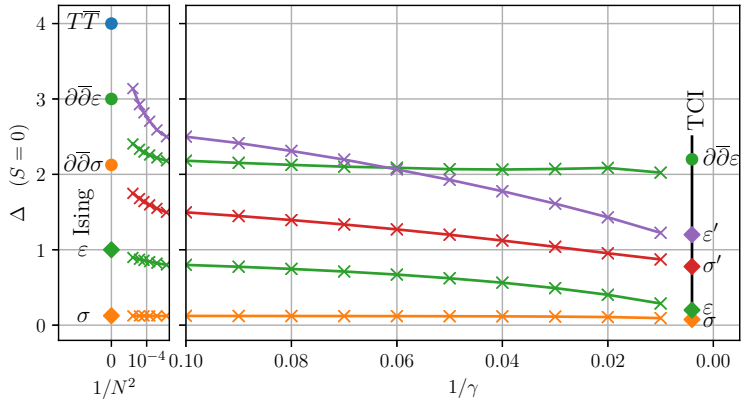

Figure 4.10: The first 5 approximate scaling dimensions (crosses), excluding $\Delta = 0$, as function of γ, extracted from the ANNNI model at momentum zero, for $N = 80, D = 38$. We also plot exact CFT scaling dimensions. Furthermore, we show to the left how the "flow" with γ links up at $\gamma = 10$ with the spectral RG flow of Fig. 4.9. We confirm the crossover between the two highest-Δ curves by tracking fidelities of excited states at different γ.

Chapter 5

Conformal fields and operator product expansion

In the previous chapter we have developed a method to extract scaling dimensions Δ_α^{CFT}, conformal spins s_α^{CFT} and central charge c^{CFT}, as well as identify primary operators and conformal towers from a generic critical quantum spin chain. However, the OPE coefficients $C_{\alpha\beta\gamma}^{CFT}$ is still missing.

In this chapter we explain how to identify each local lattice operator $\mathcal{O}$, acting on the spin chain, with a corresponding linear combination of CFT scaling operators,

$$\mathcal{O} \sim \sum_\alpha a_\alpha \psi_\alpha^{CFT} \equiv \mathcal{O}^{CFT}. \tag{5.1}$$

More specifically, we show how to numerically compute the first few dominant terms in this expansion, corresponding to the CFT operators with the smallest scaling dimensions. As a main application, we then explain how to extract a lattice estimate $C_{\alpha\beta\gamma}$ of the OPE coefficients $C_{\alpha\beta\gamma}^{CFT}$, by computing the matrix element analogous to Eq. (2.60),

$$C_{\alpha\beta\gamma} \equiv \left(\frac{2\pi}{N}\right)^{-\Delta_\alpha} \langle \phi_\beta | \phi_\alpha(0) | \phi_\gamma \rangle \tag{5.2}$$

where ϕ_α is an approximate lattice realization of the CFT primary operator ϕ_α^{CFT} and $|\phi_\beta\rangle$ and $|\phi_\gamma\rangle$ are a pair of primary states of the critical spin chain. In this way we successfully complete Cardy's ambitious program to extract conformal data from a critical lattice Hamiltonian H by exploiting the operator-state correspondence. We demonstrate

the approach, valid for any quantum spin chain, by computing the leading terms of the expansion (5.1) for all one-site and two-site operators of the critical Ising model, see Table 5.4, and its non-trivial OPE coefficient $C^{CFT}_{\sigma\sigma\epsilon}$. We also outline other future applications.

5.1 Exciting the CFT vacuum with local operators

In order to understand the correspondence between lattice operators and CFT operators, we first need to understand how CFT operators act on the vacuum state. Consider a $1+1$ dimensional CFT on the cylinder $S^1 \times \mathbb{R}$, where the compactified dimension represents space, with coordinate $x \in [0, L)$, and the other dimension represents Euclidean time, with coordinate $\tau \in \mathbb{R}$. On the $\tau = 0$ circle we build the Hilbert space, spanned by the states $|\psi^{CFT}_\alpha\rangle$. Let $\mathcal{O}^{CFT}(x)$ denote a local operator acting on this circle, with Fourier mode decomposition

$$\mathcal{O}^{CFT}(x) = \sum_{s\in\mathbb{Z}} \mathcal{O}^{CFT,s} e^{-is2\pi x/L}, \tag{5.3}$$

$$\mathcal{O}^{CFT,s} \equiv \frac{1}{L}\int_0^L dx\, \mathcal{O}^{CFT}(x)\, e^{is2\pi x/L}. \tag{5.4}$$

Applying Fourier mode $\mathcal{O}^{CFT,s}$ on the vacuum $|0^{CFT}\rangle$ results in an eigenstate of P^{CFT} with momentum $(2\pi/L)s$. When $\mathcal{O}^{CFT}(x)$ is a primary field $\phi^{CFT}_\alpha(x)$, we obtain

$$\phi^{CFT,s}_\alpha |0^{CFT}\rangle = \left(\frac{2\pi}{L}\right)^{\Delta^{CFT}_\alpha} \sum_{m,\bar m\geq 0} c^s_{\alpha,(m,\bar m)} |\phi^{CFT}_{\alpha,(m,\bar m)}\rangle, \tag{5.5}$$

where $\phi^{CFT}_{\alpha,(m,\bar m)}(x) \equiv \partial^m \bar\partial^{\bar m} \phi^{CFT}_\alpha(x)$ denotes a derivative descendant with spin $s^{CFT}_\alpha + m - \bar m$, and

$$c^s_{\alpha,(m,\bar m)} \equiv \delta_{m-\bar m+s^{CFT}_\alpha,s} \sqrt{\frac{\Gamma(m+2h^{CFT}_\alpha)\Gamma(\bar m+2\bar h^{CFT}_\alpha)}{m!\bar m!\Gamma(2h^{CFT}_\alpha)\Gamma(2\bar h^{CFT}_\alpha)}}. \tag{5.6}$$

More generally, analogous expressions can be obtained when $\mathcal{O}^{CFT}$ is not a primary operator. Here we will use the specific case where $\mathcal{O}^{CFT}$ is a derivative descendant $\phi^{CFT}_{\alpha,(k,\bar k)}$ of the primary ϕ^{CFT}_α, for which one finds

$$\phi^{CFT,s}_{\alpha,(k,\bar k)} |0^{CFT}\rangle = \left(\frac{2\pi}{L}\right)^{\Delta^{CFT}_\alpha+k+\bar k} \times \sum_{m,\bar m\geq 0} (m+h^{CFT}_\alpha)^k (\bar m+\bar h^{CFT}_\alpha)^{\bar k} c^s_{\alpha,(m,\bar m)} |\phi^{CFT}_{\alpha,(m,\bar m)}\rangle. \tag{5.7}$$

For the stress tensor operator T^{CFT}, we have

$$T^{CFT,s}|0^{CFT}\rangle = \left(\frac{2\pi}{L}\right)^2 \sqrt{\frac{c^{CFT}}{12}s(s^2-1)}|\partial^{s-2}T^{CFT}\rangle \quad (s \geq 2) \tag{5.8}$$

$$T^{CFT,s}|0^{CFT}\rangle = \left(\frac{2\pi}{L}\right)^2 \left(-\frac{c^{CFT}}{24}\delta_{s,0}\right)|0^{CFT}\rangle \quad (s < 2). \tag{5.9}$$

Similar relations hold for $\bar{T}^{CFT}$,

$$\bar{T}^{CFT,-s}|0^{CFT}\rangle = \left(\frac{2\pi}{L}\right)^2 \sqrt{\frac{c^{CFT}}{12}s(s^2-1)}|\bar{\partial}^{s-2}\bar{T}^{CFT}\rangle \quad (s \geq 2) \tag{5.10}$$

$$\bar{T}^{CFT,-s}|0^{CFT}\rangle = \left(\frac{2\pi}{L}\right)^2 \left(-\frac{c^{CFT}}{24}\delta_{s,0}\right)|0^{CFT}\rangle \quad (s < 2). \tag{5.11}$$

Similar formula for general descenant operators can be derived, but they are far more complicated. We outline the procedure in the end of this section. Nevertheless, it turns out that Eqs. (5.6)-(5.11) are enough in our particular case in this chapter. The proof of these formula is given below, where the CFT superscript is omitted throughout the proof.

5.1.1 Primary operators

A primary field $\phi(\tau, x)$ can be mapped to the complex plane with coordinates $(z, \bar{z})$ by the conformal transformation Eq. (2.47). Using the transformation rule Eq. (2.23) and $dz/dw = 2\pi z/L$ we obtain

$$\phi(\tau, x) = \left(\frac{dz}{dw}\right)^h \left(\frac{d\bar{z}}{d\bar{w}}\right)^{\bar{h}} \phi(z, \bar{z}) \tag{5.12}$$

$$= \left(\frac{2\pi}{L}\right)^{\Delta} z^h \bar{z}^{\bar{h}} \phi(z, \bar{z}), \tag{5.13}$$

where $h, \bar{h}$ are the conformal dimensions of $\phi(z, \bar{z})$, and $\Delta = h + \bar{h}$ is its scaling dimension.

On the complex plane, the field can be Laurent expanded around the origin,

$$\phi(z, \bar{z}) = \sum_{m \in Z-h, \bar{m} \in Z-\bar{h}} z^{-m-h} \bar{z}^{-\bar{m}-\bar{h}} \phi_{m,\bar{m}}, \tag{5.14}$$

or equivalently

$$\phi_{-m-h,-\bar{m}-\bar{h}} = \oint_z \oint_{\bar{z}} \frac{dz}{2\pi i} \frac{d\bar{z}}{2\pi i} z^{-m-1} \bar{z}^{-\bar{m}-1} \phi(z, \bar{z}). \tag{5.15}$$

The Laurent expansion becomes a Fourier expansion on the time slice $\tau = 0$ of the cylinder,

$$\phi(0,x) = \left(\frac{2\pi}{L}\right)^{\Delta} \sum_{m,\bar{m}\in Z} e^{2\pi i(m-\bar{m}+s_\phi)x/L} \phi_{-m-h,-\bar{m}-\bar{h}}, \tag{5.16}$$

where $s_\phi = h - \bar{h}$ is the conformal spin.

Acting with $\phi(z,\bar{z})$ on the ground state gives

$$\begin{aligned} \phi(z,\bar{z})|0\rangle &= e^{zL_{-1}} e^{\bar{z}\bar{L}_{-1}} \phi(0,0)|0\rangle & (5.17) \\ &= \sum_{m,\bar{m}\geq 0} \frac{z^m \bar{z}^{\bar{m}}}{m!\bar{m}!} L_{-1}^m \bar{L}_{-1}^{\bar{m}} |\phi\rangle, & (5.18) \end{aligned}$$

where we have used the fact that L_{-1} generates translation and the operator-state correspondence, Eq. (2.35). Combining Eq. (5.15) and Eq. (5.18) gives

$$\phi_{-m-h,-\bar{m}-\bar{h}}|0\rangle = \begin{cases} \frac{1}{m!\bar{m}!} L_{-1}^m \bar{L}_{-1}^{\bar{m}} |\phi\rangle & m,\bar{m} \geq 0 \\ 0 & \text{otherwise} \end{cases} \tag{5.19}$$

Therefore, acting with $\phi(0,x)$ in Eq. (5.16) on the ground state creates the state $|\phi\rangle$ and all its derivative descendants,

$$L_{-1}^m \bar{L}_{-1}^{\bar{m}} |\phi\rangle = C_{m,\bar{m}} |\phi_{(m,\bar{m})}\rangle, \tag{5.20}$$

where $|\phi_{(m,\bar{m})}\rangle$ is a normalized state with conformal dimensions $(m+h, \bar{m}+\bar{h})$ and

$$C_{m,\bar{m}} = \sqrt{m!\bar{m}! \frac{\Gamma(m+2h)\Gamma(\bar{m}+2\bar{h})}{\Gamma(2h)\Gamma(2\bar{h})}} \tag{5.21}$$

is a normalization constant, which can be obtained by successively applying the Virasoro algebra Eq. (2.14).

Finally, consider the Fourier mode

$$\phi^s = \frac{1}{L} \int_0^L dx\, \phi(0,x) e^{-2\pi i s x/L} \tag{5.22}$$

which selects all modes $\phi_{-m-h,-\bar{m}-barh}$ in Eq. (5.16) with $m - \bar{m} + s_\alpha = s$, we then obtain

$$\phi_\alpha^s |0\rangle = \left(\frac{2\pi}{L}\right)^{\Delta_\alpha} \sum_{m,\bar{m}\geq 0} c^s_{\alpha,(m,\bar{m})} |\phi_{\alpha,(m,\bar{m})}\rangle, \tag{5.23}$$

where

$$c^s_{\alpha,(m,\bar{m})} = \delta_{m-\bar{m}+s_\alpha,s} \sqrt{\frac{\Gamma(m+2h_\alpha)\Gamma(\bar{m}+2\bar{h}_\alpha)}{m!\bar{m}!\Gamma(2h_\alpha)\Gamma(2\bar{h}_\alpha)}}, \tag{5.24}$$

5.1.2 Derivative descendants

Let us generalize the above equations to derivative descendant operators. The temporal and spatial derivatives can be obtained by commutator with H and P,

$$\partial_\tau \phi(\tau, x) = [H, \phi(\tau, x)]. \tag{5.25}$$
$$i\partial_x \phi(\tau, x) = [P, \phi(\tau, x)]. \tag{5.26}$$

Combining them together and using Eqs. (2.54)(2.55), we obtain

$$\partial \phi(\tau, x) = \frac{2\pi}{L}[L_0, \phi(\tau, x)]. \tag{5.27}$$
$$\bar{\partial} \phi(\tau, x) = \frac{2\pi}{L}[\bar{L}_0, \phi(\tau, x)]. \tag{5.28}$$

Acting Eq. (5.27) on the ground state and setting $\tau = 0$, we obtain an expression similar to Eq. (5.23),

$$(\partial \phi_\alpha)^s |0\rangle = \left(\frac{2\pi}{L}\right)^{\Delta_\alpha + 1} \sum_{m,\bar{m} \geq 0} (m + h_\alpha) c^s_{\alpha,(m,\bar{m})} |\phi_{\alpha,(m,\bar{m})}\rangle. \tag{5.29}$$

More generally, we have

$$(\partial^k \bar{\partial}^{\bar{k}} \phi_\alpha)^s |0\rangle = \left(\frac{2\pi}{L}\right)^{\Delta_\alpha + k + \bar{k}} \sum_{m,\bar{m} \geq 0} (m + h_\alpha)^k (\bar{m} + \bar{h}_\alpha)^{\bar{k}} c^s_{\alpha,(m,\bar{m})} |\phi_{\alpha,(m,\bar{m})}\rangle. \tag{5.30}$$

For later use, let us consider a special case $\partial_x \phi_\alpha \equiv i(\partial - \bar{\partial})\phi_\alpha$,

$$(\partial_x \phi_\alpha)^s |0\rangle = \left(\frac{2\pi}{L}\right)^{\Delta_\alpha + 1} i \sum_{m,\bar{m} \geq 0} (m - \bar{m} + s_\alpha) c^s_{\alpha,(m,\bar{m})} |\phi_{\alpha,(m,\bar{m})}\rangle \tag{5.31}$$
$$= \left(\frac{2\pi}{L}\right)^{\Delta_\alpha + 1} i \sum_{m,\bar{m} \geq 0} s c^s_{\alpha,(m,\bar{m})} |\phi^{CFT}_{\alpha,(m,\bar{m})}\rangle, \tag{5.32}$$

where the first equality follows from linear combing the cases of $k = 1, \bar{k} = 0$ and $k = 0, \bar{k} = 1$ in Eq. (5.30) and $s_\alpha = h_\alpha - \bar{h}_\alpha$, and the second equality follows from $\delta_{m-\bar{m}+s_\alpha,s}$ in Eq. (5.24).

5.1.3 General descendants

We first consider the case for the stress tensors. Their Fourier modes are Virasoro generators,

$$T^s = \left(\frac{2\pi}{L}\right)^2 \left(L_{-s} - \frac{c}{24}\delta_{s,0}\right) \tag{5.33}$$

$$\bar{T}^s = \left(\frac{2\pi}{L}\right)^2 \left(\bar{L}_s - \frac{c}{24}\delta_{s,0}\right) \tag{5.34}$$

Applying the $L_{-s}, \bar{L}_{-s}$ to the ground state produces

$$L_{-s}|0\rangle = C_s|\partial^{s-2}T^{CFT}\rangle \tag{5.35}$$

$$\bar{L}_{-s}|0\rangle = C_s|\bar{\partial}^{s-2}\bar{T}^{CFT}\rangle, \tag{5.36}$$

for $s \geq 2$, where

$$C_s = \sqrt{\frac{c}{12}s(s^2-1)} \tag{5.37}$$

is the normalization constant. This proves Eqs. (5.8)-(5.11).

In order to consider more general descendant operators, we first recall that they are composite operators of the stress tensors and primary operators,

$$T(w)\phi(w',\bar{w}') = \sum_{n=-2}^{\infty} (w-w')^n L_{-n-2}\phi(w',\bar{w}'), \tag{5.38}$$

where $n = -2$ and $n = -1$ correspond to the primary operator and the derivative descendant, respectively. We can then transform each operator in the LHS of Eq. (5.38) to the complex plane to derive the transformation rule for descendant operators. The rest is similar to the derivation for primary operators. We can use Eq. (5.18) (which equally holds for descendant operators) to compute the state $L_{-n-2}\phi(x)|0\rangle$, up to a normalization that follows from Virasoro algebra. Finally we can pick up the contribution from any Fourier mode of $L_{-n-2}\phi(x)$.

5.2 Lattice operators as CFT scaling operators

5.2.1 Constraining lattice operators without OPE coefficients

Consider now a critical quantum spin chain and a local operator $\mathcal{O}$, acting on a small number of spins, to which we would like to assign a linear combination of CFT scaling

operators as in Eq. (5.1). In practice we will produce an approximate, truncated expansion of the form

$$\mathcal{O} \overset{\text{approx}}{\sim} \sum_{\alpha\in\mathcal{A}} a_\alpha \psi_\alpha^{CFT} \equiv \tilde{\mathcal{O}}^{CFT} \tag{5.39}$$

using only operators ψ_α^{CFT} in a preselected finite set $\mathcal{A}$. By optimizing the coefficients a_α (see below), we hope to obtain a truncated expansion (5.39) such that

$$\langle\psi_\beta|\mathcal{O}|\psi_\alpha\rangle = \langle\psi_\beta^{CFT}|\tilde{\mathcal{O}}^{CFT}|\psi_\alpha^{CFT}\rangle + O\left(\frac{1}{N^{\Delta_c}}\right), \tag{5.40}$$

where the matrix elements are between low energy states $|\psi_\alpha\rangle$ and $|\psi_\beta\rangle$, we have equated the size N of the spin chain with the size L of the CFT circle, and Δ_c is the lowest scaling dimension among operators not included in $\mathcal{A}$. Thus, the accuracy of the expansion should systematically improve (the subleading finite-size corrections be further reduced) by adding more scaling operators in $\mathcal{A}$.

On the lattice, we first Fourier expand $\mathcal{O}$,

$$\mathcal{O}(j) = \sum_s \mathcal{O}^s e^{-is2\pi j/N}, \qquad \mathcal{O}^s \equiv \frac{1}{N}\sum_{j=1}^{N} \mathcal{O}(j) e^{is2\pi j/N}. \tag{5.41}$$

There is a subtlety involving nonzero s for multi-site operators $O(j)$, and we will treat it in Appendix B. Given a finite set $\mathcal{B}$ of low energy states $|\psi_\beta\rangle$ and a range $\mathcal{S}$ of values s, we can numerically evaluate the matrix elements $b_{\beta,s} \equiv \langle\psi_\beta|\mathcal{O}^s|0\rangle$ between the spin chain ground state $|0\rangle$ and state $|\psi_\beta\rangle$, for all $|\psi_\beta\rangle \in \mathcal{B}$ and $s \in \mathcal{S}$. With the ability to analytically compute $B^\alpha_{\beta,s} \equiv \langle\psi_\beta^{CFT}|\psi_\alpha^{CFT,s}|0^{CFT}\rangle$ (using e.g. Eqs. (5.5)-(5.7)), we can also evaluate the corresponding CFT matrix elements

$$\langle\psi_\beta^{CFT}|\tilde{\mathcal{O}}^{CFT,s}|0^{CFT}\rangle = \sum_{\alpha\in\mathcal{A}} a_\alpha \langle\psi_\beta^{CFT}|\psi_\alpha^{CFT,s}|0^{CFT}\rangle. \tag{5.42}$$

In this way we can search for the coefficients a_α such that $\langle\psi_\beta^{CFT}|\tilde{\mathcal{O}}^{CFT,s}|0^{CFT}\rangle$ best approximates $\langle\psi_\beta|\tilde{\mathcal{O}}^s|0\rangle$ for all relevant s and β, by minimizing the cost function

$$f_N^{\mathcal{O}}(\{a_\alpha\}) \equiv \sum_{\beta,s} \left|\langle\psi_\beta|\mathcal{O}^s|0\rangle - \langle\psi_\beta^{CFT}|\tilde{\mathcal{O}}^{CFT,s}|0^{CFT}\rangle\right|^2 \tag{5.43}$$

$$= \sum_{\beta,s} \left| b_{\beta,s} - \sum_\alpha a_\alpha B^\alpha_{\beta,s} \right|^2 \tag{5.44}$$

Importantly, $f_N^{\mathcal{O}}(\{a_\alpha\})$ depends only on matrix elements involving the vacuum and one excited state (analogous to a CFT *two-point* correlator) and not on matrix elements involving two excited states (analogous to a *three-point* correlator), so that it does not require any knowledge of the OPE coefficients $C_{\alpha\beta\gamma}^{CFT}$. Below we describe in more detail the algorithm of computing a_α's.

5.2.2 Algorithm

The algorithm is divided into two parts, involving states and operators, respectively.

Low-energy states

taking the critical Hamiltonian $H = \sum_{j=1}^{N} h(j)$ of a periodic spin chain as the only input, we compute low energy eigenstates of H, using e.g. exact diagonalization for small N and puMPS for larger N . We then use the techniques of Chapter 4 to (i) for each low energy state $|\psi_\alpha\rangle \sim |\psi_\alpha^{CFT}\rangle$, obtain estimates Δ_α and s_α for its scaling dimension and conformal spin; (ii) identify primary states $|\phi_\alpha\rangle \sim |\phi_\alpha^{CFT}\rangle$ and their descendants, thus organizing the low energy states into conformal towers. The above tasks involve a large-N extrapolation. At this point we make a judicious choice of sets $\mathcal{A}$, $\mathcal{B}$, and $\mathcal{S}$.

Note that the eigenstates $|\psi_\alpha\rangle$ from diagonalization have random phases. However, in order to compute a_α's properly, the phases of eigenstates have to be fixed. This is achieved by two parts. First we fix relative phases between the states in the same conformal tower, and second we fix the relative phases between primary states.

First, Fourier modes $H_s \sim L_{-s}^{CFT} + \bar{L}_s^{CFT}$ $(s \neq 0)$ of the lattice Hamiltonian density $h(j)$ are ladder operators in the scaling limit. In a CFT, raising operators connect eigenstates with real and postive matrix elements,

$$\langle (L_{-n}\psi_\alpha)^{CFT} | L_{-n}^{CFT} | \psi_\alpha^{CFT} \rangle > 0, \tag{5.45}$$

$$\langle (\bar{L}_{-n}\psi_\alpha)^{CFT} | \bar{L}_{-n}^{CFT} | \psi_\alpha^{CFT} \rangle > 0. \tag{5.46}$$

Accordingly, we will require that the equivalent lattice matrix elements also satisfy

$$\langle L_{-n}\psi_\alpha | H_n | \psi_\alpha \rangle > 0, \tag{5.47}$$

$$\langle \bar{L}_{-n}\psi_\alpha | H_{-n} | \psi_\alpha \rangle > 0, \tag{5.48}$$

up to finite-size corrections. In practice, for a given conformal tower, we fix relative phases between descendant states and the primary state $|\phi\rangle$ level by level. Starting with $|\psi_\alpha\rangle =$

$|\phi\rangle$, we require the above matrix elements with $n = 1$ and $n = 2$ to be real and positive. Then we continue to $|\psi_\alpha\rangle = |L_{-n}\phi\rangle$ and $|\bar{L}_{-n}\phi\rangle$ $(n = 1, 2)$ and fix the phases of higher level descendants. This is done until all the states in $\mathcal{B}$ have their phases fixed with respect to the primary states.

In the remaining we would like to fix relative phases between primary states $|\phi_\alpha\rangle$. In the CFT,

$$\langle \phi_\alpha^{CFT} | \phi_\alpha^{CFT, s_\alpha} | 0^{CFT} \rangle > 0. \tag{5.49}$$

On the lattice, we first find an operator O_α which has ϕ_α^{CFT} in its expansion, and then require

$$\langle \phi_\alpha | O_\alpha^{s_\alpha} | 0 \rangle > 0. \tag{5.50}$$

There is still freedom in choosing O_α for each primary states, but any choice suffices.

Operators

For a fixed system size N, we compute the CFT matrix elements $\langle \psi_\beta^{CFT} | \psi_\alpha^{CFT, s} | 0^{CFT} \rangle$ for all $\psi_\alpha^{CFT} \in \mathcal{A}$, $|\psi_\beta^{CFT}\rangle \in \mathcal{B}$ and $s \in \mathcal{S}$ using the corresponding analytical expressions. However, here we employ the previously *estimated* conformal dimensions $h_\alpha \equiv (\Delta_\alpha + s_\alpha)/2, \bar{h}_\alpha \equiv (\Delta_\alpha - s_\alpha)/2$ instead of their unknown *exact* values $h_\alpha^{CFT}, \bar{h}_\alpha^{CFT}$, so that no previous knowledge of the emergent CFT is required. Then, for each choice of lattice operator $\mathcal{O}$, we compute $\langle \psi_\beta | \mathcal{O}^s | 0 \rangle$ for all $\psi_\beta \in \mathcal{B}$ and $s \in \mathcal{S}$, where the phases of each eigenstates relative to the ground state is fixed by the previous part, and use linear least-squares regression to minimize $f_N^{\mathcal{O}}(\{a_\alpha\})$ in Eq. (5.43), resulting in a set of optimal coefficients $a_\alpha(N)$. Finally, we repeat the entire calculation for several values of N and extrapolate to $N \to \infty$, which results in the coefficients a_α in Eq. (5.39).

Thus we obtain a correspondence between lattice operators and a linear combination of CFT operators. We can invert the relation and find lattice operators that correspond to a particular CFT operator, (e.g. primary operator $\phi_\alpha \sim \phi_\alpha^{CFT}$) and compute the OPE coefficient via Eq, (5.2).

5.3 Example: critical Ising model

5.3.1 Lattice operators as CFT operators

Consider the critical Ising model Eq. (3.13), we used puMPS with bond dimension in the range $12 \leq D \leq 22$ to address systems of size $18 \leq N \leq 48$, with the largest system

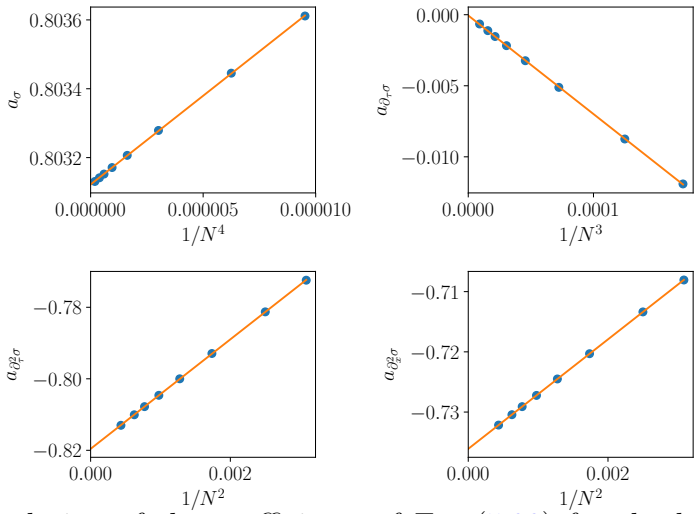

Figure 5.1: Extrapolation of the coefficients of Eq. (5.39) for the lattice operator $\mathcal{O} = XZ + ZX$. The extrapolated values are $a_\sigma = 0.803121$, $a_{\partial_\tau\sigma} = 0.0000$, $a_{\partial_\tau^2\sigma} = 0.820$, $a_{\partial_x^2\sigma} = -0.736$. See Table 5.4.

size requiring several minutes on a laptop with 4 CPU (2.8 GHz) and 2 GB RAM. We got all three primary operators and their low-lying descendants. For the set $\mathcal{A}$ we choose operators

$$\text{(identity) } \mathbf{1}, \qquad \text{(stress tensor) } T,\ \bar{T} \tag{5.51}$$

in the identity conformal tower (notice that $\mathbf{1}$, T and $\bar{T}$ are present in any CFT) and the primaries and first and second derivative descendants in the other two towers,

$$\text{(spin) } \sigma, \quad \partial_\tau\sigma,\ \partial_x\sigma, \quad \partial_\tau^2\sigma,\ \partial_x\partial_\tau\sigma,\ \partial_x^2\sigma, \tag{5.52}$$

$$\text{(energy density) } \epsilon, \quad \partial_\tau\epsilon,\ \partial_x\epsilon, \quad \partial_\tau^2\epsilon,\ \partial_x\partial_\tau\epsilon,\ \partial_x^2\epsilon. \tag{5.53}$$

For $\mathcal{B}$ we choose all states $|\psi_\beta\rangle$ with scaling dimension $\Delta_\alpha \leq 3 + 1/8$, namely the 23 lowest energy states. Finally, for $\mathcal{S}$ we choose $-3 \leq s \leq 3$.

We optimized the truncated expansion (5.39) for each Pauli operator X, Y, Z acting on a single spin, for pairs of Pauli operators acting on two continuous spins, etc, see Table 5.4 and Fig. 5.1. Some of the coefficients a_α reproduce up to 6 significant digits of their exact value, obtained using the exact solution of the Ising model. Also note that the coefficients are consistent with the spin flip $\mathbb{Z}_2$ symmetry and the Kramers-Wannier duality (see below).

Lattice	CFT
X	$0.803121\sigma - 0.017\partial_\tau^2\sigma - 0.033\partial_x^2\sigma$
Y	$0.8031i\partial_\tau\sigma$
Z	$0.6366201 - 0.15915(T+\bar{T}) - 0.31831\epsilon + 0.010\partial_\tau^2\epsilon$
XX	$0.6366201 - 0.15915(T+\bar{T}) + 0.31831\epsilon - 0.010\partial_\tau^2\epsilon$
YY	$-0.2122071 + 0.4774(T+\bar{T}) + 0.31831\epsilon - 0.089\partial_\tau^2\epsilon$
ZZ	$0.5403801 - 0.5403(T+\bar{T}) - 0.54038\epsilon + 0.067\partial_\tau^2\epsilon - 0.051\partial_x^2\epsilon$
$XY+YX$	$0.3184i\partial_\tau\epsilon$
$XY-YX$	$0.6366(T-\bar{T})$
$XZ+ZX$	$0.803121\sigma - 0.820\partial_\tau^2\sigma - 0.736\partial_x^2\sigma$
$XZ-ZX$	$1.205\partial_x\sigma$
$YZ+ZY$	$2.41i\partial_\tau\sigma$
$YZ-ZY$	$-0.4015i\partial_\tau\partial_x\sigma$
XIX	$0.5403801 - 0.5403(T+\bar{T}) + 0.54038\epsilon - 0.067\partial_\tau^2\epsilon + 0.051\partial_x^2\epsilon$
XZX	$0.2122071 - 0.4774(T+\bar{T}) + 0.31831\epsilon - 0.089\partial_\tau^2\epsilon$

Table 5.1: Expansion (5.39) for simple lattice operators in the Ising model. Two-spin operators $A(j)B(j+1)$ are organized into terms that are even or odd terms under exchange $j \leftrightarrow j+1$, e.g. $XY \pm YX$. The set $\mathcal{A}$ of CFT operators is given in Eqs. (5.51)-(5.53). Coefficients smaller than 5×10^{-3} are not shown. The number of significant digits is determined case by case by requiring that a particular digit does not change under extrapolation with different sets of system sizes up to $N = 96$. Note that we omit the superscript $_{CFT}$ on the CFT scaling operators.

5.3.2 CFT operators as lattice operators

By inverting the relations in Table 5.4, we can build linear combinations of lattice operators whose leading contribution is a targeted CFT scaling operator ψ_α^{CFT}. For instance, if the target is the spin primary σ^{CFT}, its simplest realization is given in terms of the Pauli matrix X

$$\sigma^{CFT} \overset{\text{approx}}{\sim} \mu X, \qquad \mu \approx 1.24514, \tag{5.54}$$

where the approximation can be seen from Table 5.4 to include both $\partial_x^2\sigma^{CFT}$ and $\partial_\tau^2\sigma^{CFT}$ as subleading corrections. An improved lattice realization is then given by

$$\sigma^{CFT} \overset{\text{approx}}{\sim} \mu' X + \nu(XZ + ZX), \tag{5.55}$$

where $\nu \approx -0.026$, $\mu' \approx 1.27$ and, importantly, the subleading corrections due to $\partial_\tau^2\sigma^{CFT}$ have been eliminated This is particularly useful below for the computation of $C_{\sigma\sigma\epsilon}$, seen to be insensitive to the correction $\partial_x^2\sigma^{CFT}$ still present in (5.55). Similarly, for the primary ϵ^{CFT} we find

$$\epsilon^{CFT} \overset{\text{approx}}{\sim} \mu(XX - Z), \qquad \mu \approx 1.5708, \tag{5.56}$$

with $\partial_\tau^2\epsilon^{CFT}$ as a subleading correction, and the improved

$$\epsilon^{CFT} \overset{\text{approx}}{\sim} \mu'(XX - Z) + \nu(YY + XZX), \tag{5.57}$$

for $\nu \approx -0.19$ and $\mu' \approx 1.76$, with no subleading corrections in $\mathcal{A}$. Finally, we can also obtain the stress tensor

$$T^{CFT}, \bar{T}^{CFT} \overset{\text{approx}}{\sim} \mu(XX + Z) \pm \nu(XY - YX) + \nu'\mathbf{1}, \tag{5.58}$$

where $\mu \approx -1.571$, $\nu \approx 0.7854$, $\nu' \approx 2.000$ and, again, there are no subleading contributions in $\mathcal{A}$.

Equipped with a lattice realization of the primary operators σ^{CFT} and ϵ^{CFT}, we can finally use Eq. (5.2) to compute estimates $C_{\alpha\beta\gamma}$ for the OPE coefficients $C_{\alpha\beta\gamma}^{CFT}$. The non-zero coefficients are

$$C_{\sigma\sigma\epsilon} \approx 0.500000, \quad C_{\sigma\epsilon\sigma} \approx 0.50000, \tag{5.59}$$

obtained by computing $\langle\sigma|\mathcal{O}_\sigma(0)|\epsilon\rangle$ and $\langle\sigma|\mathcal{O}_\epsilon(0)|\sigma\rangle$, with $\mathcal{O}_\sigma$ and $\mathcal{O}_\epsilon$ the lattice operators in Eqs. (5.55) and (5.57) and extrapolating to the thermodynamic limit. Fig. 5.2 shows a change in scaling from N^{-2} to N^{-4} in the error of $C_{\sigma\sigma\epsilon}$ when replacing the lattice realization (5.54) of σ^{CFT} with the improved lattice realization (5.55).

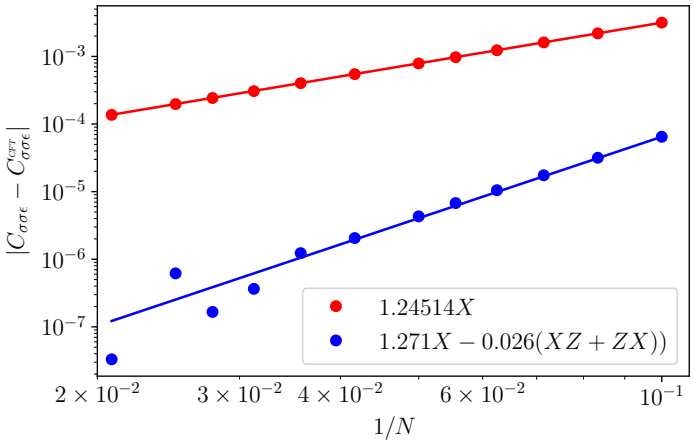

Figure 5.2: Error in the OPE coefficient $C_{\sigma\sigma\epsilon}$ as a function of system size for the two lattice realizations (5.54) and (5.55) of σ^{CFT}. Lines correspond to N^{-2} (red) and N^{-4} (blue) scaling.

5.3.3 Exact solution

In this subsection we first exactly compute some matrix elements in the low energy spectrum of the Ising model using the free fermion representation. We will use these exact matrix elements to obtain an exact expression for some of the (numerical) coefficients in Table 5.4.

Free fermion representation

Consider the critical Ising model with periodic boundary conditions,

$$H = \sum_{j=1}^{N} h(j), \tag{5.60}$$

$$h(j) = -X(j)X(j+1) - Z(j), \tag{5.61}$$

where site $j = N+1$ is identified with site $j = 1$. The model has a $\mathbb{Z}_2$ symmetry generated by

$$G_S = \prod_{j=1}^{N} Z_j. \tag{5.62}$$

It is easy to check that $[G_S, H] = 0$. G_S and H can be then simultaneously diagonalized, resulting in the eigenvectors of H divided into parity even ($G_S = 1$) and parity odd ($G_S = -1$) sectors.

The Jordan-Wigner transformation

$$\psi(2j-1) = \left(\prod_{1\le k<j} Z(k)\right) \frac{X(j)}{\sqrt{2}} \tag{5.63}$$

$$\psi(2j) = \left(\prod_{1\le k<j} Z(k)\right) \frac{Y(j)}{\sqrt{2}} \tag{5.64}$$

maps the Ising model with N spins to a spinless fermion chain with $2N$ Majorana fermions, where

$$\psi^\dagger(j) = \psi(j) \tag{5.65}$$

and

$$\{\psi(j), \psi(l)\} = \delta_{jl}. \tag{5.66}$$

They are fermionic operators because they anticommute on different sites (as opposed to spin operators which commute on different sites). Also notice that the Majorana operators are nonlocal in terms of spin operators. Local spin operators with odd Z_2 symmetry are mapped to a string of fermion operators, while those with even Z_2 symmetry are mapped to local operators in the fermion picture. We list some examples in table 6.1.

spin operator	fermion operator
$X(j)X(j+1)$	$-2i\psi(2j)\psi(2j+1)$
$Z(j)$	$-2i\psi(2j-1)\psi(2j)$
$X(j)Y(j+1)$	$-2i\psi(2j)\psi(2j+2)$
$Y(j)X(j+1)$	$2i\psi(2j-1)\psi(2j+1)$
$Y(j)Y(j+1)$	$2i\psi(2j-1)\psi(2j+2)$
$Z(j)Z(j+1)$	$-4\psi(2j-1)\psi(2j)\psi(2j+1)\psi(2j+2)$
$X(j)I(j+1)X(j+2)$	$-4\psi(2j)\psi(2j+1)\psi(2j+2)\psi(2j+3)$
$X(j)Z(j+1)X(j+2)$	$-2i\psi(2j)\psi(2j+3)$

Table 5.2: Lattice operators with even Z_2 symmetry and their representation using Majorana fermion operators

Let us represent the Ising Hamiltonian with the fermionic variables,

$$H = \sum_{j=1}^{N-1} 2i \left[\psi(2j-1)\psi(2j) + \psi(2j)\psi(2j+1)\right] \tag{5.67}$$

$$+ \quad 2i \left[\psi(2N-1)\psi(2N) - G_S\psi(2N)\psi(1)\right]. \tag{5.68}$$

One has to be careful with the boundary term. In the even $\mathbb{Z}_2$ sector, the fermionic chain has the anti-periodic boundary condition, $\psi(2N+j) = -\psi(j)$, which is usually referred to as the Neveu-Schwarz (NS) sector. On the other hand, in the odd $\mathbb{Z}_2$ sector, the fermionic chain has periodic boundary condition, $\psi(2N+j) = \psi(j)$, which is usually referred to as the Ramond (R) sector. We shall only consider the even $\mathbb{Z}_2$ sector below.

Assuming the NS boundary condition, the Hamiltonian can be written more compactly as

$$H = \sum_{j=1}^{2N} 2i\psi(j)\psi(j+1) \tag{5.69}$$

Note that the Hamiltonian is quadratic in fermionic variables. This makes it a free theory, which can be solved exactly using a Fourier transformation.

Symmetry and duality

In fermionic variables, the generator of the $\mathbb{Z}_2$ symmetry can be expressed as

$$G_S = (-2i)^N \prod_{j=1}^{2N} \psi(j). \tag{5.70}$$

It is then easy to see that G_S commutes with fermionic bilinears, of the form $\psi(j)\psi(j')$, but anti-commutes with operators linear in $\psi(j)$.

The Ising model at criticality possesses the famous Kramers-Wannier self-duality. This becomes a translation in the Majorana fermion picture,

$$\psi(2j-1) \to \psi(2j), \;\; \psi(2j) \to \psi(2j+1). \tag{5.71}$$

The Hamiltonian Eq. (5.69) is then manifestly invariant under the duality transformation. Note that applying the duality transformation twice corresponds to a translation by one site in spin variables.

Using the fermionic representation of local spin operators (Table 6.1), it is easy to see how they transform into each other under the duality transformation.

$$\begin{aligned} Z(j) &\to X(j)X(j+1) \\ &\to Z(j+1), \end{aligned} \tag{5.72}$$

$$\begin{aligned} Y(j)X(j+1) &\to -X(j)Y(j+1) \\ &\to Y(j+1)X(j+2), \end{aligned} \tag{5.73}$$

$$\begin{aligned} Y(j)Y(j+1) &\to -X(j)Z(j+1)X(j+2) \\ &\to Y(j+1)Y(j+2), \end{aligned} \tag{5.74}$$

$$\begin{aligned} Z(j)Z(j+1) &\to X(j)I(j+1)X(j+2) \\ &\to Z(j+1)Z(j+2). \end{aligned} \tag{5.75}$$

We can then combine them into duality even operators (e.g., $XX+Z$) and duality odd operators (e.g., $XX-Z$). In the Ising model, operators that are $\mathbb{Z}_2$ even and duality even belong to the conformal tower of the identity primary, while operators that are $\mathbb{Z}_2$ even and duality odd belong to the ϵ tower. $\mathbb{Z}_2$ odd operators belongs to the σ tower. We see that Table 5.4 is consistent with the symmetry and the duality.

Ground state correlation functions

Define the Fourier modes of fermion operators as

$$\psi(p) = \frac{1}{\sqrt{2N}} \sum_{j=1}^{2N} \psi(j) e^{ipj}, \tag{5.76}$$

where the boundary conditions impose

$$p = p_n \equiv \frac{2\pi}{2N}\left(n+\frac{1}{2}\right), \ n = -N, -N+1, \cdots, N-1. \tag{5.77}$$

The inverse Fourier transform is

$$\psi(j) = \frac{1}{\sqrt{2N}} \sum_{n=-N}^{N-1} \psi(p_n) e^{-ip_n j}, \tag{5.78}$$

Eqs (5.65)-(5.66) imply

$$\psi^\dagger(p) = \psi(-p), \tag{5.79}$$

$$\{\psi(p), \psi(q)\} = \delta_{p+q,0}. \tag{5.80}$$

Then $\psi(-p), \psi(p)$ can be understood as fermionic creation and annihilation operator of the mode p. Therefore we shall only include the modes with $p > 0$ as independent variables.

The Hamiltonian can be rewritten as

$$H = \sum_{n=0}^{N-1} (-2 \sin p_n + 4 \sin p_n \psi^\dagger(p_n)\psi(p_n)). \tag{5.81}$$

It follows that the ground state satisfies

$$\psi(p_n)|0\rangle = 0, \ \ n = 0, 1, \cdots, N-1. \tag{5.82}$$

The two point correlation function in momentum space is then

$$\langle 0|\psi(p_n)\psi(-p_m)|0\rangle = \delta_{nm}, \tag{5.83}$$

for $p_n > 0$ and 0 otherwise. Fourier transforming it back to position space yields

$$\langle 0|\psi(j)\psi(l)|0\rangle = \frac{1}{2N} \sum_{n=0}^{N-1} e^{-ip_n(j-l)}. \tag{5.84}$$

In the thermodynamic limit $N \to \infty$, the above sum becomes an integral,

$$\frac{1}{2\pi} \int_0^\pi dp\, e^{-i(j-l)p} = \frac{i}{2\pi(j-l)} (e^{-i\pi(j-l)} - 1) \tag{5.85}$$

$$= -\frac{i}{\pi(j-l)}, \ \ j-l \ \text{ odd}, \tag{5.86}$$

and 0 if $j - l$ is even and nonzero.

For later use, we also present how the correlation function at finite N behaves,

$$\langle 0|\psi(j)\psi(l)|0\rangle = -\frac{i}{j-l} \left(1 + \frac{\pi^2}{24N^2}(j-l)^2 + O(N^{-4})\right), \tag{5.87}$$

if $j - l$ is odd.

When $j = l$, we have

$$\langle 0|\psi(j)^2|0\rangle = \frac{1}{2}. \tag{5.88}$$

We then have all the two point correlation functions in the thermodynamic limit.

For example,

$$\lim_{N\to\infty}\langle 0|Z(j)|0\rangle = -2i\langle 0|\psi(2j-1)\psi(2j)|0\rangle = \frac{2}{\pi}. \tag{5.89}$$

And similarly,

$$\lim_{N\to\infty}\langle 0|X(j)X(j+1)|0\rangle = \frac{2}{\pi} \tag{5.90}$$

$$\lim_{N\to\infty}\langle 0|Y(j)Y(j+1)|0\rangle = -\frac{2}{3\pi} \tag{5.91}$$

$$\lim_{N\to\infty}\langle 0|X(j)Z(j+1)X(j+2)|0\rangle = -\frac{2}{3\pi} \tag{5.92}$$

We can then derive higher point correlation functions by Wick's theorem. For example, in the thermodynamic limit,

$$\langle 0|\psi(2j)\psi(2j+1)\psi(2j+2)\psi(2j+3)|0\rangle \tag{5.93}$$

$$\begin{aligned} = \ & \langle 0|\psi(2j)\psi(2j+1)|0\rangle\langle 0|\psi(2j+2)\psi(2j+3)|0\rangle \\ & +\langle 0|\psi(2j)\psi(2j+3)|0\rangle\langle 0|\psi(2j+1)\psi(2j+2)|0\rangle \end{aligned}$$

$$= -\frac{4}{3\pi^2}. \tag{5.94}$$

Then

$$\lim_{N\to\infty}\langle 0|X(j)I(j+1)X(j+2)|0\rangle = \frac{16}{3\pi^2} \tag{5.95}$$

$$\lim_{N\to\infty}\langle 0|Z(j)Z(j+1)|0\rangle = \frac{16}{3\pi^2} \tag{5.96}$$

The ground state expectation value of a lattice operator in the thermodynamic limit gives the coefficient of the identity operator in the corresponding CFT operator. For example

$$XX \sim \frac{2}{\pi}\mathbf{1}^{CFT} + \cdots, \tag{5.97}$$

where $\cdots$ represents other scaling operators. In this way, we obtain the coefficient in front of the identity operator for all $\mathbb{Z}_2$ even operators in Table 5.4, as listed in Table 6.2.

Excited states

In order to consider other CFT operators in the expansion, we have to compute low-energy excited states. Excited states are created by applying creation operators $\psi^\dagger(p_n)(p_n > 0)$ on the ground state. There are two sets of creation operators at low energy, those with p_n near $p = 0$ and near $p = \pi$, corresponding to chiral and anti-chiral excitations. In the $\mathbb{Z}_2$ even sector, there is an even number of fermions. The lowest lying excitations are

$$
\begin{aligned}
|\epsilon\rangle &= e^{i\theta_\epsilon}\psi^\dagger(p_0)\psi^\dagger(p_{N-1})|0\rangle && (5.98)\\
|T\rangle &= e^{i\theta_T}\psi^\dagger(p_0)\psi^\dagger(p_1)|0\rangle && (5.99)\\
|\bar{T}\rangle &= e^{i\theta_{\bar{T}}}\psi^\dagger(p_{N-1})\psi^\dagger(p_{N-2})|0\rangle. && (5.100)
\end{aligned}
$$

The above phases will be determined shortly.

Matrix elements of lattice operators involving these excited states can then be computed by multi-point correlation functions of Majorana operator. For example,

$$
\begin{aligned}
& \langle\epsilon|X(j)X(j+1)|0\rangle \\
= \; & -2ie^{-i\theta_\epsilon}\langle 0|\psi(p_{N-1})\psi(p_0)\psi(2j)\psi(2j+1)|0\rangle \\
= \; & -2ie^{-i\theta_\epsilon}[\langle 0|\psi(p_0)\psi(2j)|0\rangle\langle 0|\psi(p_{N-1})\psi(2j+1)|0\rangle \\
& -\langle 0|\psi(p_0)\psi(2j+1)|0\rangle\langle 0|\psi(p_{N-1})\psi(2j)|0\rangle] \\
= \; & -2ie^{-i\theta_\epsilon}[\frac{1}{\sqrt{2N}}e^{ip_0 2j}\frac{1}{\sqrt{2N}}e^{ip_{N-1}(2j+1)} \\
& -\frac{1}{\sqrt{2N}}e^{ip_0(2j+1)}\frac{1}{\sqrt{2N}}e^{ip_{N-1}2j}] \\
= \; & -\frac{ie^{-i\theta_\epsilon}}{N}(e^{ip_{N-1}} - e^{ip_0}) \\
= \; & \frac{2ie^{-i\theta_\epsilon}}{N}\cos p_0, && (5.101)
\end{aligned}
$$

where the first equality follows from Table 6.1, the second equality follows from the Wick theorem, the third equality follows from Eq. (5.83) and Eq. (5.78), and the last two equalities follows from $p_0 + p_{N-1} = \pi$.

At large sizes,

$$
\langle\epsilon|X(j)X(j+1)|0\rangle = \frac{2ie^{-i\theta_\epsilon}}{N}\left[1 - \frac{\pi^2}{8N^2} + O(N^{-4})\right]. \qquad (5.102)
$$

As stated in section 5.2, we fix the phase $\theta_\epsilon = \pi/2$ by requiring the above matrix element to be real and positive.

Comparing to the CFT result

$$\langle \epsilon^{CFT} | \epsilon^{CFT}(x) | 0^{CFT} \rangle = \frac{2\pi}{L} \tag{5.103}$$

and

$$\langle \epsilon^{CFT} | \partial_\tau^2 \epsilon^{CFT}(x) | 0^{CFT} \rangle = \left(\frac{2\pi}{L} \right)^3 \tag{5.104}$$

(derived from Eq. (5.30)), we can read off

$$XX \sim \frac{1}{\pi} \epsilon^{CFT} - \frac{1}{32\pi} \partial_\tau^2 \epsilon^{CFT} + \cdots , \tag{5.105}$$

where $\cdots$ may contain $\partial_x^2 \epsilon^{CFT}$ and higher scaling dimensions in the ϵ tower, as well as operators in the identity tower.

Similarly, we can compute

$$\langle T | X(j) X(j+1) | 0 \rangle = -\frac{i e^{-i\theta_T}}{N} e^{i 2\pi s_T j/N} (e^{ip_1} - e^{ip_0}), \tag{5.106}$$

where $s_T = 2$ is the conformal spin of T.

Expanding it with respect to $1/N$ gives

$$\langle T | X(j) X(j+1) | 0 \rangle = \pi \frac{e^{-i\theta_T}}{N^2} e^{i 2\pi s_T j/N}. \tag{5.107}$$

By requiring it to be negative, we fix $\theta_T = \pi$. Then we can compare it to

$$\langle T^{CFT} | T^{CFT}(x) | 0^{CFT} \rangle = \left(\frac{2\pi}{L} \right)^2 \sqrt{\frac{c^{CFT}}{2}} e^{i 2\pi s_T x/L}, \tag{5.108}$$

where $c^{CFT} = 1/2$ is the central charge, to obtain

$$XX \sim -\frac{1}{2\pi} T^{CFT} + \cdots , \tag{5.109}$$

where $\cdots$ contains other scaling operators. In the same way,

$$XX \sim -\frac{1}{2\pi} \bar{T}^{CFT} + \cdots . \tag{5.110}$$

Now we can combine Eqs. (5.97),(5.105),(5.109),(5.110) to obtain

$$XX \sim \frac{2}{\pi}\mathbf{1}^{CFT} - \frac{1}{2\pi}(T^{CFT} + \bar{T}^{CFT}) + \frac{1}{\pi}\epsilon^{CFT} - \frac{1}{32\pi}\partial_\tau^2\epsilon^{CFT} + \cdots , \tag{5.111}$$

where $\cdots$ contains other scaling operators with scaling dimension 3 or higher.

Since XX and Z are related by a duality transformation, they have the same coefficients in front of operators in the identity tower, and opposite coefficients in front of operators in the ϵ tower. Then

$$Z \sim \frac{2}{\pi}\mathbf{1}^{CFT} - \frac{1}{2\pi}(T^{CFT} + \bar{T}^{CFT}) - \frac{1}{\pi}\epsilon^{CFT} + \frac{1}{32\pi}\partial_\tau^2\epsilon^{CFT} + \cdots . \tag{5.112}$$

Proceeding as above for other lattice operators as listed in Table 6.1, we reproduce part of Table 5.4 analytically, as listed in Table 6.2. We note that the subleading term in Eq. (5.87) is important in deriving the coefficient in front of $\partial_\tau^2\epsilon^{CFT}$ for XIX and ZZ, which are quartic in fermionic variables. The coefficient in front of $\partial_x^2\epsilon^{CFT}$ cannot be computed by the matrix elements $\langle\epsilon|O(j)|0\rangle$ because $\langle\epsilon^{CFT}|\partial_x^2\epsilon^{CFT}|0^{CFT}\rangle = 0$. Instead, we have to use matrix elements involving a state in the ϵ tower with non-vanishing conformal spin, such as $|\partial\epsilon\rangle$.

In Table 6.2, we also show the first 5 digits of each analytically computed coefficient, to be compared with numerical results in the main text.

Comparing Table 6.2 with Table 5.4 in the main text, we see that in general, the coefficients in front of CFT operators with lower scaling dimensions are, as expected, more accurate.

Finally, we note that in order to reproduce the expansion for $\mathbb{Z}_2$ odd operators analytically, we have to work with states in the Ramond sector and string operators in the fermion language. This is more complicated and we omit it here.

5.4 Source of error

We have found the expansion of lattice operators in terms of CFT operators, i.e., the coefficients in Eq. (5.39). Reversing the expansion, we found lattice operators for primary CFT operators, and then we compute the OPE coefficients. In this section we analyze possible source of error, including finite-size errors and truncation errors. We will first consider general lattice models and then analyze the example of critical Ising model in detail.

Lattice operator	CFT operator
Z	$(2/\pi)\mathbf{1} - 1/(2\pi)(T+\bar{T}) - (1/\pi)\epsilon + 1/(32\pi)\partial_\tau^2\epsilon$
XX	$(2/\pi)\mathbf{1} - 1/(2\pi)(T+\bar{T}) + (1/\pi)\epsilon - 1/(32\pi)\partial_\tau^2\epsilon$
YY	$-2/(3\pi)\mathbf{1} + 3/(2\pi)(T+\bar{T}) + (1/\pi)\epsilon - 9/(32\pi)\partial_\tau^2\epsilon$
ZZ	$16/(3\pi^2)\mathbf{1} - 16/(3\pi^2)(T+\bar{T}) - 16/(3\pi^2)\epsilon + 2/(3\pi^2)\partial_\tau^2\epsilon$
XZX	$2/(3\pi)\mathbf{1} - 3/(2\pi)(T+\bar{T}) + (1/\pi)\epsilon - 9/(32\pi)\partial_\tau^2\epsilon$
XIX	$16/(3\pi^2)\mathbf{1} - 16/(3\pi^2)(T+T) + 16/(3\pi^2)\epsilon - 2/(3\pi^2)\partial_\tau^2\epsilon$
$-i(XY+YX)$	$(1/\pi)\partial_\tau\epsilon$
$XY-YX$	$(2/\pi)(T-\bar{T})$

Lattice operator	CFT operator
Z	$0.63662\mathbf{1} - 0.15915(T+\bar{T}) - 0.31831\epsilon + 0.00995\partial_\tau^2\epsilon$
XX	$0.63662\mathbf{1} - 0.15915(T+\bar{T}) + 0.31831\epsilon - 0.00995\partial_\tau^2\epsilon$
YY	$-0.21221\mathbf{1} + 0.47746(T+\bar{T}) + 0.31831\epsilon - 0.08952\partial_\tau^2\epsilon$
ZZ	$0.54038\mathbf{1} - 0.54038(T+\bar{T}) - 0.54038\epsilon + 0.06755\partial_\tau^2\epsilon$
XZX	$0.21221\mathbf{1} - 0.47746(T+\bar{T}) + 0.15915\epsilon - 0.08952\partial_\tau^2\epsilon$
XIX	$0.54038\mathbf{1} - 0.54038(T+\bar{T}) + 0.54038\epsilon - 0.06755\partial_\tau^2\epsilon$
$-i(XY+YX)$	$0.31831\partial_\tau\epsilon$
$XY-YX$	$0.63662(T-\bar{T})$

Table 5.3: Correspondence between lattice operators and CFT operators for the Ising model. The truncated set of CFT operators contains $\mathbf{1}, T, \bar{T}, \epsilon, \partial_\tau\epsilon, \partial_\tau^2\epsilon$. Coefficients are obtained analytically in the top table. The bottom table is the same as the top table except that coefficients are shown their approximate values to 5 digits to compare with numerical results. The subscript "CFT" is omitted in the column of CFT operators.

5.4.1 General lattice models

In general, there are three sources of errors in our method of finding the correspondence between lattice operators and CFT operators in Section 5.2.

1. The CFT operator space is truncated to a finite set $\mathcal{A}$. This precludes an exact correspondence between CFT operators and lattice operators.

2. The lattice has a finite number N of sites, which leads to errors (due to subleading finite-size corrections) in the numerical estimates of the scaling dimensions and central charge used in order to evaluate CFT matrix elements in the cost function.

3. The numerical diagonalization of the Hamiltonian (e.g. using puMPS) produces approximate eigenstates (e.g. due to the finite bond dimension of the puMPS).

It will be argued in this section that the first source causes errors in the expansion coefficients that decay as $1/N^p$, with the power depending on the truncated space $\mathcal{A}$ of CFT operators. The power-law convergence of expansion coefficients is confirmed numerically by the results obtained with the Ising model, which is detailed in next subsection. We also briefly comment on the other two sources of error, which are assumed to be subdominant.

Errors due to a truncated set $\mathcal{A}$ of CFT operators

Given a truncated set $\mathcal{A}$ of CFT scaling operators $\{\psi_\alpha^{CFT}(x)\}$ and a lattice operator $\mathcal{O}$, we find the coefficients $a_\alpha(N)$ such that

$$\tilde{O}^{CFT}(x) = \sum_\alpha a_\alpha(N)\psi_\alpha^{CFT}(x) \tag{5.113}$$

minimizes the cost function

$$f_N^O(\{a_\alpha\}) = \sum_{\beta,s} \left| \langle\psi_\beta|O^s|0\rangle - \langle\psi_\beta^{CFT}|\tilde{O}^{CFT,s}|0^{CFT}\rangle \right|^2. \tag{5.114}$$

The exactly correspondent CFT operator O^{CFT}, which involves an infinite sum of scaling operators, satisfies

$$\langle\psi_\beta|O^s|0\rangle = \langle\psi_\beta^{CFT}|O^{CFT,s}|0^{CFT}\rangle \tag{5.115}$$

for any β and s. The goal is to estimate how far the coefficient $a_\alpha(N)$ that minimizes the cost function is away from the exact value a_α.

Denote by $\mathcal{A}_c$ the set of scaling operators $\{\psi_{c,\alpha'}^{CFT}(x)\}$ (c means "complementary") that together with $\{\psi_\alpha^{CFT}(x)\}$ form a basis that expands $O^{CFT}(x)$, then we can expand

$$O^{CFT}(x) = \sum_\alpha a_\alpha\psi_\alpha^{CFT}(x) + \sum_{\alpha'} b_{\alpha'}\psi_{c,\alpha'}^{CFT}(x). \tag{5.116}$$

Denote the difference $\delta a_\alpha(N) = a_\alpha - a_\alpha(N)$. Using Eqs. (5.113)-(5.115), we can express the cost function solely in terms of CFT matrix elements,

$$f_N^O(\{a_\alpha(N)\}) = \sum_\beta \left| \sum_\alpha \delta a_\alpha(N)\langle\psi_\beta^{CFT}|\psi_\alpha^{CFT,s_\beta}|0^{CFT}\rangle + \sum_{\alpha'} b_{\alpha'}\langle\psi_\beta^{CFT}|\psi_{c,\alpha'}^{CFT,s_\beta}|0^{CFT}\rangle \right|^2. \tag{5.117}$$

For simplicity, we first consider the case where the expansion Eq. (5.116) only involves operators in one conformal tower. In the limit of large N, the second term scales as $N^{-\Delta_c}$,

where Δ_c denotes the smallest scaling dimension of the operators in $\{\psi^{CFT}_{c,\alpha'}(x)\}$ that have nonzero coefficient $b_{\alpha'_0} \neq 0$. Moreover, the leading contribution of the second term cannot be completely eliminated by fine tuning $\delta a_\alpha(N)$, since otherwise $\psi^{CFT}_{c,\alpha'_0}(x)$ would be a linear combination of $\{\psi^{CFT}_\alpha(x)\}$. Therefore, the minimum of the cost function f^O_N scales as $N^{-2\Delta_c}$, and

$$\delta a_\alpha(N) \sim N^{-(\Delta_c - \Delta_\alpha)}, \tag{5.118}$$

where Δ_α is the scaling dimension of ψ^{CFT}_α. In practice, we include in $\mathcal{A}$ all possible operators in $\{\psi^{CFT}_\alpha(x)\}$ up to scaling dimension $\Delta_{\max}$. Then by definition $\Delta_c > \Delta_{\max}$. Therefore, the error becomes smaller as we include operators in $\mathcal{A}$ with higher scaling dimensions so as to increase $\Delta_{\max}$. Another way to reduce error is to go to large sizes, whenever other sources of error are still subdominant.

If the expansion Eq. (5.116) involves operators in different conformal towers, then in Eq. (5.117) the sum over β splits into different conformal towers. For each conformal tower, the sum over α and α' are restricted to the same conformal tower. Following the same arguments, we define Δ_c for each conformal tower as the smallest scaling dimension in $\{\psi^{CFT}_{c,\alpha'}(x)\}$ in that conformal tower, and Eq. (5.118) still holds for operators ψ^{CFT}_α in that conformal tower.

Other sources of error

Error due to extrapolation of Δ and c to the thermodynamic limit can be reduced by enlarging the maximal size $N_{\max}$. As shown in Chapter 4, the error usually decays polynomially with $N_{\max}$. We can therefore make this error subleading by using larger $N_{\max}$.

Error introduced during the diagonalization of the Hamiltonian will result in errors in $a_\alpha(N)$ that grow with both the scaling dimension Δ_α of the operator and the system size N. This is because, in the cost function Eq. (5.117), the coefficient $\delta a_\alpha(N)$ is multiplied by a matrix element that scales as $N^{-\Delta_\alpha}$. This error is negligible if we do not go to too large sizes N or too large scaling dimensions in $\mathcal{A}$. In the example of Ising model we only go to $N \leq 48$, much smaller than the maximal size ($N = 228$) that our diagonalization technique (puMPS) can reach. We only keep up to level-2 descendants in $\mathcal{A}$, while we could identify conformal towers up to level 6.

Error in numerical estimates of OPE coefficients

The OPE coefficients are approximately computed by

$$C_{\alpha\beta\gamma} = \left(\frac{2\pi}{N}\right)^{-\Delta_\beta} \langle \phi_\alpha | \mathcal{O}_{\phi_\beta}^{s_\alpha - s_\gamma} | \phi_\gamma \rangle, \tag{5.119}$$

where $\mathcal{O}_{\phi_\beta}$ is a lattice operator that corresponds to $\mathcal{O}_{\phi_\beta}^{CFT} \approx \phi_\beta^{CFT}$. Expanding in terms of scaling operators,

$$\mathcal{O}_{\phi_\beta}^{CFT} = a_0 \phi_\beta^{CFT} + \sum_{\beta' \geq 1} a_{\beta'} \psi_{\beta'}^{CFT}, \tag{5.120}$$

where $a_0 \approx 1$ and $\psi_{\beta'}^{CFT}$ represents other scaling operators. Then

$$C_{\alpha\beta\gamma} - C_{\alpha\beta\gamma}^{CFT} = (a_0 - 1) C_{\alpha\beta\gamma}^{CFT} \tag{5.121}$$

$$+ \left(\frac{2\pi}{N}\right)^{\Delta_\beta} \sum_{\beta' \geq 1} a_{\beta'} \langle \phi_\alpha^{CFT} | \psi_{\beta'}^{CFT, s_\alpha - s_\gamma} | \phi_\gamma^{CFT} \rangle. \tag{5.122}$$

We see that the error of $C_{\alpha_\beta\gamma}$ has two contributions. The first contribution, Eq. (5.121), contributes to a constant proportional to $a_0 - 1$, which is determined by the accuracy of the expansion coefficients of each lattice operator that are used to construct $\mathcal{O}_{\phi_\beta}$. The second contribution, Eq. (5.122), scales as $N^{-(\Delta_{\beta_0'} - \Delta_\beta)}$, where $\Delta_{\beta_0'}$ is the lowest scaling dimension of $\psi_{\beta_0'}^{CFT}$ that appears in Eq. (5.122).

Therefore, in order to increase the accuracy of $C_{\alpha\beta\gamma}$, we can either compute Eq. (5.119) at larger sizes N, or obtain more significant digits of a_0. We shall see that for the Ising model that both could lead to a significant improvement of accuracy.

5.4.2 Example of critical Ising model

Convergence of expansion coefficients $a_\alpha(N)$

We start with the numerical extrapolation of some of the expansion coefficients a_α presented in Table 5.4 in the main text. We show that the convergence of $a_\alpha(N)$ is as $1/N^p$, where $p = \Delta_c - \Delta_\alpha$ is the predicted power law in Eq. (5.118).

The first example is $\mathcal{O} = XZ + ZX$ with

$$\tilde{\mathcal{O}}^{CFT} = a_\sigma \sigma^{CFT} + a_{\partial_\tau \sigma} \partial_\tau \sigma^{CFT} + a_{\partial_x^2 \sigma} \partial_x^2 \sigma^{CFT} + a_{\partial_\tau^2 \sigma} \partial_\tau^2 \sigma^{CFT}. \tag{5.123}$$

The error due to using a truncated set $\mathcal{A}$ of CFT scaling operators is determined by $\Delta_c > 2 + 1/8$. It turns out that this particular lattice operator $\mathcal{O} = XZ + ZX$ does not have a contribution from the σ tower at level 3, and $\Delta_c = 4 + 1/8$. According to Eq. (5.118), we obtain

$$\begin{aligned} \delta a_\sigma &\sim N^{-4}, && (5.124)\\ \delta a_{\partial_\tau \sigma} &\sim N^{-3}, && (5.125)\\ \delta a_{\partial_\tau^2 \sigma} &\sim N^{-2}, && (5.126)\\ \delta a_{\partial_x^2 \sigma} &\sim N^{-2}. && (5.127) \end{aligned}$$

The numerical results is shown in Fig. 5.1, consistent with the prediction above.

The second example is $\mathcal{O} = ZZ$ and

$$\begin{aligned} \tilde{\mathcal{O}}^{CFT} &= a_{\mathbf{1}} \mathbf{1}^{CFT} + a_T (T^{CFT} + \bar{T}^{CFT}) \\ &+ a_\epsilon \epsilon^{CFT} + a_{\partial_\tau \epsilon} \partial_\tau \epsilon^{CFT} + a_{\partial_x^2 \epsilon} \partial_x^2 \epsilon^{CFT} + a_{\partial_\tau^2 \epsilon} \partial_\tau^2 \epsilon^{CFT}. \end{aligned}$$

In this case, the leading operator in the complementary set $\mathcal{A}_c$ has scaling dimension $\Delta_c = 4$ for the identity tower and $\Delta_c = 5$ for the ϵ tower. Then

$$\begin{aligned} \delta a_{\mathbf{1}} &\sim N^{-4}, && (5.128)\\ \delta a_T &\sim N^{-2}, && (5.129)\\ \delta a_\epsilon &\sim N^{-4}, && (5.130)\\ \delta a_{\partial_\tau \epsilon} &\sim N^{-3}, && (5.131)\\ \delta a_{\partial_\tau^2 \epsilon} &\sim N^{-2}, && (5.132)\\ \delta a_{\partial_x^2 \epsilon} &\sim N^{-2}. && (5.133) \end{aligned}$$

The numerical results are shown in Fig. 5.3.

Some additional comments are in order. First, we cannot determine Δ_c a priori in general. Instead, we have to try extrapolation using different possible Δ_c to make the best fit. Second, for some coefficient $a_\alpha(N)$, the error in numerical diagonalization may be important in the extrapolation. For example, this happens for $a_{\partial_\tau^2 \sigma} \approx -0.017$ for $\mathcal{O} = X$ with Eq. (5.123), see Fig. 5.4. Third, the extrapolation assumes the asymptotic scaling of $\delta a_\alpha(N)$ at large sizes. Numerically, we can determine a_α more accurately by using data from larger sizes, in the situation where other sources of error are negligible. In the operators that are considered, we find that for $\mathcal{O} = -i(YZ + ZY)$ with Eq. (5.123), the coefficients $a_{\partial_\tau^2 \sigma}$ and $a_{\partial_x^2 \sigma}$ are only obviously below 10^{-2} when extrapolating with data up to $N = 96$, see Fig. 5.5.

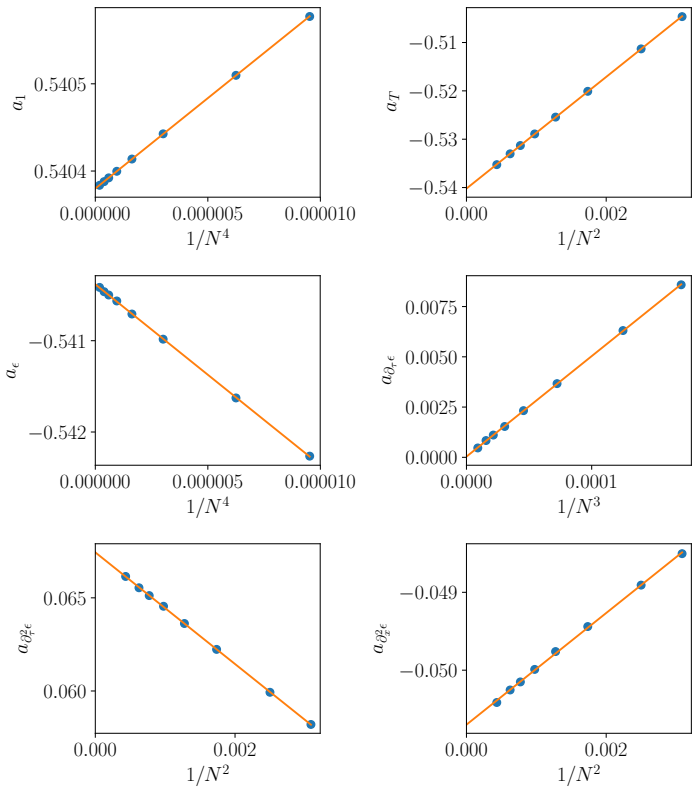

Figure 5.3: Convergence of the coefficients with Eq. (5.128) for $\mathcal{O} = ZZ$. Coefficients are obtained by minimizing the cost function for systems sizes $18 \leq N \leq 48$.

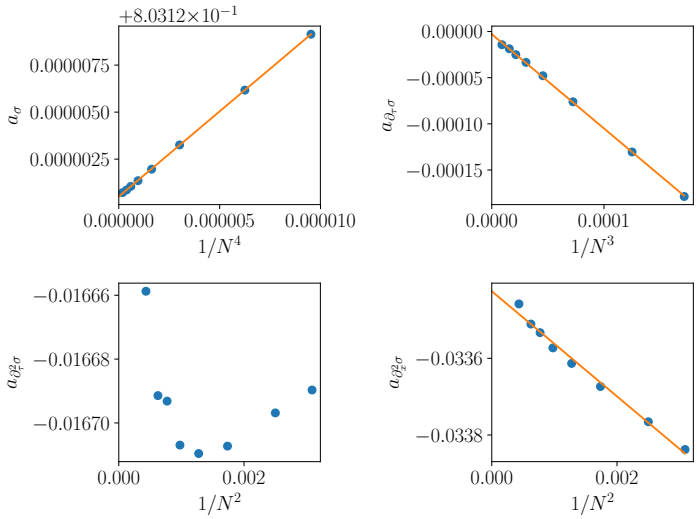

Figure 5.4: Convergence of the coefficients with Eq. (5.123) for $\mathcal{O} = X$. Coefficients are obtained by minimizing the cost function for systems sizes $18 \leq N \leq 48$.

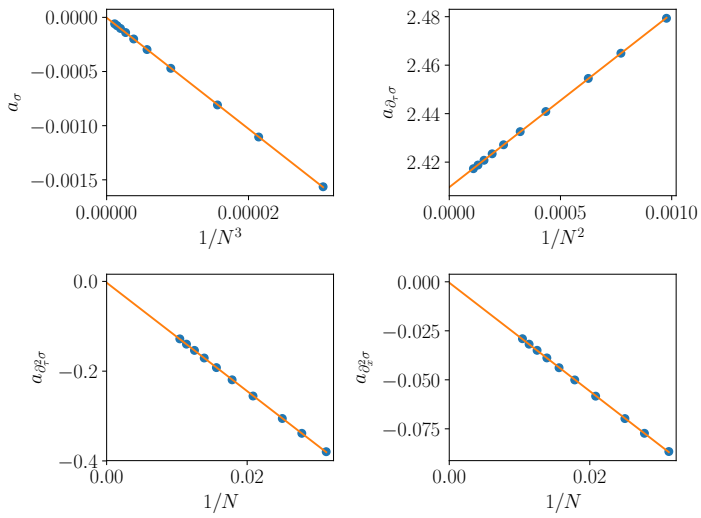

Figure 5.5: Convergence of the coefficients with Eq. (5.123) for $\mathcal{O} = -i(YZ + ZY)$. Coefficients are obtained by minimizing the cost function for systems sizes $36 \leq N \leq 96$.

Convergence of OPE coefficients

According to Table 5.4 in the main text, we can have the following three ansatz for $\mathcal{O}_\sigma$, all of which corrspond to a CFT operator of the form Eq. (5.120), with $\phi_\beta^{CFT} = \sigma^{CFT}, a_0 \approx 1$. They are

$$\mathcal{O}_{\sigma 1} = \mu_1 X, \tag{5.134}$$
$$\mathcal{O}_{\sigma 2} = \mu_2 (XZ + ZX), \tag{5.135}$$
$$\mathcal{O}_{\sigma 3} = \mu_3 (X + \nu_3 (XZ + ZX)). \tag{5.136}$$

We quote the expansion coefficients that are used here for reader's convenience (see Table 5.4),

$$X \sim 0.803121\sigma^{CFT} - 0.017\partial_\tau^2 \sigma^{CFT} + \cdots \tag{5.137}$$
$$XZ + ZX \sim 0.803121\sigma^{CFT} - 0.820\partial_\tau^2 \sigma^{CFT} + \cdots, \tag{5.138}$$

where we omit the $\partial_x^2 \sigma^{CFT}$ term because it does not contribute to the OPE coefficient. In the following, we shall regard the coefficient of σ^{CFT} in the above two expansions numerically the same, as they coincide with the highest accuracy (6 digits) among all coefficients that are computed.

In order to have $a_0 \approx 1$, we determine

$$\mu_1 = \mu_2 = \mu_3/(1+\nu_3) \approx 1/0.803121 \approx 1.24514. \tag{5.139}$$

Since a_0 has 6 significant digits and its error can be negligible to the finite-size errors below, we shall ignore the difference between a_0 and 1.

The subleading operator in Eq. (5.120) for $\mathcal{O}_{\sigma 1}$ and $\mathcal{O}_{\sigma 2}$ is $\partial_\tau^2 \sigma^{CFT}$, with coefficient $a_{(\partial_\tau^2\sigma)1} = -0.017\mu_1 \approx -0.021$ and $a_{(\partial_\tau^2\sigma)2} = -0.820\mu_2 \approx -1.02$. Therefore, the corresponding OPE coefficients are, according to Eqs. (5.121)-(5.122),

$$C_{\sigma\sigma\epsilon 1} \approx C_{\sigma\sigma\epsilon}^{CFT} + \left(\frac{2\pi}{N}\right)^2 a_{(\partial_\tau^2\sigma)1} C_{\sigma\partial^2\sigma\epsilon}^{CFT} \tag{5.140}$$
$$C_{\sigma\sigma\epsilon 2} \approx C_{\sigma\sigma\epsilon}^{CFT} + \left(\frac{2\pi}{N}\right)^2 a_{(\partial_\tau^2\sigma)2} C_{\sigma\partial^2\sigma\epsilon}^{CFT}, \tag{5.141}$$

where we have defined

$$C_{\sigma\partial^2\sigma\epsilon}^{CFT} = \left(\frac{2\pi}{L}\right)^{-(2+\Delta_\sigma^{CFT})} \langle \sigma^{CFT} | \partial_\tau^2 \sigma^{CFT}(0) | \epsilon^{CFT} \rangle \tag{5.142}$$
$$= \frac{49}{128}, \tag{5.143}$$

and we have used CFT relations

$$\langle \phi_\alpha^{CFT} | (\partial_\tau^n \phi_\beta^{CFT})^{s_\alpha - s_\gamma} | \phi_\gamma^{CFT} \rangle = \left(\frac{2\pi}{L}\right)^{\Delta_\beta^{CFT}+n} (\Delta_\alpha^{CFT} - \Delta_\gamma^{CFT})^n C_{\alpha\beta\gamma}^{CFT} \tag{5.144}$$

$$\langle \phi_\alpha^{CFT} | (\partial_x^n \phi_\beta^{CFT})^{s_\alpha - s_\gamma} | \phi_\gamma^{CFT} \rangle = \left(\frac{2\pi}{L}\right)^{\Delta_\beta^{CFT}+n} (i(s_\alpha^{CFT} - s_\gamma^{CFT}))^n C_{\alpha\beta\gamma}^{CFT}, \tag{5.145}$$

which follows from Eq. (5.27) and its antiholomorphic analogue.

Substituting numbers into Eqs. (5.140)-(5.141) gives

$$C_{\sigma\sigma\epsilon 1} \approx 0.5 - \frac{0.32}{N^2} \tag{5.146}$$

$$C_{\sigma\sigma\epsilon 2} \approx 0.5 - \frac{15.4}{N^2}, \tag{5.147}$$

Eqs. (5.146)-(5.147) are confirmed with numerical results, see Fig. 5.6.

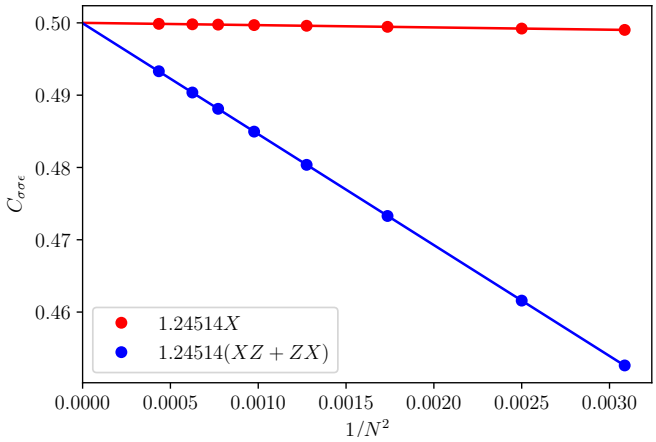

Figure 5.6: Convergence of the OPE coefficients $C_{\sigma\sigma\epsilon}$ with $\sigma^{CFT} \sim \mathcal{O}_{\sigma 1}, \mathcal{O}_{\sigma 2}$. Sizes $18 \leq N \leq 48$ are used. Linear extrapolation with $1/N^2$ is used. The intercept the the extrapolation are approximately 0.5000003 and 0.49994 respectively. The slope are approximately -0.315 and -15.34 respectively.

We see that using $\sigma^{CFT} \sim \mathcal{O}_{\sigma 1}$ results in much smaller errors, although they scale with the same power of N as the errors in $\sigma^{CFT} \sim \mathcal{O}_{\sigma 2}$. This originates from the fact that the coefficient of $\partial_\tau^2 \sigma^{CFT}$ in Eq. (5.137) has a much smaller amplitude than that in Eq. (5.138).

The point of introducing the third lattice realization $\mathcal{O}_{\sigma 3}$ is to completely eliminate the $\partial_\tau^2 \sigma^{CFT}$ contribution. Therefore, $\nu_3 \approx -0.017/0.820 \approx -0.021$ and it follows that $\mu_3 \approx 1.27$. This results in

$$C_{\sigma\sigma\epsilon 3} = C^{CFT}_{\sigma\sigma\epsilon} + O(1/N^4), \tag{5.148}$$

which is confirmed in Fig. 5.2.

We will analyze the cases for the other OPE coefficient $C_{\sigma\epsilon\sigma}$ in the same way. We have used 4 different lattice realizations that approximately correspond to ϵ^{CFT},

$$\begin{aligned}
\mathcal{O}_{\epsilon 1} &= \mu_1(XX - Z) && (5.149)\\
\mathcal{O}_{\epsilon 2} &= \mu_2(YY + XZX) && (5.150)\\
\mathcal{O}_{\epsilon 3} &= \mu_3(ZZ - XIX) && (5.151)\\
\mathcal{O}_{\epsilon 4} &= \mu_4(XX - Z + \nu_4(YY + XZX)), && (5.152)
\end{aligned}$$

where $\mu_1 \approx \mu_2 = 1/0.63662 \approx 1.5708$ and $\mu_3 = 1/(-1.0876) \approx -0.92527$. The last operator is to eliminate the $\partial_\tau^2 \epsilon^{CFT}$ contribution. Therefore, $\nu_4 = -0.010/0.089 \approx -0.11$ and $\mu_4 \approx \mu_1/(1+\nu_4) \approx 1.76$. However, since

$$\langle \sigma^{CFT} | \partial_\tau^2 \epsilon^{CFT}(0) | \sigma^{CFT} \rangle = 0, \tag{5.153}$$

it does not improve the scaling of $C_{\sigma\epsilon\sigma}$. The numerical results for $C_{\sigma\epsilon\sigma}$ using these operators are shown in Fig. 5.7. We omit the OPE coefficient computed with $\mathcal{O}_{\epsilon 4}$, which almost coincides with that with $\mathcal{O}_{\epsilon 1}$. We see that only $\mathcal{O}_{\epsilon 3}$ has significant finite-size error in this OPE coefficient, which hints that in the expansion of $\mathcal{O}^{CFT}_{\epsilon 3}$ there is a significant contribution from $(L_{-4} + \bar{L}_{-4})\epsilon^{CFT}$. For the other two operators $\mathcal{O}_{\epsilon 1}$ and $\mathcal{O}_{\epsilon 2}$, there is no significant finite-size error in $C_{\sigma\epsilon\sigma}$, which suggests that the only subleading CFT operators in the ϵ tower up to level 4 are derivative descendants that do not contribute to the OPE coefficient. This may be explained by the fact that $\mathcal{O}_{\epsilon 1}$ and $\mathcal{O}_{\epsilon 2}$ are quadratic in fermionic variables, which renormalize into fermion bilinear operators in the Ising CFT, and that only ϵ^{CFT} and derivative descendants are fermion bilinear operaters in the ϵ tower.

5.5 Conclusion

Given a critical quantum spin chain Hamiltonian H as the only input, in this chapter we have explained how to identify a local lattice operator with a corresponding expansion (5.39) in terms of scaling operators ψ^{CFT}_α of the emergent CFT. As demonstrated for the

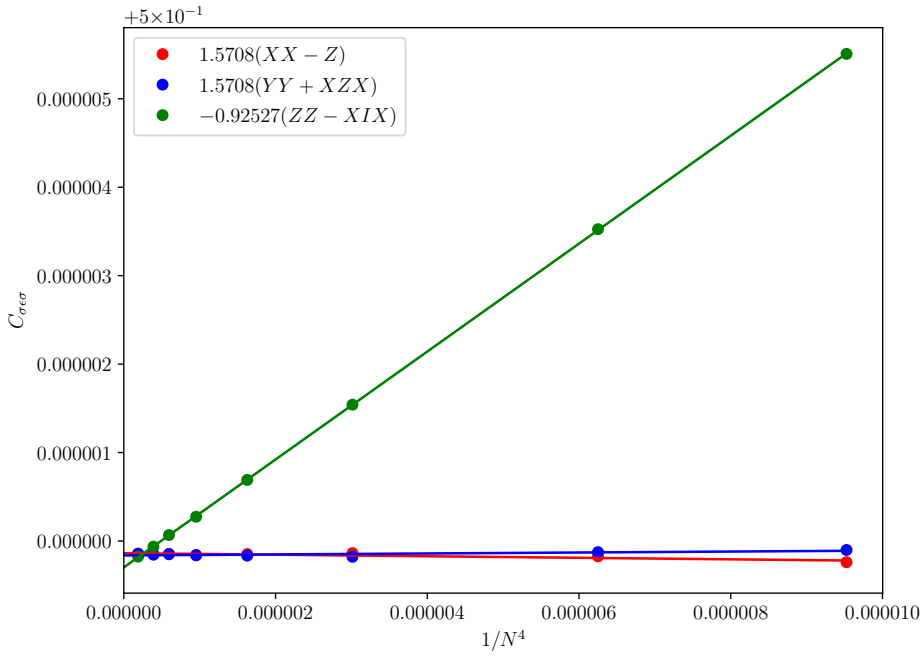

Figure 5.7: Convergence of the OPE coefficient $C_{\sigma\epsilon\sigma}$ with $\sigma^{CFT} \sim \mathcal{O}_{\epsilon 1}, \mathcal{O}_{\epsilon 2}, \mathcal{O}_{\epsilon 3}$. Sizes $18 \leq N \leq 48$ are used. Linear extrapolation with $1/N^4$ is used. The intercept of the extrapolations are approximately 0.4999999, 0.4999999 and 0.4999997 respectively. Only $\mathcal{O}_{\epsilon 3}$ has significant finite-size error in this OPE coefficient, with a slope approximately 0.61 in the extrapolation.

critical Ising model, this allows us to build lattice versions of specific CFT scaling operators. In particular, by targeting primary operators, one can compute OPE coefficients, thereby completing Cardy's program to numerically extract the conformal data from low-energy states of a critical spin chain by exploiting the operator-state correspondence. Our approach, which can be extended to address non-local scaling operators (explained in Chapter 6), has other useful applications. For instance, in a generic critical quantum spin chain one can now modify the original Hamiltonian by adding relevant (or irrelevant) scaling operators on demand. Then, using e.g. the techniques demonstrated in Section 4.3, one can study, fully non-perturbatively, the renormalization group flow away from (respectively, back to) the initial CFT, along pre-determined directions. Conversely, given a near-critical lattice Hamiltonian, one can tune it closer to criticality by removing relevant perturbations from it.

We conclude this chapter with the following table that summarizes the correspondence between lattice quantities and CFT quantities.

CFT	Lattice (at low energies)
Energy/momentum eigenstate $\|\psi_\alpha^{CFT}\rangle$	Energy/momentum eigenstate $\|\psi_\alpha\rangle$
Primary state $\|\phi_\alpha^{CFT}\rangle$	Primary state $\|\phi_\alpha\rangle$
Energy $E_\alpha^{CFT} = \frac{2\pi}{L}(\Delta_\alpha^{CFT} - c^{CFT}/12)$	Energy $E_\alpha \approx NA + \frac{B}{2\pi}E_\alpha^{CFT}$ (Eq. (4.2))
Momentum $P_\alpha^{CFT} = \frac{2\pi}{L}s_\alpha^{CFT}$	Momentum $P_\alpha = P_\alpha^{CFT}$ (Eq. (4.1))
Local operator $\mathcal{O}^{CFT} = \sum_\alpha a_\alpha \psi_\alpha^{CFT}$	Local operator $\mathcal{O}$
Fourier mode $\mathcal{O}^{CFT,s}$ (Eq. (5.4))	Fourier mode $\mathcal{O}^s$ (Eq. (5.41))
$H_n^{CFT} = L_n^{CFT} + \bar{L}_{-n}^{CFT} - c^{CFT}/12\delta_{n,0}$	H_n (Eq. (4.6))
Primary operator ϕ_β^{CFT}	Operator $\mathcal{O}_{\phi_\beta}$
$C_{\alpha\beta\gamma}^{CFT} = (2\pi/L)^{-\Delta_\beta^{CFT}}\langle\phi_\alpha^{CFT}\|\phi_\beta^{CFT,s_\alpha - s_\gamma}\|\phi_\gamma^{CFT}\rangle$	$C_{\alpha\beta\gamma} = (2\pi/N)^{-\Delta_\beta}\langle\phi_\alpha\|\mathcal{O}_{\phi_\beta}^{s_\alpha - s_\gamma}\|\phi_\gamma\rangle \approx C_{\alpha\beta\gamma}^{CFT}$

Table 5.4: Correspondence of lattice objects and CFT objects. The "$\approx$" means equal up to finite-size corrections.

Chapter 6

Anti-periodic boundary conditions and supersymmetry

In this chapter, we generalize the method of previous chapters to critical spins chains with APBC (more general twisted boundary conditions can be addressed in a similar way). We propose a systematic way of extracting complete conformal data involving scaling operators in the APBC sector. The efficient diagonalization method of low energy eigenstates is also generalized to APBC. As an application, we then extract accurate and complete conformal data for two models with APBC, namely the Ising model and the OF model. For the latter case the APBC excitations enable us to study the emergent superconformal symmetry.

More specifically, given a critical quantum spin chain with PBC and APBC, we first diagonalize the low-energy eigenstates and identify each eigenstate on the lattice with a CFT scaling operator in the continuum. In particular, primary states can their conformal towers are identified for both boundary conditions. Then we find lattice operators that correspond to CFT primary operators in the continuum limit. All OPE coefficients involving primary operators can then be extracted. Furthermore, in the case where the conformal symmetry is enhanced by supersymmetry, such as the OF model at the TCI point, we can identify generators of the extended algebra (supervirasoro algebra) on the lattice. By studying the action of supervirasoro generators on the low-energy subspace, we can identify supervirasoro primary states and supervirasoro conformal towers.

In this chapter, we first review the definition of APBC for spin chains and APBC for CFT and discuss their relations. Then we propose a systematic way of extracting conformal data based on the low energy spectrum of the spin chain with APBC, as what we did in previous chapters. In addition, we generalize the efficient diagonalization of low

energy eigenstates of a critical quantum spin chain from PBC to APBC. Then we extract conformal data from the Ising model and the OF model at the TCI point. Finally, in the OF model we construct lattice representations of superconformal generators that connect eigenstates in PBC sector and APBC sector and verify the superconformal structure of low energy excitations. This chapter is based on Ref. [142].

6.1 Anti-periodic boundary conditions (APBC)

In this section we review the definition and implications of antiperiodic boundary conditions (APBC) [18, 23, 61, 15, 1, 60] for spin chains and CFT.

6.1.1 APBC for spin chains

In contrast with PBC, which can be defined for any spin chain, the APBC is only defined for a spin chain with an on-site $\mathbb{Z}_2$ symmetry. Denote the Hamiltonian density as h_j, the lattice translation operator as $\mathcal{T}$, and the $\mathbb{Z}_2$ generator as $\prod_j \mathcal{Z}_j$, we can define a twisted translation operator as

$$\tilde{\mathcal{T}} = \mathcal{Z}_1 \mathcal{T}. \tag{6.1}$$

The Hamiltonian for APBC is

$$H^{APBC} = \sum_{j=1}^{N} \tilde{\mathcal{T}}^{j-1} h_1 \tilde{\mathcal{T}}^{\dagger j-1}, \tag{6.2}$$

which is invariant under the twisted translation $\tilde{\mathcal{T}}$. Recall that the Hamiltonian with PBC is Eq. (3.5). The Hamiltonians with both boundary conditions are invariant under the $\mathbb{Z}_2$ transformation,

$$H^{PBC} = \mathcal{Z} H^{PBC} \mathcal{Z}^\dagger. \tag{6.3}$$
$$H^{APBC} = \mathcal{Z} H^{APBC} \mathcal{Z}^\dagger. \tag{6.4}$$

Let us illustrate the APBC with two models. The first example is the critical Ising model,

$$h_{Ising,j} = -X_j X_{j+1} - Z_j, \tag{6.5}$$

The Hamiltonian with APBC is

$$H^{APBC}_{Ising} = -\sum_{j=1}^{N-1} X_j X_{j+1} - \sum_{j=1}^{N} Z_j + X_N X_1. \tag{6.6}$$

The other example is the OF model at the TCI point,

$$h_{TCI,j} = h_{Ising,j} + \lambda^*(X_jX_{j+1}Z_{j+2} + Z_jX_{j+1}X_{j+2}), \tag{6.7}$$

where $\lambda^* \approx 0.428$ is the tricritical point. It is also $\mathbb{Z}_2$ invariant under the global spin flip. The Hamiltonian with APBC is

$$\begin{aligned} H_{TCI}^{APBC} &= H_{Ising}^{APBC} + \lambda^* \sum_{j=1}^{N-2}(X_jX_{j+1}Z_{j+2} + Z_jX_{j+1}X_{j+2}) \\ &+ \lambda^*(X_{N-1}X_NZ_1 - X_NX_1Z_2) \qquad (6.8) \\ &+ \lambda^*(-Z_{N-1}X_NX_1 + Z_NX_1X_2). \qquad (6.9) \end{aligned}$$

We stress that the boundary term in the APBC Hamiltonian does not always have opposite sign to that of the PBC Hamiltonian, as is evident from Eqs. (6.8),(6.9). In a spin-1/2 chain with $\mathcal{Z}_j = Z_j$, the APBC is simply

$$\begin{aligned} X_{N+j} &= -X_j \qquad (6.10) \\ Y_{N+j} &= -Y_j \qquad (6.11) \\ Z_{N+j} &= Z_j. \qquad (6.12) \end{aligned}$$

Energy eigenstates can be labelled by eigenvalues of $H^{PBC}, \mathcal{T}, \mathcal{Z}$ in the PBC, i.e., Eq. (3.9)-(3.11). In the APBC, the eigenstates are labelled by eigenvalues of $H^{APBC}, \tilde{\mathcal{T}}, \mathcal{Z}$.

$$\begin{aligned} H^{APBC}|\psi_\alpha^{APBC}\rangle &= E_\alpha^{APBC}|\psi_\alpha^{APBC}\rangle \qquad (6.13) \\ \tilde{\mathcal{T}}|\psi_\alpha^{APBC}\rangle &= e^{iP_\alpha^{APBC}}|\psi_\alpha^{APBC}\rangle \qquad (6.14) \\ \mathcal{Z}|\psi_\alpha^{APBC}\rangle &= \mathcal{Z}_\alpha^{APBC}|\psi_\alpha^{APBC}\rangle. \qquad (6.15) \end{aligned}$$

The momenta are quantized in both cases. Denote

$$\begin{aligned} P_\alpha^{PBC} &= \frac{2\pi}{N}s_\alpha^{PBC} \qquad (6.16) \\ P_\alpha^{APBC} &= \frac{2\pi}{N}s_\alpha^{APBC}. \qquad (6.17) \end{aligned}$$

Since $\mathcal{T}^N = \mathbf{1}$ (a translation by N sites in PBC is trivial) and $\tilde{\mathcal{T}}^N = \mathcal{Z}\mathcal{T}^N = \mathcal{Z}$ (a translation by N sites in APBC amounts to a global spin flip),

$$\begin{aligned} s_\alpha^{PBC} &\in \mathbb{Z} \qquad (6.18) \\ s_\alpha^{APBC} &\in \mathbb{Z} \quad (\mathcal{Z}_\alpha^{APBC} = 1) \qquad (6.19) \\ s_\alpha^{APBC} &\in \mathbb{Z} + \frac{1}{2} \quad (\mathcal{Z}_\alpha^{APBC} = -1), \qquad (6.20) \end{aligned}$$

For critical theories, it means that the conformal spin of a $\mathbb{Z}_2$ even operator in APBC is integer but that of a $\mathbb{Z}_2$ odd operator is half integer in APBC.

6.1.2 APBC for CFT

The PBC and APBC for a conformal field theory on the cylinder are defined as

$$\Psi^{CFT}(x+L) = \pm\Psi^{CFT}(x) \tag{6.21}$$

for some fundamental field $\Psi^{CFT}(x)$, where $+$ is for PBC and $-$ is for APBC. Any field can be expanded into Fourier modes,

$$\psi_\alpha^{CFT,s} \equiv \frac{1}{L}\int_0^L dx\, \psi_\alpha^{CFT}(x) e^{isx2\pi/L}. \tag{6.22}$$

In the path integral formalism, the choice of boundary condition affects the Fourier mode of fields that enter into the partition function [23]. Therefore the boundary condition affects the operator content of the CFT.

For concretness, we will consider the case where the fundamental field $\Psi^{CFT}(x)$ is a fermionic operator. The boundary conditions $\pm$ are usually referred to as Ramond (R) [101] and Neveu-Schwarz (NS) [82], respectively.

If the field $\psi_\alpha^{CFT}(x)$ is a fermionic field, then the only nonvanishing Fourier modes have $s \in \mathbb{Z} + 1/2$ in the NS sector, and $s \in \mathbb{Z}$ in the R sector. If the field $\psi_\alpha^{CFT}(x)$ is a bosonic field (e.g. product of two fermionic fields), then the only nonvanishing Fourier modes have $s \in \mathbb{Z}$ in both NS and R sectors. As a result, the conformal spins of the scaling operators satisfy

$$s_\alpha^{CFT} \in \mathbb{Z} + \frac{1}{2} \quad (\text{NS, fermion}) \tag{6.23}$$

$$s_\alpha^{CFT} \in \mathbb{Z} \quad (\text{NS, boson}) \tag{6.24}$$

$$s_\alpha^{CFT} \in \mathbb{Z} \quad (\text{R}) \tag{6.25}$$

The similiarity of Eqs. (6.18)-(6.20) to Eqs. (6.23)-(6.25) may be explained by the Jordan-Wigner transformation, introduced in Section 5.3. Consider a Majorana fermion chain with boundary conditions,

$$\psi(2N) = \pm\psi(1), \tag{6.26}$$

which correspond to R (NS) boundary conditions, respectively. Applying Jordan-Wigner transormation Eqs. (5.63)(5.64) to Eqs. (6.10)-(6.12), we see that the R boundary condition for the fermion chain corresponds to the $\mathbb{Z}_2$ odd sector of PBC of the spin chain, and the $\mathbb{Z}_2$ even sector of APBC of the spin chain. The NS boundary condition for the fermion

chain corresponds to the $\mathbb{Z}_2$ even sector of PBC of the spin chain and the $\mathbb{Z}_2$ odd sector of APBC of the spin chain, i.e.,

$$\text{NS} = \text{PBC}(\mathcal{Z} = 1) \ + \ \text{APBC}(\mathcal{Z} = -1) \tag{6.27}$$

$$\text{R} = \text{PBC}(\mathcal{Z} = -1) \ + \ \text{APBC}(\mathcal{Z} = 1). \tag{6.28}$$

The conformal spins of scaling operators in each boundary condition, i.e., Eqs. (6.18)-(6.20) for spin chains and Eqs. (6.23)-(6.25) for fermion chains are consistent with this assignment.

6.2 Extraction of conformal data from spin chains with APBC

6.2.1 The Hilbert space

We shall first comment on the Hilbert space of the spin chain with PBC and APBC. It is clear that low energy states of PBC and APBC reside in the *same* Hilbert space on the lattice. However, the low energy states with respect to H^{PBC} are not low energy eigenstates with respect to H^{APBC} (and vice versa). Indeed the boundary defect costs $O(1)$ energy as opposed to $O(1/N)$ (Eq. (4.2)). Therefore, the low energy subspaces of PBC and APBC are orthogonal in the thermodynamic limit. This is to be expected because they correspond to different primary operators, and states in different conformal towers are orthogonal in the CFT. Later, we will call a CFT operator a (A)PBC operator if the corresponding state appears in the low-energy spectrum of the spin chain with (A)PBC.

Fourier modes of local operators can only connect low-energy states within the same boundary condition. To connect low-energy PBC states and low-energy APBC states, we need nonlocal string operators (introduced below). As a result, lattice operators that correspond to APBC scaling operators are string operators, in contrast to local operators which correspond to PBC scaling operators.

6.2.2 Scaling dimensions and conformal spins

Since Eqs. (2.52),(2.53) is still valid for the CFT [18], we expect that Eqs. (4.1),(4.2) are also valid for excitations with APBC. Therefore, scaling dimensions and conformal spins

can still be extracted by

$$\Delta_\alpha^{APBC} = 2\frac{E_\alpha^{APBC} - E_0^{PBC}}{E_T^{PBC} - E_0^{PBC}} \tag{6.29}$$

$$s_\alpha^{APBC} = \frac{N}{2\pi} P_\alpha^{APBC}. \tag{6.30}$$

The only difference from the PBC is that now s_α^{APBC} can be integer or half integer depending on the $\mathbb{Z}_2$ sector.

6.2.3 Virasoro generators

Eq. (2.57) is still valid for CFT with both boundary conditions. However, on the lattice, the boundary term of H_n should be chosen such that it respects the boundary condition. For PBC, Eq. (4.6) can be rewritten as

$$H_n^{PBC} = \frac{N}{B}\sum_{j=1}^{N} \mathcal{T}^{j-1} h_1 \mathcal{T}^{\dagger j-1} e^{inj2\pi/N}. \tag{6.31}$$

H_n^{PBC} is covariant under the translation operator of PBC,

$$\mathcal{T} H_n^{PBC} \mathcal{T}^\dagger = e^{-in2\pi/N} H_n^{PBC}. \tag{6.32}$$

For the APBC, the translation operator is $\tilde{\mathcal{T}}$. The definition of Fourier modes is changed accordingly. We can define

$$H_n^{APBC} = \frac{N}{B}\sum_{j=1}^{N} \tilde{\mathcal{T}}^{j-1} h_1 \tilde{\mathcal{T}}^{\dagger j-1} e^{inj2\pi/N}, \tag{6.33}$$

which is covariant under $\tilde{\mathcal{T}}$,

$$\tilde{\mathcal{T}} H_n^{APBC} \tilde{\mathcal{T}}^\dagger = e^{-in2\pi/N} H_n^{APBC}. \tag{6.34}$$

It is expected that

$$H_n^{APBC} \sim H_n^{CFT} = L_{-n}^{CFT} + \bar{L}_n^{CFT} - \frac{c^{CFT}}{12}\delta_{n,0} \tag{6.35}$$

for low energy states in APBC.

Note that Eq. (6.33) is a sum of local operators, and therefore it only connects low energy states within APBC in the thermodynamic limit. This is consistent with the action of Virasoro generators, since scaling operators in different boundary conditions necessarily belong to different conformal towers.

Once we have the lattice Virasoro generators, we can proceed as in the case of PBC [68, 80, 140] to identify primary and descendant states.

6.2.4 Local operators and OPE coefficients

For a general local lattice operator $\mathcal{O}_j$, we can define its Fourier modes with respect to the translation operator $\mathcal{T}$ for PBC and $\tilde{\mathcal{T}}$ for APBC as

$$\mathcal{O}^s = \frac{1}{N}\sum_{j=1}^{N} \mathcal{T}^{j-1}\mathcal{O}_1\mathcal{T}^{\dagger j-1}e^{-isj2\pi/N}, \tag{6.36}$$

which is just a rewritten form of the Eq. (5.41), and

$$\tilde{\mathcal{O}}^s = \frac{1}{N}\sum_{j=1}^{N} \tilde{\mathcal{T}}^{j-1}\mathcal{O}_1\tilde{\mathcal{T}}^{\dagger j-1}e^{-isj2\pi/N}. \tag{6.37}$$

For the latter case (APBC), s is integer if $\mathcal{O}$ is $\mathbb{Z}_2$ even, and s is half integer if $\mathcal{O}$ is $\mathbb{Z}_2$ odd.

Given a local operator $\mathcal{O}_{\phi_\beta}$ corresponding to a PBC primary field $\phi_\beta^{CFT,PBC}$, OPE coefficients can be extracted by

$$C^{PPP}_{\alpha\beta\gamma} = \left(\frac{2\pi}{N}\right)^{-\Delta_\beta^{PBC}} \langle\phi_\alpha^{PBC}|\mathcal{O}_{\phi_\beta}^{s_\alpha - s_\gamma}|\phi_\gamma^{PBC}\rangle. \tag{6.38}$$

$$C^{APA}_{\alpha\beta\gamma} = \left(\frac{2\pi}{N}\right)^{-\Delta_\beta^{PBC}} \langle\phi_\alpha^{APBC}|\tilde{\mathcal{O}}_{\phi_\beta}^{s_\alpha - s_\gamma}|\phi_\gamma^{APBC}\rangle, \tag{6.39}$$

where we have divided nonzero OPE coefficients into two classes, the first one involving only PBC primary operators (with superscript PPP), and the second one involving one PBC primary operator and two APBC primary operators (with superscript APA). The rest of combinations of operators must have vanishing OPE coefficients.

Note that in Eq. (6.39) momentum conservation automatically forces $\mathbb{Z}_2$ parity conservation. Consider, for example, the case where $\mathcal{O}$ is $\mathbb{Z}_2$ even, then $s_\alpha - s_\gamma \in \mathbb{Z}$. Then Eqs. (6.19),(6.20) imply that $|\phi_\alpha^{APBC}\rangle$ and $|\phi_\gamma^{APBC}\rangle$ neccessarily have the same parity.

For Hermitian primary operators, OPE coefficients transform in a simple way when the indices get permuted. Under an even permutation, the OPE coefficient does not change, such as $C^{CFT,PPP}_{\alpha\beta\gamma} = C^{CFT,PPP}_{\beta\gamma\alpha}$. Under an odd permutation, the OPE coefficient becomes complex conjugated, such as $C^{CFT,AAP}_{\beta\alpha\gamma} = C^{CFT,APA*}_{\alpha\beta\gamma}$. It is a nontrivial check of our method if we can also directly compute $C^{AAP}_{\beta\alpha\gamma}$ (to be defined in Eq. (6.52)) with a lattice representation of $\phi^{CFT,APBC}_{\alpha}$, which we demonstrate below.

6.2.5 String operators and OPE coefficients

A lattice representation of scaling operators in the APBC should connect the ground state (in PBC) with states in APBC. To connect states in different boundary conditions, we introduce *string operators*,

$$\mathcal{S}_{\mathcal{O},j} = \left(\prod_{n=1}^{j-1} \mathcal{Z}_n\right) \mathcal{O}_j, \tag{6.40}$$

where $\mathcal{O}$ is a local operator. Its Fourier modes are defined by

$$\mathcal{S}^s_{\mathcal{O}} = \sum_{j=1}^{N} \tilde{\mathcal{T}}^{j-1} \mathcal{O}_1 \mathcal{T}^{\dagger j-1} e^{-isj2\pi/N}, \tag{6.41}$$

where s can either be integer or half integer. Notice that we use both $\mathcal{T}$ and $\tilde{\mathcal{T}}$. If $\mathcal{O}$ is a one-site operator, then it is manifest that

$$\mathcal{S}^s_{\mathcal{O}} = \sum_{j=1}^{N} \mathcal{S}_{\mathcal{O},j} e^{-isj2\pi/N}. \tag{6.42}$$

For a multi-site operator $\mathcal{O}$, Eq. (6.42) is no longer valid. However, it is still not hard to compute all the terms in $\mathcal{S}^s_{\mathcal{O}}$ from the definition Eq. (6.41). For example,

$$\mathcal{S}^s_{YZ} = \sum_{j=1}^{N-1} e^{-isj2\pi/N} \left(\prod_{l=1}^{j-1} Z_l\right) Y_j Z_{j+1} + \mathcal{B}^s_{YZ}, \tag{6.43}$$

where

$$\mathcal{B}^s_{YZ} = e^{-is2\pi} I_1 \left(\prod_{l=2}^{N-1} Z_l\right) Y_N. \tag{6.44}$$

The covariance of Eq. (6.41) under translations is more involved. Recall that $\mathcal{S}^s_{\mathcal{O}}$ maps PBC states to APBC states. First, we can always decompose $\mathcal{S}_{\mathcal{O}}$ into $\mathbb{Z}_2$ even and $\mathbb{Z}_2$ odd parts. Therefore we will only consider $\mathcal{S}_{\mathcal{O}}$ with definite parity,

$$\mathcal{Z}\mathcal{S}_{\mathcal{O},j}\mathcal{Z}^\dagger = \mathcal{Z}_{\mathcal{O}}\mathcal{S}_{\mathcal{O},j}, \tag{6.45}$$

where $\mathcal{Z}_{\mathcal{O}} = \pm 1$ is the parity of both $\mathcal{O}$ and $\mathcal{S}_{\mathcal{O}}$. We will show that, when acting with $\mathcal{S}^s_{\mathcal{O}}$ on a PBC eigenstate $|\psi^{PBC}_\alpha\rangle$ with conformal spin s^{PBC}_α, the result is a linear combination of APBC eigenstates $|\psi^{APBC}_\beta\rangle$ with conformal spin $s^{APBC}_\beta = s + s^{PBC}_\alpha$ if and only if

$$e^{-is2\pi} = \mathcal{Z}_{\mathcal{O}}\mathcal{Z}^{PBC}_\alpha. \tag{6.46}$$

Given an operator $\mathcal{S}_{\mathcal{O}}$ with definite parity, this constrains whether s should be an integer or a half integer when acting $\mathcal{S}^s_{\mathcal{O}}$ on a PBC state.

In order to map $|\psi^{PBC}_\alpha\rangle$ to the eigenstate of $\tilde{\mathcal{T}}$, it is enough that the operator $\mathcal{S}^s_{\mathcal{O}}$ satisfies

$$\tilde{\mathcal{T}}\mathcal{S}^s_{\mathcal{O}}\mathcal{T}^\dagger|\psi^{PBC}_\alpha\rangle = e^{is2\pi/N}\mathcal{S}^s_{\mathcal{O}}|\psi^{PBC}_\alpha\rangle. \tag{6.47}$$

However, this is not manifestly true for all states $|\psi^{PBC}_\alpha\rangle$. We can explicitly compute that

$$\tilde{\mathcal{T}}\mathcal{S}^s_{\mathcal{O}}\mathcal{T}^\dagger - e^{is2\pi/N}\mathcal{S}^s_{\mathcal{O}} = e^{-is2\pi}\mathcal{Z}\mathcal{O}_1 - \mathcal{O}_1. \tag{6.48}$$

Then Eq. (6.47) is satisfied if and only if

$$e^{-is2\pi}\mathcal{Z}\mathcal{O}_1|\psi^{PBC}_\alpha\rangle = \mathcal{O}_1|\psi^{PBC}_\alpha\rangle, \tag{6.49}$$

which is equivalent to Eq. (6.46).

Similar to the case of PBC, we can relate a lattice string operator $\mathcal{S}_{\mathcal{O}}$ to a linear combination of APBC scaling operators in the CFT,

$$\mathcal{S}_{\mathcal{O}} \sim \mathcal{O}^{CFT} = \sum_\alpha a_\alpha \psi^{CFT,APBC}_\alpha \tag{6.50}$$

The variational parameters can be obtained by minimizing a similar cost function as Eq. (5.43),

$$f^{\mathcal{O}}(\{a_\alpha\}) = \sum_\beta |\langle\psi^{APBC}_\beta|\mathcal{S}^{s_\beta}_{\mathcal{O}}|0\rangle - \langle\psi^{CFT}_\beta|\mathcal{O}^{CFT,s_\beta}|0^{CFT}\rangle|^2. \tag{6.51}$$

Note that Eq. (6.46) is automatically satisfied if we choose all $|\psi^{APBC}_\beta\rangle$ to be in the correct parity sector, i.e., $\mathcal{Z}^{APBC}_\beta = \mathcal{Z}_{\mathcal{O}}$, since the ground state is always $\mathbb{Z}_2$ even and $e^{is^{APBC}_\beta 2\pi} = \mathcal{Z}^{APBC}_\beta$.

Again, Eq. (6.50) allows us to construct a lattice representation of primary fields $\phi_\beta^{CFT,APBC}$ as a string operator, denoted as $\mathcal{S}_{\phi_\beta}$. The OPE coefficients can be extracted by

$$C_{\alpha\beta\gamma}^{AAP} = \left(\frac{2\pi}{N}\right)^{-\Delta_\beta^{APBC}} \langle\psi_\alpha^{APBC}|\mathcal{S}_{\phi_\beta}^{s_\alpha - s_\gamma}|\psi_\gamma^{PBC}\rangle. \tag{6.52}$$

We conclude with a table that summarizes the correspondence between lattice objects and CFT objects for the APBC.

CFT	Lattice (at low energies)
Energy/momentum eigenstate $\|\psi_\alpha^{CFT,APBC}\rangle$	Energy/momentum eigenstate $\|\psi_\alpha^{APBC}\rangle$
Primary state $\|\phi_\alpha^{CFT,APBC}\rangle$	Primary state $\|\phi_\alpha^{APBC}\rangle$
Energy $E_\alpha^{CFT} = \frac{2\pi}{L}(\Delta_\alpha^{CFT,APBC} - c^{CFT}/12)$	Energy $E_\alpha^{APBC} \approx NA + \frac{B}{2\pi}E_\alpha^{CFT}$ (Eq. (6.29))
Momentum $P_\alpha^{CFT} = \frac{2\pi}{L}s_\alpha^{CFT,APBC}$	Momentum $P_\alpha^{APBC} = P_\alpha^{CFT}$ (Eq. (6.30))
Fourier mode of a PBC operator $\mathcal{O}^{CFT,s}$	Fourier mode $\tilde{\mathcal{O}}^s$
$H_n^{CFT} = L_n^{CFT} + \bar{L}_{-n}^{CFT} - c^{CFT}/12\delta_{n,0}$	H_n^{APBC} (Eq. (6.33))
$C_{\alpha\beta\gamma}^{APA,CFT} = (2\pi/L)^{-\Delta_\beta^{CFT}}\langle\phi_\alpha^{CFT,APBC}\|\phi_\beta^{CFT,s_\alpha - s_\gamma}\|\phi_\gamma^{CFT,APBC}\rangle$	$C_{\alpha\beta\gamma}^{APA} = (2\pi/N)^{-\Delta_\beta}\langle\phi_\alpha^{APBC}\|\tilde{\mathcal{O}}_{\phi_\beta}^{s_\alpha - s_\gamma}\|\phi_\gamma^{APBC}\rangle \approx C_{\alpha\beta\gamma}^{APA,CFT}$
APBC operator $\mathcal{O}^{CFT} = \sum_\alpha a_\alpha \psi_\alpha^{CFT,APBC}$	String operator $\mathcal{S}_\mathcal{O}$ (Eq. (6.40))
Fourier mode of an APBC operator $\mathcal{O}^{CFT,s}$	Fourier mode $\mathcal{S}_\mathcal{O}^s$ (Eq. (6.41))
APBC primary operator $\phi_\beta^{CFT,APBC}$	String operator $\mathcal{S}_{\phi_\beta}$
$C_{\alpha\beta\gamma}^{AAP,CFT} = (2\pi/L)^{-\Delta_\beta^{CFT}}\langle\phi_\alpha^{CFT,APBC}\|\phi_\beta^{CFT,s_\alpha - s_\gamma}\|\phi_\gamma^{CFT,PBC}\rangle$	$C_{\alpha\beta\gamma}^{AAP} = (2\pi/N)^{-\Delta_\beta}\langle\phi_\alpha^{APBC}\|\mathcal{S}_{\phi_\beta}^{s_\alpha - s_\gamma}\|\phi_\gamma^{PBC}\rangle \approx C_{\alpha\beta\gamma}^{AAP,CFT}$

Table 6.1: Correspondence of lattice objects and CFT objects for spin chains with APBC

6.3 puMPS techniques for APBC

In this section we will generalize the puMPS techniques to obtain low-energy eigenstates with APBC. We note that the generalization is in a sense similar to [138] where MPS is used to represent spinon excitations on an infinite line, although here we work on the circle. The generalization allows us to compute all low-energy eigenstates in APBC, as well as matrix elements of both local operators and string operators, with a computational cost that scales as $O(ND^6)$, as in the case of PBC. However, the extraction of conformal data is independent of how the low-energy states are diagonalized. Therefore, unless specifically interested in the use of puMPS, the reader may skip this section.

6.3.1 Symmetric tensors

To proceed to APBC, we first need the notion of *symmetric tensors* [111, 112, 113], which we review below.

For the spin-1/2 chain in this paper, we will use $\mathbb{Z}_2$ symmetric tensors A of the form

$$A^1 = \begin{bmatrix} A^1_{11} & 0 \\ 0 & A^1_{22} \end{bmatrix}, \quad A^2 = \begin{bmatrix} 0 & A^2_{12} \\ A^2_{21} & 0 \end{bmatrix}, \tag{6.53}$$

where each block is a $D/2 \times D/2$ matrix (more generally the two blocks can have different dimensions which add up to D). The tensor is invariant under the on-site $\mathbb{Z}_2$ symmetry up to a gauge transformation,

$$\sum_{s'} \mathcal{Z}_{ss'} A^{s'} = U_B(\mathcal{Z}) A^s U_B^\dagger(\mathcal{Z}), \tag{6.54}$$

where $\mathcal{Z}_{ss'} = Z_{ss'}$ (that is the ss' component of the Pauli matrix Z) is the representation of the $\mathbb{Z}_2$ generator on one site of the lattice ($\mathcal{Z}_j$ in Eq. (3.6)), and

$$U_B(\mathcal{Z}) = \begin{bmatrix} I_{D/2} & 0 \\ 0 & -I_{D/2} \end{bmatrix} \tag{6.55}$$

is a $D \times D$ dimensional representation of the $\mathbb{Z}_2$ generator on the bond, where $I_{D/2}$ is a $D/2$ dimensional identity matrix. Importantly, the use of $\mathbb{Z}_2$ symmetric tensors forces the puMPS to be invariant under $\mathbb{Z}_2$,

$$\mathcal{Z}|\Psi(A)\rangle = |\Psi(A)\rangle. \tag{6.56}$$

This can be seen by

$$\begin{aligned}
& \mathcal{Z}|\Psi(A)\rangle \\
= & \sum_{\vec{s}=1}^{d} \mathrm{Tr}(A^{s_1} A^{s_2} \cdots A^{s_N}) \mathcal{Z}|\vec{s}\rangle \\
= & \sum_{\vec{s}=1}^{d} \mathrm{Tr}(\mathcal{Z}_{s_1 s_1'} A^{s_1'} \mathcal{Z}_{s_2 s_2'} A^{s_2} \cdots \mathcal{Z}_{s_N s_N'} A^{s_N}) |\vec{s}\rangle \\
= & \sum_{\vec{s}=1}^{d} \mathrm{Tr}(U_B(\mathcal{Z}) A^{s_1} U_B^\dagger(\mathcal{Z}) \cdots U_B(\mathcal{Z}) A^{s_N} U_B^\dagger(\mathcal{Z})) |\vec{s}\rangle \\
= & \sum_{\vec{s}=1}^{d} \mathrm{Tr}(A^{s_1} A^{s_2} \cdots A^{s_N}) |\vec{s}\rangle \\
= & |\Psi(A)\rangle,
\end{aligned}$$

where in the third line we change the order of tensor contraction, in the fourth line we use the definition of symmetric tensors, Eq. (6.54), and in the fifth line we use the cyclic property of trace and unitarity of $U_B(\mathcal{Z})$.

The excitation ansatz can also be forced to be $\mathbb{Z}_2$ invariant by requiring that

$$\sum_{s'} \mathcal{Z}_{ss'} B^{s'} = \pm U_B(\mathcal{Z}) B^s U_B^\dagger(\mathcal{Z}), \tag{6.57}$$

where the $\pm$ represents $\mathbb{Z}_2$ even or odd excitations,

$$\mathcal{Z}|\Phi_p(B;A)\rangle = \pm|\Phi_p(B;A)\rangle. \tag{6.58}$$

The use of symmetric tensors has three advantages. First, it reduces the number of variational parameters by one half, leading to more efficient algorithms. Second, it enables us to diagonalize states separately in each symmetry sector, with the symmetry forced exactly. Third and most importantly, it allows us to write down a simple generalization of the excitation ansatz to APBC, and more generally, twisted boundary conditions.

6.3.2 puMPS for eigenstates in APBC

We propose that low energy eigenstates of critical quantum spin chains with APBC can be represented by

$$|\Phi_p^{APBC}(B;A)\rangle = \sum_{j=1}^{N} e^{-ipj} \tilde{\mathcal{T}}^j \sum_{\vec{s}=1}^{d} \mathrm{Tr}(B^{s_1} A^{s_2} \cdots A^{s_N}) |\vec{s}\rangle, \tag{6.59}$$

where A is the same tensor appearing the ground state ansatz Eq. (3.34) for the spin chain with *periodic boundary conditions*, where Eq. (6.54) can be enforced. The tensor B satisfies Eq. (6.57), where the $\pm$ determines the $\mathbb{Z}_2$ sector $\mathcal{Z} = \pm 1$ of the state. The momentum p is restricted to

$$p \in \frac{2\pi}{N}\mathbb{Z} \ (\mathcal{Z} = 1). \tag{6.60}$$

$$p \in \frac{2\pi}{N}\left(\mathbb{Z} + \frac{1}{2}\right) \ (\mathcal{Z} = -1). \tag{6.61}$$

Importantly, the explicit enforcement of $\mathbb{Z}_2$ symmetry ensures the ansatz to be translation invariant under $\tilde{\mathcal{T}}$,

$$\tilde{\mathcal{T}}|\Phi_p^{APBC}(B;A)\rangle = e^{ip}|\Phi_p^{APBC}(B;A)\rangle. \tag{6.62}$$

This can be readily seen by

$$
\begin{aligned}
& \tilde{\mathcal{T}}|\Phi_p^{APBC}(B;A)\rangle \\
= & \sum_{j=1}^{N} e^{-ipj}\tilde{\mathcal{T}}^{j+1}\sum_{\vec{s}=1}^{d}\mathrm{Tr}(B^{s_1}A^{s_2}\cdots A^{s_N})|\vec{s}\rangle \\
= & \sum_{j=2}^{N+1} e^{-ip(j-1)}\tilde{\mathcal{T}}^{j}\sum_{\vec{s}=1}^{d}\mathrm{Tr}(B^{s_1}A^{s_2}\cdots A^{s_N})|\vec{s}\rangle \\
= & e^{ip}\sum_{j=2}^{N+1} e^{-ipj}\tilde{\mathcal{T}}^{j}\sum_{\vec{s}=1}^{d}\mathrm{Tr}(B^{s_1}A^{s_2}\cdots A^{s_N})|\vec{s}\rangle \\
= & e^{ip}\left[\sum_{j=2}^{N} e^{-ipj}\tilde{\mathcal{T}}^{j}\sum_{\vec{s}=1}^{d}\mathrm{Tr}(B^{s_1}A^{s_2}\cdots A^{s_N})|\vec{s}\rangle\right. \\
& \left. + e^{-ip(N+1)}\tilde{T}^{N+1}\sum_{\vec{s}=1}^{d}\mathrm{Tr}(B^{s_1}A^{s_2}\cdots A^{s_N})|\vec{s}\rangle\right] \\
= & e^{ip}|\Phi_p(B;A)\rangle.
\end{aligned}
$$

In the last equality we have used

$$
\begin{aligned}
& e^{-ip(N+1)}\tilde{\mathcal{T}}^{N+1}\sum_{\vec{s}=1}^{d}\mathrm{Tr}(B^{s_1}A^{s_2}\cdots A^{s_N})|\vec{s}\rangle \\
= & e^{-ip}\tilde{\mathcal{T}}\left(e^{-ipN}\mathcal{Z}\sum_{\vec{s}=1}^{d}\mathrm{Tr}(B^{s_1}A^{s_2}\cdots A^{s_N})|\vec{s}\rangle\right) \\
= & \pm e^{-ipN}\left(e^{-ip}\tilde{\mathcal{T}}\sum_{\vec{s}=1}^{d}\mathrm{Tr}(B^{s_1}A^{s_2}\cdots A^{s_N})|\vec{s}\rangle\right) \\
= & e^{-ip}\tilde{\mathcal{T}}\sum_{\vec{s}=1}^{d}\mathrm{Tr}(B^{s_1}A^{s_2}\cdots A^{s_N})|\vec{s}\rangle, \qquad (6.63)
\end{aligned}
$$

where in the third line $e^{-ipN} = \pm 1$ depending on which of Eqs. (6.60),(6.61) is satisfied.

We reiterate that, given the A tensor for the PBC ground state, we use the ansatz Eq. (6.59) to represent *any* low-energy eigenstate of APBC with sufficiently low energy, including the APBC ground state. The tensor B can be determined by requiring the state to be at a saddle point of the energy functional with respect to H^{APBC}. The algorithm is

quite similar to the case of PBC and has the same numerical cost $\mathcal{O}(ND^6)$. For more details, see Appendix C.

6.4 Ising model with APBC

In this section we apply the techniques in previous sections to the critical Ising model with APBC. For completeness, we also include the study of Ising model with PBC, which is already discussed in Chapter 4 and Chapter 5.

6.4.1 Ising CFT

The Ising CFT has 3 primary operators in the PBC sector, as we have already denoted as $\mathbf{1}, \epsilon, \sigma$, and 3 primary operators in the APBC sector, denoted as $\mu, \psi, \bar{\psi}$ [18]. As we noted in Chapter 5, the Ising model can be mapped to a free Majorana fermion chain via the Jordan-Wigner transformation. Primary operators can also be classified by the boundary condition of the fermion, see Table 6.2. Under the Kramers-Wannier duality, $|\mathbf{1}\rangle, |\bar{\psi}\rangle$ are even, and $|\epsilon\rangle, |\psi\rangle$ are odd. $|\sigma\rangle$ and $|\mu\rangle$ are not eigenstates of the duality.

ϕ_α^{CFT}	Δ_α^{CFT}	s_α^{CFT}	$\mathcal{Z}_\alpha$	spin chain B.C.	fermion B.C.
$\mathbf{1}$	0	0	+	PBC	NS
ϵ	1	0	+	PBC	NS
σ	1/8	0	–	PBC	R
ψ	1/2	1/2	–	APBC	NS
$\bar{\psi}$	1/2	–1/2	–	APBC	NS
μ	1/8	0	+	APBC	R

Table 6.2: Primary fields of the Ising CFT.

There are 5 nonzero OPE coefficients [44, 52] (up to permutation of indices) that do not involve the identity operator,

$$C_{\sigma\sigma\epsilon}^{CFT} = \frac{1}{2} \tag{6.64}$$

$$C_{\mu\mu\epsilon}^{CFT} = -\frac{1}{2}, \quad C_{\bar{\psi}\psi\epsilon}^{CFT} = i \tag{6.65}$$

$$C_{\psi\mu\sigma}^{CFT} = \frac{1}{2}(1-i), \quad C_{\bar{\psi}\mu\sigma}^{CFT} = \frac{1}{2}(1+i). \tag{6.66}$$

Notice that other OPE coefficients (such as $C^{CFT}_{\sigma\sigma\sigma}, C^{CFT}_{\epsilon\epsilon\epsilon}$) vanish because otherwise they are incompatible with either $\mathbb{Z}_2$ symmetry or the Kramers-Wannier duality.

The fact that σ^{CFT} and μ^{CFT} have the same scaling dimension can be explained by the free fermion picture [14]. They are related by

$$|\mu^{CFT}\rangle = b_0^{CFT}|\sigma^{CFT}\rangle \tag{6.67}$$
$$|\sigma^{CFT}\rangle = b_0^{CFT}|\mu^{CFT}\rangle, \tag{6.68}$$

where

$$b_0^{CFT} \propto \psi^{CFT,s=0} = \frac{1}{L}\int_0^L dx\, \psi^{CFT}(x) \tag{6.69}$$

is the fermionic zero mode. In the free fermion CFT, the fermionic zero mode commutes with L_0^{CFT}. Therefore the action of b_0^{CFT} leaves the scaling dimension invariant. The fermionic zero mode is present only in the R sector of the free fermion CFT as a result of Eqs. (6.23),(6.25). Actually there is a general theorem saying that the double degeneracy is a robust feature for all Majorana fermion chains (whether free or interacting) with Kramers-Wannier self duality [64]. Later, we will see another example, namely the TCI CFT, where similar degeneracy is explained by supersymmetry.

6.4.2 Scaling dimensions, conformal spins and central charge from the Ising model

We use puMPS with bond dimension $18 \leq D \leq 44$ to diagonalize the low-energy spectrum of the Ising model with both PBC and APBC for $32 \leq N \leq 160$. For example, at $N = 64$, we use puMPS with bond dimension $D = 28$ to compute eigenstates with both boundary conditions up to $\Delta^{CFT} \leq 6 + 1/8$. The results are shown in Fig. (6.1). Comparing with the CFT spectrum, we see that all low energy eigenstates in both boundary conditions are captured. The difference from Chapter 4 is that here we have employed $\mathbb{Z}_2$ symmetric tensors.

Primary states and conformal towers are identified using the matrix elements of H_n^{PBC} and H_n^{APBC} in Eqs. (6.31),(6.33), with eigenstates in the PBC and APBC sectors, respectively. We found that the identification of conformal towers is correct for all eigenstates in the figure.

We can compute dimensions and conformal spins using Eqs.(4.4),(4.5),(6.29),(6.30) with different N, and then extrapolate the scaling dimensions to the thermodynamic limit. For example, the extrapolation for Δ_μ and Δ_ψ is shown in Fig. 6.2. Table 6.3 shows the

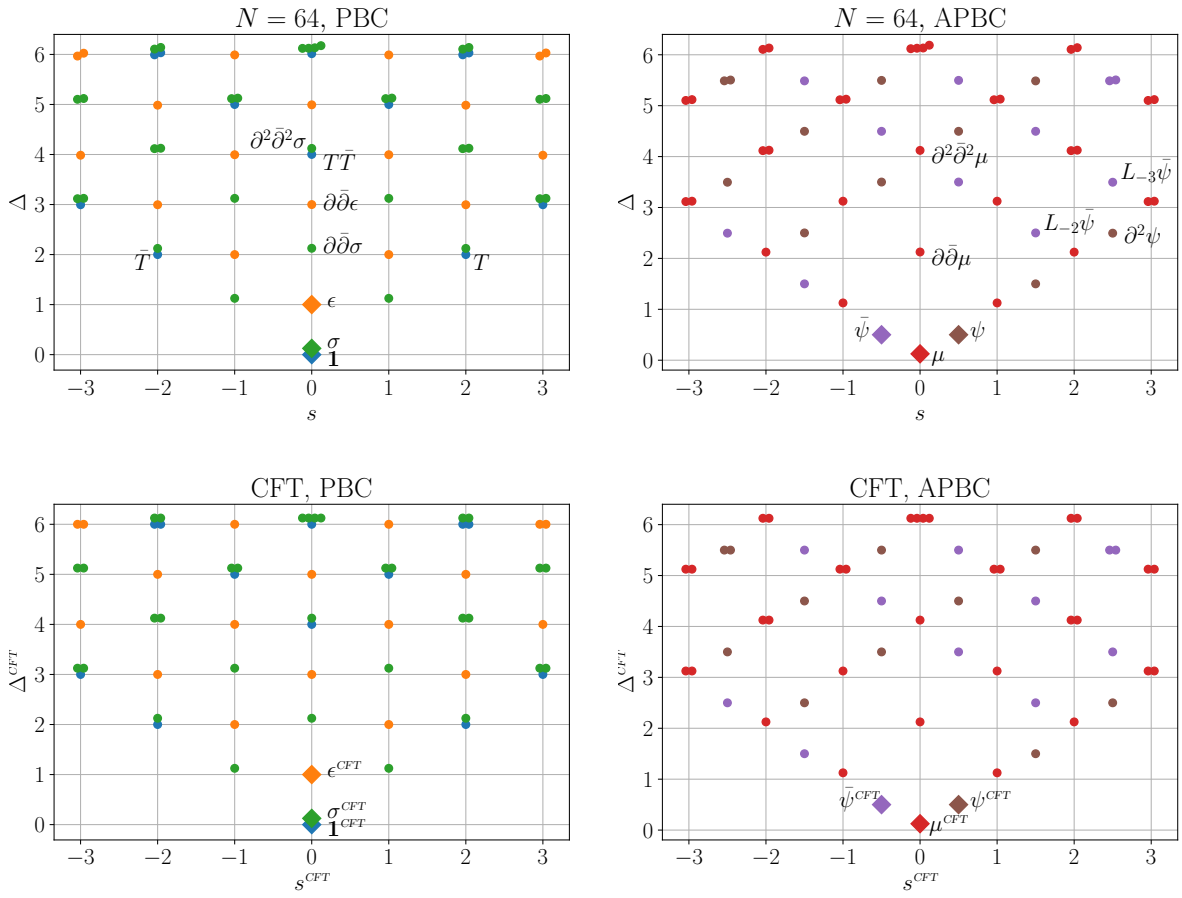

Figure 6.1: (Top two) Low-energy spectrum of the Ising model with the PBC and the APBC at $N = 64$, diagonalized using puMPS with bond dimension $D = 28$. Different colors indicate different conformal towers, with diamonds labeling the primary states. We have only shown the states with conformal spins $|s| \leq 3$. (Bottom two) The spectrum of the Ising CFT up to $\Delta^{CFT} \leq 6 + 1/8$ and $-3 \leq s^{CFT} \leq 3$.

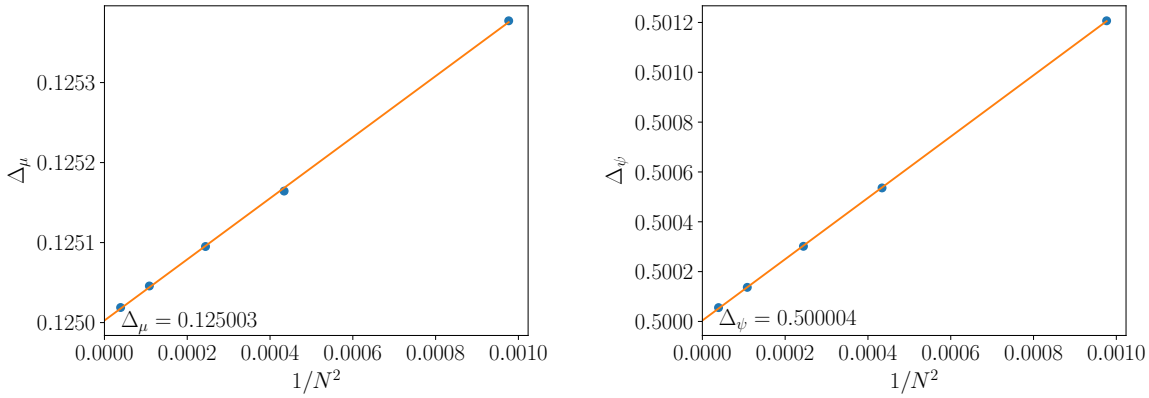

Figure 6.2: Extrapolation of the scaling dimensions Δ_μ (left) and Δ_ψ (right) for the Ising model with $32 \leq N \leq 160$.

comparison between the numerical estimations of scaling dimensions with the exact values for all primary states and several descendant states. For completeness, we also extract the central charge with Eq. (4.8).

We see that the accuracy of the scaling dimensions is better for lower-lying excited states. As explained in Chapter 4 for the case of PBC, the errors come from finite sizes and finite bond dimension, where only the former one can be reduced by finite-size extrapolation. In the above example, the finite-D error is much smaller than the finite-size error for the $|\mu\rangle$ and $|\psi\rangle$ states, as is evident from Fig. (6.2). However, for higher excited states such as $|T\bar{T}\rangle$ and $|\partial^2\bar{\partial}^2\mu\rangle$, the finite-$D$ error is comparable to the finite-size error, which makes the extrapolation not as accurate.

6.4.3 OPE coefficients from the Ising model

In order to extract the OPE coefficients, we first associate each lattice operator with a truncated expansion of scaling operators in the CFT, as Eqs. (5.39),(6.50) for local operators and string operators, respectively. For the purpose of finding the lattice primary operators for the Ising model, it is sufficient to limit the scaling operators in the expansion to the primary operators, i.e., $\mathbf{1}^{CFT}, \sigma^{CFT}, \epsilon^{CFT}$ in the PBC, and $\mu^{CFT}, \psi^{CFT}, \bar{\psi}^{CFT}$ in the APBC. The coefficients a_α can be obtained by minimizing the cost functions Eqs. (5.43),(6.51) for local operators and string operators, respectively. The cost function is specified by a set of low-energy eigenstates $|\psi_\beta\rangle$, which we choose to be the set of primary states $|\phi_\beta\rangle$ for

	Exact	puMPS	error
c	0.5	0.499996	4×10^{-6}
Δ_ϵ	1	1.000001	10^{-6}
Δ_σ	0.125	0.125005	5×10^{-6}
Δ_ψ	0.5	0.500004	4×10^{-6}
$\Delta_{\bar{\psi}}$	0.5	0.500004	4×10^{-6}
Δ_μ	0.125	0.125003	3×10^{-6}
$\Delta_{\partial\bar{\partial}\epsilon}$	3	3.00002	2×10^{-5}
$\Delta_{T\bar{T}}$	4	4.001	10^{-3}
$\Delta_{\partial\bar{\partial}\sigma}$	2.125	2.12501	10^{-5}
$\Delta_{\partial^2\bar{\partial}^2\sigma}$	4.125	4.126	10^{-3}
$\Delta_{\partial^2\psi}$	2.5	2.499995	5×10^{-6}
$\Delta_{L_{-2}\bar{\psi}}$	2.5	2.50001	10^{-5}
$\Delta_{L_{-3}\bar{\psi}}$	3.5	3.50002	2×10^{-5}
$\Delta_{\partial\bar{\partial}\mu}$	2.125	2.125003	3×10^{-6}
$\Delta_{\partial^2\bar{\partial}^2\mu}$	4.125	4.1256	6×10^{-4}

Table 6.3: Scaling dimensions from the Ising model with $32 \leq N \leq 160$.

simplicity. The CFT matrix elements in the cost function Eq. (5.43) are

$$\langle \phi_\beta^{CFT} | \phi_\alpha^{CFT,s_\beta} | 0^{CFT} \rangle = \left(\frac{2\pi}{L}\right)^{\Delta_\alpha^{CFT}} \delta_{\alpha\beta}. \tag{6.70}$$

The cost function Eq. (5.43) becomes

$$f^{\mathcal{O}}(\{a_\alpha\}) = \sum_\alpha \left| \langle \phi_\alpha | \mathcal{O}^{s_\alpha} | 0 \rangle - \left(\frac{2\pi}{N}\right)^{\Delta_\alpha^{CFT}} a_\alpha \right|^2. \tag{6.71}$$

Its minimum is achieved by

$$a_\alpha = \left(\frac{2\pi}{N}\right)^{-\Delta_\alpha^{CFT}} \langle \phi_\alpha | \mathcal{O}^{s_\alpha} | 0 \rangle. \tag{6.72}$$

Similar expressions hold for string operators, with ϕ_α APBC operators and $\mathcal{O}^s$ substituted with $\mathcal{S}^s_{\mathcal{O}}$. We will apply Eq. (6.72) to several lattice operators and extrapolate the a_α coefficients to the thermodynamic limit. The resulting expansions

$$\mathcal{O} \sim \sum_\alpha a_\alpha \phi_\alpha^{CFT} \tag{6.73}$$

for several operarors $\mathcal{O}$'s are shown in Table 6.4. We start by considering single site lattice operators $\mathcal{O}$ and add operators with larger support (two-site, etc) if they are needed to invert the expansion Eq. (6.73) to obtain a lattice representation of the primary operators. We note that the expansions Eqs. (5.1),(6.50) may also involve descendant fields, where the extra coefficients in the expansion are used to obtain improved lattice representations of primary fields. This could lead to an improvement of finite-size corrections. However, in this chapter, we will only consider the leading order in the expansions Eqs. (5.1),(6.50), which is already enough for extracting OPE coefficients.

For the Ising model, we have computed a_α's for local operators $\mathcal{O}_j = X_j, Y_j, Z_j, X_jX_{j+1}$ and string operators $\mathcal{S}_{\mathcal{O},j} = \mathcal{S}_{I,j}, \mathcal{S}_{X,j}, \mathcal{S}_{Y,j}$ with $20 \leq N \leq 96$. Note that the Y operator does not correspond to any primary field, but to the descendant $\partial_\tau \sigma^{CFT}$ in the CFT. We can then find lattice operators that correspond to CFT primary operators, listed in Table 6.4. Notice that the result is consistent with the $\mathbb{Z}_2$ symmetry and the Kramers-Wannier duality. For example, the lattice operator corresponding to $\bar{\psi}^{CFT}$ is odd under $\mathbb{Z}_2$ and even under the duality.

Lattice	CFT
X	$0.80312\sigma^{CFT}$
Y	$0.0000\sigma^{CFT}$
Z	$0.636621\mathbf{1}^{CFT} - 0.31831\epsilon^{CFT}$
XX	$0.636621\mathbf{1}^{CFT} + 0.31831\epsilon^{CFT}$
$\mathcal{S}_I$	$0.80312\mu^{CFT}$
$\mathcal{S}_X$	$0.39894\psi^{CFT} + 0.39894\overline{\psi}^{CFT}$
$\mathcal{S}_Y$	$-0.39894\psi^{CFT} + 0.39894\overline{\psi}^{CFT}$

CFT	Lattice
σ^{CFT}	$1.2451X$
ϵ^{CFT}	$1.5708XX - 1.5708Z$
μ^{CFT}	$1.2451\mathcal{S}_X$
ψ^{CFT}	$1.2533\mathcal{S}_X - 1.2533\mathcal{S}_Y$
$\overline{\psi}^{CFT}$	$1.2533\mathcal{S}_X + 1.2533\mathcal{S}_Y$

Table 6.4: Correspondence between lattice operators and CFT operators for the Ising model. (Top) Lattice operators expressed as a linear combination of a truncated set of CFT operators. (Bottom) CFT primary operators expressed as a linear combination of lattice operators by inverting the top table.

We can then use these lattice operators to compute OPE coefficients from Eqs. (6.38),(6.39).

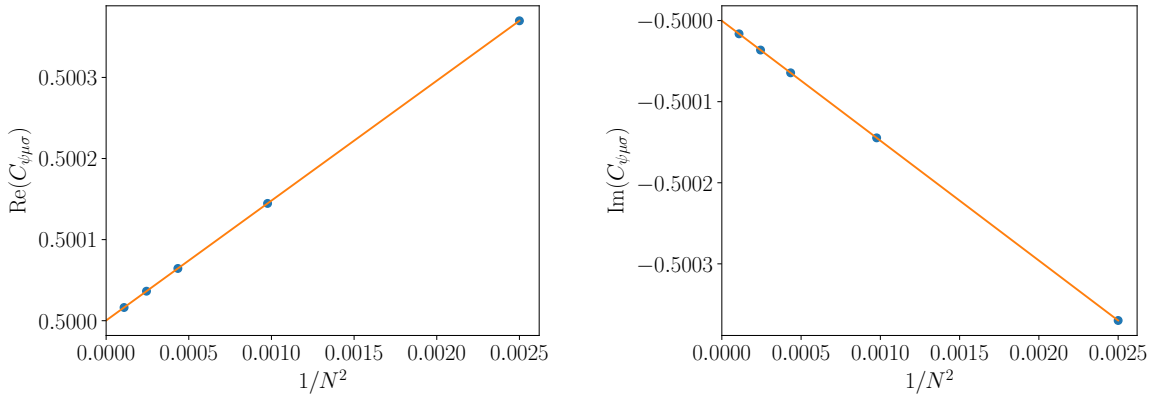

Figure 6.3: Extrapolation of the real (top) and imaginary (bottom) part of the OPE coefficient $C_{\psi\mu\sigma}$.

Again, an extrapolation to the thermodynamic limit is performed. For complex OPE coefficients, the real part and the imaginary part are extrapolated independently. The extrapolation of $C_{\psi\mu\sigma}$ is shown in Fig. (6.3) as an example.

Recall that each OPE coefficient can be computed in different ways by permuting the indices, where the second index labels the lattice primary operators and the other indices label the eigenstates. We tried all possible permutation of the indices for each nontrivial OPE coefficient of the Ising model, and the results are listed in Table 6.5. All numerical results agree with the exact results in at least 5 digits.

6.5 The O'Brien-Fendley model with APBC

In this section we apply our methods to the OF model at the tricritical point. It has a well known emergent supersymmetry combined with the conformal symmmetry [47]. In this section we will proceed as if we did not know about the emergent supersymmetry and extract complete conformal data. In the next section we will analyze the emergent supersymmetry in more detail.

OPE coefficient	Exact	Numerical
$C_{\sigma\sigma\epsilon}$	0.5	0.500001
$C_{\sigma\epsilon\sigma}$	0.5	0.500000
$C_{\mu\mu\epsilon}$	-0.5	-0.500000
$C_{\mu\epsilon\mu}$	-0.5	-0.500000
$C_{\psi\mu\sigma}$	$0.5-0.5i$	$0.500000-0.500000i$
$C_{\psi\sigma\mu}$	$0.5+0.5i$	$0.500000+0.500000i$
$C_{\mu\psi\sigma}$	$0.5+0.5i$	$0.500003+0.500003i$
$C_{\bar{\psi}\mu\sigma}$	$0.5+0.5i$	$0.500000+0.500000i$
$C_{\bar{\psi}\sigma\mu}$	$0.5-0.5i$	$0.500000-0.500000i$
$C_{\mu\bar{\psi}\sigma}$	$0.5-0.5i$	$0.500003-0.500003i$
$C_{\psi\epsilon\bar{\psi}}$	i	$1.00000i$
$C_{\bar{\psi}\psi\epsilon}$	i	$1.00001i$
$C_{\psi\bar{\psi}\epsilon}$	$-i$	$-1.00001i$

Table 6.5: OPE coefficients computed from the Ising model with $20 \leq N \leq 96$. Numerical data are kept up to 6 digits.

6.5.1 TCI CFT

The TCI CFT has 6 primary fields in the PBC sector, $\mathbf{1}, \epsilon, \epsilon', \epsilon'', \sigma, \sigma$, and 6 primary fields in the APBC sector, $\psi, \bar{\psi}, T_F, \bar{T}_F, \mu, \mu'$ [70]. Similar to the Ising CFT, we can also classify the above primary fields by the fermionic boundary conditions. The primary fields are summarized in Table 6.6. Again, operators in the NS sector can be classified with the eigenvalue under the Kramers-Wannier duality. $|\mathbf{1}\rangle, |\epsilon'\rangle, |\bar{\psi}\rangle, |T_F\rangle$ are even under the duality and $|\epsilon\rangle, |\epsilon''\rangle, |\psi\rangle, |\bar{T}_F\rangle$ are odd [70].

As in the Ising CFT, we see a double degeneracy in the R sector. The degenerate states are related to each other by a supersymmetry transformation, which we will discuss in detail in the next section.

As in the Ising model, the OPE must be consistent with the $\mathbb{Z}_2$ symmetry and the

ϕ_α^{CFT}	Δ_α^{CFT}	s_α^{CFT}	$\mathcal{Z}_\alpha$	spin chain B.C.	fermion B.C.
$\mathbf{1}$	0	0	+	PBC	NS
ϵ	1/5	0	+	PBC	NS
ϵ'	6/5	0	+	PBC	NS
ϵ''	3	0	+	PBC	NS
σ	3/40	0	–	PBC	R
σ'	7/8	0	–	PBC	R
ψ	7/10	1/2	–	APBC	NS
$\overline{\psi}$	7/10	–1/2	–	APBC	NS
T_F	3/2	3/2	–	APBC	NS
$\overline{T}_F$	3/2	–3/2	–	APBC	NS
μ	3/40	0	+	APBC	R
μ'	7/8	0	+	APBC	R

Table 6.6: Virasoro primary fields of the TCI CFT.

duality. The nonzero nontrivial ones (up to permutation of indices) are

$$\text{PBC} - \text{PBC} - \text{PBC}$$

$$C_{\epsilon\epsilon\epsilon'}^{CFT} = c_1, \quad C_{\epsilon'\epsilon'\epsilon'}^{CFT} = c_1, \quad C_{\epsilon\epsilon'\epsilon''}^{CFT} = 3/7 \tag{6.74}$$

$$C_{\sigma\sigma\epsilon}^{CFT} = 3c_1/2, \quad C_{\sigma\sigma\epsilon'}^{CFT} = c_1/4, \quad C_{\sigma\sigma\epsilon''}^{CFT} = 1/56 \tag{6.75}$$

$$C_{\sigma\sigma'\epsilon}^{CFT} = 1/2, \quad C_{\sigma\sigma'\epsilon'}^{CFT} = 3/4, \quad C_{\sigma'\sigma'\epsilon''}^{CFT} = 7/8 \tag{6.76}$$

$$\text{APBC} - \text{APBC} - \text{PBC}, \quad \mathcal{Z} = -1, -1, +1$$

$$C_{\psi\psi\epsilon}^{CFT} = C_{\bar{\psi}\bar{\psi}\epsilon'}^{CFT} = -c_1 \tag{6.77}$$

$$C_{\bar{\psi}\psi\epsilon'}^{CFT} = -ic_1, \quad C_{\bar{\psi}\psi\epsilon''}^{CFT} = 3i/7 \tag{6.78}$$

$$C_{\psi T_F\epsilon}^{CFT} = C_{\bar{\psi}\bar{T}_F\epsilon}^{CFT*} = -i\sqrt{3/7}, \quad C_{\bar{T}_F T_F\epsilon''}^{CFT} = -i \tag{6.79}$$

$$C_{\bar{\psi}T_F\epsilon'}^{CFT} = C_{\psi\bar{T}_F\epsilon'}^{CFT} = \sqrt{3/7} \tag{6.80}$$

$$\text{APBC} - \text{APBC} - \text{PBC}, \quad \mathcal{Z} = +1, -1, -1$$

$$C^{CFT}_{\mu T_F \sigma} = C^{CFT*}_{\mu \bar{T}_F \sigma} = \sqrt{1/56} e^{-i\pi/4} \tag{6.81}$$

$$C^{CFT}_{\mu' T_F \sigma'} = C^{CFT*}_{\mu' \bar{T}_F \sigma'} = \sqrt{7/8} e^{-3i\pi/4} \tag{6.82}$$

$$C^{CFT}_{\mu \psi \sigma} = C^{CFT*}_{\mu \bar{\psi} \sigma} = \sqrt{3/8} c_1 e^{-i\pi/4} \tag{6.83}$$

$$C^{CFT}_{\mu' \psi \sigma} = C^{CFT*}_{\mu' \bar{\psi} \sigma} = \sqrt{3/8} e^{-3i\pi/4} \tag{6.84}$$

$$C^{CFT}_{\mu \psi \sigma'} = C^{CFT*}_{\mu \bar{\psi} \sigma'} = \sqrt{3/8} e^{-3i\pi/4} \tag{6.85}$$

$$\text{APBC} - \text{APBC} - \text{PBC}, \quad \mathcal{Z} = +1, +1, +1$$

$$C^{CFT}_{\mu\mu\epsilon} = -3c_1/2, \; C^{CFT}_{\mu\mu\epsilon'} = c_1/4, \; C^{CFT}_{\mu\mu\epsilon''} = -1/56 \tag{6.86}$$

$$C^{CFT}_{\mu'\mu\epsilon} = -1/2, \; C^{CFT}_{\mu'\mu\epsilon'} = 3/4, \; C^{CFT}_{\mu'\mu'\epsilon''} = -7/8, \tag{6.87}$$

where

$$c_1 = \frac{2}{3}\sqrt{\frac{\Gamma(4/5)\Gamma^3(2/5)}{\Gamma(1/5)\Gamma^3(3/5)}} \approx 0.61030. \tag{6.88}$$

OPE coefficients involving APBC operators are generally complex. Their phases depend on the convention of the normalization of scaling operators. Here we have chosen the convention such that they match the lattice calculations below.

6.5.2 Scaling dimensions, conformal spins and central charge from the TCI model

We use puMPS with bond dimension $20 \leq D \leq 44$ to diagonalize the low-energy spectrum of the TCI model with both boundary conditions for $20 \leq N \leq 80$. Similar to the Ising model, we plot the low-energy eigenstates up to scaling dimension $\Delta^{CFT} \leq 3.2$ for the PBC and $\Delta^{CFT} \leq 2.7$ for the APBC. The result is shown in Fig. 6.4. We also see that all eigenstates corresponding to the CFT scaling operators in this range are captured by the puMPS ansatz.

Again, scaling dimensions and the central charge can be extracted with an extrapolation to the thermodynamic limit. The result is shown in Table 6.7. For simplicity we only show the scaling dimensions of the primary states. We see the error occurs after 3 significant digits, which roughly agrees with the accuracy of the tricritical point λ^* in Eq. (6.7).

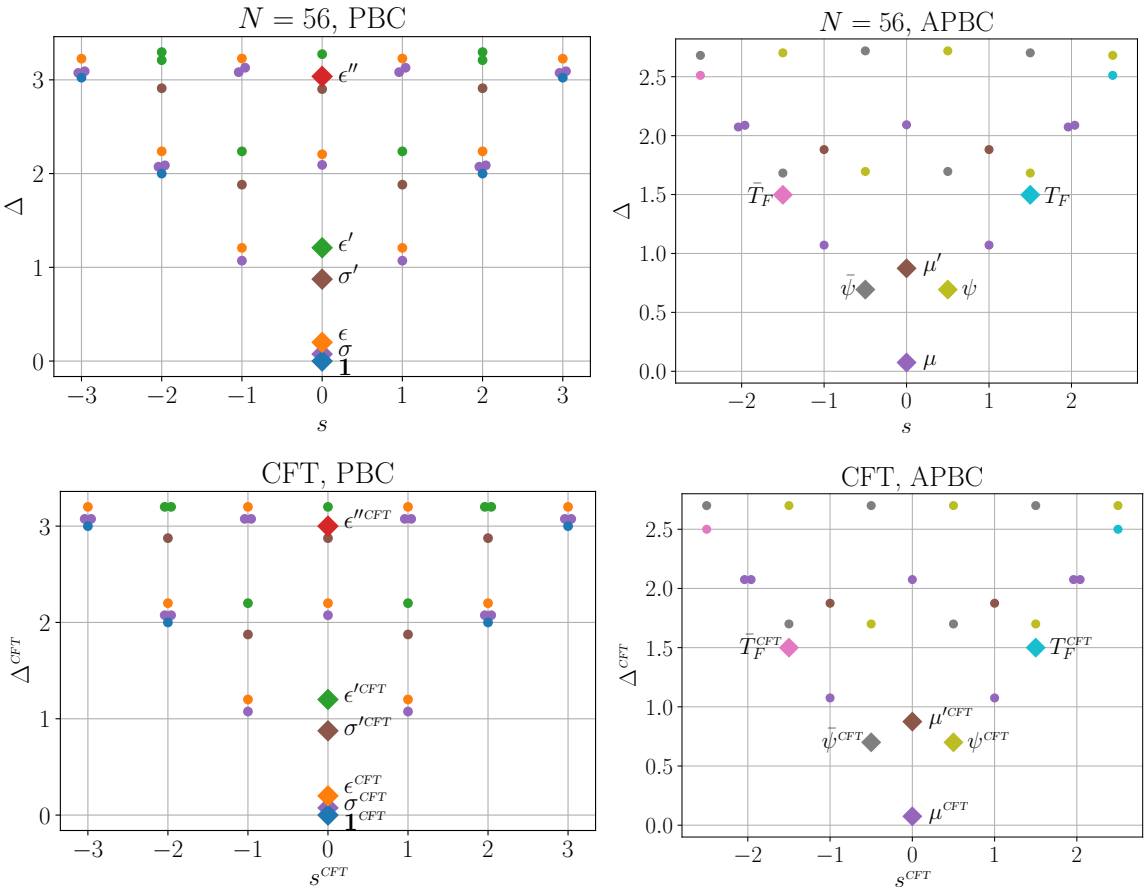

Figure 6.4: (Top two) Low-energy spectrum of the TCI model with PBC and APBC at $N = 56$, diagonalized using puMPS with bond dimension $D = 36$. Different colors indicate different conformal towers, with diamonds labeling the primary states. The exceptions are that the $\sigma(\sigma')$ and $\mu(\mu')$ towers are plotted with the same color. (Bottom two) The spectrum of the TCI CFT up to $\Delta^{CFT} \leq 3.2$ for PBC and $\Delta^{CFT} \leq 2.7$ for APBC.

	Exact	puMPS	error
c	0.7	0.6987	1.3×10^{-3}
Δ_ϵ	0.2	0.2002	2×10^{-4}
$\Delta_{\epsilon'}$	1.2	1.203	3×10^{-3}
$\Delta_{\epsilon''}$	3	3.006	6.0×10^{-3}
Δ_σ	0.075	0.07493	7×10^{-5}
$\Delta_{\sigma'}$	0.875	0.8748	2×10^{-4}
Δ_ψ	0.7	0.6979	2.1×10^{-3}
$\Delta_{\bar{\psi}}$	0.7	0.6979	2.1×10^{-3}
Δ_{T_F}	1.5	1.500	1×10^{-4}
$\Delta_{\bar{T}_F}$	1.5	1.500	1×10^{-4}
Δ_μ	0.075	0.07493	7×10^{-5}
$\Delta_{\mu'}$	0.875	0.8748	2×10^{-4}

Table 6.7: Scaling dimensions from the TCI model. All numerical values are extrapolated using $40 \leq N \leq 80$, except $\Delta_{\epsilon''}$ where we use $20 \leq N \leq 56$. All numerical values are kept to 4 significant digits.

6.5.3 OPE coefficients from the TCI model

Following the general prescription in Section II and IV, we first need to construct lattice operators corresponding to CFT primary fields variationally. Here we choose to compute lattice representations of $\epsilon, \epsilon', \sigma, \sigma', \mu, \mu', \psi, \bar{\psi}, T_F, \bar{T}_F$. These operators correspond to $\Delta_\alpha^{CFT} \leq 1.2$ in the PBC sector and $\Delta_\alpha^{CFT} \leq 1.5$ in the APBC sector. Notice that we will not construct the lattice operator for ϵ'' with $\Delta_{\epsilon''}^{CFT} = 3$ because it is numerically difficult. The reason is that it requires a linear combination of many lattice operators with fine-tuned coefficients such that all contributions with lower scaling dimensions vanish. With an extrapolation of the finite-size a_α's, we obtain the results listed in Table 6.8.

We can then work out all OPE coefficients $C_{\alpha\beta\gamma}$ where $\phi_\beta \neq \epsilon''$ with Eqs. (6.38),(6.39). For those OPE coefficients that are related by permuting indices, we will only show one particular order of indices for simplicity, e.g., we will compute $C_{\sigma\sigma\epsilon}$ but not $C_{\sigma\epsilon\sigma}$. With indices appropriately permuted, only the computation of $C_{\epsilon''\epsilon''\epsilon''}$ requires a lattice operator for ϵ'', but we know $C^{CFT}_{\epsilon''\epsilon''\epsilon''}$ vanishes because ϵ'' is odd under Kramers-Wannier duality. Therefore in this case we can still extract a complete set of nonvanishing OPE coefficients, see Tables 6.9, 6.10.

Lattice	CFT
X	$0.7808\sigma^{CFT} - 0.1866\sigma'^{CFT}$
$XZ + ZX$	$0.3551\sigma^{CFT} - 0.9060\sigma'^{CFT}$
Z	$0.5821\mathbf{1}^{CFT} - 0.4753\epsilon^{CFT} - 0.1760\epsilon'^{CFT}$
XX	$0.5821\mathbf{1}^{CFT} + 0.4753\epsilon^{CFT} - 0.1760\epsilon'^{CFT}$
$\mathcal{S}_I$	$0.7808\mu^{CFT} - 0.1866\mu'^{CFT}$
$\mathcal{S}_{XX} - \mathcal{S}_{YY}$	$0.3551\mu^{CFT} - 0.9060\mu'^{CFT}$
$\mathcal{S}_X$	$0.4042(\psi^{CFT} + \bar{\psi}^{CFT}) + 0.2462(T_F^{CFT} + \bar{T}_F^{CFT})$
$\mathcal{S}_Y$	$-0.4042(\psi^{CFT} - \bar{\psi}^{CFT}) + 0.2462(T_F^{CFT} - \bar{T}_F^{CFT})$
$\mathcal{S}_{IX}$	$0.4695(\psi^{CFT} + \bar{\psi}^{CFT}) + 0.0829(T_F^{CFT} + \bar{T}_F^{CFT})$
$\mathcal{S}_{YZ}$	$-0.4695(\psi^{CFT} - \bar{\psi}^{CFT}) + 0.0829(T_F^{CFT} - \bar{T}_F^{CFT})$

CFT	Lattice
σ^{CFT}	$1.413X - 0.2910(XZ + ZX)$
σ'^{CFT}	$0.5539X - 1.218(XZ + ZX)$
ϵ^{CFT}	$1.052XX - 1.052Z$
ϵ'^{CFT}	$3.307I - 2.841XX - 2.841Z$
μ^{CFT}	$1.413\mathcal{S}_I - 0.2910(\mathcal{S}_{XX} - \mathcal{S}_{YY})$
μ'^{CFT}	$0.5539\mathcal{S}_I - 1.218(\mathcal{S}_{XX} - \mathcal{S}_{YY})$
ψ^{CFT}	$-0.5072(\mathcal{S}_X - \mathcal{S}_Y) + 1.506(\mathcal{S}_{IX} - \mathcal{S}_{YZ})$
$\bar{\psi}^{CFT}$	$-0.5072(\mathcal{S}_X + \mathcal{S}_Y) + 1.506(\mathcal{S}_{IX} + \mathcal{S}_{YZ})$
T_F^{CFT}	$2.860(\mathcal{S}_X + \mathcal{S}_Y) - 2.462(\mathcal{S}_{IX} + \mathcal{S}_{YZ})$
$\bar{T}_F^{CFT}$	$2.860(\mathcal{S}_X - \mathcal{S}_Y) - 2.462(\mathcal{S}_{IX} - \mathcal{S}_{YZ})$

Table 6.8: Correspondence between lattice operators and CFT operators for the O'Brien-Fendley model. (Top) Correspondence between some lattice operators and a linear combination of CFT primary operators. We have neglected the contribution from the ϵ''^{CFT} operator because it has a larger scaling dimension and contributes to higher order in $1/N$ in all matrix elements. (Bottom) Lattice operators that correspond to CFT primary operators (except ϵ''^{CFT}), obtained by inverting the top table.

OPE coefficient	Exact	Numerical
$C_{\sigma\sigma\epsilon}$	0.9155	0.9154
$C_{\sigma\sigma\epsilon'}$	0.1526	0.1531
$C_{\sigma\sigma\epsilon''}$	0.0179	0.0177
$C_{\sigma'\sigma\epsilon}$	0.5	0.5007
$C_{\sigma'\sigma\epsilon'}$	0.75	0.752
$C_{\sigma'\sigma'\epsilon''}$	0.875	0.869
$C_{\epsilon\epsilon\epsilon'}$	0.610	0.608
$C_{\epsilon'\epsilon\epsilon''}$	0.429	0.437
$C_{\epsilon'\epsilon'\epsilon'}$	0.61	0.58

OPE coefficient	Exact	Numerical
$C_{\psi T_F\epsilon}$	$-0.655i$	$-0.662i$
$C_{\bar{\psi}T_F\epsilon'}$	0.655	0.664
$C_{\bar{T}_F T_F\epsilon''}$	$-i$	$-0.03-1.02i$
$C_{\bar{\psi}\bar{T}_F\epsilon}$	$0.655i$	$0.662i$
$C_{\psi\bar{T}_F\epsilon'}$	0.655	0.664
$C_{\psi\psi\epsilon'}$	-0.610	-0.613
$C_{\bar{\psi}\bar{\psi}\epsilon'}$	-0.610	-0.613
$C_{\bar{\psi}\psi\epsilon}$	$0.610i$	$0.612i$
$C_{\bar{\psi}\psi\epsilon''}$	$0.43i$	$0.01+0.41i$

Table 6.9: OPE coefficients of the TCI CFT computed from the TCI model. The organization of the table follows the exact results listed before. All numerical results are kept to the last significant digits, and the exact results are shown with the same number of significant digit. All OPE coefficients involving ϵ'' are extrapolated with data from $20 \leq N \leq 56$, while those not involving ϵ'' are extrapolated with data from $32 \leq N \leq 72$.

OPE coefficient	Exact	Numerical
$C_{\mu T_F\sigma}$	$0.094-0.094i$	$0.097-0.097i$
$C_{\mu\bar{T}_F\sigma}$	$0.094+0.094i$	$0.097+0.097i$
$C_{\mu' T_F\sigma'}$	$-0.661+0.661i$	$-0.669+0.669i$
$C_{\mu'\bar{T}_F\sigma'}$	$-0.661-0.661i$	$-0.669-0.669i$
$C_{\mu\psi\sigma}$	$0.265-0.265i$	$0.264-0.264i$
$C_{\mu\psi\sigma'}$	$-0.433+0.433i$	$-0.434+0.434i$
$C_{\mu'\psi\sigma}$	$-0.433+0.433i$	$-0.434+0.434i$
$C_{\mu\bar{\psi}\sigma}$	$0.264+0.264i$	$0.264+0.264i$
$C_{\mu'\bar{\psi}\sigma}$	$-0.433-0.433i$	$-0.434-0.434i$
$C_{\mu'\bar{\psi}\sigma}$	$-0.433-0.433i$	$-0.434-0.434i$

OPE coefficient	Exact	Numerical
$C_{\mu\mu\epsilon}$	-0.9154	-0.9153
$C_{\mu\mu\epsilon'}$	0.1526	0.1532
$C_{\mu\mu\epsilon''}$	-0.0179	-0.0172
$C_{\mu'\mu\epsilon}$	-0.5	-0.5008
$C_{\mu'\mu\epsilon'}$	0.75	0.752
$C_{\mu'\mu'\epsilon''}$	-0.875	-0.86

Table 6.10: OPE coefficients of the TCI CFT computed from the TCI model (continued).

6.6 Emergence of superconformal symmetry

In this section we study the emergent superconformal symmetry in the TCI model. We first review the $\mathcal{N}=1$ superconformal algebra. We then show how to find the lattice operators that correspond to supervirasoro generators. We verify the action of the supervirasoro generators on low energy subspaces of the TCI model with both PBC and APBC. Some matrix elements are checked quantitatively with analytical results. In particular, a formula analogous to Eq. (4.8) for the central charge is proposed and checked numerically.

6.6.1 $\mathcal{N}=1$ supersymmetry and the OF model

The $\mathcal{N}=1$ supersymmetry for $1+1$ dimensional quantum field theories is defined with two *supercharges* Q^{QFT} and $\bar{Q}^{QFT}$ which satisfy

$$Q^{QFT\dagger} = Q^{QFT} \tag{6.89}$$
$$\bar{Q}^{QFT\dagger} = \bar{Q}^{QFT} \tag{6.90}$$
$$[Q^{QFT}, \bar{Q}^{QFT}] = 0 \tag{6.91}$$
$$H^{QFT} = (Q^{QFT})^2 + (\bar{Q}^{QFT})^2. \tag{6.92}$$

The supercharges are fermionic operators. They map bosonic excitations into fermionic excitations and vice versa.

Each supercharge is associated with a *supercurrent*, $T_F^{QFT}, \bar{T}_F^{QFT}$, which are the density of the supercharges,

$$Q^{QFT} = \int dx\, T_F^{QFT}(x), \quad \bar{Q}^{QFT} = \int dx\, \bar{T}_F^{QFT}(x). \tag{6.93}$$

For a lattice model which flows into a supersymmetric quantum field theory, such as the TCI model Eq. (6.7), the lattice version of Eqs. (6.91),(6.92) may not be exact. As pointed out by O'brien and Fendley [83], the TCI Hamiltonian with density Eq. (6.7) can be expressed as

$$H_{TCI} = Q^2 + \bar{Q}^2 + E_0, \tag{6.94}$$

where E_0 is an energy shift, and

$$Q = \sum_j T_{F,j} \tag{6.95}$$
$$\bar{Q} = \sum_j \bar{T}_{F,j}, \tag{6.96}$$

where

$$T_F \propto (\mathcal{S}_X + \mathcal{S}_Y) - 2\lambda^*(\mathcal{S}_{YZ} + \mathcal{S}_{IX}), \tag{6.97}$$
$$\bar{T}_F \propto (\mathcal{S}_X - \mathcal{S}_Y) + 2\lambda^*(\mathcal{S}_{YZ} - \mathcal{S}_{IX}). \tag{6.98}$$

It is simple to check that Q and $\bar{Q}$ are Hermitian but $[Q, \bar{Q}] \neq 0$. Therefore, supersymmetry is not exact on the lattice. However, it has been shown numerically [83] that, under the RG flow, not only Q and $\bar{Q}$ flow to the supercharges, but also T_F and $\bar{T}_F$ flow to the supersymmetry currents. In the previous section, we have variationally found $T_{F,j}$ and $\bar{T}_{F,j}$ (Table 6.8) without exploiting Eq. (6.94),

$$T_F = 2.86[(\mathcal{S}_X + \mathcal{S}_Y) - 0.861(\mathcal{S}_{YZ} + \mathcal{S}_{IX})], \tag{6.99}$$
$$\bar{T}_F = 2.86[(\mathcal{S}_X - \mathcal{S}_Y) + 0.861(\mathcal{S}_{YZ} - \mathcal{S}_{IX})]. \tag{6.100}$$

They agree quantitatively with Eqs. (6.97),(6.98) up to normalization, with the error in the third digit.

We also note that in [83] the lattice operators corresponding to ψ^{CFT} and $\bar{\psi}^{CFT}$ were also proposed,

$$\psi \propto (\mathcal{S}_X - \mathcal{S}_Y) - 2\lambda^*(\mathcal{S}_{YZ} - \mathcal{S}_{IX}), \tag{6.101}$$
$$\bar{\psi} \propto (\mathcal{S}_X + \mathcal{S}_Y) + 2\lambda^*(\mathcal{S}_{YZ} + \mathcal{S}_{IX}). \tag{6.102}$$

In this paper we obtain a very different coefficient between the two terms (see Table 6.8). However, the two results do not contradict each other. They both correspond to $\psi^{CFT}(\bar{\psi}^{CFT})$ as the leading contribution, but our result also eliminates the contribution from $T_F^{CFT}, \bar{T}_F^{CFT}$. In this sense, we provide an improved lattice operator corresponding to ψ^{CFT} (as well as $\bar{\psi}^{CFT}$).

6.6.2 The superconformal algebra

If conformal symmetry is enhanced by the supersymmetry, the resulting quantum field theory is a *superconformal* field theory (SCFT). In a SCFT, the supercurrent $T_F^{CFT}(\bar{T}_F^{CFT})$ are Virasoro primary fields with conformal dimensions $(3/2, 0)$ and $(0, 3/2)$, respectively. Expanding T_F^{CFT} in Fourier modes gives *supervirasoro generators*

$$G_n^{CFT} = \left(\frac{2\pi}{L}\right)^{-1/2} \int_0^L dx\, T_F^{CFT}(x) e^{inx2\pi/L}. \tag{6.103}$$

Together with L_n^{CFT}, they satisfy the superconformal algebra

$$[L_n^{CFT}, L_m^{CFT}] = (n-m)L_{n+m}^{CFT} + \frac{c^{CFT}}{12} n(n^2-1)\delta_{n+m,0} \tag{6.104}$$

$$[L_n^{CFT}, G_m^{CFT}] = \left(\frac{1}{2}n - m\right) G_{n+m}^{CFT} \tag{6.105}$$

$$\{G_n^{CFT}, G_m^{CFT}\} = 2L_{n+m}^{CFT} + \frac{c^{CFT}}{3}\left(n^2 - \frac{1}{4}\right)\delta_{n+m,0}, \tag{6.106}$$

where the first identity is the Virasoro algebra, the second identity follows from the fact that T_F^{CFT} is a primary field with conformal dimensions $(3/2, 0)$, and the third identity is the crucial feature of a supersymmetric theory that the anticommutator of two supersymmetry generators yields the generator of a spacetime transformation. Analogous to the Virasoro algebra, there is a copy of the same superconformal algebra for the anti-holomorphic generators $\bar{L}_n^{CFT}, \bar{G}_m^{CFT}$. Since T_F^{CFT} is a fermionic field, it follows from Eqs. (6.23)(6.25) that $m \in \mathbb{Z} + 1/2$ for the NS boundary condition, and $m \in \mathbb{Z}$ for the R boundary condition. The corresponding superconformal algebras are called the NS algebra and the R algebra, respectively.

Let us analyze the action of the supervirasoro generators in more detail. First, let $n = 0$ in Eq. (6.105). We obtain

$$[L_0^{CFT}, G_m^{CFT}] = -mG_m^{CFT}, \tag{6.107}$$

which means that G_m^{CFT} changes the holomorphic dimension by $-m$. Therefore, G_m^{CFT} with $m < 0$ is a raising operator, whereas with $m > 0$ a lowering operator. A superconformal primary state $|\Phi_\alpha^{CFT}\rangle$ is defined by

$$L_n^{CFT}|\Phi_\alpha^{CFT}\rangle = 0, \quad G_m^{CFT}|\Phi_\alpha^{CFT}\rangle = 0, \ (n, m > 0) \tag{6.108}$$

$$\bar{L}_n^{CFT}|\Phi_\alpha^{CFT}\rangle = 0, \quad \bar{G}_m^{CFT}|\Phi_\alpha^{CFT}\rangle = 0, \ (n, m > 0). \tag{6.109}$$

By virtue of Eqs. (6.104),(6.105), the above equalities hold for all $n > 0, m > 0$ if they hold for $n = 1, 2$ and $m = 1/2, 3/2$ for the NS algebra (or $m = 1$ for the R algebra).

In the R algebra, G_0^{CFT} needs more attention. First, Eq. (6.106) implies

$$(G_0^{CFT})^2 = L_0^{CFT} - \frac{c^{CFT}}{24}. \tag{6.110}$$

Then, the Hamiltonian can be written as

$$H^{CFT} = \frac{2\pi}{L}((G_0^{CFT})^2 + (\bar{G}_0^{CFT})^2), \tag{6.111}$$

which follows from Eq. (2.52). We see that G_0^{CFT} and $\bar{G}_0^{CFT}$ are proportional to supercharges, in accordance with Eqs. (6.92),(6.103). Second, G_0^{CFT} commutes with L_0^{CFT}. This means that $G_0|\Phi_\alpha^{CFT}\rangle$, if non-vanishing, has the same conformal dimensions as $|\Phi_\alpha^{CFT}\rangle$. Eq. (6.110) implies that $G_0|\Phi_\alpha^{CFT}\rangle$ is nonvanishing if

$$h_\alpha^{CFT} \neq \frac{c^{CFT}}{24}. \tag{6.112}$$

If this is true for some supervirasoro primary state in the R sector, the supervirasoro primary state is at least double degenerate. As a result, all descendant states will also be at least double degenerate. In this case the supersymmetry is said to be spontaneously broken [47]. We have seen that indeed there is a double degeneracy for each state in the R sector of the TCI model, one in the PBC of the spin chain and the other in the APBC of the spin chain.

6.6.3 Supervirasoro primary states in the TCI CFT

As noted in the previous section, there are 12 Virasoro primary states in the TCI CFT, where 8 of them are in the NS sector and 4 of them are in the R sector. In the R sector, all Virasoro primary states are also supervirasoro primary states. $\sigma^{CFT}(\sigma'^{CFT})$ is the superpartner of $\mu^{CFT}(\mu'^{CFT})$. They are related by the supercharge $Q^{CFT} \propto G_0^{CFT}$,

$$G_0^{CFT}|\sigma^{CFT}\rangle = a_\sigma|\mu^{CFT}\rangle \tag{6.113}$$
$$G_0^{CFT}|\sigma'^{CFT}\rangle = a_{\sigma'}|\mu'^{CFT}\rangle, \tag{6.114}$$

where

$$a_\alpha = \sqrt{h_\alpha^{CFT} - \frac{c^{CFT}}{24}}, \tag{6.115}$$

by virtue of Eq. (6.110), where $h_\sigma^{CFT} = 3/80$, $h_{\sigma'}^{CFT} = 7/16$, $c^{CFT} = 7/10$.

In the NS sector, only $\mathbf{1}^{CFT}$ and ϵ^{CFT} are superconformal primary states. The rest of virasoro primary states are connected to the supervirasoro primary states by the G_m^{CFT}, shown in Fig. 6.5. The matrix elements are

$$\langle\psi^{CFT}|G_{-1/2}^{CFT}|\epsilon^{CFT}\rangle = \langle\bar{\psi}^{CFT}|\bar{G}_{-1/2}^{CFT}|\epsilon^{CFT}\rangle = a_\epsilon \tag{6.116}$$
$$\langle\epsilon'^{CFT}|G_{-1/2}^{CFT}|\bar{\psi}^{CFT}\rangle = \langle\epsilon'^{CFT}|\bar{G}_{-1/2}^{CFT}|\psi^{CFT}\rangle = a_\epsilon \tag{6.117}$$
$$\langle T_F^{CFT}|G_{-3/2}^{CFT}|0^{CFT}\rangle = \langle\bar{T}_F^{CFT}|\bar{G}_{-3/2}^{CFT}|0^{CFT}\rangle = a_{\mathbf{1}} \tag{6.118}$$
$$\langle\epsilon''^{CFT}|G_{-3/2}^{CFT}|\bar{T}_F^{CFT}\rangle = \langle\epsilon''^{CFT}|\bar{G}_{-3/2}^{CFT}|T_F^{CFT}\rangle = a_{\mathbf{1}}, \tag{6.119}$$

where $a_\epsilon = \sqrt{2h_\epsilon^{CFT}} = 1/\sqrt{5}$ and $a_{\mathbf{1}} = \sqrt{2c^{CFT}/3} = \sqrt{7/15}$. These matrix elements indicate that $|\psi^{CFT}\rangle, |\bar{\psi}^{CFT}\rangle, |\epsilon'^{CFT}\rangle$ are supervirasoro descendants of $|\epsilon^{CFT}\rangle$, and $|T_F^{CFT}\rangle, |\bar{T}_F^{CFT}\rangle, |\epsilon''^{CFT}\rangle$ are supervirasoro descendants of $|\mathbf{1}^{CFT}\rangle$.

Let us derive Eqs. (6.116)-(6.119) with the supervirasoro algebra. Superscript $_{CFT}$ is omitted in the following proof. First, Eq. (6.118)

$$
\begin{aligned}
& |\langle T_F|G_{-3/2}|0\rangle|^2 && (6.120)\\
=\ & \langle 0|G_{3/2}G_{-3/2}|0\rangle && (6.121)\\
=\ & \langle 0|\{G_{3/2}, G_{-3/2}\}|0\rangle && (6.122)\\
=\ & \frac{2c}{3}, && (6.123)
\end{aligned}
$$

where in the second line we use the fact that $G_{-3/2}$ acting on the ground state only gives the $|T_F\rangle$ state, in the third line we use the fact that $G_{3/2}$ annihilates the ground state, and in the last line we use the supervirasoro algebra and that L_0 annihilates the ground state. We can choose the phase of G_n such that

$$
\langle T_F|G_{-3/2}|0\rangle = \sqrt{\frac{2c}{3}}. \tag{6.124}
$$

Similar calculation can be performed on other matrix elements. For example, in the NS sector we can compute

$$
\begin{aligned}
& |\langle \psi|G_{-1/2}|\epsilon\rangle|^2 && (6.125)\\
=\ & \langle \epsilon|G_{1/2}G_{-1/2}|\epsilon\rangle && (6.126)\\
=\ & \langle \epsilon|\{G_{1/2}, G_{-1/2}\}|\epsilon\rangle && (6.127)\\
=\ & \langle \epsilon|2L_0|\epsilon\rangle && (6.128)\\
=\ & \Delta_\epsilon + s_\epsilon && (6.129)\\
=\ & 0.2 && (6.130)
\end{aligned}
$$

and

$$
\begin{aligned}
& |\langle \epsilon'|\bar{G}_{-1/2}|\psi\rangle|^2 && (6.131)\\
=\ & \langle \psi|\bar{G}_{1/2}\bar{G}_{-1/2}|\psi\rangle && (6.132)\\
=\ & \langle \psi|2\bar{L}_0|\psi\rangle && (6.133)\\
=\ & \Delta_\psi - s_\psi && (6.134)\\
=\ & 0.2. && (6.135)
\end{aligned}
$$

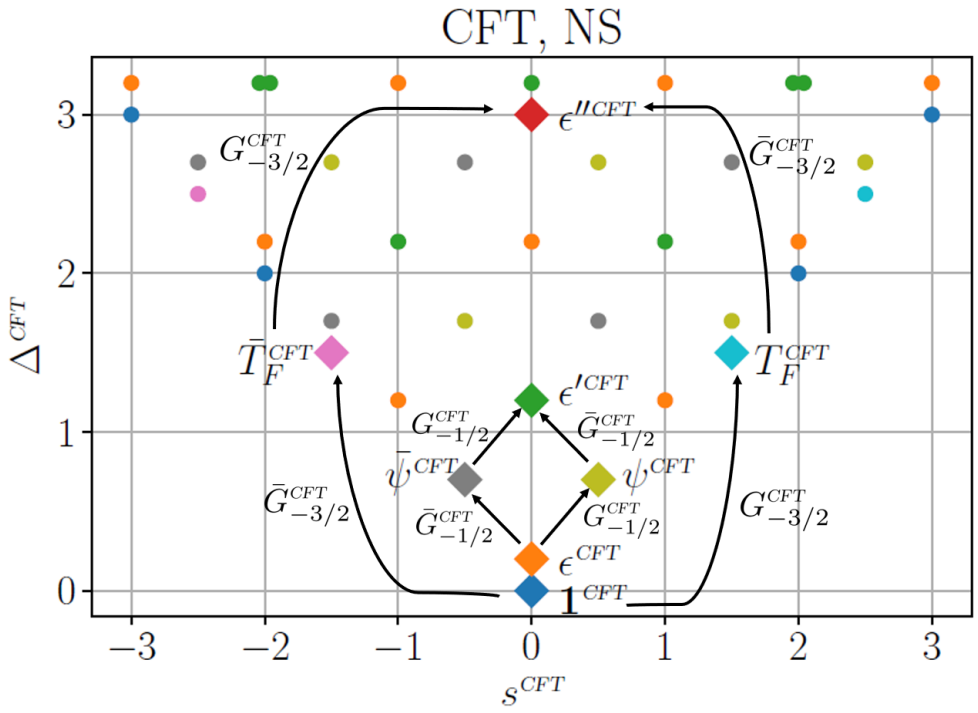

Figure 6.5: Spectrum of the TCI CFT in the NS sector. Primary states are labelled as diamonds. Arrows indicate that the primary states are related by the supervirasoro generators G_m^{CFT}.

In the R sector we can compute

$$|\langle\mu|G_0|\sigma\rangle|^2 \tag{6.136}$$
$$= \langle\sigma|G_0^2|\sigma\rangle \tag{6.137}$$
$$= \langle\sigma|L_0 - \frac{c}{24}|\sigma\rangle \tag{6.138}$$
$$= h_\sigma - \frac{c}{24}. \tag{6.139}$$

Similarly $|\langle\mu'|G_0|\sigma'\rangle|^2$ can be computed.

6.6.4 Lattice supervirasoro generators

In the CFT, the supervirasoro generators are Fourier modes of the fermionic stress tensors, Eq. (6.103). Therefore, we expect that on the lattice Fourier modes of the string operator

T_F also realize the supervirasoro operators at low energies. Recall the definition Eq. (6.41),

$$G_n = \eta \sum_{j=1}^{N} \tilde{\mathcal{T}}^{j-1} T_{F,1} \mathcal{T}^{\dagger j-1} e^{inj2\pi/N}, \tag{6.140}$$

where $\mathcal{T}$ and $\tilde{\mathcal{T}}$ are translation operators for the Hamiltonian with PBC and APBC, respectively, and η is a normalization factor. The equation above applies to both the NS sector ($n \in 1/2 + \mathbb{Z}$) and the R sector ($n \in \mathbb{Z}$). To fix the normalization factor η, we require that

$$\langle T_F | G_{1/2} | T \rangle = \sqrt{3}. \tag{6.141}$$

This comes from the CFT identity

$$\langle T_F^{CFT} | G_{1/2}^{CFT} | T^{CFT} \rangle = \sqrt{3}. \tag{6.142}$$

This can be derived by

$$\langle T_F^{CFT} | G_{1/2}^{CFT} | T^{CFT} \rangle \tag{6.143}$$

$$= \sqrt{\frac{3}{2c^{CFT}}} \langle 0^{CFT} | G_{3/2}^{CFT} G_{1/2}^{CFT} | T^{CFT} \rangle \tag{6.144}$$

$$= \sqrt{\frac{3}{2c^{CFT}}} \langle 0^{CFT} | 2L_2^{CFT} | T^{CFT} \rangle \tag{6.145}$$

$$= \sqrt{\frac{3}{2c^{CFT}}} 2\sqrt{\frac{c^{CFT}}{2}} \tag{6.146}$$

$$= \sqrt{3}, \tag{6.147}$$

where in the second line we use Eq. (6.124), in the third line we use the supervirasoro algebra and the fact that $G_{3/2}$ annihilates $|T\rangle$, and in the fourth line we use Eq. (4.8). Note that both $|T^{CFT}\rangle$ and $|T_F^{CFT}\rangle$ necessarily exist in a SCFT, such that the normalization condition Eq. (6.141) is universally applicable.

Below we compare the matrix elements of G_n on the lattice with the CFT matrix elements Eqs. (6.113)-(6.119). In particular, Eq. (6.118) provides a way of verifying that central charge in Eqs. (6.104) and (6.106) are the same,

$$c' = \frac{3}{2} |\langle T_F | G_{-3/2} | 0 \rangle|^2, \tag{6.148}$$

which equals the central charge c^{CFT} in the thermodynamic limit. This equation can be viewed as the "superpartner" of Eq. (4.8). The result is shown in Fig. (6.6), where we

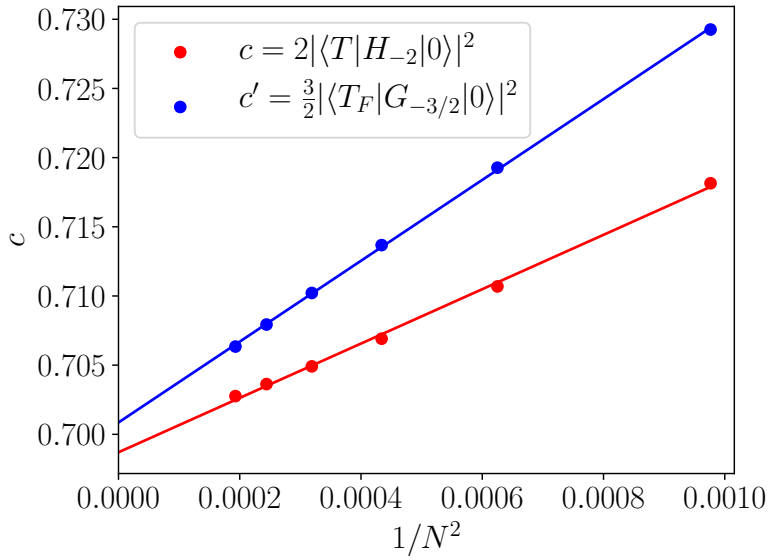

Figure 6.6: The central charge from Eqs. (4.8),(6.118).

also plot the result of Eq. (4.8) for comparison. We obtain $c' = 0.701$ and $c = 0.699$, with the errors on the same order. The other matrix elements in the NS sector are plotted in Fig.(6.7). We see that all matrix elements shown in the figure approximately converge to the nonzero CFT values Eqs. (6.116), (6.117), and (6.119) in the thermodynamic limit. Similarly, we can compute the matrix elements of $\bar{G}_n$, which are the Fourier modes of $\bar{T}_F$, and see that they agree with the CFT values in the thermodynamic limit. Therefore, we have verified in the TCI model that $|\psi\rangle, |\bar{\psi}\rangle, |\epsilon'\rangle$ are supervirasoro descendants of $|\epsilon\rangle$, and $|T_F\rangle, |\bar{T}_F\rangle, |\epsilon''\rangle$ are supervirasoro descendants of $|\mathbf{1}\rangle$. The only supervirasoro primaries in the NS sector are $|\mathbf{1}\rangle$ and $|\epsilon\rangle$.

In the R sector, we can similarly compute the matrix elements of G_n ($n \in \mathbb{Z}$). An important example is G_0 that relates superpartners, as in Eqs. (6.113) and (6.114). The matrix elements can be computed on the lattice, shown in Fig. (6.8). We also see that the numerical results agree with the CFT matrix elements.

To conclude, we have proposed the lattice supervirasoro generators G_n as Fourier modes of the lattice string operator T_F, where the latter is found variationally. We have examined the action of G_n in both NS and R sectors and seen that it agrees with the supervirasoro algebra. The whole construction only relies on the low-energy spectrum of the critical

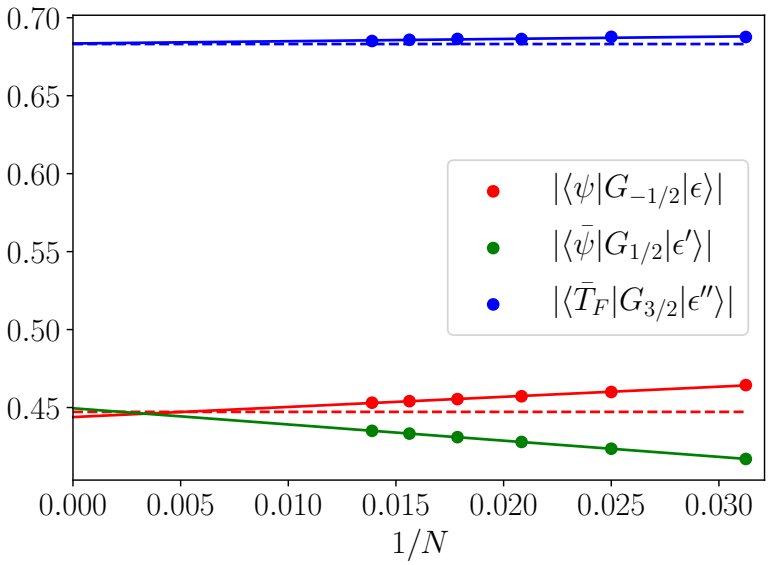

Figure 6.7: Matrix elements of G_n in the NS sector of the TCI model. The dashed lines represent the corresponding CFT matrix element Eqs. (6.116),(6.117),(6.119). The CFT matrix elements Eqs. (6.116),(6.117) have the same modulus, so we only show one of them in the figure.

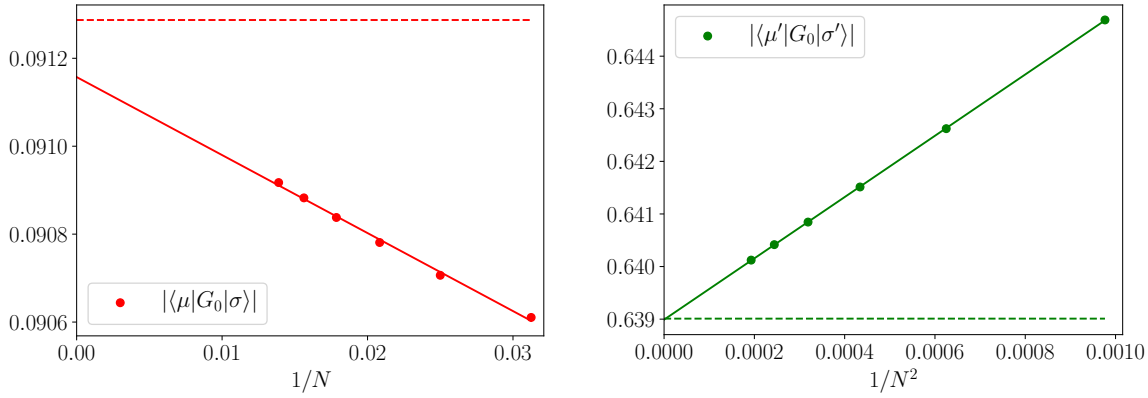

Figure 6.8: Matrix elements of G_n in the R sector of the TCI model. The dashed lines represent the corresponding CFT matrix elements in Eqs. (6.113),(6.114).

quantum spin chain. Therefore we expect that the above lattice construction of G_n gives a generic method to identify supervirasoro primaries and superconformal towers.

6.7 Conclusion

In this chapter, we have generalized the method [140, 141] of extracting conformal data from a critical quantum spin chains from PBC to APBC.

Starting with the lattice Hamiltonian density, we first build the Hamiltonians H^{PBC} and H^{APBC} with PBC and APBC. We then diagonalize the low-energy eigenstates with both boundary conditions and various sizes N. To go beyond exact diagonalization, a generalized puMPS technique has been used. The scaling dimensions Δ_α and conformal spins s_α of scaling operators can be extracted from the energies E_α and momenta P_α of the eigenstates with both boundary conditions. Fourier modes H_n of the Hamiltonian density with respect to the translation operator $\mathcal{T}$ ($\tilde{\mathcal{T}}$) of the (A)PBC Hamiltonian act as a linear combination of Virasoro generators on the low-energy subspace with (A)PBC. They allow us to identify each eigenstate with a CFT scaling operator. In particular, primary states and their conformal towers are identified. The central charge can be extracted with the matrix elements of H_{-2}.

We have shown that local operators correspond to PBC operators in the CFT, and that string operators correspond to APBC operators in the CFT. Given a lattice operator, we can associate it with a truncated linear combination of CFT scaling operators, whose coefficients are determined by minimizing a cost function. The lattice operators that correspond to CFT primary operators can be obtained by inverting the truncated linear expansion. OPE coeffcients can then be extracted from the matrix elements of the Fourier modes of the local or string operators that correspond to CFT primary fields. In the case of emergent superconformal symmetry, the fermionic stress tensor states $|T_F\rangle, |\bar{T}_F\rangle$ are always present in the low-energy spectrum of H^{APBC}. The lattice supervirasoro generators $G_n, \bar{G}_n$ can be constructed as Fourier modes of the string operators that correspond to $T_F, \bar{T}_F$. They can be used to identify supervirasoro primary states and supervirasoro conformal towers. The matrix element of $G_{-3/2}$ gives another estimation of the central charge, which converges to the central charge of the SCFT in the thermodynamic limit.

As an illustration of the general method, we have extracted complete conformal data of the Ising CFT and TCI CFT from the Ising spin chain and the OF model at the TCI point. We have correctly identified all primary states and their conformal towers. Scaling dimensions, conformal spins, the central charges and all OPE coefficients are obtained with

high accuracy. For the OF model, we have verified the action of the lattice supervirasoro generators on the low-energy eigenstates and showed that they agree with the expectation from the superconformal algebra. We stress that the only input of our method is the critical lattice Hamiltonian. It is interesting to apply our method to the cases where the underlying CFT has not been completely solved.

Apart from a complete set of conformal data, generators of extended symmetries (if any) can also be constructed on the lattice. In this paper we have investigated the superconformal symmetry, but other extended symmetry can be treated in the same way, such as the Kac-Moody algebra [127].

Our method can be generalized to other twisted boundary conditions that preserve emergent conformal symmetry. For an on-site symmetry defect, the generalization is straightforward. It is still an open question how to deal with more general conformal defects with our method. We would like to point out that for some topological conformal defects other methods such as tensor network renormalization [60] and entanglement renormalization [35] are available.

Chapter 7

Conclusion and Future directions

In this thesis, we have proposed a systematic method to extract complete conformal data from a critical quantum spin chain based on the operator-state correspondence, thus completing the project initiated by Cardy and others in the 80's. There are several ingredients that are of great significance of the method. First, the Koo-Saleur lattice Virasoro generators allow us to identify primary states and conformal towers within the low-energy eigenstates of the critical quantum spin chain. Second, it is crucial that we can identify lattice operators with CFT operators. This not only enables us to compute OPE coefficients, but also allows us to study the emergence of extended symmetries such as superconformal symmetry. Finally, the puMPS techniques make it possible to obtain accurate low-energy eigenstates for critical quantum spin chains up to several hundreds of spins, which significantly reduces finite-size corrections.

There are several potential applications of the present work in the theis. Roughly speaking, there are two directions. Firstly, one may want to explore CFTs and RG flows that are less well understood. Secondly, one may consider other extended symmetries and conformal defects beyond on-site symmetry defect.

Within the first class, there are several proposed quantum critical points that are not yet completely numerically verfied. One prominent example is the complex CFTs, where conformal data becomes complex rather than real. It has been proposed that the Q-state Potts model with $Q > 4$ can realize such complex CFTs with some perturbations [54, 75]. With our identification of lattice operators and CFT operators, it is possible to find the perturbation and locate the complex critical point. The trajectory of the RG flow near the complex fixed points is more complicated than unitary real CFTs. In the example of the Potts model, it shows a spiral RG flow in the parameter space. It would be very interesting

to explore the RG flow near the complex fixed points.

Within the second class, one may consider Kac-Moody algebra or the W algebra, which can be realized by the XXZ quantum spin chain and the 3-state Potts model, respectively. The presence of more symmetries also means the possibility of general conformal defects. For example, it is interesting to study the Kramers-Wannier duality defect of the Ising CFT [60] and defects with respect to the current algebra in the XXZ model [127].

References

[1] David Aasen, Roger S K Mong, and Paul Fendley. Topological defects on the lattice: I. the ising model. *Journal of Physics A: Mathematical and Theoretical*, 49(35):354001, aug 2016.

[2] P.-A. Absil, R. Mahony, and R. Sepulchre. *Optimization Algorithms on Matrix Manifolds*. Princeton University Press, USA, 2007.

[3] Ian Affleck. Universal term in the free energy at a critical point and the conformal anomaly. *Phys. Rev. Lett.*, 56(7):746–748, February 1986.

[4] Francisco C Alcaraz, Michael N Barber, and Murray T Batchelor. Conformal invariance, the xxz chain and the operator content of two-dimensional critical systems. *Annals of Physics*, 182(2):280 – 343, 1988.

[5] Francisco Castilho Alcaraz, Miguel Ibanez Berganza, and German Sierra. Entanglement of low-energy excitations in conformal field theory. *Phys. Rev. Lett.*, 106:201601, May 2011.

[6] P. W. Anderson. More is different. *Science*, 177(4047):393–396, 1972.

[7] V. V. Bazhanov, S. L. Lukyanov, and A. B. Zamolodchikov. Integrable Quantum Field Theories in Finite Volume: Excited State Energies. *Nuclear Physics B*, 489(3):487–531, April 1997.

[8] Matteo Beccaria, Massimo Campostrini, and Alessandra Feo. Density-matrix renormalization-group study of the disorder line in the quantum axial next-nearest-neighbor Ising model. *Physical Review B*, 73(5), February 2006.

[9] A. A. Belavin, A. M. Polyakov, and A. B. Zamolodchikov. Infinite conformal symmetry in two-dimensional quantum field theory. *Nucl. Phys. B*, 241(2):333–380, July 1984.

[10] H. W. J. Blöte, John L. Cardy, and M. P. Nightingale. Conformal invariance, the central charge, and universal finite-size amplitudes at criticality. *Phys. Rev. Lett.*, 56(7):742, February 1986.

[11] H. W. J. Blte, John L. Cardy, and M. P. Nightingale. Conformal Invariance, the Central Charge, and Universal Finite-Size Amplitudes at Criticality. *Phys. Rev. Lett.*, 56(7):742, 1986.

[12] N. M. Bogoliubov, A. G. Izergin, and V. E. Korepin. Quantum inverse scattering method and correlation functions. In *Exactly Solvable Problems in Condensed Matter and Relativistic Field Theory*, Lecture Notes in Physics, pages 220–316. Springer, Berlin, Heidelberg, 1985.

[13] R. Bondesan, J. Dubail, A. Faribault, and Y. Ikhlef. Chiral SU(2)_k currents as local operators in vertex models and spin chains. *J. Phys. A: Math. Theor.*, 48(6):065205, February 2015.

[14] Daniel Boyanovsky. Field theory of the two-dimensional Ising model: Conformal invariance, order and disorder, and bosonization. *Physical Review B*, 39(10):6744–6756, April 1989.

[15] T W Burkhardt and I Guim. Finite-size scaling of the quantum ising chain with periodic, free, and antiperiodic boundary conditions. *Journal of Physics A: Mathematical and General*, 18(1):L33–L38, jan 1985.

[16] J. W. Cai, Q. N. Chen, H. H. Zhao, Z. Y. Xie, M. P. Qin, Z. C. Wei, and T. Xiang. Translation invariant tensor product states in a finite lattice system. *Chinese Physics B*, 20(11):117501, November 2011.

[17] Pasquale Calabrese and John Cardy. Entanglement Entropy and Quantum Field Theory. *J. Stat. Mech.*, 2004(06):P06002, June 2004.

[18] J L Cardy. *Journal of Physics A: Mathematical and General*, 17(18):L961–L964, dec 1984.

[19] J. L. Cardy. Conformal invariance and universality in finite-size scaling. *J. Phys. A: Math. Gen.*, 17(7):L385, 1984.

[20] J. L. Cardy. Logarithmic corrections to finite-size scaling in strips. *J. Phys. A: Math. Gen.*, 19(17):L1093, 1986.

[21] John Cardy. *Scaling and Renormalization in Statistical Physics*. Cambridge University Press, 1 edition edition, April 1996.

[22] John L. Cardy. Operator content of two-dimensional conformally invariant theories. *Nucl. Phys. B*, 270:186–204, 1986.

[23] John L. Cardy. Boundary conditions, fusion rules and the verlinde formula. *Nuclear Physics B*, 324(3):581 – 596, 1989.

[24] Andrea Cavaglià, Stefano Negro, István M. Szécsényi, and Roberto Tateo. $t\bar{T}$-deformed 2d quantum field theories. *J. High Energ. Phys.*, 2016(10):–, October 2016.

[25] Xie Chen, Zheng-Cheng Gu, and Xiao-Gang Wen. Classification of gapped symmetric phases in one-dimensional spin systems. *Phys. Rev. B*, 83:035107, Jan 2011.

[26] Xie Chen, Zheng-Cheng Gu, and Xiao-Gang Wen. Complete classification of one-dimensional gapped quantum phases in interacting spin systems. *Phys. Rev. B*, 84:235128, Dec 2011.

[27] Andrea Coser, Luca Tagliacozzo, and Erik Tonni. On renyi entropies of disjoint intervals in conformal field theory. *Journal of Statistical Mechanics: Theory and Experiment*, 2014(1):P01008, January 2014.

[28] C. Degli, E. Boschi, and F. Ortolani. Investigation of quantum phase transitions using multi-target DMRG methods. *Eur. Phys. J. B*, 41(4):503–516, October 2004.

[29] G. Delfino, G. Mussardo, and P. Simonetti. Correlation functions along a massless flow. *Phys. Rev. D*, 51(12):R6620–R6624, June 1995.

[30] Dayasindhu Dey, Debasmita Maiti, and Manoranjan Kumar. An Efficient Density Matrix Renormalization Group Algorithm for Chains with Periodic Boundary Condition. *Papers in Physics*, 8(0), November 2016.

[31] Philippe Di Francesco, Pierre Mathieu, and David Senechal. *Conformal Field Theory*. Springer, New York, December 2012.

[32] Patrick Dorey and Roberto Tateo. Excited states by analytic continuation of TBA equations. *Nuclear Physics B*, 482(3):639–659, December 1996.

[33] Jerome Dubail, Jesper Lykke Jacobsen, and Hubert Saleur. Conformal field theory at central charge $c = 0$: A measure of the indecomposability (b) parameters. *Nucl. Phys. B*, 834(3):399–422, August 2010.

[34] J. Eisert, M. Cramer, and M. B. Plenio. Colloquium: Area laws for the entanglement entropy. *Rev. Mod. Phys.*, 82:277–306, Feb 2010.

[35] G. Evenbly, P. Corboz, and G. Vidal. Nonlocal scaling operators with entanglement renormalization. *Phys. Rev. B*, 82:132411, Oct 2010.

[36] G. Evenbly and G. Vidal. Tensor Network Renormalization. *Phys. Rev. Lett.*, 115(18):180405, October 2015.

[37] G. Evenbly and G. Vidal. Local scale transformations on the lattice with tensor network renormalization. *Phys. Rev. Lett.*, 116:040401, Jan 2016.

[38] Glen Evenbly and Guifre Vidal. Quantum Criticality with the Multi-scale Entanglement Renormalization Ansatz. In Adolfo Avella and Ferdinando Mancini, editors, *Strongly Correlated Systems*, number 176 in Springer Series in Solid-State Sciences, pages 99–130. Springer Berlin Heidelberg, 2013.

[39] M. Fannes, B. Nachtergaele, and R. F Werner. Finitely correlated states on quantum spin chains. *Commun. Math. Phys.*, 144(3):443–490, 1992.

[40] Adrian Feiguin, Simon Trebst, Andreas W. W. Ludwig, Matthias Troyer, Alexei Kitaev, Zhenghan Wang, and Michael H. Freedman. Interacting Anyons in Topological Quantum Liquids: The Golden Chain. *Phys. Rev. Lett.*, 98(16):160409, April 2007.

[41] Paul Fendley. Excited-state thermodynamics. *Nuclear Physics B*, 374(3):667–691, May 1992.

[42] G. Feverati and P. Grinza. Integrals of motion from TBA and lattice-conformal dictionary. *Nucl. Phys. B*, 702(3):495–515, December 2004.

[43] Giovanni Feverati, Paul A. Pearce, and Francesco Ravanini. Lattice Approach to Excited TBA Boundary Flows: Tricritical Ising Model. *Physics Letters B*, 534(1-4):216–223, May 2002.

[44] P. Di Francesco, H. Saleur, and J.B. Zuber. Critical ising correlation functions in the plane and on the torus. *Nuclear Physics B*, 290:527 – 581, 1987.

[45] Stefan Fredenhagen, Matthias R. Gaberdiel, and Cornelius Schmidt-Colinet. Bulk flows in Virasoro minimal models with boundaries. *Journal of Physics A: Mathematical and Theoretical*, 42(49):495403, December 2009.

[46] Daniel Friedan, Zongan Qiu, and Stephen Shenker. Conformal Invariance, Unitarity, and Critical Exponents in Two Dimensions. *Phys. Rev. Lett.*, 52(18):1575–1578, April 1984.

[47] Daniel Friedan, Zongan Qiu, and Stephen Shenker. Superconformal invariance in two dimensions and the tricritical ising model. *Physics Letters B*, 151(1):37 – 43, 1985.

[48] M. Fuehringer, S. Rachel, R. Thomale, M. Greiter, and P. Schmitteckert. DMRG studies of critical SU(N) spin chains. *Ann. Phys. (Berlin)*, 17(12):922–936, December 2008.

[49] A. M. Gainutdinov, J. L. Jacobsen, N. Read, H. Saleur, and R. Vasseur. Logarithmic Conformal Field Theory: A Lattice Approach. *J. Phys. A: Math. Theor.*, 46(49):494012, December 2013.

[50] A. M. Gainutdinov and R. Vasseur. Lattice fusion rules and logarithmic operator product expansions. *Nucl. Phys. B*, 868(1):223–270, March 2013.

[51] Martin Ganahl, Julián Rincón, and Guifre Vidal. Continuous matrix product states for quantum fields: An energy minimization algorithm. *Phys. Rev. Lett.*, 118:220402, Jun 2017.

[52] Paul Ginsparg. Applied Conformal Field Theory. *lecture notes*, November 1988.

[53] Philip Giokas and Gerard Watts. The renormalisation group for the truncated conformal space approach on the cylinder. June 2011.

[54] Victor Gorbenko, Slava Rychkov, and Bernardo Zan. Walking, weak first-order transitions, and complex CFTs. *Journal of High Energy Physics*, 2018(10):108, October 2018.

[55] Paulo R. Colares Guimares, Joo A. Plascak, Francisco C. S Barreto, and Joo Florencio. Quantum phase transitions in the one-dimensional transverse Ising model with second-neighbor interactions. *Physical Review B*, 66(6), August 2002.

[56] Jutho Haegeman, J. Ignacio Cirac, Tobias J. Osborne, Iztok Pižorn, Henri Verschelde, and Frank Verstraete. Time-Dependent Variational Principle for Quantum Lattices. *Phys. Rev. Lett.*, 107(7):070601, August 2011.

[57] Jutho Haegeman, Spyridon Michalakis, Bruno Nachtergaele, Tobias J. Osborne, Norbert Schuch, and Frank Verstraete. Elementary Excitations in Gapped Quantum Spin Systems. *Phys. Rev. Lett.*, 111(8):080401, August 2013.

[58] Jutho Haegeman, Tobias J. Osborne, and Frank Verstraete. Post-matrix product state methods: To tangent space and beyond. *Phys. Rev. B*, 88(7):075133, August 2013.

[59] Martin Hasenbusch. Two- and three-point functions at criticality: Monte Carlo simulations of the improved three-dimensional Blume-Capel model. *Physical Review E*, 97(1), January 2018.

[60] Markus Hauru, Glen Evenbly, Wen Wei Ho, Davide Gaiotto, and Guifre Vidal. Topological conformal defects with tensor networks. *Phys. Rev. B*, 94(11):115125, September 2016.

[61] M Henkel. Finite-size scaling and universality in the spectrum of the quantum ising chain. i. periodic and antiperiodic boundary condition. *Journal of Physics A: Mathematical and General*, 20(4):995–1010, mar 1987.

[62] Malte Henkel. *Conformal Invariance and Critical Phenomena*. Springer, New York, 1999.

[63] C. Holzhey, F. Larsen, and F. Wilczek. Geometric and Renormalized Entropy in Conformal Field Theory. *Nucl. Phys. B*, 424(3):443–467, August 1994.

[64] Timothy H. Hsieh, Gábor B. Halász, and Tarun Grover. All majorana models with translation symmetry are supersymmetric. *Phys. Rev. Lett.*, 117:166802, Oct 2016.

[65] P. Jordan and E. Wigner. Über das Paulische Äquivalenzverbot. *Zeitschrift fur Physik*, 47:631–651, September 1928.

[66] D. A. Kastor, E. J. Martinec, and S. H. Shenker. RG flow in N = 1 discrete series. *Nucl. Phys. B*, 316(3):590–608, April 1989.

[67] Timothy R. Klassen and Ezer Melzer. Spectral flow between conformal field theories in 1 + 1 dimensions. *Nucl. Phys. B*, 370(3):511–550, February 1992.

[68] W. M. Koo and H. Saleur. Representations of the Virasoro algebra from lattice models. *Nucl. Phys. B*, 426(3):459–504, September 1994.

[69] V. E. Korepin, N. M. Bogoliubov, and A. G. Izergin. *Quantum Inverse Scattering Method and Correlation Functions*. Cambridge University Press, March 1997. Google-Books-ID: VbgLaZ40aN8C.

[70] Michael Lässig, Giuseppe Mussardo, and John L. Cardy. The scaling region of the tricritical Ising model in two dimensions. *Nucl. Phys. B*, 348(3):591–618, January 1991.

[71] Andreas M. Läuchli. Operator content of real-space entanglement spectra at conformal critical points. *arXiv:1303.0741 [cond-mat, physics:hep-th, physics:quant-ph]*, March 2013.

[72] F. Lesage, H. Saleur, and P. Simonetti. Boundary flows in minimal models. *Physics Letters B*, 427(1-2):85–92, May 1998.

[73] Michael Levin and Cody P. Nave. Tensor renormalization group approach to two-dimensional classical lattice models. *Phys. Rev. Lett.*, 99:120601, Sep 2007.

[74] Andreas W. W. Ludwig and John L. Cardy. Perturbative evaluation of the conformal anomaly at new critical points with applications to random systems. *Nucl. Phys. B*, 285(Supplement C):687–718, January 1987.

[75] Han Ma and Yin-Chen He. Shadow of complex fixed point: Approximate conformality of $q > 4$ potts model. *Phys. Rev. B*, 99:195130, May 2019.

[76] Márcio José Martins. Complex excitations in the thermodynamic Bethe-anzatz approach. *Phys. Rev. Lett.*, 67(4):419–421, July 1991.

[77] I. P. McCulloch. Infinite size density matrix renormalization group, revisited. April 2008.

[78] Lauren McGough, Márk Mezei, and Herman Verlinde. Moving the CFT into the bulk with $T\bar T$. November 2016.

[79] A. Milsted, L. Seabra, I. C. Fulga, C. W. J. Beenakker, and E. Cobanera. Statistical translation invariance protects a topological insulator from interactions. *Phys. Rev. B*, 92(8):085139, August 2015.

[80] Ashley Milsted and Guifre Vidal. Extraction of conformal data in critical quantum spin chains using the Koo-Saleur formula. *Phys. Rev. B*, 96:245105, December 2017.

[81] Alessandro Mossa and Giuseppe Mussardo. Analytic properties of the free energy: the tricritical ising model. *Journal of Statistical Mechanics: Theory and Experiment*, 2008(03):P03010, mar 2008.

[82] A. Neveu and J. H. Schwarz. Tachyon-free dual model with a positive-intercept trajectory. *Physics Letters B*, 34(6):517 – 518, 1971.

[83] Edward O'Brien and Paul Fendley. Lattice supersymmetry and order-disorder coexistence in the tricritical Ising model. *Phys. Rev. Lett.*, 120:206403, May 2018.

[84] Roman Orus. Advances on Tensor Network Theory: Symmetries, Fermions, Entanglement, and Holography. *The European Physical Journal B*, 87(11), November 2014.

[85] Sung-Been Park and Min-Chul Cha. Matrix product state approach to the finite-size scaling properties of the one-dimensional critical quantum Ising model. *Journal of the Korean Physical Society*, 67(9):1619–1623, November 2015.

[86] Paul A. Pearce, Leung Chim, and Changrim Ahn. Excited TBA Equations I: Massive Tricritical Ising Model. *Nuclear Physics B*, 601(3):539–568, May 2001.

[87] Paul A. Pearce, Leung Chim, and Changrim Ahn. Excited TBA Equations II: Massless Flow from Tricritical to Critical Ising Model. *Nuclear Physics B*, 660(3):579–606, June 2003.

[88] Michael E. Peskin and Daniel V. Schroeder. *An Introduction To Quantum Field Theory*. Westview Press, 1995.

[89] Peter Pippan, Steven R. White, and Hans Gerd Evertz. Efficient matrix-product state method for periodic boundary conditions. *Phys. Rev. B*, 81(8):081103, February 2010.

[90] B. Pirvu, F. Verstraete, and G. Vidal. Exploiting translational invariance in matrix product state simulations of spin chains with periodic boundary conditions. *Phys. Rev. B*, 83(12):125104, March 2011.

[91] B. Pirvu, G. Vidal, F. Verstraete, and L. Tagliacozzo. Matrix product states for critical spin chains: Finite-size versus finite-entanglement scaling. *Phys. Rev. B*, 86(7):075117, August 2012.

[92] Bogdan Pirvu, Jutho Haegeman, and Frank Verstraete. A matrix product state based algorithm for determining dispersion relations of quantum spin chains with periodic boundary conditions. *Phys. Rev. B*, 85(3):035130, January 2012.

[93] David Poland, Slava Rychkov, and Alessandro Vichi. The Conformal Bootstrap: Theory, Numerical Techniques, and Applications. 2018.

[94] Joseph Polchinski. Scale and conformal invariance in quantum field theory. *Nuclear Physics B*, 303(2):226–236, June 1988.

[95] F Pollmann and J E Moore. Entanglement spectra of critical and near-critical systems in one dimension. *New Journal of Physics*, 12(2):025006, feb 2010.

[96] Frank Pollmann, Subroto Mukerjee, Ari M. Turner, and Joel E. Moore. Theory of finite-entanglement scaling at one-dimensional quantum critical points. *Phys. Rev. Lett.*, 102:255701, Jun 2009.

[97] Alexander M. Polyakov. Conformal symmetry of critical fluctuations. *JETP Lett.*, 12:381–383, 1970. [Pisma Zh. Eksp. Teor. Fiz.12,538(1970)].

[98] Armin Rahmani, Xiaoyu Zhu, Marcel Franz, and Ian Affleck. Emergent Supersymmetry from Strongly Interacting Majorana Zero Modes. *Phys. Rev. Lett.*, 115(16):166401, October 2015.

[99] Armin Rahmani, Xiaoyu Zhu, Marcel Franz, and Ian Affleck. Phase Diagram of the Interacting Majorana Chain Model. *Phys. Rev. B*, 92(23):235123, December 2015.

[100] Mykhailo V. Rakov and Michael Weyrauch. Bilinear-biquadratic spin-1 rings: An SU(2)-symmetric MPS algorithm for periodic boundary conditions. *Journal of Physics Communications*, 1(1):015007, August 2017.

[101] P. Ramond. Dual theory for free fermions. *Phys. Rev. D*, 3:2415–2418, May 1971.

[102] N. Read and H. Saleur. Associative-algebraic approach to logarithmic conformal field theories. *Nucl. Phys. B*, 777(3):316–351, August 2007.

[103] N. Read and H. Saleur. Enlarged symmetry algebras of spin chains, loop models, and S-matrices. *Nucl. Phys. B*, 777(3):263–315, August 2007.

[104] Stefan Rommer and Stellan Östlund. Class of ansatz wave functions for one-dimensional spin systems and their relation to the density matrix renormalization group. *Phys. Rev. B*, 55(4):2164–2181, January 1997.

[105] Davide Rossini, Vittorio Giovannetti, and Rosario Fazio. Stiffness in 1D Matrix Product States with periodic boundary conditions. *Journal of Statistical Mechanics: Theory and Experiment*, 2011(05):P05021, May 2011.

[106] Subir Sachdev. *Quantum Phase Transitions*. Cambridge University Press, 2 edition, May 2011.

[107] Anders W. Sandvik. Computational Studies of Quantum Spin Systems. *AIP Conf. Proc.*, 1297(1):135–338, November 2010.

[108] U. Schollwöck. The density-matrix renormalization group. *Rev. Mod. Phys.*, 77(1):259–315, April 2005.

[109] Ulrich Schollwöck. The density-matrix renormalization group in the age of matrix product states. *Annals of Physics*, 326(1):96–192, January 2011.

[110] Walter Selke. The ANNNI model — Theoretical analysis and experimental application. *Phys. Rep.*, 170(4):213–264, November 1988.

[111] Sukhwinder Singh, Robert N. C. Pfeifer, and Guifre Vidal. Tensor network decompositions in the presence of a global symmetry. *Phys. Rev. A*, 82:050301, Nov 2010.

[112] Sukhwinder Singh, Robert N. C. Pfeifer, and Guifre Vidal. Tensor network states and algorithms in the presence of a global $u(1)$ symmetry. *Phys. Rev. B*, 83:115125, Mar 2011.

[113] Sukhwinder Singh and Guifre Vidal. Global symmetries in tensor network states: Symmetric tensors versus minimal bond dimension. *Phys. Rev. B*, 88:115147, Sep 2013.

[114] F. A. Smirnov and A. B. Zamolodchikov. On space of integrable quantum field theories. *Nucl. Phys. B*, 915:363–383, February 2017.

[115] Mark Srednicki. *Quantum Field Theory*. Cambridge Univ. Press, Cambridge, 2007.

[116] Vid Stojevic, Jutho Haegeman, I. P. McCulloch, Luca Tagliacozzo, and Frank Verstraete. Conformal data from finite entanglement scaling. *Phys. Rev. B*, 91(3):035120, January 2015.

[117] L. Tagliacozzo, Thiago. R. de Oliveira, S. Iblisdir, and J. I. Latorre. Scaling of entanglement support for matrix product states. *Phys. Rev. B*, 78(2):024410, July 2008.

[118] Laurens Vanderstraeten, Frank Verstraete, and Jutho Haegeman. Scattering particles in quantum spin chains. *Phys. Rev. B*, 92(12):125136, September 2015.

[119] Romain Vasseur, Azat M. Gainutdinov, Jesper Lykke Jacobsen, and Hubert Saleur. The puzzle of bulk conformal field theories at central charge $c = 0$. *Phys. Rev. Lett.*, 108:161602, April 2012.

[120] Romain Vasseur and Jesper Lykke Jacobsen. Operator content of the critical Potts model in d dimensions and logarithmic correlations. *Nuclear Physics B*, 880:435–475, March 2014.

[121] F. Verstraete and J. I. Cirac. Matrix product states represent ground states faithfully. *Phys. Rev. B*, 73:094423, Mar 2006.

[122] F. Verstraete, J. I. Cirac, J. I. Latorre, E. Rico, and M. M. Wolf. Renormalization-Group Transformations on Quantum States. *Phys. Rev. Lett.*, 94(14):140601, April 2005.

[123] F. Verstraete, D. Porras, and J. I. Cirac. DMRG and periodic boundary conditions: A quantum information perspective. *Phys. Rev. Lett.*, 93(22):227205, November 2004.

[124] G. Vidal. Classical Simulation of Infinite-Size Quantum Lattice Systems in One Spatial Dimension. *Phys. Rev. Lett.*, 98:070201, February 2007.

[125] G. Vidal. Entanglement Renormalization. *Phys. Rev. Lett.*, 99(22):220405, November 2007.

[126] Guifré Vidal. Efficient Simulation of One-Dimensional Quantum Many-Body Systems. *Phys. Rev. Lett.*, 93(4):040502, July 2004.

[127] Ruoshui Wang, Yijian Zou, and Guifré Vidal. Upcoming. *Upcoming*, 2019.

[128] Steven Weinberg. *The Quantum Theory of Fields, Volume 1: Foundations*. Cambridge University Press, 2005.

[129] Steven R. White. Density matrix formulation for quantum renormalization groups. *Phys. Rev. Lett.*, 69(19):2863–2866, November 1992.

[130] Kenneth G. Wilson. The renormalization group: Critical phenomena and the Kondo problem. *Rev. Mod. Phys.*, 47(4):773–840, October 1975.

[131] Kenneth G. Wilson and J. Kogut. The renormalization group and the ϵ expansion. *Phys. Rep.*, 12(2):75–199, August 1974.

[132] J. C. Xavier. Entanglement entropy, conformal invariance, and the critical behavior of the anisotropic spin-s Heisenberg chains: DMRG study. *Phys. Rev. B*, 81(22):224404, June 2010.

[133] A. B. Zamolodchikov. Renormalization group and perturbation theory about fixed points in two-dimensional field theory. *Sov. J. Nucl. Phys.*, 46(6):1090–1096, 1987.

[134] Al. B. Zamolodchikov. From tricritical Ising to critical Ising by thermodynamic Bethe ansatz. *Nucl. Phys. B*, 358(3):524–546, July 1991.

[135] Al. B. Zamolodchikov. Thermodynamic Bethe ansatz for RSOS scattering theories. *Nucl. Phys. B*, 358(3):497–523, July 1991.

[136] Al. B. Zamolodchikov. Mass scale in the sine–gordon model and its reductions. *Int. J. Mod. Phys. A*, 10(08):1125–1150, March 1995.

[137] V. Zauner-Stauber, L. Vanderstraeten, M. T. Fishman, F. Verstraete, and J. Haegeman. Variational optimization algorithms for uniform matrix product states. *Phys. Rev. B*, 97:045145, January 2018.

[138] V. Zauner-Stauber, L. Vanderstraeten, J. Haegeman, I. P. McCulloch, and F. Verstraete. Topological nature of spinons and holons: Elementary excitations from matrix product states with conserved symmetries. *Phys. Rev. B*, 97:235155, Jun 2018.

[139] Modjtaba Shokrian Zini and Zhenghan Wang. Conformal Field Theories as Scaling Limit of Anyonic Chains. June 2017.

[140] Yijian Zou, Ashley Milsted, and Guifre Vidal. Conformal data and renormalization group flow in critical quantum spin chains using periodic uniform matrix product states. *Phys. Rev. Lett.*, 121:230402, Dec 2018.

[141] Yijian Zou, Ashley Milsted, and Guifre Vidal. Conformal fields and operator product expansion in critical quantum spin chains. *Phys. Rev. Lett.*, 124:040604, Jan 2020.

[142] Yijian Zou and Guifre Vidal. Emergence of conformal symmetry in quantum spin chains: Antiperiodic boundary conditions and supersymmetry. *Phys. Rev. B*, 101:045132, Jan 2020.

APPENDICES

Appendix A

Matrix product operators

In this appendix we review the matrix product operators (MPOs) that are used in the main text. The MPOs are used to represent the Hamiltonians or more generally Fourier modes of local operators. We will split them into a bulk contribution, which is represented by a MPO with open boundary conditions (OBC) and a boundary term.

A.1 Hamiltonian and H_n operator

For the critical Ising model

$$H = \left[-\sum_{j=1}^{N-1} X_j X_{j+1} - \sum_{j=1}^{N} Z_j \right] - X_N X_1. \tag{A.1}$$

The term in the bracket is represented as a MPO with OBC

$$\left[-\sum_{j=1}^{N-1} X_j X_{j+1} - \sum_{j=1}^{N} Z_j \right] = \sum_{\vec{s},\vec{s'}} (M_1^{s_1 s'_1} M_2^{s_2 s'_2} \cdots M_N^{s_N s'_N} |\vec{s}\rangle\langle\vec{s'}|, \tag{A.2}$$

where the tensors are

$$M_2 = \cdots = M_{N-1} = \begin{bmatrix} I & 0 & 0 \\ X & 0 & 0 \\ -Z & -X & I \end{bmatrix} \tag{A.3}$$

$$M_1 = \begin{bmatrix} -Z & -X & I \end{bmatrix} \quad M_N = \begin{bmatrix} I \\ X \\ -Z \end{bmatrix}. \tag{A.4}$$

Similarly, the Fourier mode H_n is (up to overall normalization)

$$H_n = \left[-\sum_{j=1}^{N-1} X_j X_{j+1} e^{in(j+1/2)2\pi/N} - \sum_{j=1}^{N} Z_j e^{inj2\pi/N} \right] - X_N X_1 e^{in\pi/N}, \tag{A.5}$$

see Appendix C for an explanation of the extra 1/2 in the phase factor. The H_n operator can be splited into a bulk contribution and a boundary contribution, where the bulk contribution can be represented as a MPO with tensors

$$M_j = \begin{bmatrix} I & 0 & 0 \\ X & 0 & 0 \\ -Ze^{inj2\pi/N} & -Xe^{in(j+1/2)2\pi/N} & I \end{bmatrix} \quad (2 \le j \le N-1) \tag{A.6}$$

$$M_1 = \begin{bmatrix} -Ze^{in2\pi/N} & -Xe^{in3\pi/N} & I \end{bmatrix} \quad M_N = \begin{bmatrix} I \\ X \\ -Z \end{bmatrix}. \tag{A.7}$$

The boundary term can be represented as a trivial MPO with bond dimenson 1.

Next, consider the OF model,

$$H = \left[\sum_{j=1}^{N-1} -X_j X_{j+1} - \sum_{j=1}^{N} Z_j + \lambda^* \sum_{j=1}^{N-2} (X_j X_{j+1} Z_{j+2} + Z_j X_{j+1} X_{j+2}) \right] \tag{A.8}$$

$$-X_N X_1 + \lambda^* (X_{N-1} X_N Z_1 + X_N X_1 Z_2 + Z_{N-1} X_N X_1 + Z_N X_1 X_2). \tag{A.9}$$

The first line is the bulk part, which can be represented as a MPO with OBC, where tensors are

$$M_2 = \cdots = M_{N-1} = \begin{bmatrix} I & 0 & 0 & 0 & 0 & 0 \\ Z & 0 & 0 & 0 & 0 & 0 \\ X & 0 & 0 & 0 & 0 & 0 \\ 0 & X & 0 & 0 & 0 & 0 \\ 0 & 0 & X & 0 & 0 & 0 \\ -Z & 0 & -X & \lambda^* X & \lambda^* Z & I \end{bmatrix} \tag{A.10}$$

$$M_1 = \begin{bmatrix} -Z & 0 & -X & \lambda^* X & \lambda^* Z & I \end{bmatrix} \quad M_N = \begin{bmatrix} I \\ Z \\ X \\ 0 \\ 0 \\ -Z \end{bmatrix}. \tag{A.11}$$

The boundary terms can be represented as a MPO on 4 sites (from site $N-1$ to site 2), where the tensors are

$$M_{N-1} = \begin{bmatrix} \lambda^* X & \lambda^* Z & I \end{bmatrix} M_N = \begin{bmatrix} X & 0 & 0 & 0 \\ 0 & X & 0 & 0 \\ 0 & -X & \lambda^* X & \lambda^* Z \end{bmatrix} \tag{A.12}$$

$$M_1 = \begin{bmatrix} Z & 0 & 0 \\ X & 0 & 0 \\ 0 & X & 0 \\ 0 & 0 & X \end{bmatrix} \quad M_2 = \begin{bmatrix} I \\ Z \\ X \end{bmatrix}. \tag{A.13}$$

The H_n operator for the OF model can be represented with a similar MPO (with maximal bond dimension 6). However, in practice, we can also represent the H_n for the OF model as the sum of the H_n for the Ising model and the two simple MPOs, namely the Fourier modes of XXZ and ZXX, see below.

A.2 Fourier mode of simple local operators

A Fourier mode of a one-site operator A_j ($A \in \{I, X, Y, Z\}$) (up to overall normalization),

$$A^s = \sum_{j=1}^{N} A_j e^{isj2\pi/N} \tag{A.14}$$

can be represented with a MPO with bond dimension 2, where tensors are

$$M_j = \begin{bmatrix} I & 0 \\ Ae^{isj2\pi/N} & I \end{bmatrix} \quad (2 \le j \le N-1) \tag{A.15}$$

$$M_1 = \begin{bmatrix} Ae^{is2\pi/N} & I \end{bmatrix} \quad M_N = \begin{bmatrix} I \\ A \end{bmatrix}. \tag{A.16}$$

Similarly, a Fourier mode of a two-site operator AB ($A, B \in \{I, X, Y, Z\}$) (up to overall normalization),

$$(AB)^s = \sum_{j=1}^{N-1} A_j B_{j+1} e^{isj2\pi/N} + A_N B_1 \tag{A.17}$$

can be represented as a MPO with OBC plus the boundary term $A_N B_1$, where the MPO has tensors

$$M_j = \begin{bmatrix} I & 0 & 0 \\ B & 0 & 0 \\ 0 & Ae^{isj2\pi/N} & I \end{bmatrix} \quad (2 \leq j \leq N-1) \tag{A.18}$$

$$M_1 = \begin{bmatrix} 0 & Ae^{is2\pi/N} & I \end{bmatrix} \quad M_N = \begin{bmatrix} I \\ B \\ 0 \end{bmatrix}. \tag{A.19}$$

For 3-site operators ABC ($A, B, C \in \{I, X, Y, Z\}$), the Fourier mode with spin s

$$(ABC)^s = \left[\sum_{j=1}^{N-2} A_j B_{j+1} C_{j+2} e^{isj2\pi/N}\right] + A_{N-1} B_N C_1 e^{-is2\pi/N} + A_N B_1 C_2 \tag{A.20}$$

can be represented with a MPO with bond dimension 4 in the bulk, and two boundary terms, where the MPO for the bulk contributions has tensors

$$M_j = \begin{bmatrix} I & 0 & 0 & 0 \\ C & 0 & 0 & 0 \\ 0 & B & 0 & 0 \\ 0 & 0 & Ae^{isj2\pi/N} & I \end{bmatrix} \quad (2 \leq j \leq N-1) \tag{A.21}$$

$$M_1 = \begin{bmatrix} 0 & 0 & Ae^{is2\pi/N} & I \end{bmatrix} \quad M_N = \begin{bmatrix} I \\ C \\ 0 \\ 0 \end{bmatrix}. \tag{A.22}$$

Fourier modes of complicated operators (e.g., 4-site operators) can be constructed similarly as a MPO with a larger bond dimension. However, we don't need them in all the models in this thesis.

Appendix B

Fourier modes of multi-site operators

Recall that the Fourier mode of a local operator $\mathcal{O}$ is defined by

$$\mathcal{O}^s = \frac{1}{N}\sum_{j=1}^{N} e^{-isx_j 2\pi/N}\mathcal{O}_j, \tag{B.1}$$

where x_j is the position of the operator $\mathcal{O}_j$ with support starting at site j. For a one-site operator, $x_j = j$. (In the main text we have use j instead of x_j for simplicity of notation.) However, this choice of x_j is ambiguous for a multi-site operator, since it can be anywhere inside the support. We have to decide how to assign a specific position $x_j \in (j, j+n)$ to it. Different assignments will lead to different expansions in terms of CFT operators. However, it is clear that any two such expansions have the same dominant CFT scaling operator, and the difference between the two expansions is dominated by the derivative of this dominant CFT operator.

Let us illustrate the above with an example for the critical Ising model. Consider $\mathcal{O}_1(j) = -X(j)X(j+1)$. We have seen that its CFT expansion $\mathcal{O}_1^{CFT}$ includes both $\mathbf{1}^{CFT}$ and ϵ^{CFT} contributions. For this lattice operator, we may assign e.g. $x_j = j$, $x_j = j + 1/2$, or $x_j = j + 1$. Only the second choice preserves spatial parity, and therefore no $\partial_x\epsilon^{CFT}$ term is allowed in the expansion of O_1^{CFT}. The other two choices would result in a $\partial_x\epsilon^{CFT}$ term in the expansion of $\mathcal{O}_1^{CFT}$, which is in accordance with the fact that our assignment of position has explicitly broken spatial parity. Nevertheless, the expansion coefficients in front of $\mathbf{1}^{CFT}$ and ϵ^{CFT} are independent of our assignment of position x_j.

The specific assignment $x_j = j + 1/2$ for $\mathcal{O}_1(j)$ is important when combining $\mathcal{O}_1(j) = -X(j)X(j+1)$ with $\mathcal{O}_2(j) = -Z(j)$ to form the Hamiltonian density of the Ising model,

$h(j) = \mathcal{O}_1(j) + \mathcal{O}_2(j)$. In order for the Fourier mode h^s to correspond to a linear combination of Virasoro generators $L_{-s}^{CFT} + \bar{L}_s^{CFT}$, it has been shown numerically [80] that the correct choice is $x_j = j + 1/2$ for $O_1(j)$ and $x_j = j$ for $O_2(j)$. If we have chosen a different x_j for $O_1(j)$, the Fourier mode h^s ($s \neq 0$) would connect states in identity tower and ϵ tower. This is exactly the consequence of the $\partial_x \epsilon^{CFT}$ term in the expansion of h. Therefore, the choice of position $x_j = j + 1/2$ for $X(j)X(j+1)$ makes the finite-size corrections in the H_n operator smaller by eliminating the $\partial_x \epsilon^{CFT}$ contribution. In general, the freedom in the assignment of positions does not affect the result we obtain for the conformal data in the thermodynamic limit, while it may change the finite-size scaling.

Similarly, a string operator

$$\mathcal{S}_{\mathcal{O},j} = \left(\prod_{l=1}^{j-1} Z_l \right) \mathcal{O}_j. \tag{B.2}$$

can be assigned some position x_j. Again, the choice of x_j affects the corresponding CFT operator up to a total spatial derivative, which changes the finite-size correction in the Fourier mode $\mathcal{S}_{\mathcal{O}}^s$. Below we list our choice of the positions that are used in the thesis.

For a local operator $\mathcal{O}_j$, if it is $\mathbb{Z}_2$ odd and its support ranges from site j to $j+n$, then we follow the "middle point rule", i.e., $x_j = j + n/2$.

If the operator is $\mathbb{Z}_2$ even, we first rewrite it as a local product of Majorana operators. The Majorana operator $\gamma_{j'}$ is assigned position $x_{j'} = j'/2 + 1/4$. If the product of Majorana operators has support from $\gamma_{j'}$ to $\gamma_{j'+n'}$, then we follow the "middle point rule" $x_j = x_{j'} + n'/4 = (2j' + n' + 1)/4$. (Notice that two adjacent Majorana modes have a distance $1/2$ rather than 1). The above alignment explicitly preserves the Kramers-Wannier duality.

If a string operator is $\mathbb{Z}_2$ odd, then it can be rewritten as a local product of Majorana operators. We can then use the "middle point rule". If the string operator is $\mathbb{Z}_2$ even, then we first use a Jordan-Wigner transformation to obtain a $\mathbb{Z}_2$ odd local operator, then the position of the string operator is assigned to the position of the local operator minus $1/2$. In summary, we list the result of x_j for the operators that have appeared in the main text in Table B.1.

$\mathcal{O}_j$	x_j	$\mathcal{S}_{\mathcal{O},j}$	x_j
X_j	j	$\mathcal{S}_{I,j}$	$j-\frac{1}{2}$
Y_j	j	$\mathcal{S}_{X,j}$	$j-\frac{1}{4}$
Z_j	j	$\mathcal{S}_{Y,j}$	$j+\frac{1}{4}$
X_jX_{j+1}	$j+\frac{1}{2}$	$\mathcal{S}_{YZ,j}$	$j+\frac{3}{4}$
X_jZ_{j+1}	$j+\frac{1}{2}$	$\mathcal{S}_{IX,j}$	$j+\frac{1}{4}$
Z_jX_{j+1}	$j+\frac{1}{2}$	$\mathcal{S}_{XX,j}$	j
$X_jX_{j+1}Z_{j+2}$	$j+\frac{5}{4}$	$\mathcal{S}_{YY,j}$	$j+1$
$Z_jX_{j+1}X_{j+2}$	$j+\frac{3}{4}$		

Table B.1: Position assignment x_j of local operators $\mathcal{O}_j$ and string operators $\mathcal{S}_{\mathcal{O},j}$.

Appendix C

Details of the puMPS algorithm for APBC

In this section we detail the puMPS algorithm for eigenstates with APBC, and how to compute matrix elements of local or string operators involving them. It is a straightforward generalization of the algorithm for eigenstates with PBC, which has been described in detail in [140].

C.1 Computing low-energy eigenstates

Recall the ansatz for APBC eigenstates with momentum p,

$$|\Phi_p^{APBC}(B;A)\rangle = \sum_{j=1}^{N} e^{-ipj}\tilde{\mathcal{T}}^j \sum_{\vec{s}=1}^{d} \mathrm{Tr}(B^{s_1}A^{s_2}\cdots A^{s_N})|\vec{s}\rangle, \tag{C.1}$$

where A is the puMPS tensor for the PBC ground state, satisfying

$$\sum_{s'} \mathcal{Z}_{ss'}A^{s'} = U_B(\mathcal{Z})A^s U_B^\dagger(\mathcal{Z}), \tag{C.2}$$

and $B = B^s_{ab}$ contains the variational parameters to be computed.

In Chapter 4, a reparametrization of the excitation ansatz has been shown useful for PBC eigenstates. Here we will use the same trick for APBC eigenstates. The trick consists of two steps. First, there is a gauge choice of the ground state puMPS tensor $A^s = A^s_C\lambda^{-1}$,

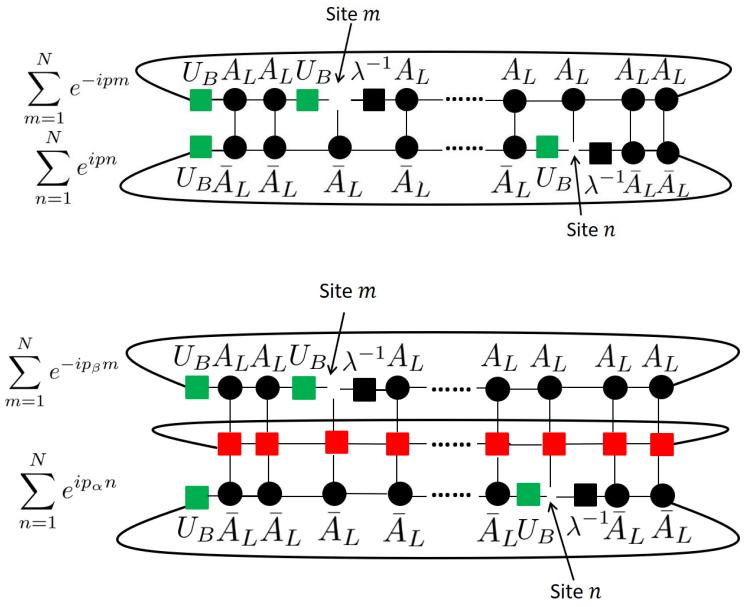

Figure C.1: (Top) The tensor network for $N^{APBC}_{\mu\nu}(p)$ in Eq. (C.6). The green tensor $U_B \equiv U_B(\mathcal{Z})$ in Eq. (6.55). (Bottom) The tensor network for $H^{APBC}_{\mu\nu}(p)$ in Eq. (C.7) if the red tensors form a matrix product operator (MPO) for the Hamiltonian H and $p_\alpha = p_\beta = p$. It also represents $O_{\mu\nu}(p_\alpha, p_\beta)$ in Eq. (C.9) if the red tensors form a MPO for $\tilde{O}^s$.

where A^s_C is a $D \times D$ matrix and λ is $D \times D$ diagonal matrix, such that $A^s_L \equiv A^s = A^s_C \lambda^{-1}$ satisfies the left canonical condition and $A^s_R \equiv \lambda^{-1} A^s_C$ satisfies the right canonical condition. Second, we will reparameterize $B^s = B^s_C \lambda^{-1}$. The new parameterization consists of a $d \times D \times D$ tensor B_C as variational parameters,

$$|\Phi^{APBC}_p(B_C; A_L)\rangle = \sum_{j=1}^{N} e^{-ipj} \tilde{\mathcal{T}}^j \sum_{\vec{s}=1}^{d} \mathrm{Tr}((B^{s_1}_C \lambda^{-1}) A^{s_2}_L \cdots A^{s_N}_L) |\vec{s}\rangle. \tag{C.3}$$

Below we use $\mu = (s, a, b)$ to denote the combined index of the physical and bond indices. Our approximation of the eigenstates of the Hamiltonian are obtained as the saddle point of the energy functional,

$$E_p(B_C, \bar{B}_C; A_L, \bar{A}_L) = \frac{\langle \Phi^{APBC}_p(\bar{B}_C; \bar{A}_L) | H | \Phi^{APBC}_p(B_C; A_L) \rangle}{\langle \Phi^{APBC}_p(\bar{B}_C; \bar{A}_L) | \Phi^{APBC}_p(B_C; A_L) \rangle}. \tag{C.4}$$

The saddle point condition translates into a generalized eigenvalue equation for B^{μ}_{C},

$$H^{APBC}_{\mu\nu}(p)B^{\nu}_{C} = EN^{APBC}_{\mu\nu}(p)B^{\nu}_{C}, \tag{C.5}$$

where

$$N^{APBC}_{\mu\nu}(p) = \left\langle \frac{\partial}{\partial \bar{B}^{\mu}_{C}}\Phi^{APBC}_{p}(\bar{B}_C;\bar{A}_L) \middle| \frac{\partial}{\partial B^{\nu}_{C}}\Phi^{APBC}_{p}(B_C;A_L)\right\rangle \tag{C.6}$$

$$H^{APBC}_{\mu\nu}(p) = \left\langle \frac{\partial}{\partial \bar{B}^{\mu}_{C}}\Phi^{APBC}_{p}(\bar{B}_C;\bar{A}_L) \middle| H \middle| \frac{\partial}{\partial B^{\nu}_{C}}\Phi^{APBC}_{p}(B_C;A_L)\right\rangle. \tag{C.7}$$

They are depicted as tensor networks in Fig. C.1. Note that the action of $\tilde{\mathcal{T}} = \mathcal{Z}_1\mathcal{T}$ can be viewed as first acting with the ordinary translation operator and then acting with $\mathcal{Z}_1$, where the latter can be lifted to the bond indices by using Eq. (C.2). Contracting the tensor networks has the same leading cost $\mathcal{O}(ND^6)$ as the PBC case. The only difference from the case of PBC is the U_B tensors appearing in the contraction. The periodic MPO for the Hamiltonian with PBC can be further decomposed into a MPO for the Hamiltonian with OBC and a local boundary term. This further lowers the cost compared to directly contracting the network with the periodic MPO.

The generalized eigenvalue equation Eq. (C.5) can be translated into an ordinary eigenvalue problem by multiplying the pseudoinverse of $N^{APBC}_{\mu\nu}$ on both sides,

$$\tilde{N}^{APBC,\rho\mu}(p)H^{APBC}_{\mu\nu}(p)B^{\nu}_{C} = EB^{\rho}_{C}, \tag{C.8}$$

where $\tilde{N}^{APBC}(p)$ is the pseudoinverse of $N^{APBC}(p)$. Then Eq. (C.8) can be solved in each momentum sector with a sparse eigenvalue solver such as the Arnoldi method.

C.2 Computing matrix elements of local operators

Matrix elements of a Fourier mode of a local operator in the low-energy basis of H^{APBC} are bilinear functions of the B tensors in Eq. (C.1),

$$\langle\Phi^{APBC}_{p_\alpha}(\bar{B}_{C,\alpha};\bar{A}_L)|\tilde{\mathcal{O}}^{s}|\Phi^{APBC}_{p_\beta}(B_{C,\beta};A_L)\rangle = \bar{B}^{\mu}_{C,\alpha}\mathcal{O}_{\mu\nu}(p_\alpha,p_\beta)B^{\nu}_{C,\beta}. \tag{C.9}$$

This expression is nonzero only if momentum is conserved,

$$p_\alpha = \frac{2\pi}{N}s + p_\beta. \tag{C.10}$$

The matrix $\mathcal{O}_{\mu\nu}(p_\alpha,p_\beta)$ is plotted at the bottom of Fig. C.1. The contraction also costs $\mathcal{O}(ND^6)$.

C.3 Computing matrix elements of string operators

Matrix elements of a Fourier mode of a string operator are also bilinear functions of the B tensors.

$$\langle \Phi^{APBC}_{p_\alpha}(\bar{B}_{C,\alpha}; \bar{A}_L) | \mathcal{S}^s_{\mathcal{O}} | \Phi^{PBC}_{p_\beta}(B_{C,\beta}; A_L) \rangle = \bar{B}^{\mu}_{C,\alpha} \mathcal{S}_{\mathcal{O},\mu\nu}(p_\alpha, p_\beta) B^{\nu}_{C,\beta}. \tag{C.11}$$

Note that the ket is now a PBC low-energy eigenstate, and the bra is a APBC low-energy eigenstate. The conservation of momentum is necessary for the matrix element to be nonzero,

$$p_\alpha = \frac{2\pi}{N} s + p_\beta. \tag{C.12}$$

Although string operators are nonlocal, they can be represented efficiently with a MPO. This means that $\mathcal{S}_{\mathcal{O},\mu\nu}(p_\alpha, p_\beta)$ can be represented as the same network as the bottom network of Fig. C.1, except that the U_B tensors in the upper layer are removed. Therefore the computation of $\mathcal{S}_{\mathcal{O},\mu\nu}(p_\alpha, p_\beta)$ has the same leading cost $\mathcal{O}(ND^6)$ as the computation of $\mathcal{O}_{\mu\nu}(p_\alpha, p_\beta)$.

If $\mathcal{O}$ is a one-site operator, then $\mathcal{S}^s_{\mathcal{O}}$ can be encoded in a MPO with bond dimension 2,

$$\begin{bmatrix} 1 & 0 \end{bmatrix} \prod_{j=1}^{N} \begin{bmatrix} Z_j & \mathcal{O}_j e^{-isj} \\ 0 & I_j \end{bmatrix} \begin{bmatrix} 0 \\ 1 \end{bmatrix}. \tag{C.13}$$

If $\mathcal{O}$ is supported on n sites, then an additional boundary term appears. In this case, $\mathcal{S}^s_{\mathcal{O}}$ can be decomposed into a MPO with bond dimension $n+1$ with open boundary conditions and a boundary term. For example, consider

$$\mathcal{S}^s_{YZ} = \sum_{j=1}^{N-1} e^{-isj2\pi/N} \left(\prod_{l=1}^{j-1} Z_l \right) Y_j Z_{j+1} + \mathcal{B}^s_{YZ}, \tag{C.14}$$

where the sum can be encoded in a MPO with open boundary conditions and bond dimenson 3, and the boundary term is

$$\mathcal{B}^s_{YZ} = e^{-is2\pi} I_1 \left(\prod_{l=2}^{N-1} Z_l \right) Y_N. \tag{C.15}$$

If we act with $\mathcal{B}^s_{YZ}$ on a PBC eigenstate with parity $\mathcal{Z}_\alpha$, then the action can be further simplified,

$$\mathcal{B}^s_{YZ} |\psi^{PBC}_\alpha\rangle = e^{-is2\pi} (iX_N Z_1) \mathcal{Z}_\alpha |\psi^{PBC}_\alpha\rangle. \tag{C.16}$$

We see that the net effect of the boundary term of $\mathcal{S}^s_{\mathcal{O}}$ acting on a PBC eigenstate is equivalent to a local boundary term. Again we decompose $\mathcal{S}^s_{\mathcal{O}}$ into a MPO with OBC and a *local* boundary term. This lowers the computational cost compared to directly contracting the tensor network with a periodic MPO.